SYNTHESIS AND STUDY OF TRANSPARENT *p*- AND *n*-TYPE SEMICONDUCTORS AND LUMINESCENT MATERIALS

CHAPTER 1

INTRODUCTION

The purpose of this work was to synthesize and study new transparent *p*- and *n*-type wide band-gap conductors and luminescent materials by using simple chemical concepts, *i.e.*, atomic number, effective nuclear charge, electronegativity, atomic size, and structural considerations, to achieve desired physical and chemical properties. Results on transparent conductors and related materials are presented in Part I and luminescent materials in Part II; transparent conductors based on chalcogenides are detailed in Part IA and *n*-type transparent conducting oxides are summarized in Part IB.

Most transparent solids like window glass are insulators, while conducting materials are opaque to visible light. Transparent conductors (TCs) are idiosyncratic materials that readily conduct electricity while also exhibiting optical transparency. These unique properties allow TCs to be used in wide range of applications, including energy-conserving windows, electrochromic mirrors and windows, flat-panel displays, solar cells, touch panels, anti-static coatings, and invisible security circuits [1]. The first report of a transparent conductive oxide

appears to be that on thin films of CdO by Badeker in 1907; a large number of additional, potential transparent conductors have been described [2, 3]. All of TCs currently in use are *n* type, *e.g.*, electrons carry the electrical current, oxide materials containing *p*-block metals with a $(n\text{-}1)d^{10}ns^0$ electron configuration, such as ZnO, In_2O_3, CdO, Ga_2O_3, Tl_2O_3, PbO_2, SnO_2, Sb_2O_5 [4, 5], Bi_2O_5 [6], Cd_2SnO_4, $ZnSnO_3$, and Zn_2SnO_4 [1]. The most commonly used *n*-type TCs are In_2O_3:Sn (ITO), fluorine-doped SnO_2, and impurity-doped ZnO [7]. Fluorine-doped SnO_2 is most often used for energy-conserving windows and touch panels, while ITO is used as the front electrode of flat-panel displays [8]. It is important to note that all of the current applications of TCs are limited to electrical applications.

To realize sophisticated, invisible *electronic* devices, *p*-type TCs in which positive charges are the carriers must be developed, as most active functions in semiconductors come from the characteristics of the junction [9, 10]. Since the report in 1997 of *p*-type conductivity in transparent $CuAlO_2$ films [11], other *p*-type materials such as $CuGaO_2$ [12], $CuInO_2$ [13], $CuScO_2$ [14, 15], $CuYO_2$ [16], $SrCu_2O_2$ [17, 18], and LaCuOQ (Q=S, Se) [19-22] have followed, and examples of transparent electronic devices have been reported [23, 24]. Some of the recently reported *p*-type transparent conducting oxide films are summarized in Table 1.1.

TABLE 1.1. Characteristics summary of selected *p*-type transparent conducting oxide films that have been recently reported.

Material	E_g (eV)	σ (S/cm)	T (%) (at 500 nm)	μ (cm^2/V s)	Ref
$CuAlO_2$	3.5	0.95	36	10.4	11
	3.5	~0.3	67	0.13	25, 26
	3.75	2	< 35	0.16	27
$CuGaO_2$	~3.4	5.6×10^{-3}	< 40		26
	3.6	6.3×10^{-2}	80 (visible region)	0.23	28
Fe:$CuGaO_2$		1			12
Ca:$CuInO_2$	3.9	2.8×10^{-3}	~70		13
$CuScO_2$	3.3				14
$CuScO_{2+x}$		15-30	< 30		14
Mg:$CuScO_{2+x}$		25	~50 (at 550 nm)		15
Ca:$CuYO_2$	3.5	1	40-50 (visible region)	< 0.5	16
Mg:$CuCrO_{2+x}$	3.1	220	< 25		29
		1	< 35		29
$SrCu_2O_2$	~3.3	3.9×10^{-3}			17, 18
K:$SrCu_2O_2$	~3.3	4.8×10^{-2}		0.46	17, 18

Most *p*-type transparent conductors are oxides, but the oxide carrier mobilities are typically 2 orders of magnitude smaller than those for their *n*-type counterparts. The conductivities of highly transparent *p*-type oxide conductors are also about 3 orders of magnitude smaller than that of ITO. Improvements in conductivity, while significant, invariably compromise transparency to an unacceptable level. Smaller carrier mobility of *p*-type transparent conducting oxides could be attributed to highly electronegative oxygen, which will attract *p*-type carrier and decrease mobility. Therefore, higher mobility will be achieved by using less electronegative atoms such as sulfur, selenium, and tellurium, instead of oxygen atom. $BaCu_2S_2$ films exhibit a Hall mobility of 3.5 cm^2/V s, which is much higher than the mobilities of order 0.1 cm^2/V s reported for most Cu-based *p*-type transparent oxides [30]. However, the band-gap energy is 2.3 eV; for the visible transparency, the band gap should be larger than 3.1 eV [9]. The work detailed in Chapters 2-6 covers the structures, optical, and electrical properties of new chalcogenide fluoride *p*-type transparent semiconductors MCuQF (M=Ba, Sr; Q=S, Se, and Te). This work has been extended to the synthesis and characterization of BaAgSF (Chapter 7), and an examination of phase stabilization and optical and electrical properties of the *p*-type conductors $BaCu_2S_2$ and $BaCu_2Se_2$ (Chapter 8).

Although current *n*-type transparent conducting oxides exhibit high conductivity and optical transparency, considerable research continues on these materials in hopes of replacing In in ITO for cost reduction and to improve conductivity and wavelength transparency for specialized and new applications [1,

7]. ITO with a conductivity of 10^4 S/cm and > 80% visible transparency for films having a thickness of several hundred nm has been unchallenged for more than 20 years [7]. In Chapter 9, new *n*-type transparent conducting oxides of W-doped In_2O_3 with higher Hall mobility than that of ITO films, and W-doped zinc indium oxide are presented along with results on transparent thin-film transistors (TTFTs) containing SnO_2 or zinc indium oxide as the channel material.

In Part II, new luminescent materials for various applications are presented, emphasizing their optical properties and crystal structures. $BaSnO_3$ is investigated for transparent conductor applications because of its large band gap (3.1 eV) and presence of Sn^{4+} ions with $(n\text{-}1)d^{10}ns^0$ electron configuration in a symmetrical O environment [31]. During investigation of its optical properties, strong near-infrared (NIR) luminescence was observed under ultraviolet excitation at room temperature, which is detailed in Chapters 10 and 11. To improve our understanding of optical property-crystal structure relationships and to develop new luminescent materials, $(La,Y)Sc_3(BO_3)_4:Eu^{3+}$ (Chapter 12) and $(Ba,Sr)_3Sc_2(BO_3)_4:Eu^{2+}$ (Chapter 14) have been prepared and investigated. This work has been extended to studies of new phosphors of $LuAl_3(BO_3)_4$:Ln (Ln = Eu, Tb, and Ce) for lamps and plasma display panels (PDPs) (Chapter 13) and Lu_2O_2S:Ln (Ln = Eu, Tb) for X-ray scintillators (Chapter 15).

A graphical summary of the contents of the dissertation is given in Figure 1.1. An introduction to luminescent materials and the experimental techniques used for their characterization are presented in the following sections.

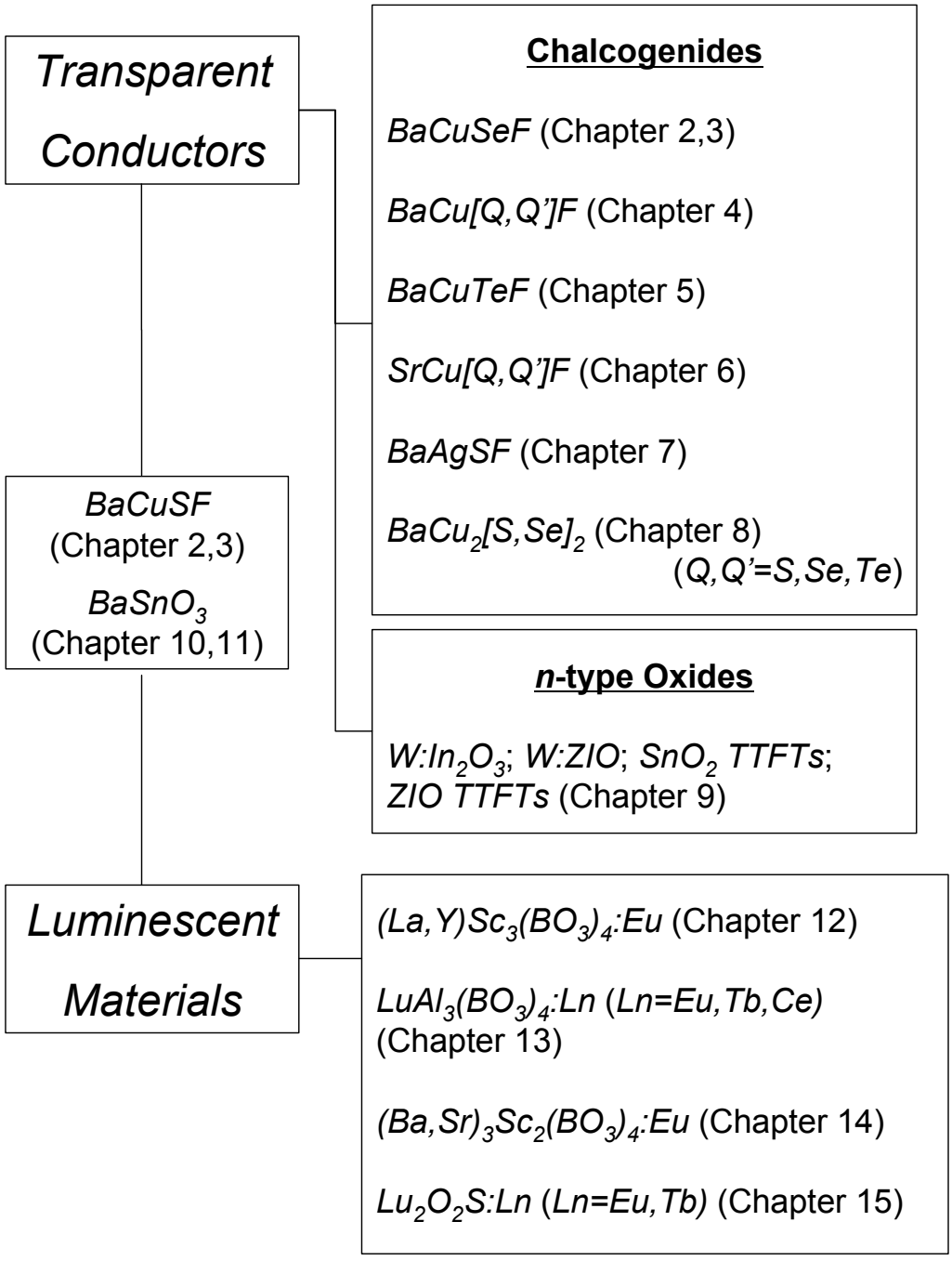

Figure 1.1. Summary of this dissertation.

CHARACTERIZATION OF TRANSPARENT CONDUCTORS

Characteristics of transparent conductors of fundamental and practical importance are electrical conductivity, carrier type (*n* or *p*), Hall mobility, carrier concentration, and optical band gap, and transmittance are also important for materials in film forms.

Electrical Conductivity Measurements

The electrical conductivity (σ) is the ratio of the electric current density to the electric field; it is given by the relation:

$$\sigma = (n \cdot e \cdot \mu_e + p \cdot e \cdot \mu_h),$$

where *n* and *p* are the concentrations (cm^{-3}) of electrons and holes, respectively; e is the charge of an electron; and μ_e and μ_h are the mobilities ($cm^2/V\ s$) of electrons and holes, respectively. The mobility is defined as the magnitude of the drift velocity of the carrier per unit electric field [32]

Practically, the electrical conductivity (σ, S/cm, or $\Omega^{-1}cm^{-1}$) of a material is obtained by taking the reciprocal of its electrical resistivity (ρ, Ωcm). The electrical resistivity of a specimen of length L (cm) and uniform cross section A (cm^2) is given by measuring its resistance R (Ω); they are related by

$$\rho = (R \cdot A) / L$$

Electrical measurements were made in the Department of Physics at Oregon State University by using a four-probe direct current (dc) technique to eliminate

contact resistance of the probes; a schematic of the setup is given in Figure 1.2. A dc current of preset magnitude is supplied to contacts A and D by a Keithley 2400 source, while the voltage drop across probes B and C is measured with a Keithley 195A digital multimeter. The resistance (R) is given by using Ohm's law, R = V / I. For round pellets, the van der Pauw method of resistivity measurement was used. This method also utilizes the advantage of four probes, but any arbitrary shaped sample can be used. Detailed descriptions can be found in Kykyneshi's thesis [33].

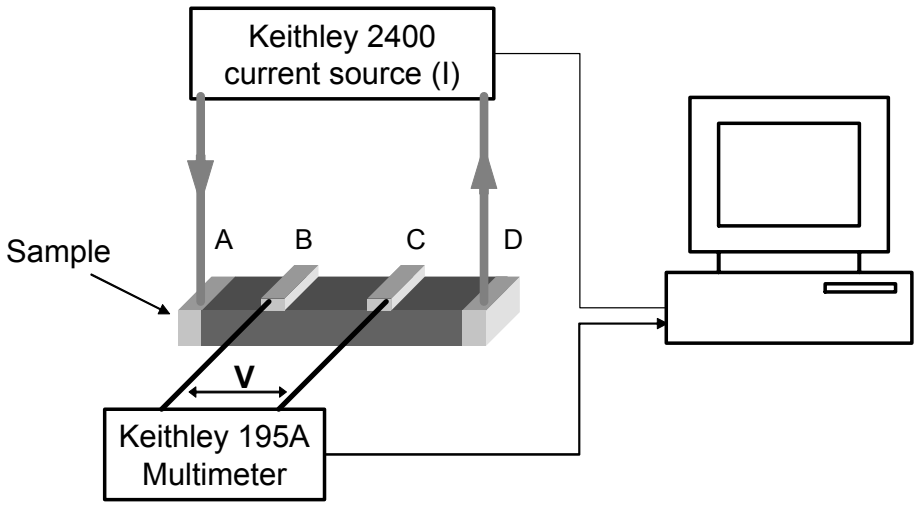

Fig.1.2. A schematic of four-probe conductivity measurement.

Hall-coefficient measurements

When an electric current (I) is passed along the x direction through a conductor in which there is a magnetic field (B_z) along the z direction, an electric field (E_y) is set up along the y axis, which is known as the Hall effect (Figure 1.3) [32, 34, 35]. For a sample of thickness t and width w, the Hall voltage is given as $V_H = -E_y \cdot w$, and the Hall resistance (R_H) is defined as $R_H = V_H / I$. The Hall resistance is also equal to $-B_z / (t \cdot n \cdot e)$, where n is the electron concentration; e is the charge of an electron, and t is sample thickness. By measuring V_H and using known values of I and B_z, the electron density n can be calculated. It is common to use the Hall coefficient (R_0), which is related to the Hall resistance by the equation of $R_0 = -(R_H \cdot t)/ B_z$, which is equal to $-1/(n \cdot e)$. If the carriers are holes, the concentration of holes p is used instead of n, and the Hall coefficient is positive. From the electrical conductivity and the Hall coefficient, Hall mobility can be calculated by using the relation of $\mu = \sigma \cdot R_0$. Hall-coefficient measurements have been performed in the Department of Physics at Oregon State University.

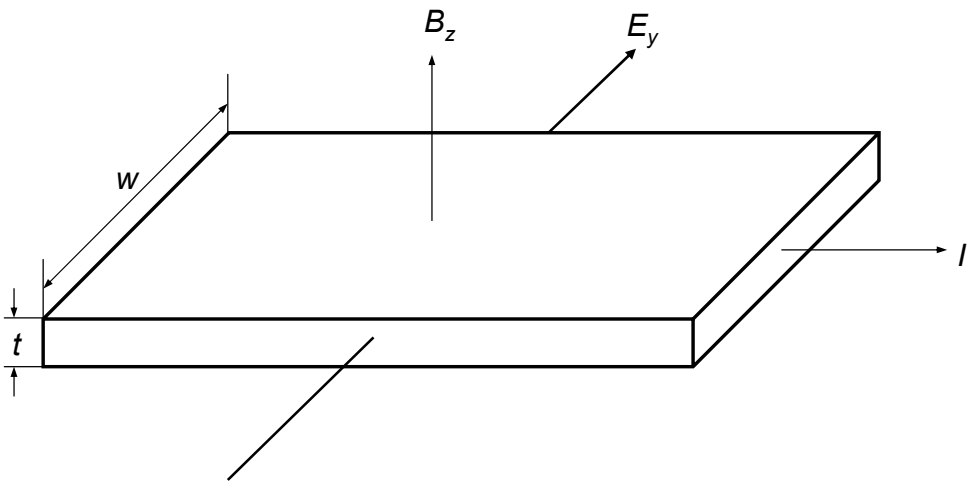

Figure 1.3. A schematic of Hall effect

Seebeck-coefficient measurements

The carrier type (*n* or *p*) can be confirmed through Seebeck-coefficient measurements. In 1821 T. J. Seebeck discovered that when two different conductors are joined into a loop, and a temperature difference is maintained between the two junctions, an electromotive force (emf) will be generated [36, 37]. The emf is generated by accumulation of excess carries at the colder end (Thomson effect). The carriers at hotter end have more thermal energy than those at the colder end, and more carriers move from hotter to colder than vice versa, resulting in accumulation of excess carriers at the colder end and a potential difference. The

two junctions are also a source of emf (the Peltier effect), which is due to the difference in Fermi levels of two different conductors.

The Seebeck-coefficient measurements have been done in the Department of Physics at Oregon State University; a schematic of the set up Seebeck-coefficient measurement is given in Figure 1.4. From the slope of a ΔV *vs.* ΔT graph and the Seebeck coefficient of a Cu block, the Seebeck coefficient of the sample is calculated. A detailed description of the method can be found in Kykyneshi's thesis [33]. A *p*-type material gives a positive Seebeck coefficient, while an *n*-type material exhibits a negative Seebeck coefficient.

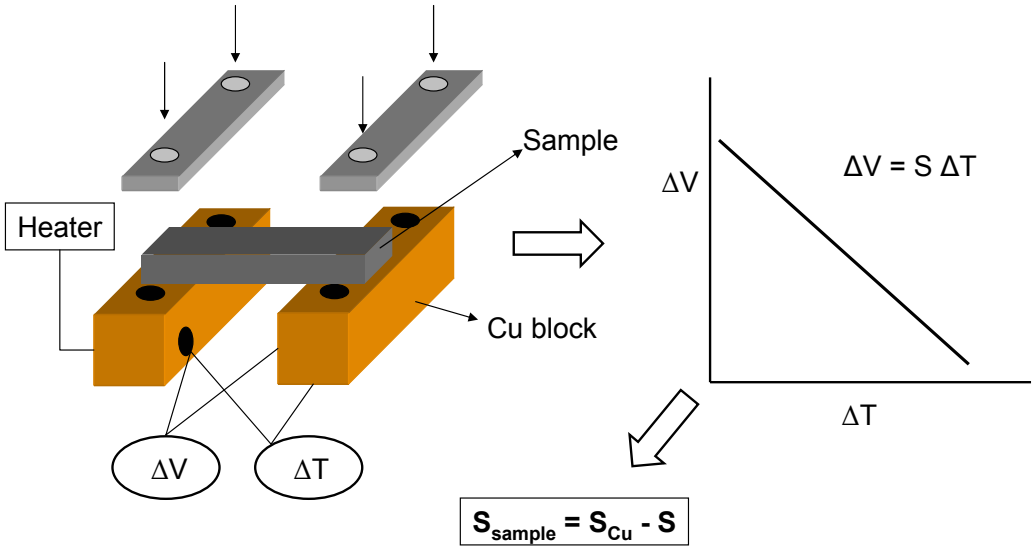

Figure 1.4. A schematic of Seebeck-coefficient measurement.

Diffuse Reflectance measurement

The band gap in semiconductors is known as the energy gap between the lowest point of the conduction band (the top empty band) and the highest point of the valence band (the bottom-filled band) [32]. Optical band gaps of powder samples were determined by using diffuse reflectance measurements. These measurements were performed in this lab and the Department of Physics at Oregon State University. In this lab, the diffuse reflectance at room temperature of a powder sample was measured with $BaSO_4$ as a reference and an optical setup comprised of an Oriel 300-W Xe lamp, a Cary model-15 prism monochromator, and a Hamamatsu R636-10 photomultiplier tube. The experimental setup in the Department of physics has been described in Kykyneshi's thesis [33].

Diffuse reflectance spectra from powders provide information similar to that obtained from transmission spectra of films or single crystals. A significant fraction of light diffusely reflected from a collection of powder crystallites has undergone not merely a single surface reflection, but has traversed a complicated path involving transmission through, and reflection from, many crystallites near the surface. Hence the diffuse reflection spectrum contains significant transmissive character and can be used to characterize absorption. The diffuse reflectance spectra can be translated into absorption spectra via the Kubelka-Munk method [38, 39]:

$$k/s = (1\text{-}R)^2 / (2R)$$

where k is the absorption coefficient, s is the scattering coefficient, and R is the reflectance. The direct band gap is extracted by extrapolating the straight-line portion of the curve of $\{(k/s)\cdot E\}^2$ *vs.* E to the zero-absorption axis (Figure 1.5).

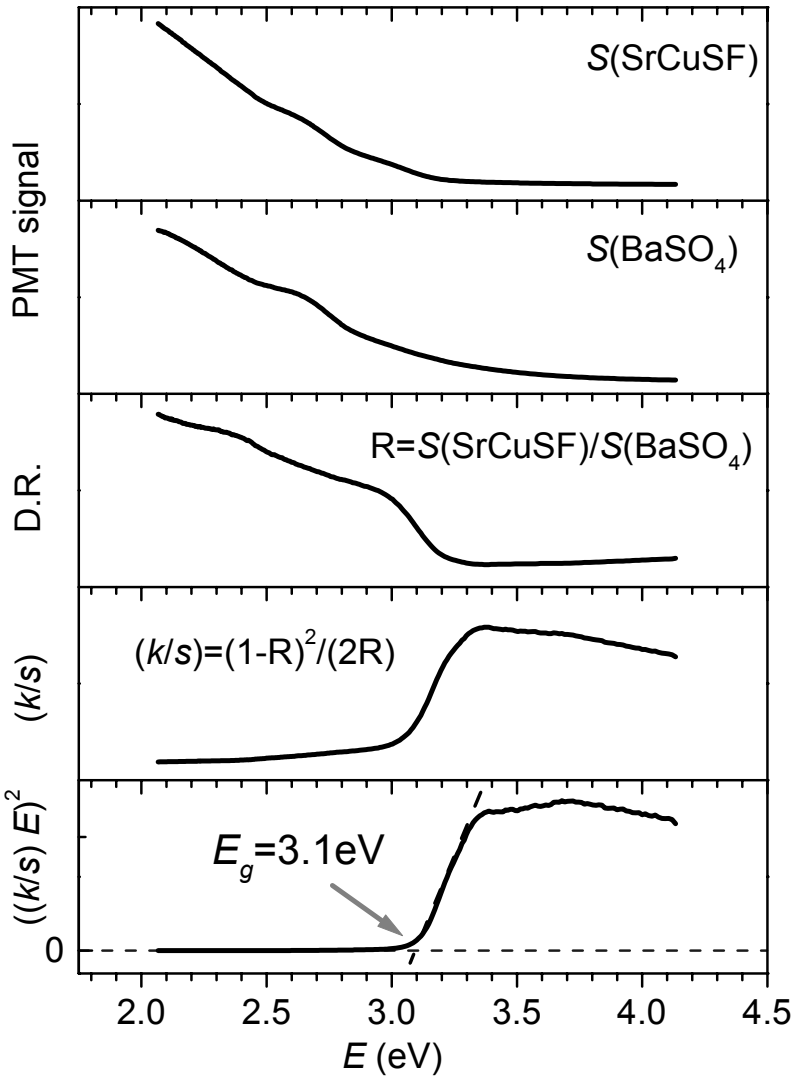

Figure 1.5. Procedure for estimating band gap of SrCuSF from diffuse reflectance. D.R is corrected diffuse reflectance signal.

LUMINESCENT MAERIALS

A luminescent material is a solid that emits light when subjected to excitation such as ultraviolet radiation, X-rays, electron bombardment, electric voltage, sound, and friction [40-42]. It is also called as a phosphor. The word "phosphor" means "light bearer" in Greek and has been used since the early 17th century [43]. The most familiar phosphors are probably those luminescent materials used in fluorescent lamps and television sets. In fluorescent lamps, phosphors are excited by the ultraviolet radiation from the discharge of mercury, and they emit light that appears white to the eye. In a color television tube three kinds of phosphors are excited by accelerated electrons; they selectively emit red, green, or blue light that can be combined to cover the gamut of color images. Phosphors have been used in a wide range of technologies, covering detector systems such as X-ray screens and light source such as lamps, information displays such as cathode ray tubes (CRTs), and plasma display panels (PDPs) [44]. To provide context for the work in this dissertation on luminescent materials, some background on lamps and PDPs is given in the following two sections.

Lamps

A standard fluorescent lamp is a low-pressure-mercury-discharge lamp whose glass tube is coated with phosphor layers. It exhibits an energy efficiency of about 22%, which is much higher than 8% of a conventional incandescent lamp [45]. Recently, for mainly environmental reasons, considerable effort has been

directed to development of a mercury-free fluorescent lamp [46]. Most mercury-substitutes such as mixtures neon and xenon gases produce vacuum ultraviolet (VUV) emission under plasma discharge conditions [47]. The resulting high-energy light, however, in general can not be used to excite common commercial lamp phosphors as efficiently as the 254-nm radiation from the mercury discharge. Therefore, development of new phosphors efficiently excited by VUV radiation is important to realize mercury-free fluorescent lamps.

White light emitting diodes (LEDs) represent a relatively new highly energy-efficient light source [48]. U.S. Department of Energy has proposed that replacement of conventional incandescent bulbs and fluorescent lamps with white-light emitting diodes can save 50% of energy used for lighting [49]. The first white LED was fabricated by using a blue GaInN/GaN LED and the phosphor Ce-doped YAG, which is excited by blue radiation and emits yellow radiation; blue radiation from the LED and yellow radiation from the phosphor produce white light. By developing new phosphors with better performance the luminous efficiency and the color purity of white LEDs can be improved. New phosphors of $(Ba,Sr)_3Sc_2(BO_3)_4:Eu^{2+}$ for white LEDs are introduced in Chapter 14.

Plasma Display Panels (PDPs)

PDPs are in use as large-scale flat-panel information and entertainment display devices. These displays have millions of tiny gas-discharge cells composed of red, green, and blue sub-cells that are coated with red-, green-, and blue-emitting

phosphor powders [50]. The gas discharge generates VUV radiation (mainly 147 nm), which excites phosphors resulting in the emission of red, green, and blue visible light. The combination of these three colors in different intensity ratios creates the rainbow of colors for images. The most common PDP phosphors are red-emitting $(Y,Gd)BO_3:Eu^{3+}$, green-emitting $Zn_2SiO_4:Mn^{2+}$, and blue-emitting $BaMgAl_{10}O_{17}:Eu^{2+}$ [51]. The red phosphor of $(Y,Gd)BO_3:Eu^{3+}$ exhibits good performance on excitation in the VUV region, but its emission color is not a true saturated red. The resulting orange hue of this phosphor is a direct manifestation of the local atomic environment about the Eu^{3+} dopant; it occupies a site with inversion symmetry, resulting in suppression of the electric-dipole emission transition $^5D_0 \rightarrow {}^7F_2$ (Figure 1.6). New host materials without inversion symmetry at the Eu^{3+} site have been examined to realize new PDP phosphors having saturated red emission.

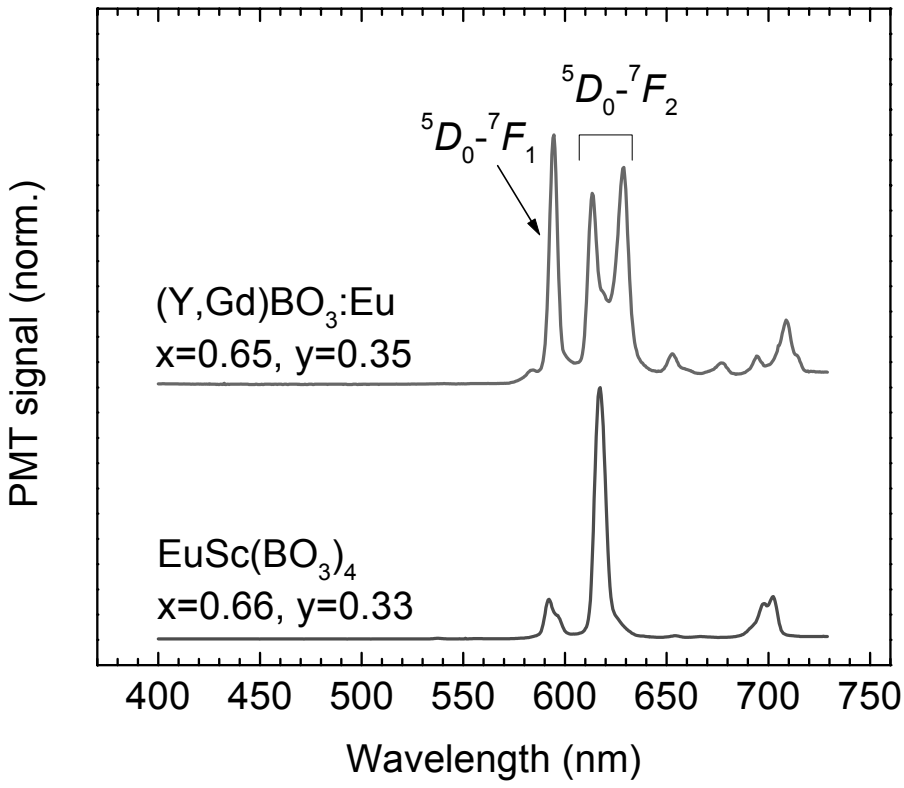

Figure 1.6. Emission spectra of commercial VUV red phosphor, (Y,Gd)BO_3:Eu^{3+}, and $EuSc(BO_3)_4$. Because of local environment of Eu^{3+} in (Y,Gd)BO_3, the electric-dipole emission transition $^5D_0 \rightarrow {}^7F_2$ is suppressed, resulting in similar emission intensity as the magnetic-dipole emission transition $^5D_0 \rightarrow {}^7F_1$ and orange-red emission color. Saturated red emission is observed in $EuSc(BO_3)_4$ where Eu^{3+} occupies a site without inversion symmetry.

Luminescence measurements

Room-temperature excitation and emission spectra were recorded on the computer-controlled spectrofluorimeter depicted in Figure 1.7. Excitation light from an Oriel 300-W Xe lamp is passed through a 50-cm water filter to protect optics from the damaging infrared, a Cary model-15 prism monochromator, and then focused onto the sample. The sample emission is passed through a suitable filter to reject second-order contribution from the excitation light, into an Oriel 22500 1/8-m monochromator, and then monitored with a Hamamatsu R636-10 photomulitplier tube (PMT) over the range 400-950 nm or a Hamamatsu R1767 PMT over the range 700-1200 nm. Current from the PMT is measured on a Keithley 486 picoammeter and sent to a computer for data storage. Each spectrum was corrected for the throughput and response of the system with Rhodamine B and a calibrated W-lamp from Eppley Laboratory, Inc.. The quantum yield and the emission maximum of Rhodamine B solution (in ethylene glycol (3 g/l)) are known to be essentially independent of excitation wavelength from 220 nm to 600 nm [52]. Variable-temperature spectra were recorded by using a Cryo Industries R102 flow cryostat equipped with a Conductus temperature controller.

Lifetime data were obtained with a Q-switched, Quanta-Ray Nd:YAG laser equipped with a frequency-mixing crystal to provide excitation at 355 nm; the pulse width (FWHM) of the laser was measured as 10 ns. The sample emission signal was detected with a PMT that was connected to a 500-MHz Tektronix digital

oscilloscope (Model TDS350) and interfaced to a PC for data collection. Emission lifetimes were determined from natural log plots of the decay curves.

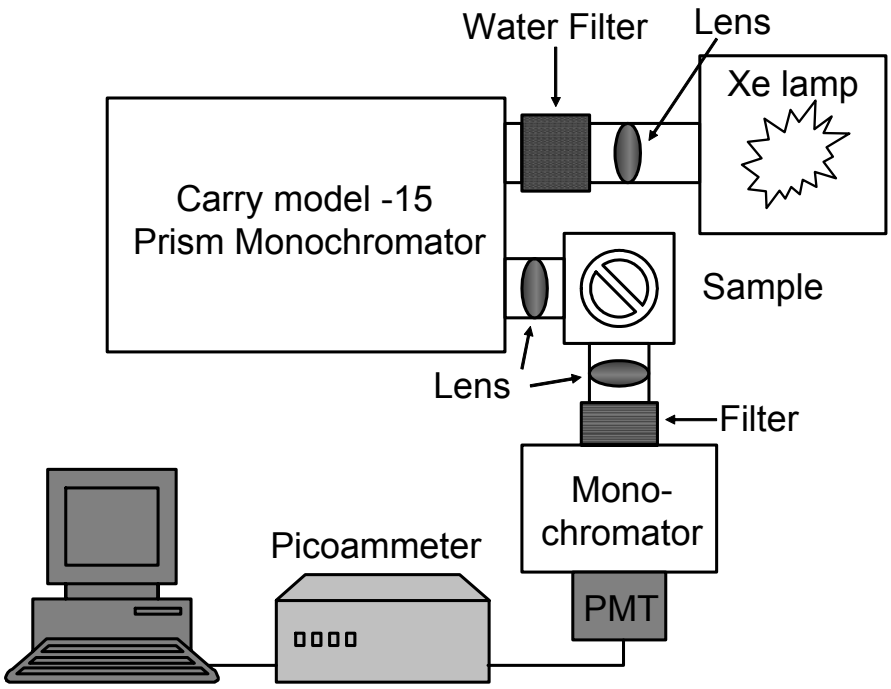

Figure 1.7. Experimental setup used for luminescence measurements.

REFERENCES

[1] R. G. Gordon, *Mater. Res. Soc. Bull.*, **25(8)**, 28 (2000).

[2] K. Badeker, *Ann. Phys.*, **22**, 749 (1907).

[3] B. G. Lewis, and D. C. Paine, *Mater. Res. Soc. Bull.*, **25(8)**, 22 (2000).

[4] H. Hosono, M. Yasukawa, and H. Kawazoe, *J. Non-Cryst. Solids*, **203**, 334 (1996).

[5] H. Kawazoe, N. Ueda, H. Un'no, H. Hsono, and H. Tanoue, *J. Appl. Phys.*, **76**, 7935 (1994).

[6] H. Mizoguchi, N. S. P. Bhuvanesh, and P. M. Woodward, *Chem. Commun.*, 1084 (2003).

[7] T. Minami, *Mater. Res. Soc. Bull.*, **25(8)**, 38 (2000).

[8] D. S. Ginley, and C. Bright, *Mater. Res. Soc. Bull.*, **25(8)**, 15 (2000).

[9] G. Thomas, *Nature*, **389**, 907 (1997).

[10] H. Ohta, and H. Hosono, *Materials Today*, **7(6)**, 42 (2004).

[11] H. Kawazoe, M. Yasukawa, H. Hyodo, M. Kurita, H. Yanagi, and H. Hosono, *Nature*, **389**, 939 (1997).

[12] J. Tate, M. K. Jayaraj, A. D. Draeseke, T. Ulbrich, A. W. Sleight, K. A. Vanaja, R. Nagarayan, J. F. Wager, and R. L. Hoffman, *Thin Soild Films*, **411(1)**, 119 (2002).

[13] H. Yanagi, T. Hase, S. Ibuki, K. Ueda, and H. Hosono, *Appl. Phys. Lett.*, **78(11)**, 1583 (2001).

[14] N. Duan, A. W. Sleight, M. K. Jayaraj, and J. Tate, *Appl. Phys. Lett.*, **77(9)**, 1325 (2000).

[15] R. Kykyneshi, B. C. Nielsen, J. Tate, J. Li, A. W. Sleight, *J. Appl. Phys.*, **96(11)**, 6188 (2004).

[16] M. K. Jayaraj, A. D. Draeseke, J. Tate, and A. W. Sleight, *Thin Soild Films*, **397(1,2)**, 244 (2001).

[17] A. Kudo, H. Yanagi, H. Hosono, H. Kawazoe, *Appl. Phys. Lett.*, **73(2)**, 220 (1998).

[18] H. Ohta, M. Orita, M. Hirano, I. Yagi, K. Ueda, and, H. Hosono, *J. Appl. Phys.*, **91(5)**, 3074 (2002).

[19] K. Ueda, S. Inoue, S. Hirose, H. Kawazoe, and H. Hosono, *Appl. Phys. Lett.*, **77(17)**, 2701 (2000).

[20] K. Ueda, S. Inoue, H. Hosono, N. Sarukura, and M. Hiranu, *Appl. Phys. Lett.*, **78(16)**, 2333 (2001).

[21] K. Ueda, and H. Hosono, *J. Appl. Phys.*, **91(7)**, 4768 (2002).

[22] H. Hiramatsu, K. Ueda, H. Ohta, M. Hirano, T. Kamiya, and H. Hosono, *Appl. Phys. Lett.*, **82(7)**, 1048 (2003).

[23] H. Hosono, H. Ohta, K. Hayashi, M. Orita, and M. Hirano, *J. Cryst. Growth*, **237-239**, 496 (2002), and references therein.

[24] R. L. Hoffman, B. J. Norris, and J. F. Wager, *Appl. Phys. Lett.*, **82**, 733 (2003).

[25] H. Yanagi, S.-I. Inoue, K. Ueda, H. Kawazoe, H. Hosono, and N. Hamada, *J. Appl. Phys.*, **88(7)**, 4159 (2000).

[26] H. Yanagi, H. Kawazoe, A. Kudo, M. Yasukawa, and H. Hosono, *J. Electroceram.*, **4(2/3)**, 407 (2000).

[27] H. Gong, Y. Wang, and Y. Luo, *Appl. Phys. Lett.*, **76(26)**, 3959 (2000).

[28] K. Ueda, T. Hase, H. Yanagi, H. Kawazoe, H. Hosono, H. Ohta, M. Orita, and M. Hirano, *J. Appl. Phys.*, **89**, 1790 (2001).

[29] R. Nagarajan, A. D. Draeseke, A. W. Sleight, and J. Tate, *J. Appl. Phys.*, **89(12)**, 8022 (2001).

[30] S. Park, D. A. Keszler, M. M. Valencia, R. L. Hoffman, J. P. Bender, and J. F. Wager, *Appl. Phys. Lett.*, **80**, 4393 (2002).

[31] H. Mizoguchi, H. W. Eng, P. M. Woodward, *Inorg. Chem.*, **43**, 1667 (2004).

[32] C. Kittel, *Introduction to Solid State Physics*, 7th ed., John Wiley & Sons, New York (1996).

[33] R. Kykyneshi, *MS thesis*, Oregon State University (2004).

[34] A. P. Sutton, *Electronic Structure of Materials*, Oxford University Press, Oxford (1996).

[35] S. M. Girvin, "Hall Effect" in *Solid-State Physics Source Book*, S. P. Parker, Ed.; McGRAW-HILL, New York (1988).

[36] J. Bass, "Themoelectricity" in *Solid-State Physics Source Book*, S. P. Parker, Ed.; McGRAW-HILL, New York (1988).

[37] A. R. West, *Solid State Chemistry and its Applications*, Chapter 15, Wiley & Sons, Singapore, (1989).

[38] P. Kubelka and F. Munk, *Z. Tech. Phys.*, **12**, 593 (1931).

[39] P. Kubelka, *J. Opt. Soc. Am.*, **38**, 448 (1948).

[40] G. Blasse, and A. Bril, *Philips Tech. Rev.*, **31**, 304 (1970).

[41] G. Blasse, and B. C. Grabmaier, *Luminescent Materials*, Springer-Verlag, Berlin (1994).

[42] R.C.Ropp, *Luminescence and the Solid State*, Elsevier Science, Amsterdam (1991).

[43] S. Shionoya, *Phosphor Handbook*, Chapter 1, S. Shionoya, and W. M. Yen (Eds.), CRC Press, Boca Raton, FL (2000).

[44] S. Shionoya, and W. M. Yen (Eds.), *Phosphor Handbook*, CRC Press, Boca Raton, FL (2000).

[45] R.C. Ropp, *Luminescence and the Solid State*, pp. 330-331, Elsevier Science, Amsterdam (1991).

[46] T. Shiga, L. C. Pitchford, J.-P. Boeuf, and S. Mikoshiba, *J. Phys. D: Appl. Phys.*, **36**, 512 (2003).

[47] M. Jinno, H. Kurokawa, and M. Aono, *Jpn. J. Appl. Phys.*, 38, 4608 (1999).

[48] E. F. Schubert, *Light-Emitting Diodes*, Chapter 12, Cambridge University Press, Cambridge (2003).

[49] http://www.eere.energy.gov/buildings/tech/lighting/phosphors.html. (accessed Dec 2004).

[50] http://www.plasmavision.com/WhitePaperPlasmaVsLCD.pdf. (accessed Dec 2004).

[51] T. Jűstel, and H. Nikol, *Adv. Mater.*, **12(7)**, 527 (2000).

[52] J. R. Lakowicz, *Principles of Fluorescence Spectroscopy*, Chapter 2, Plenum Press, New York (1983).

CHAPTER 2

CRYSTAL STRUCTURES OF SINGLE CRYSTAL BaCuSF, AND POLYCRYSTALLINE BaCuQF (Q=S, Se)

ABSTRACT

Single crystals of BaCuSF and polycrystalline samples of BaCuQF (Q=S, Se) were prepared for crystal-structure determinations by using X-ray diffraction techniques. Single crystal BaCuSF crystallizes in the tetragonal space group *P4/nmm* with $Z = 2$, $a = 4.1164(5)$ Å, $c = 9.0079(9)$ Å, and $V = 152.64(3)$ Å^3. The structure is a layered type with anti-fluorite (Ba_2F_2) layers alternating with (Cu_2S_2) sheets along the *c* axis. The Ba and Q atoms occupy square antiprismatic sites; the Cu and F atoms are located in distorted tetrahedral sites. The two-dimensional Cu_2S_2 tetragonal sheet structure is characterized by edge-sharing linkages of the distorted CuS_4 tetrahedra, which produces a relatively short Cu···Cu distance of 2.9107(4) Å. Polycrystalline BaCuSF has cell parameters of $a = 4.1220(1)$ Å and $c = 9.0143(1)$ Å. The structure of BaCuSeF has also been determined with polycrystalline powders by using Rietveld refinement methods. It is isostructural to BaCuSF, crystallizing with $a = 4.2398(1)$ Å, $c = 9.1150(1)$ Å, and $V = 163.85(1)$ Å^3.

.

INTRODUCTION

The compounds BaCuQF (Q = S, Se) exhibit a unique combination of *p*-type conductivity and band gaps that allow transmission of much of the visible spectrum [1-3]. Their room-temperature electrical conductivities can be greatly enhanced by the substitution of several percent of K for Ba; the highest conductivities are 82 S/cm for $Ba_{0.9}K_{0.1}CuSF$ and 43 S/cm for $Ba_{0.9}K_{0.1}CuSeF$ [3]. Undoped BaCuSF also exhibits strong red luminescence near 630 nm under ultraviolet excitation. To better understand these materials, information on their crystal structures is important. The crystal structure of BaCuSeF was first described in the report on BaCuQF by Zhu, Huang, Wu, *et al.* in 1994 [4]; they reported only the structure of BaCuSeF refined from powder data.

In this contribution, we report structure refinements from single-crystal data on BaCuSF and powder data for BaCuSF and BaCuSeF.

EXPERIMENTAL

Reagents of synthesis of BaCuSF and $Ba_{0.9}K_{0.1}CuSF$ were $BaCO_3$ (Cerac, 99.9%), Cu_2S (Cerac, 99.5%), BaF_2 (Cerac, 99.9%), and K_2CO_3 (Aldrich, 99.995%). Stoichiometric mixtures were heated at 450°C under flowing H_2S(g) for 1 h, and cooled to room temperature under flowing Ar(g). Transparent single crystals of BaCuSF were obtained by heating pellets of BaCuSF and $Ba_{0.9}K_{0.1}CuSF$ together under flowing H_2S(g) in an Al_2O_3 boat at 870°C for 1 h. Powder samples of BaCuSeF were prepared by heating stoichiometric mixtures of BaSe (Cerac, 99.5%), Cu_2Se (Cerac, 99.5%), and BaF_2 (Cerac, 99.9%) at 500°C for 12 h in an evacuated silica tube.

X-ray data for BaCuSF were collected from a small crystal (0.1 x 0.05 x 0.01 mm^3) on a Rigaku/MSC Rapid diffractometer by using Ag-Kβ radiation (λ = 0.49707 Å). Procedures for image collection, determination of crystallographic parameters, extraction of integrated intensities, and correction for absorption have been described elsewhere [5]. Images were integrated in the range $3.16 < \theta < 29.98^o$, yielding a highly redundant data set composed of 32098 reflections, and after applying an absorption correction with the program Sortav (T_{min} = 0.8448, T_{max} = 1.0000), a final data set of 1742 reflections (R_{int} = 0.048) was produced. The structure was solved and refined by using SHELXL-97 with 428 unique reflections and 11 parameters (R_1 = 0.0377 (all reflections), wR_2 = 0.0792 (all reflections)). The final difference electron density map was largely featureless

exhibiting a maximum peak height corresponding to 9% of a Ba atom. Crystallographic details and final atomic parameters are given in Table 2.1 and 2.3, respectively.

Data for the Rietveld structural refinement were collected on powder samples of BaCuSF and BaCuSeF by using a Siemens D5000 diffractometer with variable slits and a locally devised variable counting time routine [6]. Data were converted to GSAS ESD format by using an in-house program [7], and structural refinements were performed by using the program Fullprof [8]. During refinement, it was noticed that there was a certain amount of anisotropic *hkl*-dependent line broadening associated with strain in the sample. In an effort to optimize the fit, the four possible parameters in Stephen's formalism [9] of strain broadening for this Laue class were refined, resulting in substantial improvements in residuals. Final crystallographic parameters for this refinement, including the calculated strain parameters, are given in Table 2.2; positional and equivalent-isotropic-displacement parameters are listed in Table 2.3.

TABLE 2.1. Crystallographic data for single crystal BaCuSF.

Formula	BaCuSF
Space group	P4/nmm (No. 129)
Z	2
a (Å)	4.1164(5)
c (Å)	9.0079(9)
Vol ($Å^3$)	152.64(3)
FW (amu)	251.94
Calculated density (g/cm^3)	5.482
Crystal dimensions (mm)	0.1 x 0.05 x 0.01
R_1 (%)	3.77
wR_2 (%)	7.92
Number of reflections	428
Number of parameters	11

TABLE 2.2. Summary of refinement data and lattice parameters of powder samples of BaCuQF (Q=S, Se).

Formula		BaCuSF	BaCuSeF
Space group		P4/nmm (No. 129)	P4/nmm (No. 129)
Z		2	2
a (Å)		4.1220(1)	4.2398(1)
c (Å)		9.0143(1)	9.1150(1)
Vol ($Å^3$)		153.16(1)	163.85(1)
FW (amu)		251.94	298.83
Calculated density (g/cm^3)		5.463	6.057
2θ range (°)		10.0-150.0	10.0-150.0
S_{400}		0.13(4)	0.55(2)
S_{004}		0.014(4)	0.069(2)
S_{220}		0.43(2)	1.74(8)
S_{202}		0.00(1)	0.00(2)
Calculated strain (%%) in given crystallographic direction	100	3.86	8.22
	101	3.22	6.85
	111	3.99	8.41
	110	4.43	9.38
	001	5.95	13.27
R_p (%)		5.52	7.13
R_{wp} (%)		3.57	5.20
R_{Bragg} (%)		6.81	9.69
Number of reflections		246	261
Number of parameters		23	23

TABLE 2.3. Atomic positions and isotropic equivalent displacement parameters ($Å^2$ x 100) for BaCuQF (Q=S, Se).

Single crystal BaCuSF

Atom	Wyckoff	x	y	z	U_{iso}
Ba	2c	¼	¼	0.32182(4)	0.921(1)
Cu	2a	¾	¼	0	2.16(2)
S	2c	¼	¼	-0.1481(2)	1.09(2)
F	2b	¾	¼	½	1.31(7)

BaCuSF

Atom	Wyckoff	x	y	z	U_{iso}
Ba	2c	¼	¼	0.32186(6)	1.92(1)
Cu	2a	¾	¼	0	3.10(5)
S	2c	¼	¼	-0.1483(2)	2.11(6)
F	2b	¾	¼	½	2.03(8)

BaCuSeF

Atom	Wyckoff	x	y	z	U_{iso}
Ba	2c	¼	¼	0.33149(13)	2.31(1)
Cu	2a	¾	¼	0	3.60(12)
Se	2c	¼	¼	-0.1579(2)	2.63(7)
F	2b	¾	¼	½	3.9(3)

RESULTS

The results of the final Rietveld refinement cycle are shown graphically in Figure 2.1 (BaCuSF) and Figure 2.2 (BaCuSeF). The compound BaCuQF (Q=S, Se) adopts the same structure type as LnCuOSe (Ln = lanthanide, Bi) and LaCuOS (Figure 2.3) [10]. The structure is a layered, tetragonal type with anti–fluorite (Ba_2F_2) layers alternating with (Cu_2Q_2) sheets along the *c* axis. Selected interatomic distances and angles for single crystal BaCuSF and powder samples of BaCuQF are given in Table 2.4. The cell volume of BaCuSF from single-crystal data is slightly smaller than that from the powder data, but interatomic distances are generally statistically equivalent.

The Ba and Q atoms occupy sites with symmetry C_{4v}. The Ba atom occupies a square antiprismatic environment with four Q atoms forming one square face and four F atoms the other. This type of square antiprismatic Ba site is also observed in BaFCl, where four Cl atoms form one square face and four F atoms the other [11]. The Ba-S distance, 3.305(1) Å, compares well with those found in compounds such as β-$BaCu_2S_2$ (3.269 Å) [12] and BaS (3.187 Å) [13]. The Ba-Se distance of 3.394(1) Å is similar to those observed in β-$BaCu_2Se_2$ (3.391 Å) [12] and $BaAl_2Se_4$ (3.398 Å) [14]. The Ba-F distance in BaCuSF (2.610 Å) is similar to that in BaCuSeF (2.622 Å) and BaF_2 (2.684 Å). The Q atom is also located at a square antiprismatic site coordinated by four Ba atoms and four Cu atoms.

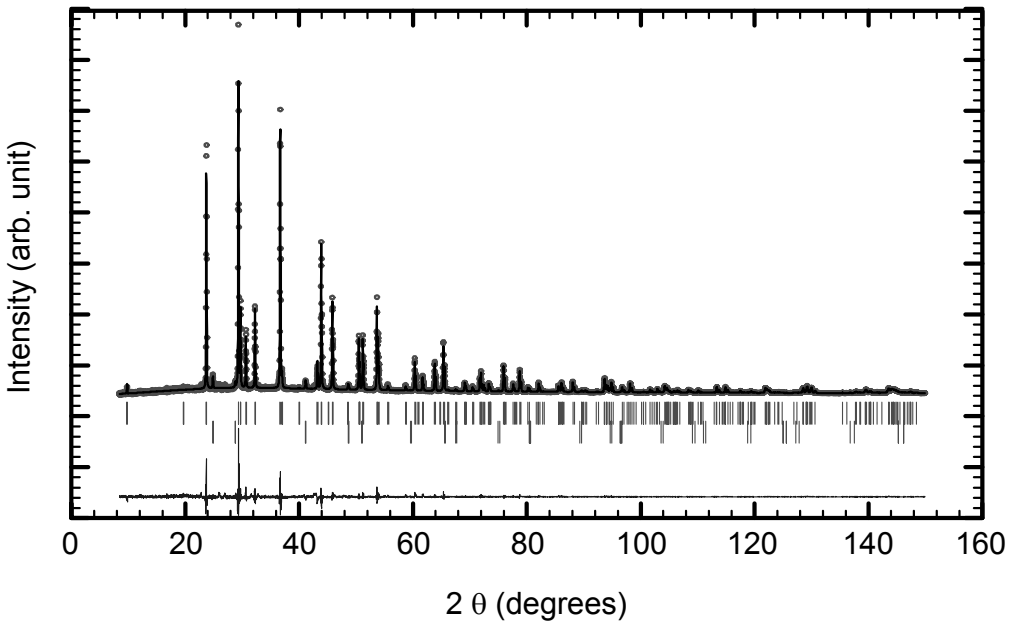

Figure 2.1. Observed (open circles) and calculated (solid line) X-ray powder diffraction pattern from refinement of BaCuSF. The bottom curve is the difference pattern on the same scale. The top vertical bars are for BaCuSF and the lower vertical bars are for LiF.

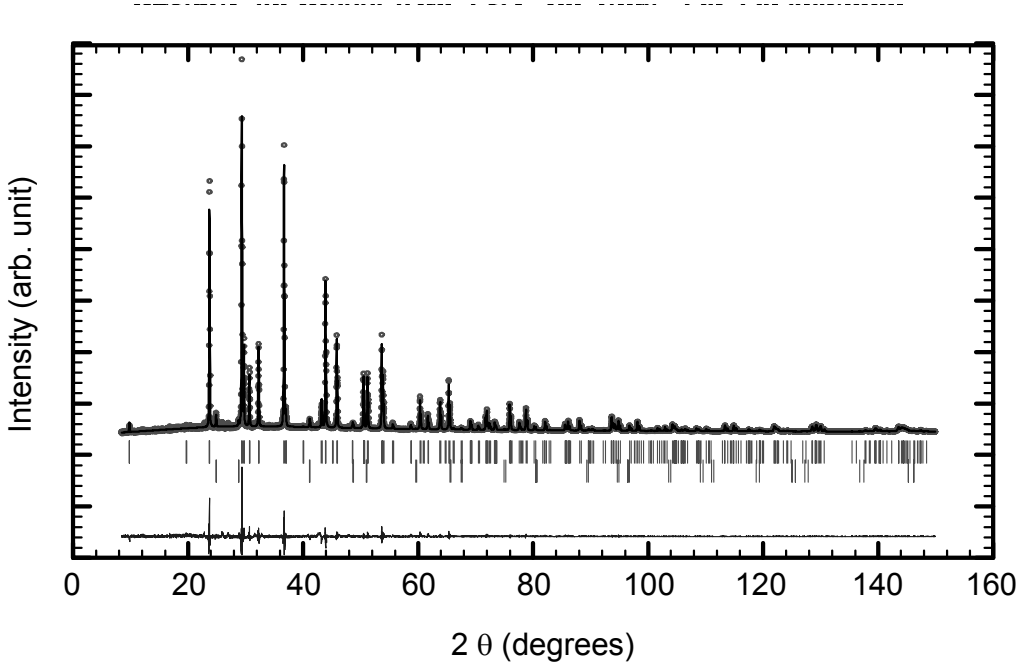

Figure 2.2. Observed (open circles) and calculated (solid line) X-ray powder diffraction pattern from refinement of BaCuSeF. The bottom curve is the difference pattern on the same scale. The top vertical bars are for BaCuSeF and the lower vertical bars are for LiF.

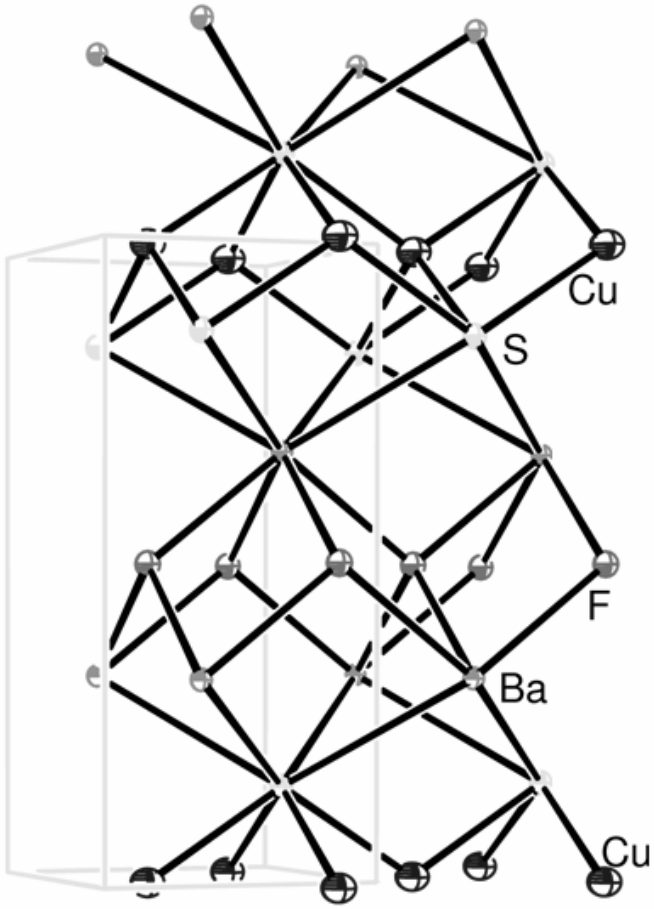

Figure 2.3. Crystal structure of BaCuSF.

TABLE 2.4. Selected interatomic distances (Å) and angles (^{o}) for BaCuQF (Q=S, Se).

	Single crystal BaCuSF	BaCuSF	BaCuSeF
Cu-Q	2.453(1)	2.456(1)	2.554(1)
Cu···Cu	2.9107(4)	2.9147(1)	2.9980(1)
Ba-Q	3.305(1)	3.308(1)	3.394(1)
Ba-F	2.610(1)	2.613(1)	2.622(1)
Q-Cu-Q	107.20(3)	107.22(6)	108.11(7)
Q-Cu-Q	114.11(7)	114.07(3)	112.22(3)
Q-Ba-Q	77.04(2)	77.07(2)	77.32(7)
Q-Ba-Q	123.47(5)	123.55(2)	124.11(2)
F-Ba-F	67.78(8)	67.81(9)	69.73(2)
F-Ba-F	104.10(2)	104.15(1)	107.89(2)
Q-Ba-F	78.47(2)	78.42(4)	76.75(4)
Q-Ba-F	141.48(1)	141.46(4)	141.34(4)

The Cu and F atoms are located on sites having D_{2d} symmetry, resulting in distorted tetrahedral environments. The Cu is coordinated to four Q atoms, and the F atom by four Ba atoms. The Cu-S bond distance of 2.453(1)Å in BaCuSF is comparable to the values in other systems such as β-$BaCu_2S_2$ (2.411 Å) and Cu_2S (2.306 Å averaged value) [15]. The two-dimensional Cu_2S_2 tetragonal sheet structure is characterized by edge-sharing linkages of the distorted CuS_4 tetrahedra, which produces relatively short Cu···Cu distances. The Cu···Cu distance in BaCuSF [2.9107(4) Å (single crystal) and 2.9147(1) (powder)] is shorter than that observed in compounds such as $CuAlS_2$ (3.720 Å) [16] and $CuCrS_2$ (3.492 Å) [17], where CuS_4 tetrahedra are linked by sharing vertexes. The Cu···Cu separation, however, is longer than the 2.763-Å distance observed across the shared S···S edges in β-$BaCu_2S_2$. This longer distance in BaCuSF derives from the S-Cu-S angle associated with the shared S···S edge linking the Cu atoms; the angles are 107.20(3)^o for BaCuSF and 110.1(1)^o for β-$BaCu_2S_2$. The larger angle forces a shorter Cu···Cu contact. In $LaCuS_2$, a shorter Cu···Cu distance of 2.651 Å and more obtuse S-Cu-S angle of 116.03^o are observed [18].

The Cu-Se bond distance of 2.554(1) Å in BaCuSeF is comparable to the values observed in other systems such as NaCuSe (2.553 Å) [19], β-$BaCu_2Se_2$ (2.497 Å) and Cu_2Se (2.529 Å) [20]. The Cu···Cu distance of 2.9980(1) Å in BaCuSeF is longer than that observed in β-$BaCu_2Se_2$ (2.856 Å); the Se-Cu-Se angle associated with the shared Se···Se edge is 108.11(7)^o for BaCuSeF and 110.2^o for β-$BaCu_2Se_2$.

CONCLUSION

The crystal structure of BaCuSF has been determined from analysis of X-ray data from single crystal and polycrystalline samples. With the exception, of the Cu···Cu distance, the chemically important nearest-neighbor distances are statistically equivalent in the single-crystal and powder refinements. The structure of BaCuSeF has also been refined by X-ray analysis of powder data. The materials adopt the layer-type structure of LaCuOS. The packing in these materials leads to distorted CuS_4 tetrahedra having S-Cu-S angles below the tetrahedral angle, leading to relatively long Cu···Cu distances. Single crystal of BaCuSF crystallizes in the tetragonal space group *P4/nmm* with a = 4.1164(5) Å, c = 9.0079(9) Å, V = 152.64(3) Å^3, and Z = 2. The structure is a layered type with anti-fluorite (Ba_2F_2) layers alternating with (Cu_2S_2) sheets along the c axis. The two-dimensional Cu_2S_2 tetragonal sheet structure is characterized by edge-sharing linkages of the distorted CuS_4 tetrahedra, which produce relatively short Cu···Cu distances of 2.9107(4) Å. Polycrystalline BaCuSF has cell parameters of a = 4.1220(1) Å, and c = 9.0143(1) Å. Structure of BaCuSeF has been also determined on polycrystalline powder by using X-ray diffraction and Rietveld refinement methods. BaCuSeF is isostructural to BaCuSF with a = 4.2398(1) Å, c = 9.1150(1) Å, and V = 163.85(1) Å^3.

ACKNOWLEDGMENTS

This material is based on work supported by the National Science Foundation under Grant No. 0245386.

REFERENCES

[1] C.-H. Park, D. A. Keszler, H. Yanagi, J. Tate, *Thin solid films*, 445, 288 (2003).

[2] H. Yanagi, S. Park, A. D. Draeseke, D. A. Keszler, and J. Tate, *J. Solid State Chem.*, **175**, 34 (2003).

[3] H. Yanagi, J. Tate, S. Park, C.-H. Park, D. A. Keszler, *Appl. Phys. Lett.*, 82, 2814 (2003).

[4] W. J. Zhu, Y. Z. Huang, F. Wu, C. Dong, H. Chen, and Z. X. Zhao, *Mater. Res. Bull.*, **29(5)**, 505 (1994).

[5] T. C. Bourland, R. G. Carter, and A. Yokochi, *Org. Biomol. Chem.*, **2**, 1315 (2004).

[6] I. C. Madsen, and R. J. Hill, *J. Appl. Crystallogr.*, **27**, 385 (1994).

[7] A. Yokochi, unpublished.

[8] J. Rodriguez-Carvajal, FULLPROF: A program for Rietveld Refinement and Pattern Matching Analysis, *In Abstract of the Satellite Meeting on Powder Diffraction of the XV Congress of the IUCr*, p 127, Thoulouse, France (1990).

[9] P. Stephens, *J. Appl. Crystallogr.*, **32**, 281 (1999).

[10] P.S. Berdonosov, A. M. Kusainova, L. N. Kholodkovskaya, V. A. Dolgikh, L. G. Akselrud, and B. A. Popovkin, *J. Solid State Chem.*, **118**, 74 (1995).

[11] N. Kodama, K. Tanaka, T. Utsunomiya, Y. Hoshino, F. Maruma, N. Ishizawa, and M. Kato, *Solid State Ionics*, **14**, 17 (1984).

[12] J. Huster, and W. Bronger, *Z. Anorg. Allg. Chem.*, **625**, 2033 (1999).

[13] O. J. Guentert, and A. Faessler, *Z. Kristallogr.*, **107**, 357 (1956).

[14] W. Klee, and H. Schaefer, *Z. Anorg. Allg. Chem.*, **479**, 125 (1981).

[15] A. Janosi, *Acta Crystallogr.*, 17(3), 311 (1964).

[16] H. Hahn, G. Frank, W. Klingler, A. D. Meyer, and G. Stoerger, *Z. Anorg. Allg. Chem.*, **271**, 153 (1953).

[17] H. Hahn, and V. de Lorent, *Z. Anorg. Allg. Chem.*, **290**, 68 (1957).

[18] M. Julien-Pouzol, S. Jaulmes, A. Mazurier, and M. Guittard, *Acta Crystallogr.*, **B37**, 1901 (1981).

[19] G. Savelsberg, and H. Schaefer, *Z. Naturforsch.* 33**B**, 370 (1978).

[20] W. Borchert, *Z. Kristallogr.*, **107**, 357 (1956).

CHAPTER 3

p-TYPE CONDUCTIVITY IN WIDE-BAND-GAP BaCuSeF AND LUMINESCENCE OF BaCuQF (Q =S, Se)

Cheol-Hee Park, Douglas A. Keszler, Hiroshi Yanagi, and Janet Tate

Modified version: *Applied Physic Letters*
Suite 1NO1, 2 Huntington Quadrangle, Melville, NY 11747-4502
vol. 82(17), 2814 (2003)

ABSTRACT

Materials of BaCuSeF, candidate transparent p-type conductors, were prepared by solid-state reaction and their bulk electrical and optical properties were evaluated. The room-temperature Seebeck coefficient and electrical conductivity of undoped BaCuSeF pellet were +32 μV/K and 0.061 S/cm. The conductivity was greatly enhanced by the substitution of several percent of K for Ba. The highest conductivity was 43 S/cm for $Ba_{0.9}K_{0.1}SeF$. The energy band gap for BaCuSeF was estimated from the diffuse reflectance spectra as 2.9 eV. Undoped BaCuSF and $Ba_{0.75}Sr_{0.25}CuSF$ exhibit strong red luminescence near 630 nm under ultraviolet excitation.

INTRODUCTION

Transparent *p*-type conducting oxides such as $CuMO_2$ (M = Al, Ga, In, Sc) [1-4] and $SrCu_2O_2$ [5] have recently attracted attention as possible components of novel transparent electronic and optoelectronic devices. However, so far it appears that optimizing electrical conductivity in such Cu-based p-type oxides compromises the optical transparency to a greater extent than is the case for *n*-type conducting oxides, so that it seems sensible to search for alternate materials. A bandgap greater than about 3.1 eV is necessary for optical transparency, and within this constraint, an improvement in hole mobility is desirable to improve conductivity [6]. The more strongly covalent nature of the Cu–S bond compared to the Cu-O bond should improve hole mobility, and suggests examination of sulfides or other chalcogenide-based materials. $BaCu_2S_2$ has a hole mobility of 3.5 cm^2/Vs, which is indeed much higher than the mobilities of order 0.1 cm^2/Vs reported for most Cu-based *p*-type transparent oxides, but the band gap energy is 2.3 eV [7]. LaCuOS is also a *p*-type transparent conducting material [8], but the mobility of 0.5 cm^2/Vs is still rather low [9].

In 1994, Zhu *et al.* reported the synthesis and crystal structure of two copper chalcogenide-fluorides of BaCuQF (Q = S, Se) [10]. BaCuQF crystal structure, which belongs to the space group *P*4/*nmm*, is a layered structure with tetragonal symmetry, in which $(Ba_2F_2)^{2+}$ and $(Cu_2Q_2)^{2-}$ layers are alternately stacked along the *c*-axis. The $(Cu_2Q_2)^{2-}$ layers, which can also be thought of as layers of edge-

sharing CuS_4 tetrahedra, have an obvious correspondence to the $BaCu_2S_2$ structure, so that this is expected to be the plane for hole conduction. The BaCuQF layered structure is very similar to that of LaCuOS, which has stacked $(La_2O_2)^{2+}$ and $(Cu_2S_2)^{2-}$ layers [11]. The similarity is interesting, because LaCuOS is not only a transparent p-type conductor, but also an ultraviolet light emitter that exhibits excitonic absorption and emission even at room temperature [12]. Experimental and theoretical analyses indicate that the $(Cu_2S_2)^{2-}$ layers contribute to both the top of the valence band and the bottom of the conduction band of LaCuOS [13]. Zhu et al reported semiconducting behavior of BaCuQF, but details were lacking [10], and no other data are available, aside from a preliminary study by Yanagi *et al.* [14]. Here we report promising p-type electrical conductivity of bulk BaCuSeF, a bandgap of 2.9 eV from diffuse reflectance measurements, and photoluminescence of BaCuQF (Q=S, Se).

EXPERIMENTAL

Powder samples of undoped and K-doped BaCuSeF were prepared by heating stoichiometric mixtures of BaSe (Cerac, 99.5%), Cu_2Se (Cerac, 99.5 %), BaF_2 (Cerac, 99,9 %) and KF (Alfa Aesar, 99 %) at 450-550 °C for 12 h in an evacuated silica tube. Powder samples of undoped BaCuSF and $Ba_{0.75}Sr_{0.25}CuSF$ were prepared by heating stoichiometric mixtures of the reagents of $BaCO_3$ (Cerac,

99.9%), Cu_2S (Cerac, 99.5 %), BaF_2 (Cerac, 99,9 %) and KF (Alfa Aesar, 99 %) at 550 °C for 1 h under a flowing stream of H_2S (g) and cooling to room temperature under flowing Ar (g). The powders are generally stable in air, but reaction is evident upon exposure to water. All of the samples were characterized by powder X-ray diffraction on a Siemens D5000 diffractometer; samples prepared in silica tube were predominantly single phase with only trace amounts of unreacted BaF_2 observed, while no BaF_2 is detected following treatment with H_2S(g). For conductivity measurements, each powder sample was pressed into a pellet and annealed at 650 °C for 1 h in an evacuated silica tube. The pellets averaged 70% - 80% of theoretical density; as detailed in Table 3.1.

The electrical conductivities of the sintered pellets were measured from 300 K to 77 K by a four-probe technique. Silver paste was used for electrodes and ohmic contact was confirmed before detailed measurements were carried out. The Seebeck coefficient was measured at room temperature with a temperature gradient of ~5 K across the pellet. The diffuse reflectance at room temperature of powdered BaCuSeF was measured against MgO powder in the uv-visible region (300 nm to 900 nm) using an integrating sphere and a double monochromator. Photoluminescence measurements were made with an Oriel 300 Watt Xe lamp and Cary model-15 prism monochromator for excitation, and an Oriel 22500 1/8-m monochromator and Hamamatsu R 636-10 photomultiplier tube for detection. Each spectrum was corrected for the response of the system by using rhodamine B and a standardized tungsten lamp.

TABLE 3.1. Electrical properties (conductivity and Seebeck coefficient) and densities of $Ba_{1-x}K_xCuSeF$ (x = 0, 0.025, 0.05, 0.1) pellets at room temperature.

K (at.%)	0	0.025	0.50	0.10
σ (S/cm)	0.061	17	27	43
S (μV/K)	+32	+34	+25	+41
Density (%)	76	69	62	76

RESULTS

The temperature dependence of the electrical conductivity of $Ba_{1-x}K_xCuSeF$ pellets is illustrated in Figure 3.1. Undoped pellet of BaCuSeF have an electrical conductivity in the range of 10^{-2} S/cm, and the conductivity increases with increasing K concentration. The room temperature conductivity of the pellets is 43 S/cm for $Ba_{0.9}K_{0.1}SeF$. This compares favorably with the values of order 1 – 20 S/cm reported for other Cu-based p-type transparent conductors, including the structurally similar $LaCuOS_{1-y}Se_y$ system (10^{-1}~10^{0} S/cm) [15]. The electrical conductivity of the undoped BaCuSeF has a very weak temperature dependence, and all of the doped pellets exhibit essentially metallic behavior. Seebeck measurements on all samples gave a positive sign, indicating that these materials are *p*-type conductors at all doping levels and all temperatures. Table 3.1 summarizes the transport measurements.

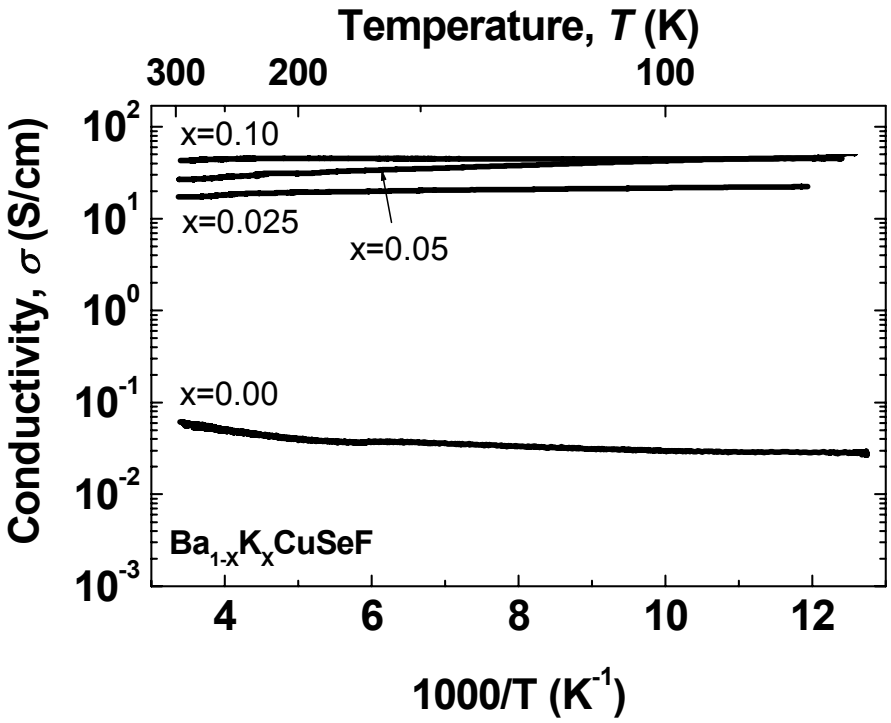

Figure 3.1. Electrical conductivity of $Ba_{1-x}K_xCuSeF$ pellets as a function of reciprocal temperature. In each case, $x = 0$, 0.025, 0.05, 0.1.

The diffuse reflectance of BaCuSeF (Figure 3.2) is low at short wavelengths and increases sharply at ~400 nm. The energy band gap of ~2.9 eV was estimated from a plot of $\{(k/s)\bullet h\nu\}^2$ vs. $h\nu$, where k and s denote absorption and scattering coefficients, and $h\nu$ is the photon energy. The ratio k/s was calculated from the reflectance via the Kubelka-Munk equation [16,17]. This gap value should be sufficient to transmit all but the deepest blue light. The band gap of BaCuSF was measured to be 3.1 eV [18]. As expected for a quasi 2-dimsnsional layered

structure like BaCuQF, the bandgap value is larger than for $BaCu_2S_2$, which has a more three-dimensional arrangement of the CuS_4 tetrahedra.

Excitation and emission spectra for undoped and doped BaCuQF compositions are summarized in Figure 3.2. Emission from each sample occurs in the orange-red to red portions of the spectrum. The onset of excitation near 425 nm for $BaCu_{0.975}SeF$ agrees well with the reflectance data, indicating excitation and emission occurs through bandgap absorption of the compound rather than an impurity. Similarly, the excitation spectrum of BaCuSF is consistent with the 3.2-eV bandgap observed from thin-film transmission data.

The emission from BaCuSF is characterized by two broad peaks centered near 560 and 630 nm, giving rise to an emission that appears orange to the eye. The peak near 560 nm can be quenched by altering the synthesis conditions or by selective doping. In the case of Mn doping, the 560-nm band is completely quenched, giving an emission with color coordinates x = 0.66 and y = 0.34, similar to those (x = 0.65 and y = 0.34) observed for the commercial red phosphor Y_2O_3:Eu. A more detailed accounting of the optical properties of these materials will be given elsewhere.

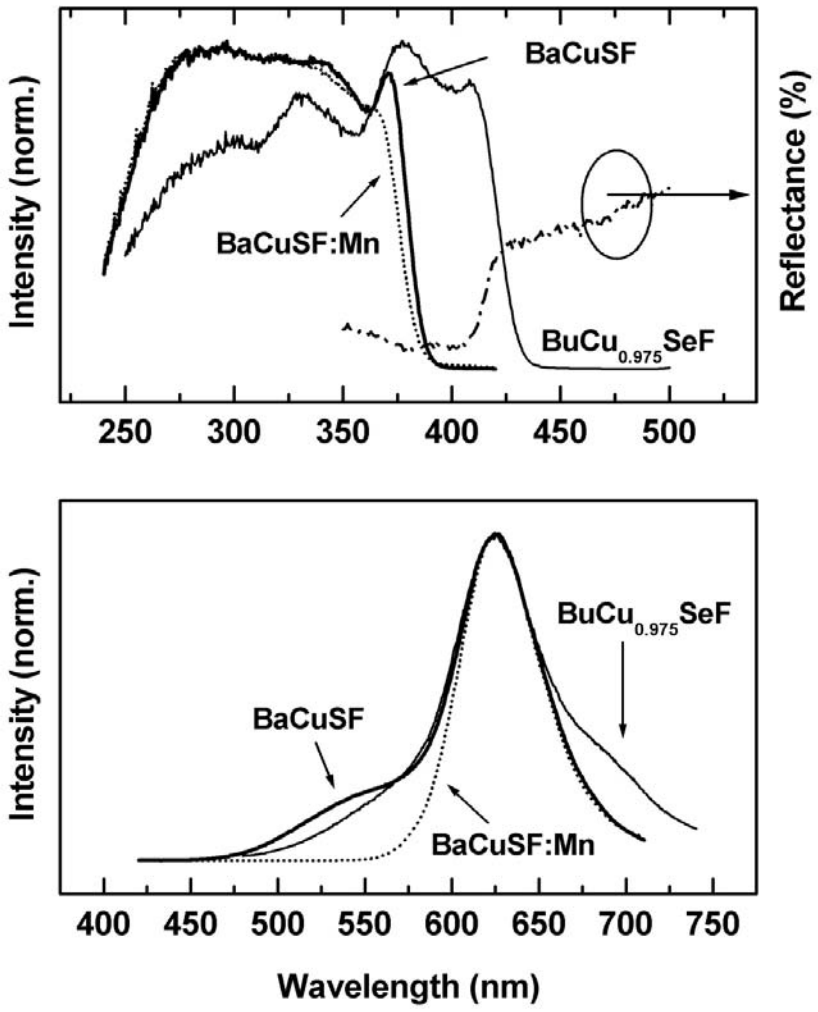

Figure 3.2. (Top) reflectance spectrum for BaCuSeF and excitation spectra for BaCuQF and (bottom) emission spectra for BaCuQF.

CONCLUSIONS

In summary, we have prepared undoped and K-doped BaCuSeF, which is a promising transparent *p*-type conductor. The electrical conductivity was controlled by K doping and the bulk conductivity is 43 S/cm for sintered pellets of BaCuSeF:K at a doping level of K of 10 at%. The Seebeck coefficients were positive, indicating that undoped and K doped BaCuSeF are *p*-type conductors. The optical band gap of BaCuSeF is 3 eV, and strong luminescence is observed near 630 nm in BaCuQF (Q=S, Se).

ACKNOWLEDGEMENT

This work was supported by the National Science Foundation (DMR 0071727), by the Army Research Office (MURI E-18-667-G3), and by the Research Corporation. We thank Prof. David McIntyre and Levi Kilcher for assistance with the diffuse reflectance measurements.

REFERENCES

[1] H. Kawazoe, M. Yasukawa, H. Hyodo, M. Kurita, H. Yanagi, and H. Hosono, *Nature*, **389**, 939 (1997).

[2] K. Ueda, T. Hase, H. Yanagi, H. Kawazoe, H. Hosono, H. Ohta, M. Orita, and M. Hirano, *J. Appl. Phys.*, **89**, 1790 (2001).

[3] H. Yanagi, T. Hase, S. Ibuki, K. Ueda, and H. Hosono, *Appl. Phys. Lett.*, **78**, 1583 (2001).

[4] N. Duan, A. W. Sleight, M. K. Jayaraj, and J. Tate, *Appl. Phys. Lett.*, **77**, 1325 (2000).

[5] A. Kudo, H. Yanagi, H. Hosono, and H. Kawazoe, *Appl. Phys. Lett.*, **73**, 220 (1998).

[6] G. Thomas, *Nature*, **389**, 907 (1997).

[7] S. Park, D. A. Keszler, M. M. Valencia, R. L. Hoffman, J. P. Bender, and J. F. Wager, *Appl. Phys. Lett.*, **80**, 4393 (2002).

[8] K. Ueda, S. Inoue, S. Hirose, H. Kawazoe, and H. Hosono, *Appl. Phys. Lett.*, **77**, 2701 (2000).

[9] H. Hiramatsu, M. Orita, M. Hirano, K. Ueda, and H. Hosono, *J. Appl. Phys.*, **91**, 9177 (2002).

[10] W. J. Zhu, Y. Z. Huang, F. Wu, C. Dong, H. Chen, and Z. X. Zhao, *Mat. Res. Bull.*, **29**, 505 (1994).

[11] M. Palazzi, *Acad. Sci., Paris, C. R.* **292**, 789 (1981).

[12] K. Ueda, S. Inoue, H. Hosono, N. Sarukura, and M. Hirano, *Appl. Phys. Lett.*, **78**, 2333 (2001).

[13] S. Inoue, K. Ueda, and H. Hosono, *Phys. Rev. B*, **64**, 245211 (2001).

[14] H. Yanagi, S. Park, A. D. Draeseke, D. A. Keszler, and J. Tate, *J. Solid State Chem*., **175**, 34 (2003).

[15] K. Ueda, and H. Hosono, *J. Appl. Phys.*, **91**, 4768 (2002).

[16] P. Kubelka, and F. Munk, *Z. Tech. Phys.*, **12**, 593 (1931).

[17] P. Kubelka, *J. Opt. Soc. Am.*, **38**, 448 (1948).

[18] C.-H. Park, D. A. Keszler, H. Yanagi, and J. Tate, *Thin Solid Films*, **445**, 288 (2003).

CHAPTER 4

GAP MODULATION IN $MCu[Q_{1-x}Q'_x]F$ (M = Ba, Sr; Q, Q' = S, Se, Te) AND RELATED MATERIALS.

Cheol-Hee Park, Douglas A. Keszler, Hiroshi Yanagi, and Janet Tate

Thin Solid Films
Brookvale Plaza, East Park, Shannon, Co. Clare, Ireland
vol. **445**, 288 (2003)

ABSTRACT

BaCuQF (Q = S, Se, Te) materials exhibit band gaps that allow transmission of much of the visible spectrum. BaCuSF is transparent in thin-film form with a band gap of 3.1 eV. Band gap estimates for powders of the solid solution series $BaCuS_{1-x}Se_xF$ were obtained from wavelength-dependent diffuse-reflectance measurements using an integrating sphere. The band gap can be tuned by the substitution of Se for S to 2.9 eV for BaCuSeF. The decrease scales almost linearly with the increase in the volume of the tetragonal unit cell, which is determined primarily by the expansion of the *a* lattice parameter; the overall volume increase is 7.0% from $x = 0$ to $x = 1$. Further reduction of the band gap is observed in $BaCuSe_{1-x}Te_xF$ solid solutions, where a unit cell volume increase of 5.5% produces a band gap of 2.7 eV in $BaCuSe_{0.5}Te_{0.5}F$. Powders and films of BaCuSF exhibit strong red luminescence under ultra-violet excitation, which is suppressed by K doping. Additional tuning of band gap and electrical properties (the materials are *p*-type conductors) can be achieved by replacing Ba with Sr.

INTRODUCTION

Many of the devices realized with narrow band gap semiconductors can in principle be realized in wide band gap semiconductors, making transparent electronics or transparent electro-optic devices possible. This requires development of wide band gap semiconductors with tunable band gaps that can be readily doped with *n*- and/or *p*-type carriers.

Transparent *n*-type conductors have been in use for decades with doped binary compounds such as In_2O_3:Sn (ITO), SnO_2:F, and recently, ZnO:Al being the most common in commercial applications. Present research on *n*-type transparent conductors focuses on new materials to replace potentially scarce indium, or to improve conductivity for specialized applications. However, ITO, with a conductivity of $\approx 10^4$ S/cm and >80% visible transparency for several-hundred-nanometer films, has been unchallenged for more than 20 years [1]. On the other hand, *p*-type conductivity is not common in transparent conductors and there are no examples of commercial applications. Since the report in 1997 of *p*-type conductivity in transparent $CuAlO_2$ films [2], other materials followed, and examples of transparent electronic devices have been reported [3,4]. Most *p*-type transparent conductors are oxides, but the oxide carrier mobilities are typically 2 orders of magnitude smaller than those for their *n*-type counterparts. The conductivities of highly transparent *p*-type oxide conductors are also about 3 orders of magnitude smaller than that of ITO. Improvements in conductivity, while

significant, invariably compromise transparency to an unacceptable level. There are reports of *p*-type conductivity among the wide band-gap oxide sulfides (LaCuOS) [5,6], sulfides ($BaCu_2S_2$) [7], and chalcogenide-fluorides (BaCuSF:K and BaCuSeF:K) [8]. These materials exhibit properties that suggest that they may be reasonable alternatives to oxides. $BaCu_2S_2$ films have a mobility of 3.5 cm^2/V s and conductivity of 17 S/cm, relatively large by *p*-type oxide standards, and the conductivities remain high and the band gap is increased in the related material BaCuSF:K. LaCuOS is an ultraviolet light emitter that exhibits excitonic absorption and emission even at room temperature [6].

The structural similarity of BaCuQF to LaCuOS suggests that BaCuQF, too, may exhibit excitonic emission, and that this might be controlled if the band gap can be tuned. Figure 4.1 shows the BaCuQF crystal structure, which belongs to the space group *P*4/*nmm*, reported in 1994 by Zhu et al. [9]. This is a layered structure with tetragonal symmetry, in which $(Ba_2F_2)^{2+}$ and $(Cu_2Q_2)^{2-}$ layers are alternately stacked along the *c* axis in the same way that $(La_2O_2)^{2+}$ and $(Cu_2S_2)^{2-}$ layers constitute LaCuOS. The $(Cu_2Q_2)^{2-}$ layers, which can also be thought of as layers of edge-sharing CuQ_4 tetrahedra, have an obvious correspondence to the $BaCu_2S_2$ structure [7], so that this is expected to be the plane for hole conduction. Experimental and theoretical analyses indicate that the $(Cu_2S_2)^{2-}$ layers contribute to both the top of the valence band and the bottom of the conduction band of LaCuOS [10], and LDA band structure calculations [11] and photoemission experiments [12] also indicate that the contribution to the top of the valence band in BaCuSF

from the $(Cu_2S_2)^{2-}$ layers is strong. Thus it is expected that the substitution of Se and Te for S should modulate the band gap both directly, due to the contribution to the top of the valence band, and indirectly, via a size effect.

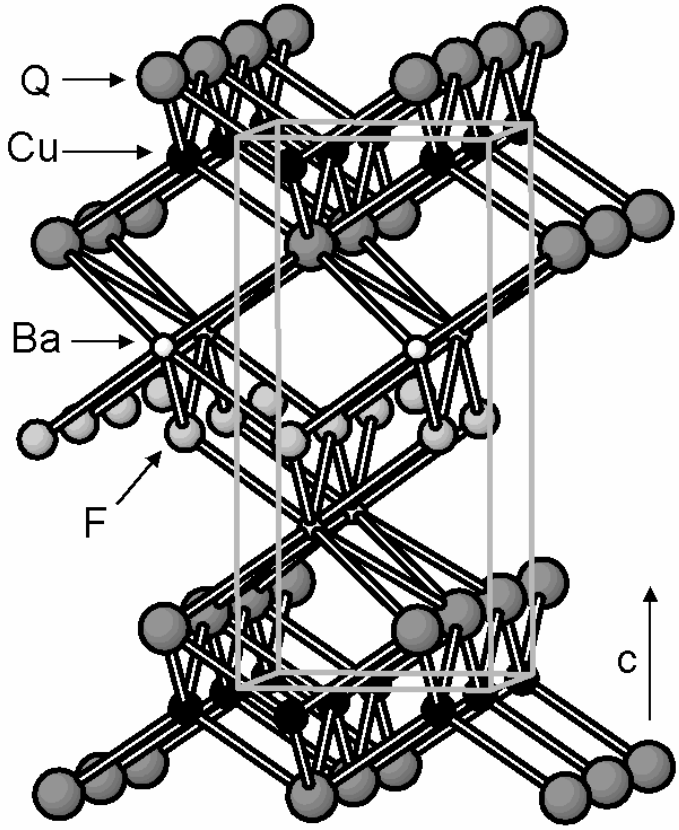

Figure 4.1. Crystal structure of BaCuQF (Q = S, Se, Te).

Zhu and co-workers reported semiconducting behavior of BaCuQF, but details were lacking. Recently, Yanagi et al. synthesized $Ba_{1-x}K_xCuSF$ and $Ba_{1-x}K_xCuSeF$ [8] and showed that in pressed pellets, the modest *p*-type conductivity present in nominally undoped BaCuQF ($x = 0$) could be improved by over 2 orders of magnitude by increasing the K dopant to $x = 0.1$. Conductivities of 82 S/cm for $Ba_{0.9}K_{0.1}CuSF$ and 43 S/cm for $Ba_{0.9}K_{0.1}CuSeF$ were reported. Furthermore, from transmission measurements on thin films of BaCuSF [13], it was concluded that the band gap was 3.1 – 3.2 eV, suitable for visible transparency. Also, red luminescence was observed in BaCuSF under UV excitation, making this material a rich source of potentially exploitable phenomena. This paper reports the successful synthesis of solid solutions of MCuQF (M = Ba, Sr; Q = S, Se, Te) and the resultant band gap modulation.

In narrow band gap semiconductor systems, quantum well devices are constructed by alternating layers of different band gaps. Compositional control of, for example, $Al_{1-x}Ga_xAs$ in alternating layers achieves the desired band gap modulation. In wide band gap p-type conductors, such gap modulation should also be possible. It is interesting to note that in the series of p-type transparent conductors $CuMO_2$ (M = Al, Ga, In) [14,15,16], the observed optical band gaps increase with increasing atomic number of the M cation in contrast to other series of group III-containing semiconductors like $CuMS_2$ [17]. This has been explained by the existence of an *indirect* gap, which does indeed decrease, with increasing

size of the M cation, but optical evidence for this gap is suppressed due to symmetry considerations [18].

EXPERIMENTAL

Powders of BaCu(S,Se)F were prepared by mixing stoichiometric proportions of BaF_2 (Cerac, 99.9 %), $BaCu_2S_2$, and $BaCu_2Se_2$. The latter two compounds were prepared in house [7]. The constituent materials were intimately mixed and placed in an evacuated silica tube at 650˚C for 15 h. A similar procedure was used for BaCu(Se,Te)F, but the starting materials were BaSe, Cu_2Se, Cu_2Te (all Cerac, 99.5 %), and BaF_2. We also prepared compounds in which Ba was partially or completely replaced by the smaller cation Sr. In this case, the reagents $BaCO_3$, $SrCO_3$, Cu_2S, BaF_2, and SrF_2 were mixed in stoichiometric proportions, placed in an alumina tube, and heated at 470˚C under flowing H_2S(g) for 2 h to produce (Sr,Ba)CuSF. Synthesis of compounds containing Ca [(Ba,Ca)CuSF and (Ca,Sr)CuSF] was also attempted following similar procedures. The thermal and chemical stability of BaCuSF was examined by heating samples to 870˚C and 500˚C in vacuum and air, respectively, and then examining X-ray diffraction patterns of the products. X-ray measurements on BaCuSF were also made following a soak in H_2O(l) at 25^{o}C.

Films of BaCuSF were obtained by using a variant of the reactive solid phase epitaxy (R-SPE) method described by Ohta, Nomura, Orita, and Hirano [19]. In our adaptation of the method, a 5-nm layer of Cu was thermally evaporated onto a MgO (100) single-crystal substrate held at 400˚C. After the substrate cooled to room temperature, BaCuSF was thermally evaporated from the powder, forming an amorphous film on the MgO/Cu. A second MgO substrate was then placed on top of the amorphous film and subsequently annealed at various temperatures from 350˚C to 750˚C for 15 h in an evacuated silica tube to induce crystallization.

Powder and thin-film x-ray diffraction patterns were obtained with Cu Kα radiation on a Siemens D-5000 diffractometer.

Diffuse reflectance spectra were used to estimate the band gap of $BaCuQ_{1-x}Q'_xF$ powders. A double-monochromater grating spectrometer illuminated by a Xe lamp generated quasi-monochromatic light tunable from about 230 nm to 900 nm with a resolution of about 2 nm. Suitable filters rejected second-order contributions from high-energy photons. The monochromatic light illuminated the powder sample that forms part of the wall of a 20-cm diameter Oriel integrating sphere. Diffusely reflected light is detected by a Si diode located in a port at 90˚ to the powder port. The diffuse reflectance spectra of the $BaCuQ_{1-x}Q'_xF$ materials were measured relative to MgO powder whose diffuse reflectance spectrum is flat over the same range. The diffuse reflectance spectra were translated into absorption spectra via the Kubelka-Munk method [20,21], and the band gap was extracted by extrapolating the straight-line portion of the curve of $(\alpha E)^2$ *vs.* E to the zero-

absorption axis. Here α is the absorption coefficient, E is the photon energy, and a direct gap has been assumed in accordance with the LDA band structure calculations [11]. In the case of thin films, the same spectrometer was used without the integrating sphere, and transmission spectra were obtained directly.

Photoluminescence measurements were made with an Oriel 300-W Xe lamp and a Cary model-15 prism monochromator for excitation and an Oriel 22500 1/8-m monochromator and Hamamatsu R636-10 photomultiplier tube for detection. Excitation spectra were corrected for the response of the system by using rhodamine B, and emission spectra were corrected with a standardized W lamp.

RESULTS AND DISCUSSION

Up to now, only the compounds BaCuSF and BaCuSeF have been described as members of the BaCuQF family. We have found that the Q site can be freely substituted with S, Se, and Te, while Ba can be replaced with Sr. Such substitutions are clearly evident from peak shifts in X-ray diffraction patterns. The results are quantified in Figure 4.2, where the *a*-axis lattice parameter and the cell volume are plotted as a function of x for the solid- solution series $BaCuS_{1-x}Se_xF$ ($0 \leq x \leq 1$) and $BaCuSe_{1-x}Te_xF$ ($0 \leq x \leq 0.5$). The essentially linear change of the a lattice parameter and cell volume with x are in agreement with Vegard's law, indicating a random distribution of the Q, Q' atoms. Since the a lattice parameter

changes by 5.1% and the *c* lattice parameter changes by only 2.2%, the volume increase with Q substitution is largely represented by expansion in the *ab* plane. (We should note that in this Se,Te series, the maximum value of $x = 0.5$ appears to be limited only by our inability to acquire or synthesize BaTe, which we would like to use as the reagent to synthesize samples having a larger value of *x*.)

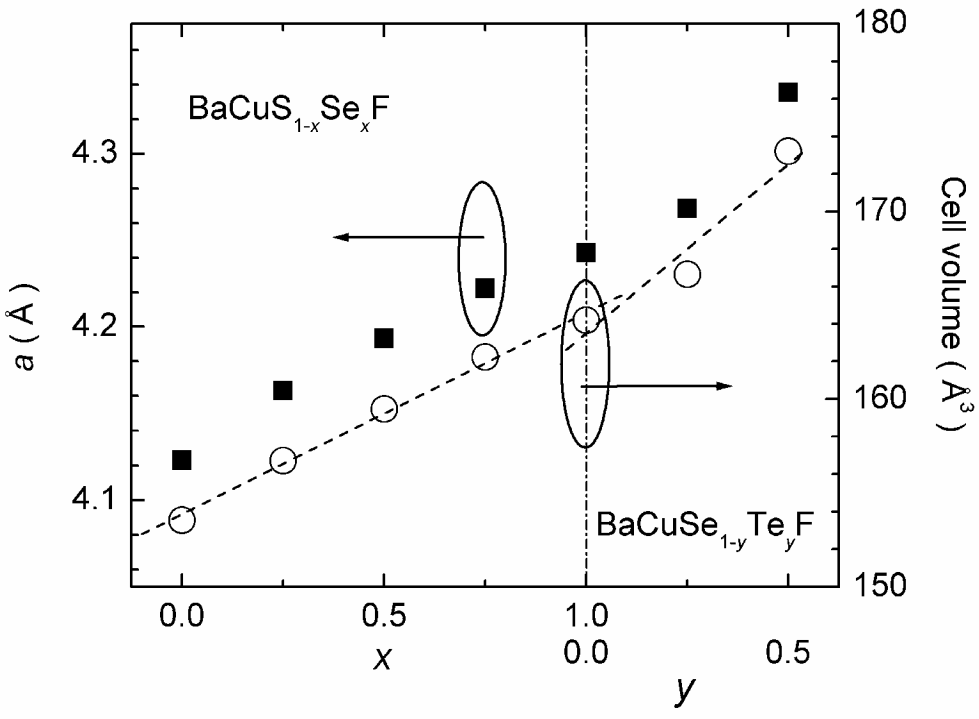

Figure 4.2. Lattice constant *a* and cell volume *vs. x* or *y* for $BaCuS_{1-x}Se_xF$ and $BaCuSe_{1-y}Te_yF$.

For the series $Ba_{1-x}Sr_xCuSF$ ($0 \leq x \leq 1$), decreases in the *a* lattice parameter and cell volume are evident with increasing Sr concentration (Figure 3.3). Here the *a* and *c* lattice parameters decrease by 3.9% and 3.8%, respectively, indicating a more isotropic volume change in comparison to the Q, Q' substitutions. For Ca substitution, i.e., $Ba_{1-x}Ca_xCuSF$ and $Sr_{1-x}Ca_xCuSF$, much more limited solubility is observed. No statistically significant reduction in cell parameters is observed for Ca substitution in the Ba phase, so any solid solubility is very low. In the case of the Sr phase, a small reduction in cell parameters is observed from $a = 3.963(2)$ and $c = 8.6749(4)$ Å in the Sr compound to $a = 3.954(2)$ and $c = 8.6572(5)$ Å in the Ca-substituted material. The latter values represent no greater than a 10 at% substitution of Ca into SrCuSF.

Diffuse reflectance spectra for the series BaCu(S,Se)F and BaCu(Se,Te)F are illustrated in Figure 3.4. Diffuse reflectance spectra from powders give information similar to that obtained from transmission spectra of films or single crystals. A significant fraction of light diffusely reflected from a collection of powder crystallites has undergone not merely a single surface reflection, but has traversed a complicated path involving transmission through, and reflection from, many crystallites near the surface. Hence the diffuse reflection spectrum contains significant transmissive character and can be used to characterize absorption. The abrupt increase of the diffuse reflectance signal seen in Figure 3.4 is thus indicative of the onset of transmission near the energy gap. As the heavier Q atom is

incorporated into the structure, the energy gap shifts to longer wavelengths and lower energies.

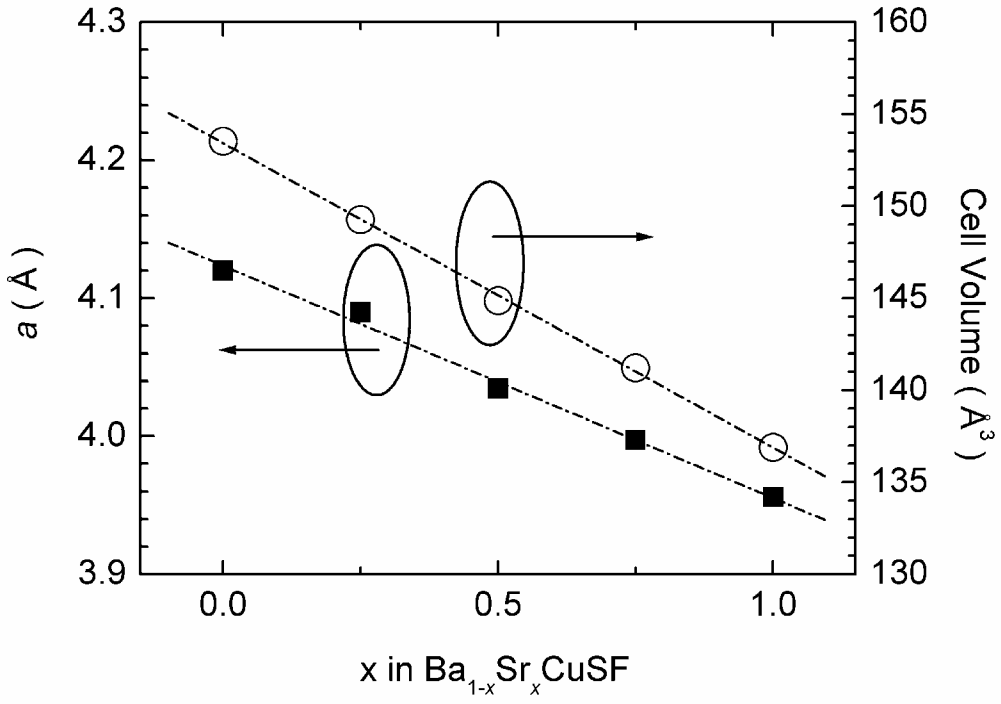

Figure 4.3. Lattice constant *a* and cell volume *vs. x* for $Ba_{1-x}Sr_xCuSF$.

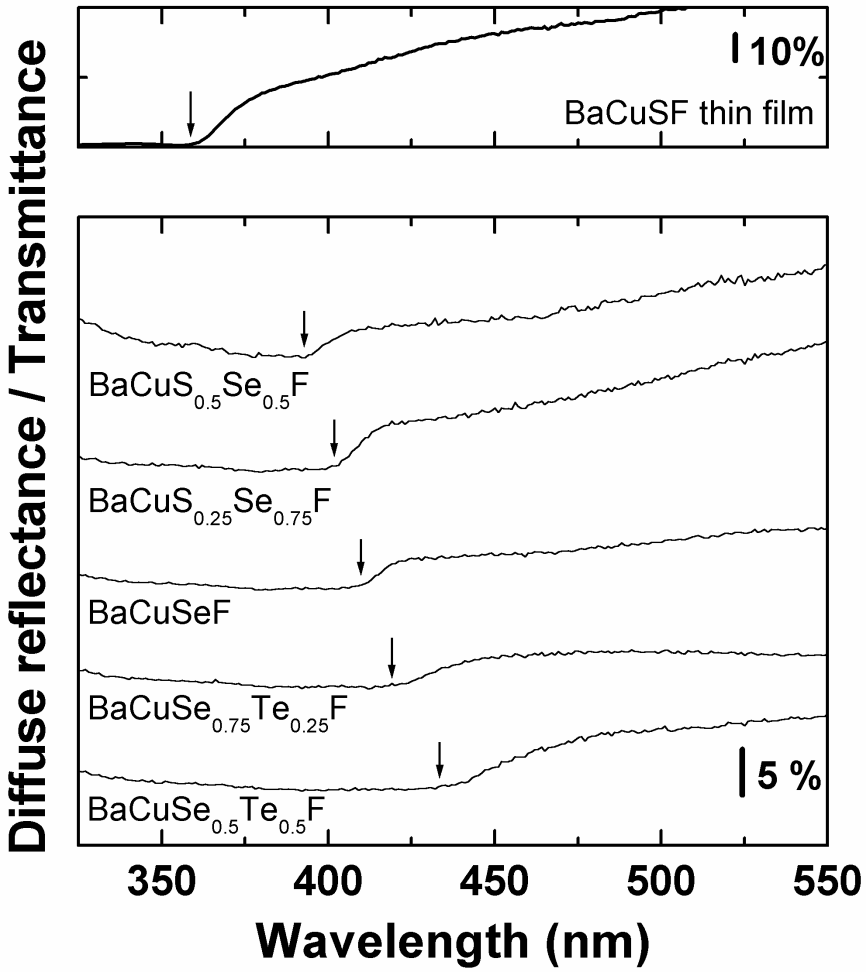

Figure 3.4. Transmission spectrum of a BaCuSF thin film (top), and diffuse reflectance spectra of $BaCuS_{1-x}Se_xF$ and $BaCuSe_{1-y}Te_yF$ powders (bottom). The arrows indicate the position of the energy gap derived via the Kubelka-Munk equation.

Derived results from the Kubelka-Munk analysis are shown in Figure 4.5, where the band gap is plotted as a function of lattice parameter for the two BaCuQQ'F series. The value for the band gap of BaCuSF was derived from the transmission spectrum of a transparent thin film. The diffuse reflectance spectrum from the BaCuSF powder was dominated by strong photoluminescence under UV excitation (see below), which obscured the absorption onset. The band gap can be tuned by the substitution of Se for S to 2.9 eV for BaCuSeF. The decrease scales almost linearly with the increase in the volume of the tetragonal unit cell, which is determined primarily by the expansion of the *a* lattice parameter. The overall volume increase is 7.0% from $x = 0$ to $x = 1$. Further reduction of the band gap is observed in $BaCuSe_{1-x}Te_xF$ solid solutions, where a unit-cell volume increase of 5.5% produced a band gap of 2.7 eV in $BaCuSe_{0.5}Te_{0.5}F$. All the materials discussed here should be suitable for transparent conductors, except perhaps for the shortest blue wavelengths. The light-gray appearance of the powders, which intensifies only slightly with the addition of the heavier Q atoms, is consistent with these changes in the band-gap energies.

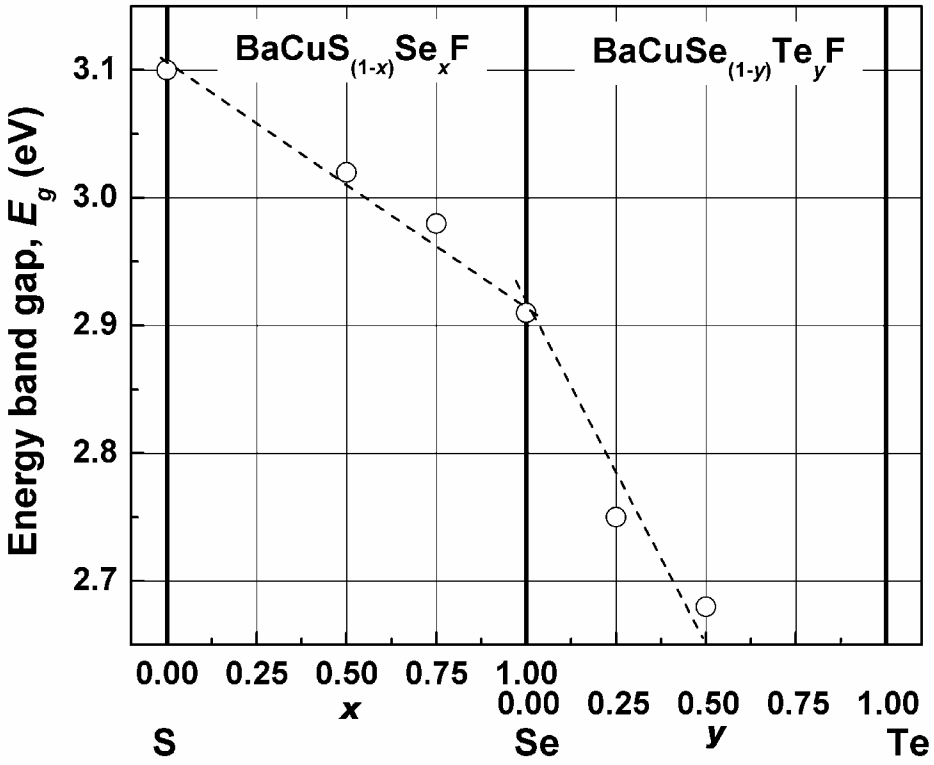

Figure 4.5. Band gap tuning of $BaCuS_{1-x}Se_xF$ and $BaCuSe_{1-y}Te_yF$.

The thermal and chemical stabilities of BaCuSF have been cursorily examined by heating in vacuum and air and by placing in water. In vacuum, the material is stable to at least 870°C; heating under flowing $H_2S(g)$ in an Al_2O_3 boat with a small amount of K_2CO_3 at 870°C results in melting and the production of single crystals [22]. BaCuSF is stable in air up to temperatures near 500°C. As shown in Figure 3.6, gradual decomposition occurs with production of $BaSO_4$ and Ba_2CuO_3 indicated from analysis of the powder diffraction patterns. While

exposure to a standard laboratory environment at room temperature does not appear to significantly affect BaCuSF, upon placement in $H_2O(l)$, the compound decomposes to give a black decomposition product.

Seebeck coefficient measurements were performed to establish the *p*-type nature of the materials.

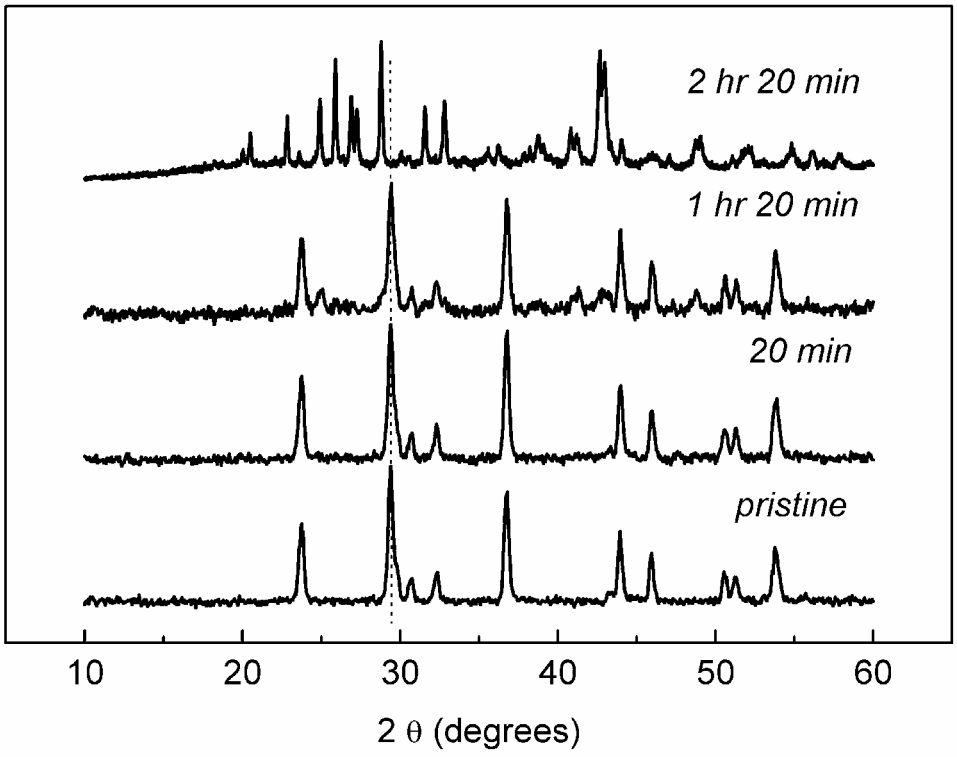

Figure 3.6. Thermal degradation of BaCuSF in air at 500˚C.

Emission and excitation spectra for the unusual red photoluminescence of BaCuSF films and powders are given in Figure 3.7 [8]. The emission peaks centered near 620 nm are identical for both the single crystal and powder forms. The onsets of the excitation bands near 400 nm are consistent with onsets in diffuse reflectance and transmission spectra (Figure 3.4), indicating the excitation process is associated with band-gap absorption. The luminescence with respect to wavelength and brightness is rather complex, being greatly affected by preparative conditions, temperature, and the incorporation of dopants. In the film, for example, photoluminescence is only observed following anneals above 550˚C, and the brightness falls with substitution of K for Ba. The characteristics of the primary luminescent centers are not yet clear, since the system displays a complex range of behaviors, but it may be that electrons at S vacancies may be combining with holes at Cu sites to produce the emission. The relatively long luminescence lifetime of 0.65 ms would be consistent with such a model, if the hole is assumed to be delocalized among the Cu atoms, a result that mirrors the electrical conductivity that has been observed in this system.

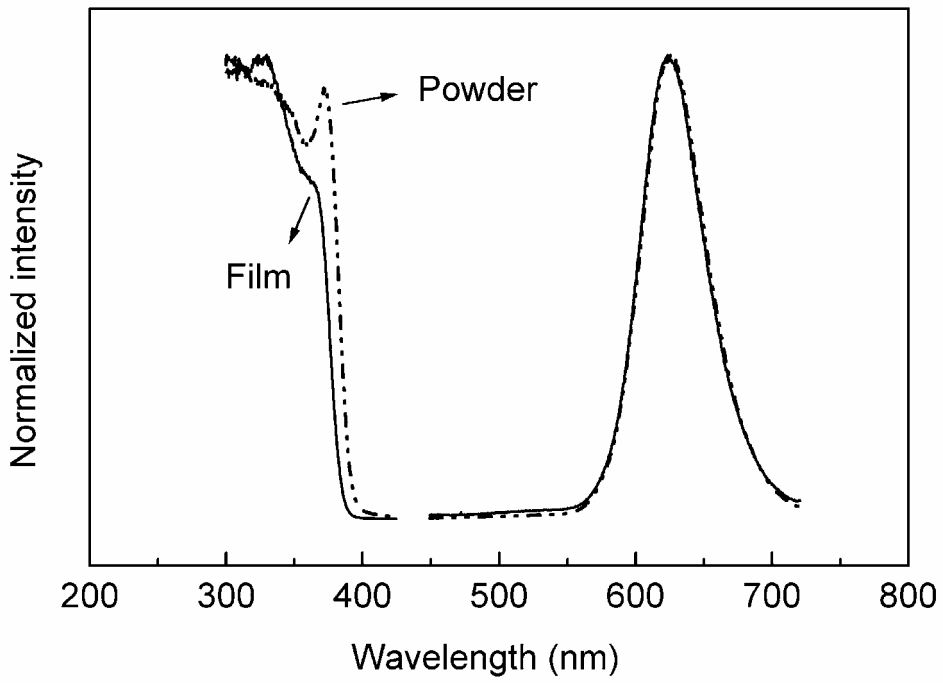

Figure 3.7. Photoluminescence spectra of BaCuSF powder and a BaCuSF film.

SUMMARY

The band gap of the *p*-type conducting system $BaCuS_{1-x}Se_xF$ changes over the entire range of solid solution from 3.1 eV (x = 0) to 2.9 eV (x = 1). Further reduction results from substitution of Te for Se in $BaCuSe_{1-x}Te_xF$ to 2.7 eV for x = 0.5. In both cases, the change is linear with x in accordance with Vegard's law. $Ba_{1-x}Sr_xCuF$ also shows a linear variation in cell volume over the entire solid-solution range, demonstrating for the first time the existence of the Sr derivative SrCuSF. Undoped BaCuSF films and powders exhibit a bright, saturated red luminescence with a relatively long decay time of 0.65 ms. Considering the ease in achieving band-gap modulation, the relatively low processing temperatures, the high *p*-type conductivity, and light emission, the materials MCuQF certainly represent a rich family for continued studies and exploitation.

ACKNOWLEDGEMENTS

This material is based upon work supported by the National Science Foundation under Grant No. 0071727. We thank Prof. H.J.F. Jansen for providing band structure calculations of BaCuQF.

REFERENCES

[1] See T. Minami, *Materials Research Bulletin*, **25**, 38-44 (2000) for a review of recent developments.

[2] H. Kawazoe, M. Yasukawa, H. Hyodo, M. Kurita, H. Yanagi, and H. Hosono, *Nature*, **389**, 939 (1997).

[3] H. Hosono, H. Ohta, K. Hayashi, M. Orita, and M. Hirano, *J. Cryst. Growth*, **237-239**, 496 (2002), and references therein.

[4] R. L. Hoffman, B. J. Norris, and J. F. Wager, *Appl. Phys. Lett.*, **82**, 733 (2003).

[5] M. Palazzi, *Acad. Sci., Paris, C. R.*, **292**, 789 (1981).

[6] K. Ueda, S. Inoue, H. Hosono, N. Sarukura, and M. Hirano, *Appl. Phys. Lett.*, **78**, 2333 (2001).

[7] S. Park, D. A. Keszler, M. M. Valencia, R. L. Hoffman, J. P. Bender, and J. F. Wager, *Appl. Phys. Lett.*, **80**, 4393 (2002).

[8] H. Yanagi, J. Tate, S. Park, C.-H. Park, D. A. Keszler, *Appl. Phys. Lett.*, **82**, 2814 (2003).

[9] W. J. Zhu, Y. Z. Huang, F. Wu, C. Dong, H. Chen, and Z. X. Zhao, *Mater. Res. Bull.*, **29**, 505 (1994).

[10] S. Inoue, K. Ueda, and H. Hosono, *Phys. Rev.*, **B 64**, 245211 (2001).

[11] H. J. F. Jansen, private communication.

[12] H. Yanagi, J. Tate, D. A. Keszler, S. Park, C.-H. Park, H. Hosono, *unpublished*.

[13] H. Yanagi, S. Park, A. D. Draeseke, D. A. Keszler, and J. Tate, *J. Solid State Chem.*, **175**, 34 (2003).

[14] H. Yanagi, S. Inoue, K. Ueda, H. Kawazoe, H. Hosono, and N. Hamada, *J. Appl. Phys.*, **88**, 4159 (2000).

[15] K. Ueda, T. Hase, H. Yanagi, H. Kawazoe, H. Hosono, H. Ohta, M. Orita, and M. Hirano, *J. Appl. Phys.*, **89**, 1790 (2001).

[16] H. Yanagi, T. Hase, S. Ibuki, K. Ueda, and H. Hosono, *Appl. Phys. Lett.*, **78**, 1583 (2001).

[17] O. Madelung and M. Schulz (Eds.), *Landolt-Bornstein: Numerical Data and Functional Relationships in Science and Technology: Group III*, vol. 22a, Springer-Verlag, Berlin (1987)

[18] X. Nie, S.-H. Wei, S. B. Zhang, *Phys. Rev. Lett.*, **88**, 066405 (2002).

[19] H. Ohta, K. Nomura, M. Orita, M. Hirano, K. Ueda, T. Suzuki, Y. Ikuhara, and H. Hosono, *Adv. Funct. Mater.*, **13**, 139-144 (2003).

[20] P. Kubelka and F. Munk, *Z. Tech. Phys.*, **12**, 593 (1931).

[21] P. Kubelka, *J. Opt. Soc. Am.*, **38**, 448 (1948).

[22] C.-H. Park and D. A. Keszler, *unpublished*.

CHAPTER 5

STRUCTURE AND PHYSICAL PROPERTIES OF BaCuTeF

Cheol-Hee Park, Robert Kykyneshi, Alexandre Yokochi, Janet Tate,
and Douglas A. Keszler

submitted to *Journal of Solid State Chemistry*
525 B Street, Suite 1900, San Diego, CA 92101-4495

ABSTRACT

The compound BaCuTeF was prepared by using high-temperature reaction methods, and its structure was determined via powder X-ray diffraction and the Rietveld refinement method, resulting in R_p / wR_p / R_{Bragg} (%) = 6.72 / 4.42 / 5.72. It crystallizes in the tetragonal space group P4/nmm (No.129) with Z = 2, a = 4.4297 (1), c = 9.3706 (1) Å, and V = 183.87 (1) Å^3. Its band gap is estimated to be 2.3 eV from wavelength-dependent diffuse reflectance measurements. Room-temperature conductivity of a pressed pellet is 8 S/cm, and variable-temperature Seebeck and electrical-conductivity measurements reveal *p*-type degenerate semiconductor behavior.

INTRODUCTION

Materials of MCuQF (M=Ba, Sr; Q=S, Se, Te) exhibit various interesting optical and electrical properties. BaCuQF (Q = S, Se) materials exhibit *p*-type conductivity and band gaps that allow transmission of much of the visible spectrum [1]. BaCuSF is transparent in thin-film form with a band gap of 3.1-3.2 eV [2]. The room-temperature Seebeck coefficient and electrical conductivity of undoped BaCuQF pellets were +56 μV/K and 0.088 S/cm, respectively, for the sulfide fluoride, and +32 μV/K and 0.061 S/cm, respectively, for the selenide fluoride. The conductivity was greatly enhanced by the substitution of several percent of K for Ba; the highest conductivities were 82 S/cm for $Ba_{0.9}K_{0.1}CuSF$ and 43 S/cm for $Ba_{0.9}K_{0.1}SeF$ [3]. Another interesting feature is strong red luminescence near 630 nm under ultraviolet excitation in undoped BaCuSF. Gradual change in emission color from the saturated red to the saturated green was observed by altering the synthesis conditions or by selective doping [4]. In addition, the band gap of MCuQF (M=Ba, Sr; Q=S, Se, Te) is easily tuned by changing Q [1,4].

In a previous work, band gap modulation was demonstrated in solid solution series of $BaCuS_{1-x}Se_xF$ and $BaCuSe_{1-x}Te_xF$ [1]. The band gap can be tuned by the substitution of Se for S to 2.9 eV for BaCuSeF, and further reduction of the band gap was achieved to 2.7 eV in $BaCuSe_{0.5}Te_{0.5}F$ in $BaCuSe_{1-x}Te_xF$ solid solutions. This decrease in band gap by substitution of Se or Te seems to be

partially due to increased size and more dispersed valence band. The decrease scales almost linearly with the increase in the volume of the tetragonal unit cell.

The temperature dependence of the electrical conductivity of undoped BaCuSF is typical of a semiconductor, while the electrical conductivity of the undoped BaCuSeF has a very weak temperature dependence [3], which also seems to be ascribed to more disperse (or broader) valence band of BaCuSeF. The top of the valence band in BaCuQF (Q=S, Se) is mainly composed of Cu 3*d* and S 3*p* (or Se 4*p*) orbitals from the LDA band structure calculations [5] and photoemission experiments [6]. Typically higher covalency will give broader bands and smaller effective masses which give rise to higher carrier mobilities [7]. Selenium and tellurium are heavier members of Group VI than sulfur, and their electronegativities are similar to or smaller than that of S ($\chi_{P,\,S} = 2.58$, $\chi_{P,\,Se} = 2.55$; Te: $\chi_{P,\,Te} = 2.10$, χ_P is the Pauling electronegativity) [8]. Therefore higher electrical conductivity is expected in BaCuTeF. At the time the work on the $BaCuSe_{1-x}Te_xF$ solid solution series was reported the maximum value of x was 0.5, limited by our inability to acquire or synthesize BaTe, which we considered a key reagent for the synthesis of samples having a Te fraction larger than 0.5. The band gap of BaCuTeF was expected to be much smaller than BaCuSeF based on the compositional dependence of the band gap; the change in the band gap with compositional change for $BaCuS_{1-x}Se_xF$ series is more significant than for $BaCuSe_{1-x}Te_xF$ series.

Higher conductivity and small band gap of BaCuTeF may satisfy the requirements for application in polycrystalline thin-film tandem solar cells.

Polycrystalline thin-film tandem solar cells constitute a promising avenue for the realization of an economically-viable renewable energy source [9,10]. For separately connected tandem solar cells, optimal band-gap combination for two- and three-terminal structures have been specified as 1.8/1.1 eV and 2.15/1.55/1.0 eV, respectively [11,12]. The high band-gap portion of the cell requires *p*-and *n*-type windows having band gaps near 2.2 eV.

Here, we report the successful synthesis of BaCuTeF, its structure, and transport and optical properties. It will be shown that its room-temperature conductivity is much larger than that of undoped BaCuSF and BaCuSeF, and that the temperature dependence of the electrical conductivity and Seebeck coefficient is consistent with *p*-type degenerate semiconductor behavior.

EXPERIMENTAL

Synthesis

Reagents for synthesis of BaCuTeF were BaTe (synthetic details given below), Cu_2Te (Cerac, 99.5%), and BaF_2 (Cerac, 99.9%). The constituent materials were intimately mixed in Stoichiometric proportions and placed in an evacuated silica tube at 500°C for 12 h. Product characterization by powder X-ray diffraction analysis revealed a mixture of the desired phase and BaF_2. The sample was subsequently annealed at 500°C under flowing H_2(5%)/N_2(95%) for 2 h, leading to a decrease in the intensity of diffraction lines attributed to BaF_2 (< 5 wt%), and leaving the remaining BaCuTeF product lines unaffected. Adding 5 wt% excess Te to the sample before annealing in the reducing atmosphere afforded single-phase BaCuTeF.

BaTe was prepared by using Ba metal (Alfa, 99.2% in oil) and Te (Alfa, 99.9%). After carefully washing the Ba several times with *n*-hexane, while preventing exposure to air, it was introduced into an Ar-filled glove box. The white oxide surface on the metal was removed with a scalpel, and the resulting material was placed in a silica tube with a stoichiometric amount of Te. The silica tube was evacuated and heated at 550°C for 5h. The powder X-ray diffraction pattern of the product agreed with that reported for BaTe [JCPDS # 39-1475].

Structural characterization.

Data for the Rietveld structural refinement were collected on a 1:1 mixture by weight of BaCuTeF and LiF by using a Siemens D5000 diffractometer with variable slits and a locally devised variable counting time routine [13]. Data were converted to GSAS ESD format by using an in-house program [14], and structural refinement was performed by using the program Fullprof [15].

During refinement, it was noticed that there was a certain amount of anisotropic *hkl*-dependent line broadening associated with strain in the sample. In an effort to optimize the fit, the four possible parameters in Stephen's formalism [16] of strain broadening for this Laue class were refined, resulting in substantial improvements in residuals. Final crystallographic parameters for this refinement, including some calculated strain parameters, are given in Table 1, and positional parameters and equivalent isotropic displacement parameters are listed in Table 2. [Note: in the program Fullprof, a integral breadth contribution due to strain (β_{str}) with units of 10^4*Å^{-1} is calculated from the refined parameters, in which case S_{HKL} = ½* β_{str} *d_{hkl}. The value thus obtained is approximately equivalent to ¼ of the value of the equivalent Stokes-Wilson apparent strain.].

Transport property measurements

For transport property measurements, powder samples were pressed into 9.5-mm diameter pellets at 3 tons and annealed at 1048 K for 5 h in evacuated silica tubes.

TABLE 5.1. Summary of refinement data and lattice parameters of BaCuTeF.

Formula		BaCuTeF
Space group		*P4/nmm* (No. 129)
Z		2
a (Å)		4.4297(1)
c (Å)		9.3706(1)
Vol ($Å^3$)		183.87(1)
FW (amu)		347.94
Calculated density		6.279 g/cm^3
2θ range (°)		8.5-150.0
S_{400}		0.37(2)
S_{004}		0.067(4)
S_{220}		1.01(10)
S_{202}		0.00(2)
Calculated strain (%%) in given crystallographic direction	100	7.52
	101	6.24
	111	7.22
	110	8.13
	001	14.40
R_p (%)		6.72
R_{wp} (%)		4.42
R_{Bragg} (%)		5.72
Number of reflections		280
Number of parameters		(13 Le Bail + 10 Rietveld)

TABLE 5.2. Final positional and isotropic equivalent displacement parameters ($Å^2$ x 100) for BaCuTeF.

	Wyckoff	x	y	z	U_{iso}
Ba	2c	¼	¼	0.3443(2)	2.51(10)
Cu	2a	¾	¼	0	4.19(19)
Te	2c	¼	¼	-0.1636(2)	2.32(10)
F	2b	¾	¼	½	1.9(4)

The conductivities of the pellets were measured by the four-probe colinear method over the temperature range 10-300 K temperature range. The carrier sign was established with Seebeck measurements, using a temperature gradient of 3 K and covering the temperature range 50-290 K; Seebeck coefficients reported herein are not corrected for the contribution from the copper leads.

The diffuse reflectance at room temperature of a powder sample was measured with $BaSO_4$ as a reference and an optical setup comprised of an Oriel 300-W Xe lamp, a Cary model-15 prism monochromator, and a Hamamatsu R636-10 photomultiplier tube, providing coverage of the UV-visible region (360-700 nm).

RESULTS

Structural Analysis

The results of the final Rietveld refinement cycle are shown graphically in Figure 5.1. The compound BaCuTeF is isostructural to the materials BaCuQF (Q=S, Se) [1] (Figure 5.2), which adopt the same structure type as RCuOSe (R = rare earth, Bi) and LaCuOS [17]. The structure is a layered, tetragonal type with anti–fluorite (Ba_2F_2) layers alternating with (Cu_2Te_2) sheets along the *c* axis. Selected interatomic distances and angles for single crystal BaCuSF and powder samples of BaCuQF are given in Table 5.3.

TABLE 5.3. Selected interatomic distances (Å) and angles (deg) for BaCuTeF.

Cu-Te	2.694(1)	Te-Cu-Te	108.90(8)
Cu···Cu	3.1321(1)	Te-Cu-Te	110.61(4)
Ba-Te	3.560(1)	Te-Ba-Te	76.94(3)
Ba-F	2.652(1)	Te-Ba-Te	123.22(3)
Ba···Ba	4.281(2)	F-Ba-F	72.38(4)
		F-Ba-F	113.23(4)
		Te-Ba-F	75.06(5)
		Te-Ba-F	141.36(5)

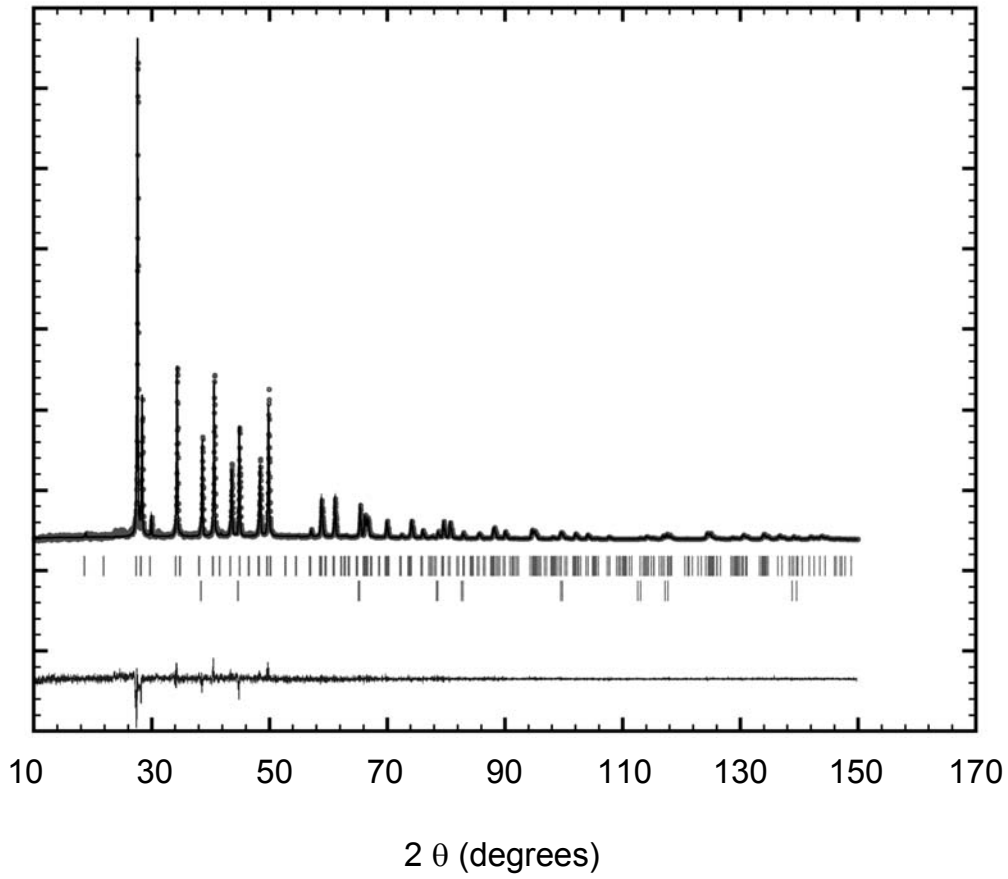

Figure 5.1. Observed (open circles) and calculated (solid line) X-ray powder diffraction pattern from refinement of BaCuTeF. The bottom curve is the difference pattern on the same scale. The top vertical bars are for BaCuTeF and the lower vertical bars are for LiF.

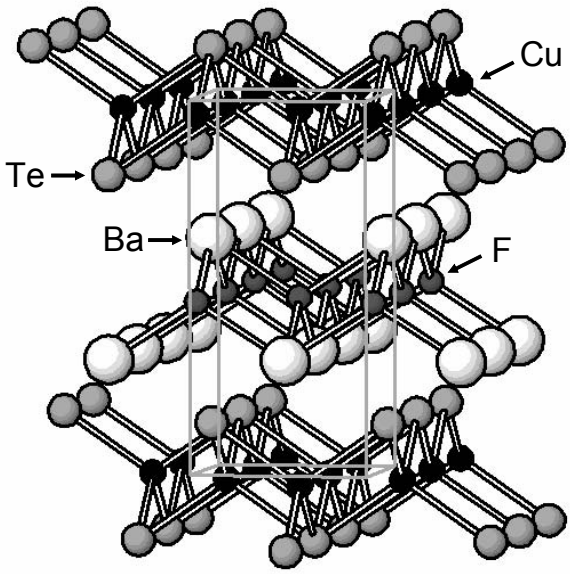

Figure 5.2. Crystal structure of BaCuTeF.

The Ba and Te atoms occupy sites with symmetry C_{4v}. The Ba atom occupies a square antiprismatic environment with four Te atoms forming one square face and four F atoms the other. The Ba-Te distance, 3.560(1) Å, compares well with those found in compounds such as $BaGa_2Te_4$ (3.562 Å) [18]. The Ba-F distance, 2.652(1) Å is similar to those observed in BaCuSF (2.613 Å), BaCuSeF (2.622 Å), and BaF_2 (2.684 Å) [19]. The Te atom is also located in a square antiprismatic site coordinated by four Ba atoms and four Cu atoms. The Cu and F atoms are located on sites having D_{2d} symmetry, resulting in distorted tetrahedral

environments. The Cu, coordinated to four Te atoms, has a Cu-Te bond distance of 2.694(1) Å, which is comparable to the sum of covalent radii-2.65 Å- [20] for each atom and values in other systems such as NaCuTe (2.704 Å) [21] and $BaCu_2Te_2$ (2.673 Å average distance) [22].

The two-dimensional Cu_2Te_2 tetragonal sheet structure has previously been observed in NaCuTe. These sheets are characterized by edge-sharing linkages of the distorted $CuTe_4$ tetrahedra, which produce relatively short Cu···Cu distances. The shortest Cu···Cu distance in BaCuTeF is 3.1321(1) Å, which is comparable to that, 3.097 Å, observed in NaCuTe, but longer than the 2.847 Å observed in $BaCu_2Te_2$. A similar situation is found in comparing Cu···Cu distances in BaCuSF (2.915 Å) and α-$BaCu_2S_2$ (2.71 Å), where CuS_4 tetrahedra share edges. The longer Cu···Cu distance for BaCuTeF in comparison to that of $BaCu_2Te_2$ derives from the Te-Cu-Te angle associated with the shared Te···Te edge; the angles are 108.90(8)^o for BaCuTeF and 115.8(1)^o for $BaCu_2Te_2$. The larger angle forces a shorter Cu···Cu contact. In a similar way, the S-Cu-S angle associated with the shortest Cu···Cu distance is 107.2^o for BaCuSF and 112.8(2)^o for α-$BaCu_2S_2$.

The bimodal distribution of the observed anisotropic strain broadening is interpreted as originating from a small probability of stacking faults in the material. This would not only result in preferential broadening of reflections with scattering vectors close to the c direction, but also in the observed strain within the layers due to slight ab plane lattice mismatch when the stacking faults do occur.

Optical Properties

The absorption spectrum of powdered BaCuTeF, which was obtained from the diffuse reflectance spectrum by using the Kubelka-Munk method [23,24], is shown in Figure 5.3. The absorption coefficient (α) increases moderately with increasing photon energy below approximately 2.2 eV. Between 2.2 and 2.8 eV, a sharp increase is observed, and at higher energy than approximately 2.9 eV, it is nearly constant. A band-gap energy of 2.3 eV was extracted by extrapolating the straight-line portion of the curve of $(\alpha E)^2$ *vs.* E to the abscissa (inset in Figure 5.3). The data are consistent with a direct band gap, which is in accordance with an LDA band-structure calculation on isomorphous BaCuSF [5]; a band-structure calculation is planned for BaCuTeF. The band gap of 2.3 eV is smaller than the band gaps of BaCuSeF (2.9 eV) and of BaCuSF (3.1 eV). The overall unit-cell volume increase is 7.0% from BaCuSF to BaCuSeF and 12% from BaCuSeF to BaCuTeF. Therefore the larger decease in band-gap energy on comparing the Te and Se *vs.* the Se and S compounds could arise in part from these cell-volume changes. The large cell volume of the Te compound reflects the larger radial extension of the Te valence orbitals, which should contribute to large band widths both through Cu-Te and Te···Te interactions.

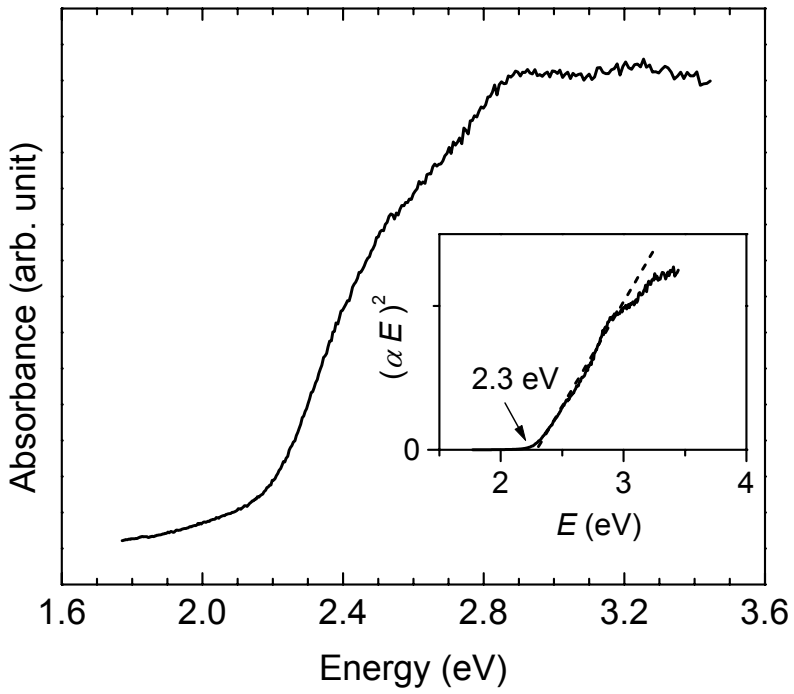

Figure 5.3. Absorption spectrum of BaCuTeF at room temperature with the curve of $(\alpha E)^2$ *vs. E* (inset).

Transport Properties

Undoped BaCuTeF exhibits a modest increase in conductivity with decreasing temperature (Figure 5.4), indicating metal-like behavior of a degenerate semiconductor. This conductivity contrasts to the activated semiconducting behavior in the conductivity of undoped BaCuSF and BaCuSeF (inset Figure 5.4) [3]. The latter two compounds exhibit metallic behavior only after *p*-type doping by K. The room temperature conductivity of BaCuTeF is 8 S/cm, two orders of magnitude higher than that of undoped BaCuSF and BaCuSeF. An anomaly is observed in the temperature dependence of the conductivity near 70 K; a similar feature was observed in $BaCu_2Te_2$ [22], which was related to changes in Cu ion conductivity. A similar change from semiconducting to metallic behavior in temperature-dependent conductivity is also observed in the orthorhombic series $BaCu_2Q_2$ (Q=S, Se, Te) [22,25]. In these compounds, the room-temperature conductivity of powdered $BaCu_2S_2$ pellet is observed to be two orders of magnitude lower than that of $BaCu_2Te_2$. The lower room temperature conductivity of BaCuTeF than that of $BaCu_2Te_2$ (127 S/cm) could be in part attributed to the longer Cu···Cu distance [7]. Another contribution may be found in the differing linkages of the $CuTe_4$ tetrahedra. In BaCuTeF, $CuTe_4$ tetrahedra are connected in only two dimensions, in contrast to the three-dimensional linkage of $CuTe_4$ tetrahedra in $BaCu_2Te_2$. The dimensional reduction in BaCuTeF should lead to an anisotropi conductivity, which in a pressed pellet would produce an under estimation of the conductivity in the Cu_2Te_2 sheets.

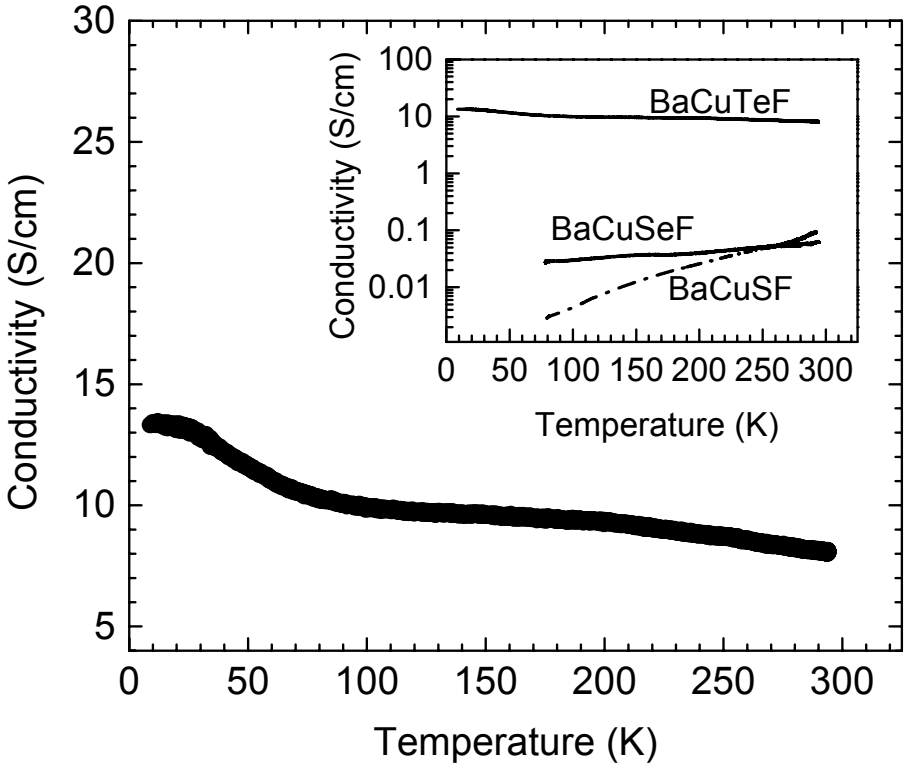

Figure 5.4. The conductivity of BaCuTeF (main graph) increases with decreasing temperature, in contrast to that on BaCuSeF and BaCuSeF (inset).

The temperature-dependence of the Seebeck coefficient for undoped BaCuTeF is illustrated in Figure 5.5. The value of +25 μV/K confirms the positive sign of carriers at room temperature, and the magnitude is similar to metals such as chromel (+20 μV/K). Between room temperature and 100 K there is linear *S vs. T* dependence, also indicating metallic behavior. Below 100 K the Seebeck coefficient of BaCuTeF must approach very closely that of copper, such that there is no measurable voltage for an established temperature gradient.

It can be concluded that BaCuTeF is a degenerate semiconductor with high carrier concentration even without any additional doping of the material. The covalency of the Cu-Te bonds provides the possibility of high mobility of carriers.

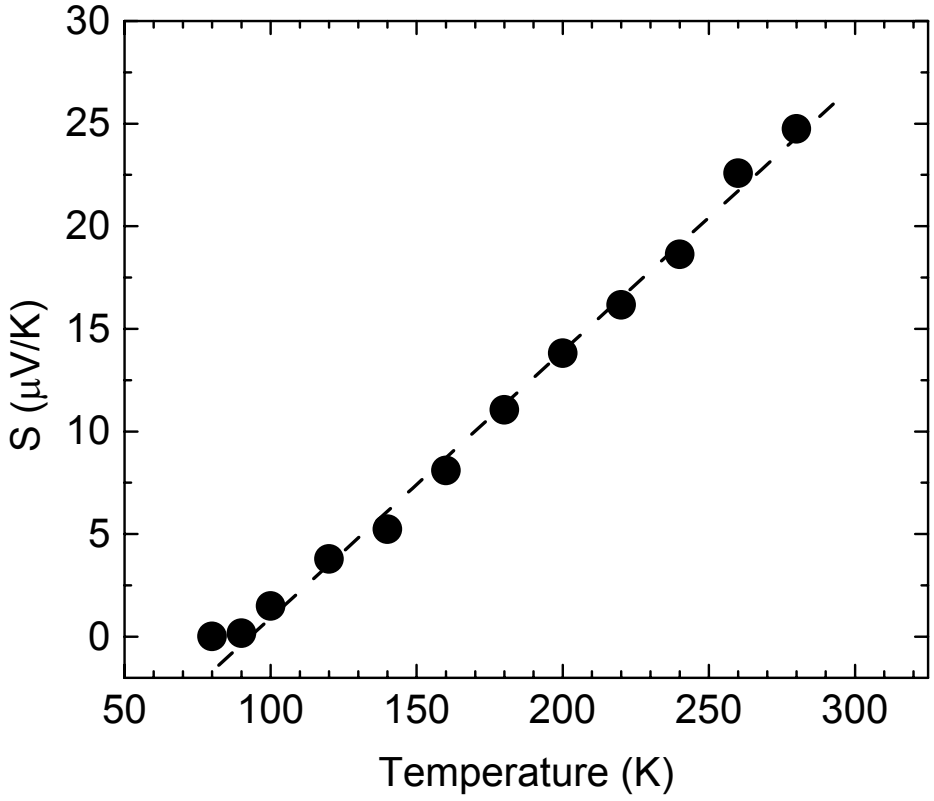

Figure 5.5. Seebeck coefficient as a function of temperature for BaCuTeF.

CONCLUSION

A new member of the BaCuQF family, BaCuTeF, was prepared by high-temperature reaction methods, and its structure was determined via the Rietveld refinement method by using powder X-ray diffraction. Its band gap is estimated to be 2.3 eV from wavelength-dependent diffuse reflectance measurements, and temperature-dependent Seebeck-coefficient and conductivity measurements clearly indicate that it is a *p*-type degenerate semiconductor.

ACKNOWLEDGMENTS

This material is based on work supported by the National Science Foundation under Grant No. DMR-0245386.

REFERENCES

[1] C.-H. Park, D. A. Keszler, H. Yanagi, J. Tate, *Thin solid films*, 445, 288 (2003).

[2] H. Yanagi, S. Park, A. D. Draeseke, D. A. Keszler, and J. Tate, *J. Solid State Chem.*, **175**, 34 (2003).

[3] H. Yanagi, J. Tate, S. Park, C.-H. Park, D. A. Keszler, *Appl. Phys. Lett.*, 82, 2814 (2003).

[4] C.-H. Park, and D. A. Keszler, unpublished.

[5] H. J. F. Jansen, private communication.

[6] H. Yanagi, J. Tate, D. A. Keszler, S. Park, C.-H. Park, H. Hosono, unpublished.

[7] P. A. Cox, "The Electronic Structure and Chemistry of Solids," Oxford University Press, Oxford, 1987.

[8] J. E. Huheey, "Inorganic Chemistry: Principles of Structure and Reactivity," 3rd ed. pp.146-147. Harper and Row, Publishers, Inc., New York, 1983.

[9] S. J. Fonash, "Solar Cell Device Physics", Academic, New York, 1981.

[10] A. L. Fahrebruch and R. H. Bube, "Fundamentals of Solar Cells," Academic, New York, 1983.

[11] M. D. Archer, and R. Hill, "Clean Electricity from Photovoltaic," Imperial College Press, London, 2001.

[12] T. J. Coutts, K. A. Emery, and J. S. Ward, *Progress in Photovotaics and Applications*, **10**, 1 (2002).

[13] I. C. Madsen, R. J. Hill, *J. Appl. Cryst.* **27**, 385 (1994).

[14] A. Yokochi, unpublished.

[15] Rodriguez-Carvajal, J. FULLPROF: A program for Rietveld Refinement and Pattern Matching Analysis. *In Abstract of the Satellite Meetig on Powder Diffraction of the XV Congress of the IUCr*, Thoulouse, France, 1990: p 127]

[16] P. Stephens, *J. Appl. Cryst.* **32**, 281 (1999).

[17] P.S. Berdonosov, A. M. Kusainova, L. N. Kholodkovskaya, V. A. Dolgikh, L. G. Akselrud, and B. A. Popovkin, *J. Solid State Chem.* **118**, 74 (1995).

[18] E. R. Franke, and H. Schaefer, *Z. Naturforsch.* **27B**, 1308 (1972).

[19] C-H. Park, A. Yokochi, D. A. Keszler, unpublished.

[20] D. Shriver, and P. Atkins, "Inorganic Chemistry," 3rd ed. p. 24. W. H. Freeman and Company, New York, 1999.

[21] G. Savelsberg, and H. Schaefer, *Z. Naturforsch.* 33**B**, 370 (1978).

[22] Y. C. Wang, and F. J. DiSalvo, *J. Solid State Chem.* **156**, 44 (2001).

[23] P. Kubelka and F. Munk, *Z. Tech. Phys.* **12**, 593 (1931).

[24] P. Kubelka, *J. Opt. Soc. Am.* **38**, 448 (1948).

[25] C.-H. Park, R. Kykyneshi, J, Tate, and D. A. Keszler, unpublished.

CHAPTER 6

STRUCTURE, *p*-TYPE CONDUCTIVITY IN WIDE-BAND-GAP SrCuSF, AND GAP MODULATION IN $SrCu[Q_{1-y}Q'_y]F$ (Q, Q' = S, Se, Te)

ABSTRACT

New Cu chalcogenide fluorides of SrCuSF, SrCuSeF, and solid solutions of $SrCu[Q_{1-y}Q'_y]F$ (Q, Q' = S, Se, and Te) were prepared by using high-temperature reaction methods. The structure of SrCuSF was determined via powder X-ray diffraction and the Rietveld refinement method, resulting in R_p / wR_p / R_{Bragg} (%) = 3.50 / 2.37 / 5.24. It crystallizes in the tetragonal space group *P4/nmm* (No.129) with a = 3.9576(1), c = 8.6625(1) Å, V = 135.68(1) Å^3, Z = 2, and d_{calc} = 4.950 g/cm^3. Its band gap is estimated to be 3.08 eV from wavelength-dependent diffuse reflectance measurements, and it can be tuned to a minimum of 2.8 eV by substitution of Se for S. The decrease scales linearly with the concentration of Se and the increase in the volume of the tetragonal unit cell; the overall volume increase is 7.9% from SrCuSF to SrCuSeF. Further reduction of the band gap is achieved by substituting Se in SrCuSeF with Te; a band gap of 2.5 eV and a unit cell volume increase of 6.5% relative to SrCuSeF are observed in $SrCuSe_{0.5}Te_{0.5}F$. Room-temperature conductivity was measured to be 1.6 S/cm for an undoped SrCuSF pellet, and 29 S/cm for a $Sr_{0.9}K_{0.1}CuSF$ pellet. The temperature dependence of the electrical conductivity and Seebeck coefficient reveal that SrCuSF is a *p*-type semiconductor.

INTRODUCTION

To realize transparent electronic and electro-optic devices, it is necessary to develop wide band-gap semiconductors having tunable band gaps that can be readily doped with *n*- and/or *p*-type carriers. Transparent *n*-type conductors have been in use for decades with doped binary compounds such as In_2O_3:Sn (ITO), SnO_2:F, and ZnO:Al being the most common in commercial applications [1]. However, *p*-type conductivity is not common in transparent conductors, and there are no examples of commercial applications. Since the report in 1997 of *p*-type conductivity in transparent $CuAlO_2$ films [2], other new materials have followed, and examples of transparent electronic devices have been reported [3,4].

In previous work, unique optical and electrical properties have been found for the family of compounds BaCuQF (Q=S, Se, Te) [5-7]. The sulfide and selenide members exhibit *p*-type conductivity and band gaps that allow transmission of much of the visible spectrum. With *p*-type doping, *e.g.*, substitution of several percent of K for Ba, the highest conductivities have been found to be 82 S/cm for $Ba_{0.9}K_{0.1}CuSF$ and 43 S/cm for $Ba_{0.9}K_{0.1}CuSeF$ [6]. Undoped BaCuSF also exhibits strong red luminescence near 630 nm under ultraviolet excitation. In addition, band gaps can easily be tuned by varying Q [7,8]. Substitution of Se for S leads to a reduction in band gap from 3.1 eV for BaCuSF to 2.9 eV for BaCuSeF, and further reduction of the gap can be realized by substituting Te for Se, leading to a gap of 2.3 eV in BaCuTeF.

In this contribution, the synthesis, crystal structure, and optical and electrical properties of the Sr sulfide and selenide members of the MCuQF family are described.

EXPERIMENTAL

Powder samples of undoped and K-doped SrCuSF were prepared by heating stoichiometric mixtures of SrS, Cu_2S (Cerac, 99.5%), SrF_2 (Cerac, 99.9%), and KF (Alfa Aesar, 99%) at 743 K for 12 h in an evacuated silica tube. SrS was prepared by heating $SrCO_3$ (Alfa Aesar, 99.9%) at 1273 K under flowing H_2S(g) for 2 h. All of the samples were characterized by powder X-ray diffraction (XRD) on a Siemens D5000 diffractometer; they were predominantly single phase, and only trace amounts of unreacted SrF_2 were observed.

Some powders of undoped and Na-doped SrCuSF were prepared by heating stoichiometric mixtures of $SrCO_3$, Cu_2S, SrF_2, and NaF (Mallinckrodt, AR) at 743 K under flowing H_2S(g) for 2 h. XRD patterns of these samples reveal single phase SrCuSF.

Solid solutions of SrCu(S,Se)F and SrCu(Se,Te)F were prepared by mixing stoichiometric proportions of SrS, SrSe (Cerac, 99.5%), SrF_2, Cu_2S (Cerac, 99.5%), Cu_2Se (Cerac, 99.5%), and Cu_2Te (Cerac, 99.5%). The constituent materials were intimately mixed and placed in an evacuated silica tube at 743-823 K for

SrCu(S,Se)F and 848-948 K for SrCu(Se,Te)F for 12 h. These samples are mainly single phase with trace amounts of unreacted SrF_2.

Data for Rietveld structural refinement were collected on SrCuQF (Q=S, Se) by using a Siemens D5000 diffractometer with variable slits and a locally devised variable counting time routine [9]. Data were converted to GSAS ESD format by using an in-house program [10], and structural refinement was performed by using the program Fullprof [11]. During refinement, the four possible parameters in Stephen's formalism [12] of strain broadening for this Laue class were refined to optimize the fit, resulting in substantial improvements in residuals. Final crystallographic parameters for the refinement, including calculated strain parameters, are given in Table 6.1, and positional parameters and equivalent isotropic displacement parameters are listed in Tables 6.2 and 6.3, respectively.

The diffuse reflectance at room temperature of a powder sample was measured with $BaSO_4$ as a reference by using an Oriel 300-W Xe lamp, a Cary model-15 prism monochromator, and a Hamamatsu R636-10 photomultiplier tube to cover the UV-visible region (360-700 nm).

For transport-property measurements, each sample was pressed into a 9.5-mm diameter pellet at 3 tons and annealed at 923 K for 1 h in an evacuated silica tube.

TABLE 6.1. Summary of refinement data and lattice parameters of SrCuQF (Q=S, Se).

Formula		SrCuSF	SrCuSeF
Space group		*P4/nmm* (No. 129)	*P4/nmm* (No. 129)
Z		2	2
a (Å)		3.9576(1)	4.0645(1)
c (Å)		8.6625(1)	8.8419(1)
Vol ($Å^3$)		135.68(1)	146.07(1)
FW (amu)		202.23	249.12
Calculated density		4.950 g/cm^3	5.664 g/cm^3
2θ range (°)		10.0-150.0	10.0-150.0
S_{400}		0.23(5)	0.155(12)
S_{004}		0.019(3)	0.010(1)
S_{220}		1.09(5)	0.73(6)
S_{202}		0.07(1)	0 (not refined)
Calculated strain (%%) in given crystallographic direction	100	4.71	4.09
	101	4.58	3.49
	111	5.81	4.80
	110	6.11	5.28
	001	6.54	5.03
R_p (%)		3.50	4.11
R_{wp} (%)		2.37	3.03
R_{Bragg} (%)		5.24	5.23
Number of reflections		213	231
Number of parameters		23	23

TABLE 6.2. Final positional and isotropic equivalent displacement parameters ($Å^2$ x 100) for SrCuSF.

	Wyckoff	x	y	z	U_{iso}
Sr	2c	¼	¼	0.33232(7)	1.98(2)
Cu	2a	¾	¼	0	3.02(5)
S	2c	¼	¼	-0.1645(2)	2.21(5)
F	2b	¾	¼	½	1.96(9)

TABLE 6.3. Final positional and isotropic equivalent displacement parameters ($Å^2$ x 100) for SrCuSeF.

	Wyckoff	x	y	z	U_{iso}
Sr	2c	¼	¼	0.34036(14)	2.45(4)
Cu	2a	¾	¼	0	3.42(6)
Se	2c	¼	¼	-0.17001(14)	2.25(5)
F	2b	¾	¼	½	2.73(15)

The conductivity of the pressed powder samples of undoped, K-, and Na-doped SrCuSF were measured by the 4-probe collinear method in the 10-300 K temperature range. Seebeck coefficient measurements were used to establish the carrier sign over the temperature range 50-290 K. A temperature gradient of 3 K was used to measure the thermoelectric voltage; the values reported here are not corrected for the Seebeck coefficient of the copper leads.

RESULTS AND DISCUSSIONS

Structural Analysis

The results of the final Rietveld refinement cycle for SrCuQF (Q=S, Se) are shown graphically in Figures 6.1 and 6.2. The compound SrCuQF is isostructural to the materials BaCuQF (Q=S, Se) [7] (Figure 6.3), which adopt the same structure type as RCuOSe (R = lanthanide, Bi) and LaCuOS [13]. The structure is a layered, tetragonal type with anti–fluorite (Sr_2F_2) layers alternating with (Cu_2Q_2) sheets along the *c* axis. Selected interatomic distances and angles are given in Tables 6.4 and 6.5.

The Sr and Q atoms occupy sites with symmetry C_{4v}. The Sr atom occupies a square antiprismatic site with four Q atoms forming one square face and four F atoms the other. The Sr-S distance in SrCuSF, 3.153(1) Å, compares well with those found in compounds such as $SrCu_2Sn_2S_4$ (3.198 Å, averaged value) [14] and SrY_2S_4 (3.142 Å, averaged value) [15]. The Sr-Se distance of 3.2448(8) Å is comparable to that observed in $SrAl_2Se_4$ (3.233 Å, averaged value) [16]. The Sr-F distance in SrCuSF (2.455(1) Å) is similar to those observed in SrCuSeF (2.4744(7) Å) and SrClF (2.494 Å) [17]. The Q atom is also located at a square antiprismatic site coordinated by four Sr atoms and four Cu atoms.

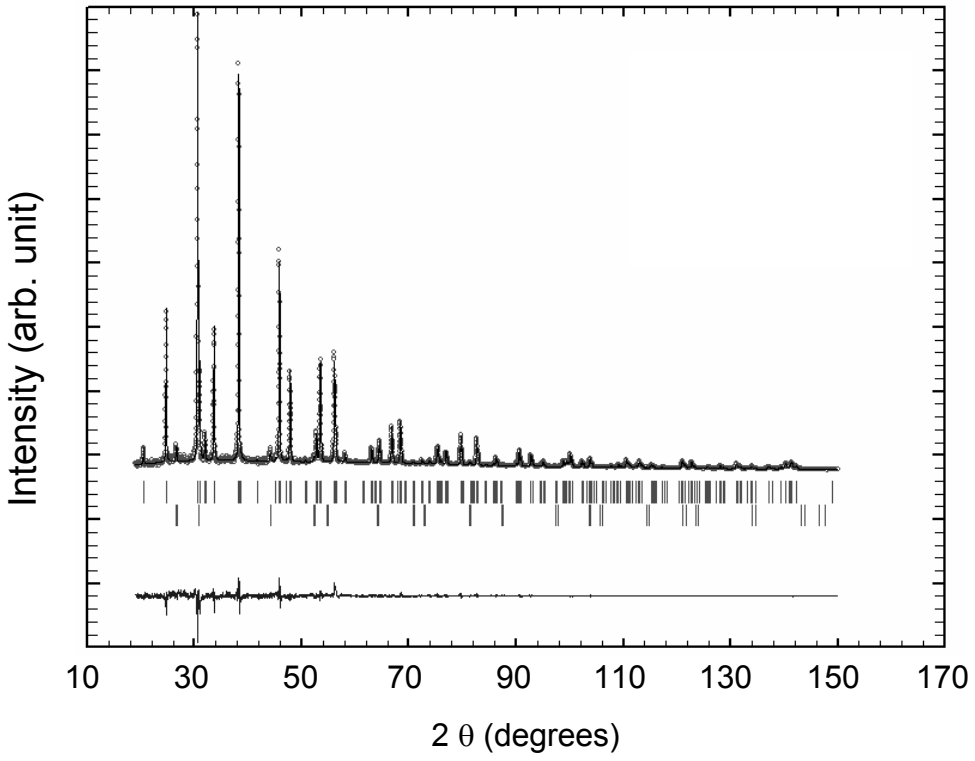

Figure 6.1. Observed (open circles) and calculated (solid line) X-ray powder diffraction pattern from refinement of SrCuSF. The bottom curve is the difference pattern on the same scale. The top vertical bars are for SrCuSF and the lower vertical bars are for SrF_2.

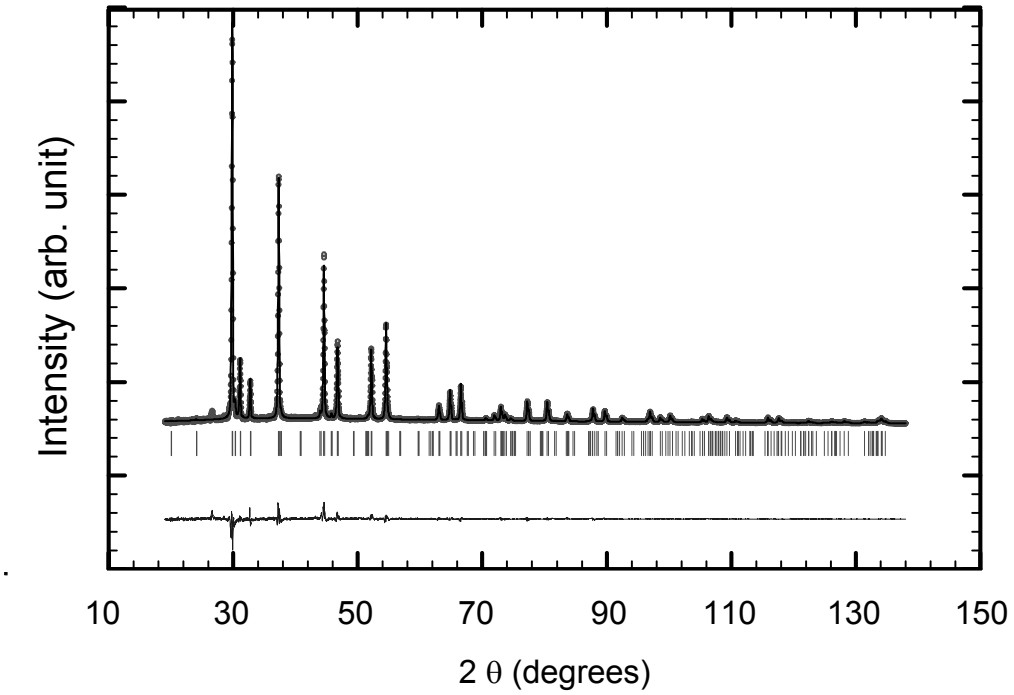

Figure 6.2. Observed (open circles) and calculated (solid line) X-ray powder diffraction pattern from refinement of SrCuSeF. The bottom curve is the difference pattern on the same scale.

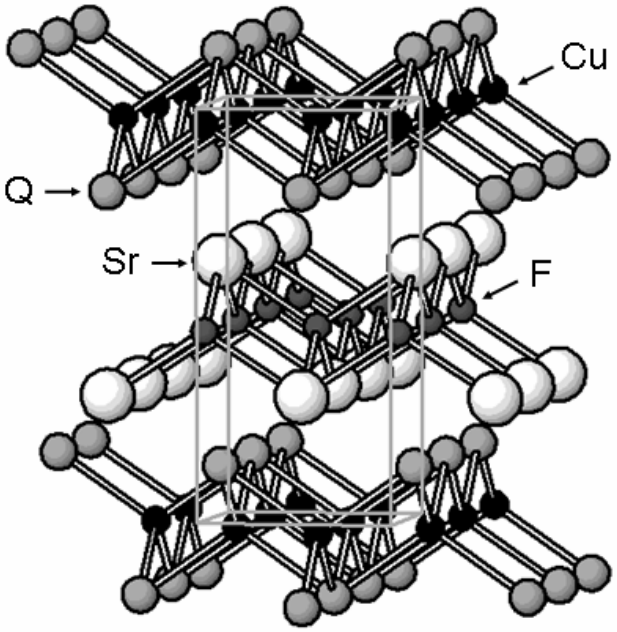

Figure 6.3. Crystal structure of SrCuQF (Q=S, Se).

TABLE 6.4. Selected interatomic distances (Å) and angles (deg) for SrCuSF.

Cu-S	2.438(1)	S-Cu-S	108.49(3)
Cu···Cu	2.7984(1)	S-Cu-S	109.96(8)
Sr-S	3.153(1)	S-Sr-S	77.73(2)
Sr-F	2.455(1)	S-Sr-S	125.09(2)
		F-Sr-F	69.50(1)
		F-Sr-F	107.44(1)
		S-Sr-F	76.53(4)
		S-Sr-F	141.14(4)

TABLE 6.5. Selected interatomic distances (Å) and angles (deg) for SrCuSeF.

Cu-Se	2.5278(7)	Se-Cu-Se	107.022(23)
Cu···Cu	2.8740(1)	Se-Cu-Se	110.709(51)
Sr-Se	3.2448(8)	Se-Sr-Se	77.756(20)
Sr-F	2.4744(7)	Se-Sr-Se	124.683(20)
		F-Sr-F	71.009(24)
		F-Sr-F	110.435(24)
		Se-Sr-F	75.547(33)
		Se-Sr-F	141.188(33)

The Cu and F atoms are located on sites having D_{2d} symmetry, resulting in distorted tetrahedral environments. The Cu, coordinated to four Q atoms, has a Cu-S bond distance of 2.438(1) Å, which is comparable to values in other systems such as BaCuSF (2.453 Å) [18] and β-$BaCu_2S_2$ (2.411 Å) [19].

The two-dimensional Cu_2Q_2 tetragonal sheet structure is characterized by edge-sharing linkages of the distorted CuQ_4 tetrahedra, which produce relatively short Cu···Cu distances. The shortest Cu···Cu distance in SrCuSF is 2.7984(1) Å, which is comparable to that, 2.7632(1) Å, observed in β-$BaCu_2S_2$, and shorter than the 2.9147(1) Å observed in BaCuSF.

The Cu-Se bond distance of 2.5278(7) Å in SrCuSeF is comparable to the values observed in other systems such as NaCuSe (2.553 Å) [20], β-$BaCu_2Se_2$ (2.497 Å) [19], and Cu_2Se (2.529 Å) [21]. The Cu···Cu distance of 2.8740(1) Å in SrCuSeF is comparable to that observed in β-$BaCu_2Se_2$ (2.856 Å).

Transport Properties

The temperature dependence of electrical conductivity of $Sr_{1-x}K_xCuSF$ (x = 0, 0.05, 0.075, and 0.1) pellets is illustrated in Figure 6.4. Undoped SrCuSF pellets have room temperature electrical conductivity near 2 S/cm. The conductivity increases with increasing K concentration, and $Sr_{0.9}K_{0.1}CuSF$ pellets exhibit room-temperature conductivity near 29 S/cm. The conductivity of the undoped SrCuSF pellets is higher than the values observed in BaCuSF pellets (< 0.1 S/cm); while that of $Sr_{0.9}K_{0.1}CuSF$ is lower than the value observed in $Ba_{0.9}K_{0.1}CuSF$ pellet (82 S/cm) [6]. The room temperature conductivity of Na-substituted material of $Sr_{0.9}Na_{0.1}CuSF$ was measured to be 20 S/cm. The temperature dependence of the electrical conductivity of $Sr_{1-x}K_xCuSF$ (x = 0, 0.05, 0.075, and 0.1) reveals activated semiconducting behavior for each x value. In the compounds of $Ba_{1-x}K_xCuSF$, the temperature dependence of the electrical conductivity shows semiconducting behavior for $x \leq 0.025$, and degenerate behavior for $x \geq 0.05$. Seebeck measurements on all samples gave a positive sign, indicating that these materials are *p*-type conductors at all doping levels. The transport measurements are summarized in Table 6.6.

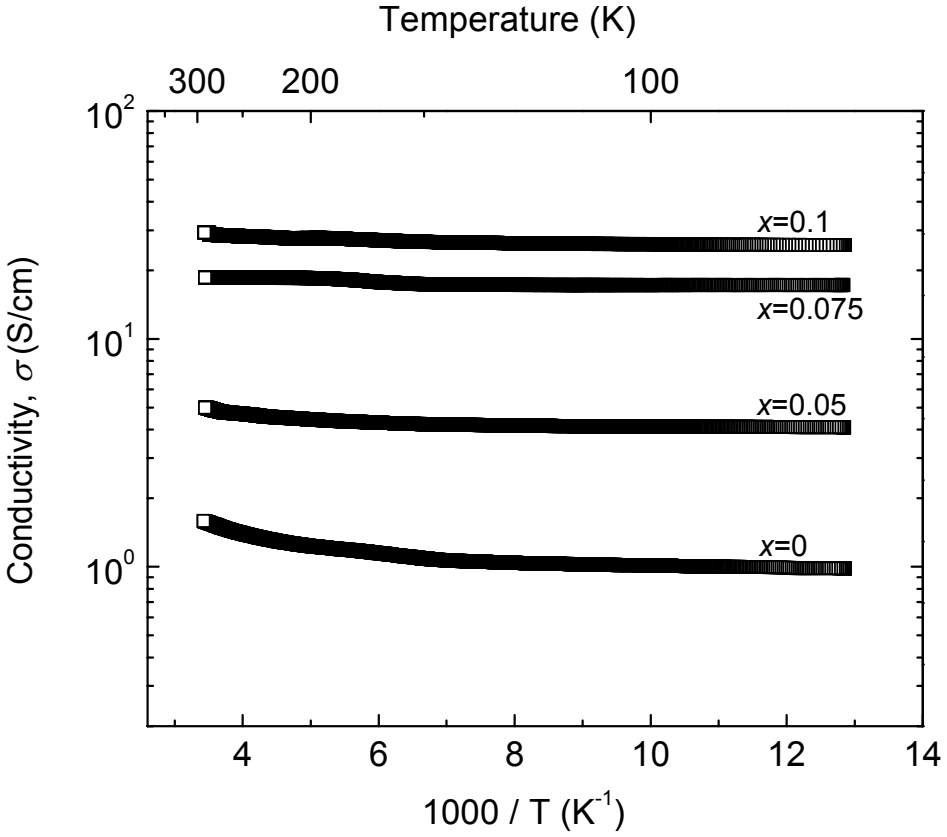

Figure 6.4. Electrical conductivity of $Sr_{1-x}K_xCuSF$ (x = 0, 0.05, 0.075, and 0.1) pellets as a function of temperature.

TABLE 6.6. Electrical properties (conductivity and Seebeck coefficient) and densities of $Sr_{1-x}K_xCuSF$ (x = 0, 0.05, 0.075, 0.1) pellets at room temperature.

K (at.%)	0	0.05	0.075	0.10
σ (S/cm)	1.6	5	18.5	29
S (μV/K)	+41	+20	+14	+18
Density (%)	69	69	69	81

Solid solutions for SrCu(S,Se)F and SrCu(Se,Te)F

It has been demonstrated that the Q site of BaCuQF can be freely substituted with S, Se, and Te [7,8]. The same phenomenon is observed in the SrCuQF series. The gradual peak shifts toward smaller angles in the X-ray diffraction patterns with increasing concentrations of heavier Q clearly reveals the existence of solid-solution behavior in the series $SrCuS_{1-x}Se_xF$ and $SrCuSe_{1-y}Te_yF$. In Figure 6.5, the *a*-axis lattice parameter and the cell volume are plotted as a function of x for the solid-solution series $SrCuS_{1-x}Se_xF$ ($0 \leq x \leq 1$) and y for the solid-solution series $SrCuSe_{1-y}Te_yF$ ($0 \leq y \leq 0.5$). The essentially linear change of the a lattice parameter and cell volume with composition follows Vegard's law, indicating a random distribution of the two types of Q atoms [22].

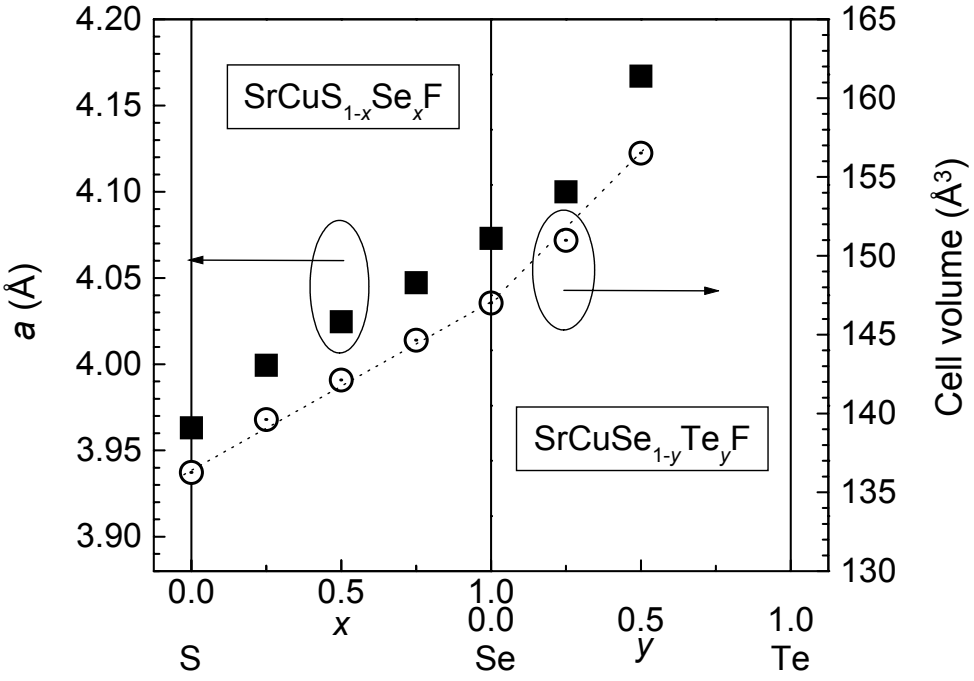

Figure 6.5. Lattice constant *a* and unit cell volume vs. *x* or *y* for $SrCuS_{1-x}Se_xF$ and $SrCuSe_{1-y}Te_yF$.

The change in the *a* lattice parameter of 5.1% from $x = 0$ to $y = 0.5$ is the same as the change in the BaCuQF series; while the *c* lattice parameter change of 3.9% over the same range is larger than that of 2.2% in BaCuQF series. The changes in cell parameters and cell volume with compositional change are more significant in $SrCuSe_{1-y}Te_yF$ than in $SrCuS_{1-x}Se_xF$, which can be ascribed to the larger size difference between Se and Te than that between S and Se; the ionic size difference between Se and Te is 150% of that between S and Se (S^{2-}: 170 pm, Se^{2-}: 184 pm, Te^{2-}: 207 pm; coordination number = 6) [23]. The volume change of $SrCuSe_{1-y}Te_yF$ from $y = 0$ to $y = 0.5$ is 150% of the volume change of $SrCuS_{1-x}Se_xF$ from $x = 0$ to $x = 0.5$. In the case of BaCuQF, the volume change of $BaCuSe_{1-y}Te_yF$ from $y = 0$ to $y = 0.5$ is 140% of the volume change of $BaCuS_{1-x}Se_xF$ from $x = 0$ to $x = 0.5$.

Optical Properties

Absorption spectra for the series of SrCu(S,Se)F and SrCu(Se,Te)F were obtained from the diffuse reflectance spectra by using the Kubelka-Munk method [24,25] (Figure 6.6). The absorption coefficient (α) increases slowly with increasing photon energy and increases abruptly at the energy corresponding to the onset of absorption near the energy gap. As expected, the incorporation of heavier Q atom in the structure leads to a smaller band gap, which is also observed in the solid solutions of BaCu(S,Se)F, BaCu(Se,Te)F, and LaCuO(S,Se) [7,26].

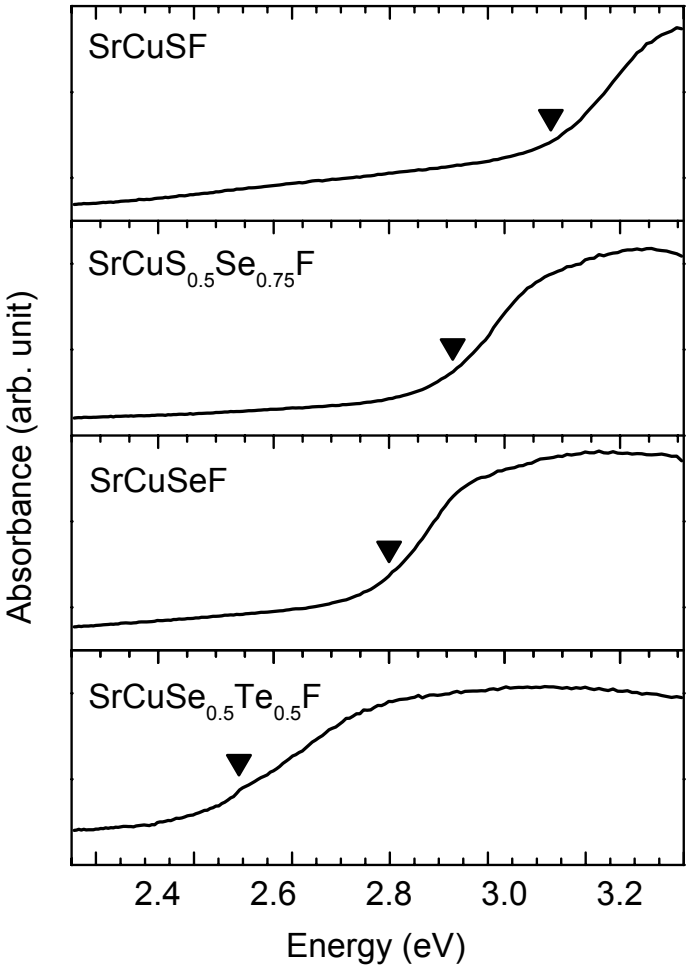

Figure 6.6. Absorption spectra for $SrCuS_{1-x}Se_xF$ and $SrCuSe_{1-y}Te_yF$ powder. The triangles indicate the positions of the band gaps.

The band gap is plotted as a function of chemical composition for the $SrCuS_{1-x}Se_xF$ and $SrCuSe_{1-y}Te_yF$ series in Figure 6.7. The band gap energy was extracted by extrapolating the straight-line portion of the curve of $(\alpha E)^2$ *vs.* E to the zero-absorption axis. Here E is the photon energy, and a direct gap has been assumed in accordance with the LDA band structure calculation of isomorphous BaCuSF [27]. The band-gap was estimated as 3.08 eV for SrCuSF and 2.8 eV for SrCuSeF. The band gap change with composition is essentially linear and more significant in the SrCuQF series than in the BaCuQF series. The band gap of the compound SrCuTeF is expected to be 2.3 eV on the basis of extrapolating from the measurements where $E_g = 3.33 - 0.52\ y$ (eV) in the $SrCuSe_{1-y}Te_yF$ series.

The band gap of 3.08 eV for SrCuSF is smaller than that of BaCuSF (3.1 – 3.25 eV). Experimental and theoretical analyses indicate that the $(Cu_2S_2)^{2-}$ layers contribute to both the top of the valence band and the bottom of the conduction band of LaCuOS [28], and LDA band structure calculations [27] and photoemission experiments [29] also indicate that the contribution to the top of the valence band in BaCuSF from the $(Cu_2S_2)^{2-}$ layers is strong. Therefore the band gap is predominantly affected by the nature of Cu-S bonding. Figure 6.8 shows the molecular orbital diagram of an isolated CuS_4 tetrahedron. For simplicity σ bonds resulting from 3*d* and 4*s* orbitals of Cu atom, and 3*p* orbitals of S atoms are considered, because contributions of π bonds are less important than those of σ bonds. The contributions of S 3*s* orbitals are also excluded, as these orbitals are energetically far removed from the Cu 3*d* level.

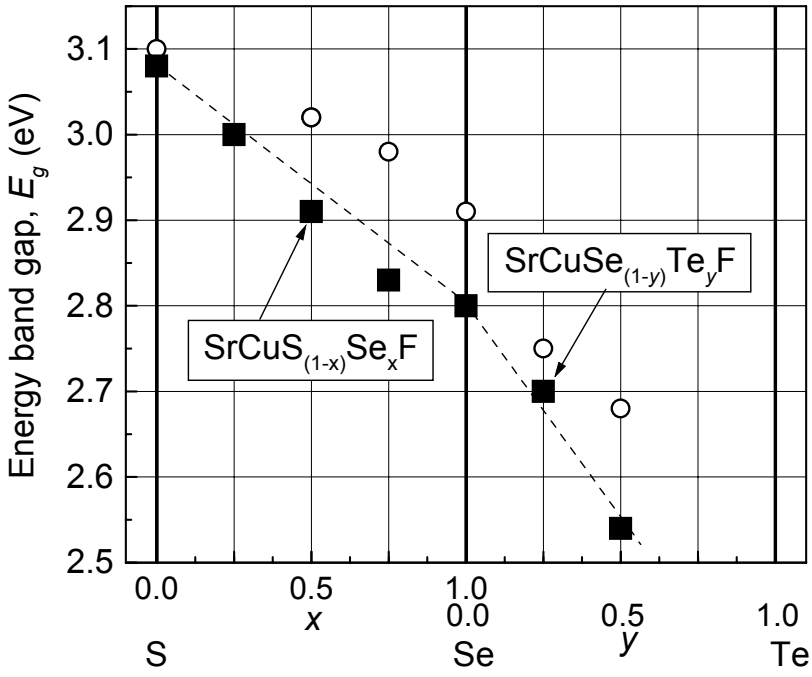

Figure 6.7. Band gap tuning of $SrCuS_{1-x}Se_xF$ and $SrCuSe_{1-y}Te_yF$. Open circles represent band gap of $BaCuS_{1-x}Se_xF$ and $BaCuSe_{1-y}Te_yF$.

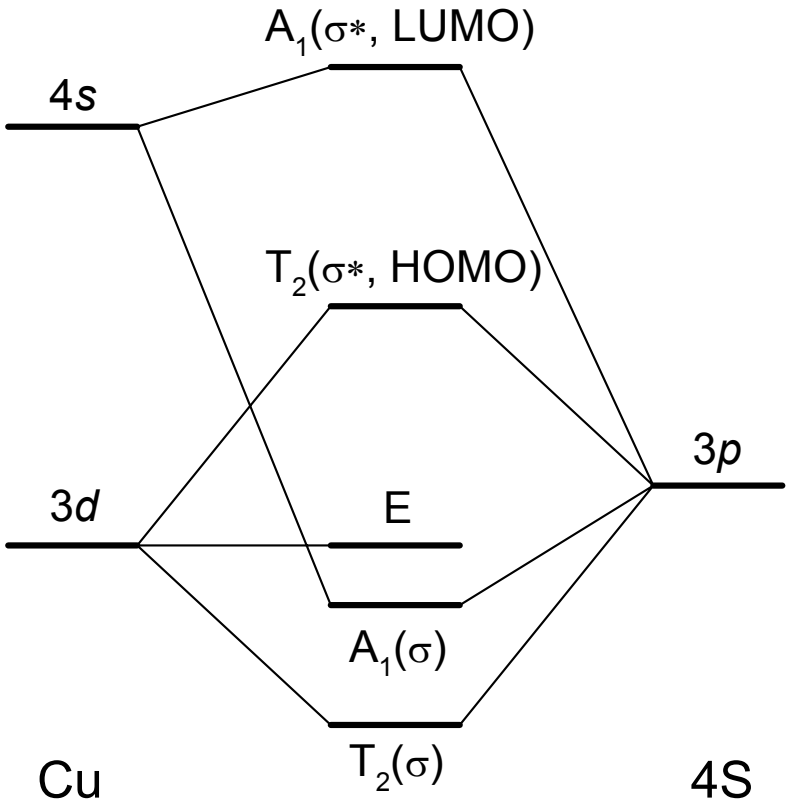

Figure 6.8. Molecular orbital diagram for an isolated CuS_4 tetrahedron.

The highest occupied molecular orbital (HOMO), which corresponds to the top of the valence band in solids, is the T_2 antibonding orbital from Cu 3*d* and S 3*p* interaction. The A_1 antibonding orbital from Cu 4*s* and S 3*p* interaction is the lowest unoccupied molecular orbital (LUMO), which is equivalent to the bottom of the conduction band in solids [30-32]. The Cu-S distance is similar in SrCuSF (2.438 Å) and in BaCuSF (2.456 Å), while the Cu···Cu distance in SrCuSF (2.798 Å) is shorter than that in BaCuSF (2.915 Å). The bands associated with the Cu 4*s* orbital disperse more than those of the Cu 3*d* orbital; therefore the width of the conduction band will increase more than that of the valence band, resulting in a decrease in band gap. A small decrease in band gap is evident by comparing SrCuSeF (2.8 eV) and BaCuSeF (2.9 eV). The Cu-Se distance is similar in these two compounds-SrCuSeF (2.5278(7) Å) and BaCuSeF (2.554(1) Å), while the Cu···Cu distance in SrCuSeF (2.8740(1) Å) is much shorter than that in BaCuSF (2.9980(1) Å). Another possible explanation for smaller band gap of SrCuSF than that of BaCuSF is that the interaction between $(Cu_2S_2)^{2-}$ layers along the *c* axis is greater in SrCuSF than in BaCuSF because of shorter distance between $(Cu_2S_2)^{2-}$ layers. The decrease in band gap with increasing interaction between $(Cu_2S_2)^{2-}$ layers along the *c* axis is clearly demonstrated in β-$BaCu_2S_2$ (1.8 eV) and BaCuSF [33]. Both have tetragonal symmetry and the same $(Cu_2S_2)^{2-}$ layers composed of edge-shared CuS_4 tetrahedra. In β-$BaCu_2S_2$ $(Cu_2S_2)^{2-}$ layers are connected by Ba^{2+} along the *c* axis; while in BaCuSF $(Cu_2S_2)^{2-}$ layers are alternately stacked with

$(Ba_2F_2)^{2-}$ layer along the *c* axis and interactions between $(Cu_2S_2)^{2-}$ layers are weaker than those in β-$BaCu_2S_2$, giving a larger band gap.

CONCLUSION

The new Cu chalcogenide fluorides SrCuSF, SrCuSeF, and the solid solution series $SrCuS_{1-x}Se_xF$ and $SrCuSe_{1-y}Te_yF$ ($y \leq 0.5$) have been prepared by using high-temperature reaction methods. The structure of SrCuSF was determined via powder X-ray diffraction and the Rietveld refinement method. Its band gap is estimated to be 3.08 eV from wavelength-dependent diffuse reflectance measurements, and it can be tuned by substitution of Se for S to 2.8 eV for SrCuSeF. Room-temperature conductivity was measured to be 2 S/cm for an undoped SrCuSF pellet, and 29 S/cm for a $Sr_{0.9}K_{0.1}CuSF$ pellet. The temperature dependence of the electrical conductivity and Seebeck coefficient indicate that undoped and K-doped samples exhibit *p*-type semiconductor behavior.

ACKNOWLEDGMENTS

This material is based upon work supported by the National Science Foundation under Grant No. 0245386.

REFERENCES

[1] T. Minami, *Mater. Res. Soc. Bull.*, **25(8)**, 38 (2000).

[2] H. Kawazoe, M. Yasukawa, H. Hyodo, M. Kurita, H. Yanagi, and H. Hosono, *Nature*, **389**, 939 (1997).

[3] H. Hosono, H. Ohta, K. Hayashi, M. Orita, and M. Hirano, *J. Cryst. Growth*, **237-239**, 496 (2002), and references therein.

[4] R. L. Hoffman, B. J. Norris, and J. F. Wager, *Appl. Phys. Lett.*, **82**, 733 (2003).

[5] H. Yanagi, S. Park, A. D. Draeseke, D. A. Keszler, and J. Tate, *J. Solid State Chem.*, **175**, 34 (2003).

[6] H. Yanagi, J. Tate, S. Park, C.-H. Park, and D. A. Keszler, *Appl. Phys. Lett.*, 82, 2814 (2003).

[7] C.-H. Park, D. A. Keszler, H. Yanagi, and J. Tate, *Thin solid films*, **445**, 288 (2003).

[8] C.-H. Park, R. Kykyneshi, A. Yokochi, J. Tate, and D. A. Keszler, *unpublished*.

[9] I. C. Madsen, and R. J. Hill, *J. Appl. Crystallogr.*, **27**, 385 (1994).

[10] A. Yokochi, *unpublished*.

[11] J. Rodriguez-Carvajal, FULLPROF: A program for Rietveld Refinement and Pattern Matching Analysis, *In Abstract of the Satellite Meeting on Powder Diffraction of the XV Congress of the IUCr*, p 127, Thoulouse, France (1990).

[12] P. Stephens, *J. Appl. Crystallogr.*, **32**, 281 (1999).

[13] P.S. Berdonosov, A. M. Kusainova, L. N. Kholodkovskaya, V. A. Dolgikh, L. G. Akselrud, and B. A. Popovkin, *J. Solid State Chem.*, **118**, 74 (1995).

[14] Chr. L. Teske, . *Anorg. Allg. Chem.,* **419**, 67 (1976).

[15] C. K. Lowe-Ma, T. A. Vanderah, *J. Solid State Chem.*, **117(2)**, 363 (1995).

[16] W. Klee, and H. Schaefer, *Z. Naturforsch.* 33**B**, 829 (1978).

[17] M. Sauvage, *Acta Crystallogr.*, **B30**, 2786 (1974).

[18] C.-H. Park, A. Yokochi, and D. A. Keszler, *unpublished*.

[19] J. Huster, and W. Bronger, *Z. Anorg. Allg. Chem.*, **625**, 2033 (1999).

[20] G. Savelsberg, and H. Schaefer, *Z. Naturforsch.* 33**B**, 370 (1978).

[21] W. Borchert, *Z. Kristallogr.*, **107**, 357 (1956).

[22] A. R. West, *Solid State Chemistry and its Application*, p.367, John Wiley & Sons, Singapore (1989).

[23] R. D. Shannon, *Acta Crystallogr.*, **A32**, 751 (1976).

[24] P. Kubelka and F. Munk, *Z. Tech. Phys.*, **12**, 593 (1931).

[25] P. Kubelka, *J. Opt. Soc. Am.*, **38**, 448 (1948).

[26] K. Udea, and H. Hosono, *J. Appl. Phys.*, **91(7)**, 4768 (2002).

[27] H. J. F. Jansen, *private communication*.

[28] S. Inoue, K. Ueda, and H. Hosono, *Phys. Rev.*, **B 64**, 245211 (2001).

[29] H. Yanagi, J. Tate, D. A. Keszler, S. Park, C.-H. Park, and H. Hosono, *unpublished*.

[30] F. A. Cotton, *Chemical Applications of Group Theory*, 3rd ed., p. 229, John Wiley & Sons, Singapore (1990).

[31] R. Hoffmann, *Solids and Surfaces: A chemist's view of Bonding in Extended Structures*, VCH Publishers, New York (1988).

[32] A. Ouammou, M. Mouallem-Bahout, O. Pena, J. Halet, J. Saillard, and C. Carel, *J. Solid State Chem.*, **117**, 73 (1995).

[33] C.-H. Park, and D. A. Keszler, *unpublished*.

CHAPTER 7

STRUCTURE AND PHYSICAL PROPERTIES OF BaAgSF

ABSTRACT

The new Ag sulfide fluoride compound BaAgSF was prepared under flowing H_2S(g) at 773 K. Its crystal structure was determined by using powder X-ray diffraction and the Rietveld refinement method, resulting in R_p / wR_p (%) = 8.90 / 7.01. The compound crystallizes in the tetragonal space group *P4/nmm* (No.129) with a = 4.2433(1) Å, c = 9.3057(1) Å, V = 167.56(1) Å^3, Z = 2, and d_{calc} = 5.872 g/cm^3. Its optical band gap is estimated to be 2.8 eV from wavelength-dependent diffuse reflectance measurements, and room-temperature conductivity has been determined to be smaller than 10^{-6} S/cm.

INTRODUCTION

The Cu chalcogenide fluoride materials in the family MCuQF (M=Ba, Sr; Q=S, Se, Te) exhibit *p*-type conductivity and band gaps that allow transmission of much of the visible spectrum [1,2]. The room-temperature electrical conductivity of these materials can be greatly enhanced by substituting several percent K for Ba; for example, conductivities of 82 S/cm for $Ba_{0.9}K_{0.1}CuSF$ and 43 S/cm for $Ba_{0.9}K_{0.1}CuSeF$ can be achieved in pressed pellets [2]. In addition to these relatively high conductivities, undoped BaCuSF exhibits strong red luminescence near 630 nm under ultraviolet excitation. Band gaps in the family can also be easily tuned by varying Q [3,4], where a gradual reduction in band gap from 3.1 to 2.3 eV is observed in the Ba compounds by first substituting Se for S and then Te for Se.

In this contribution, we examine the effects of substituting Ag for Cu, describing the synthesis, crystal structure, and optical properties of BaAgSF.

EXPERIMENTAL

Reagents for synthesis of BaAgSF and $Ba_{0.9}K_{0.1}AgSF$ were $BaCO_3$ (Cerac, 99.9%), Ag_2O (Cerac, 99.5%), BaF_2 (Cerac, 99.9%), and K_2CO_3 (Aldrich, 99.995%). The stoichiometric mixtures were heated at 773 K under flowing H_2S(g) for 2 h and cooled to room temperature under flowing Ar(g). For transport property measurements, powder samples were pressed into 9.5-mm diameter pellets at 3 tons and annealed at 923 K for 1 h in an evacuated silica tube.

Data for the Rietveld structural refinement were collected on a 1:1 mixture by weight of BaAgSF and LiF by using a Siemens D5000 diffractometer with variable slits and a locally devised variable counting time routine [5]. Data were converted to GSAS ESD format by using an in-house program [6], and structural refinement was performed by using the program Fullprof [7].

During refinement, it was noticed that there was a certain amount of anisotropic *hkl*-dependent line broadening associated with strain in the sample. In an effort to optimize the fit, the four possible parameters in Stephen's formalism [8] of strain broadening for this Laue class were refined, resulting in substantial improvements in residuals. Final crystallographic parameters for the refinement, including calculated strain parameters, are given in Table 7.1; positional and equivalent isotropic displacement parameters are listed in Table 7.2.

TABLE 7.1. Summary of refinement data and lattice parameters of BaAgSF.

Formula		BaAgSF
Space group		*P4/nmm* (No. 129)
Z		2
a (Å)		4.2433(1)
c (Å)		9.3057(1)
Vol ($Å^3$)		167.56(1)
FW (amu)		296.26
Calculated density		5.872 g/cm^3
2θ range (°)		10.0–150.0
S_{400}		0.11(11)
S_{004}		0.017(1)
S_{220}		0.72(15)
S_{202}		0.00(1)
Calculated strain (%%) in given crystallographic direction	100	3.77
	101	3.03
	111	4.87
	110	5.47
	001	7.14
R_p (%)		8.90
R_{wp} (%)		7.01
R_{Bragg} (%)		5.39
Number of reflections		257
Number of parameters		(13 Le Bail + 10 Rietveld)

TABLE 7.2. Final positional and isotropic equivalent displacement parameters ($Å^2$ x 100) for BaAgSF.

	Wyckoff	x	y	z	U_{iso}
Ba	2c	¼	¼	0.33346(7)	2.23(2)
Ag	2a	¾	¼	0	3.42(4)
S	2c	¼	¼	-0.1799(3)	2.18(7)
F	2b	¾	¼	½	2.73(16)

TABLE 7.3. Selected interatomic distances (Å) and angles (deg) for BaAgSF.

Ag-S	2.702(1)	S-Ag-S	103.46(5)
Ag···Ag	3.0005(1)	S-Ag-S	112.56(1)
Ba-S	3.324(1)	S-Ba-S	79.34(3)
Ba-F	2.627(1)	S-Ba-S	129.06(3)
		F-Ba-F	69.64(1)
		F-Ba-F	107.71(1)
		S-Ba-F	74.82(6)
		S-Ba-F	140.28(6)

The diffuse reflectance at room temperature of a powder sample was measured with $BaSO_4$ as a reference by using an Oriel 300-W Xe lamp, a Cary model-15 prism monochromator, and a Hamamatsu R636-10 photomultiplier tube to cover the UV-visible region (360-700 nm).

RESULTS

The structure for BaAgSF is described in space group *P4/nmm* with Ba at ¼ ¼ z (z ~0.33), Ag at ¾ ¼ 0, S at ¼ ¼ z (z ~-0.18), and F at ¾ ¼ ½ (Figure 7.1). The results of the final Rietveld refinement cycle are shown graphically in Figure 7.2. The compound is isostructural to LaAgOS [9] and the Cu materials BaCuQF (Q=S, Se, Te) [3,4], RCuOSe (R = rare earth, Bi), and LaCuOS [10]. The structure is a layered, tetragonal type with anti-fluorite (Ba_2F_2) layers alternating with (Ag_2S_2) sheets along the *c* axis.

The Ba and S atoms have site symmetry C_{4v}. The Ba atom is located in a square antiprismatic site with four S atoms forming one square face and four F atoms the other. The Ba-S distance of 3.324(1) Å and the Ba-F distance of 2.627(1) Å compare well with the values of 3.308(1) and 2.613(1) observed in BaCuSF [11]. The S atom is also located in a square antiprismatic site coordinated by four Ba atoms and four Ag atoms.

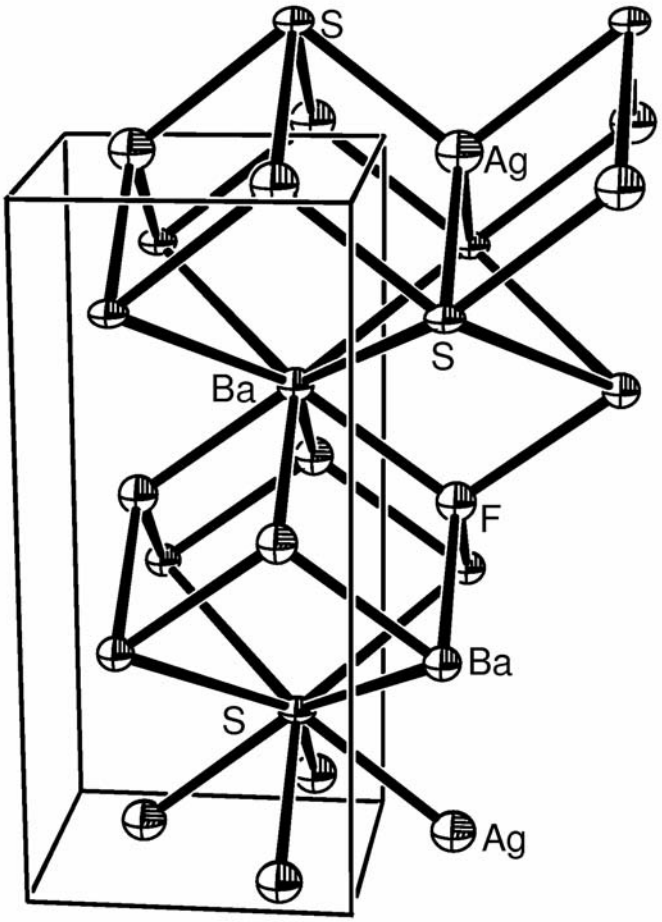

Figure 7.1. Crystal structure of BaAgSF.

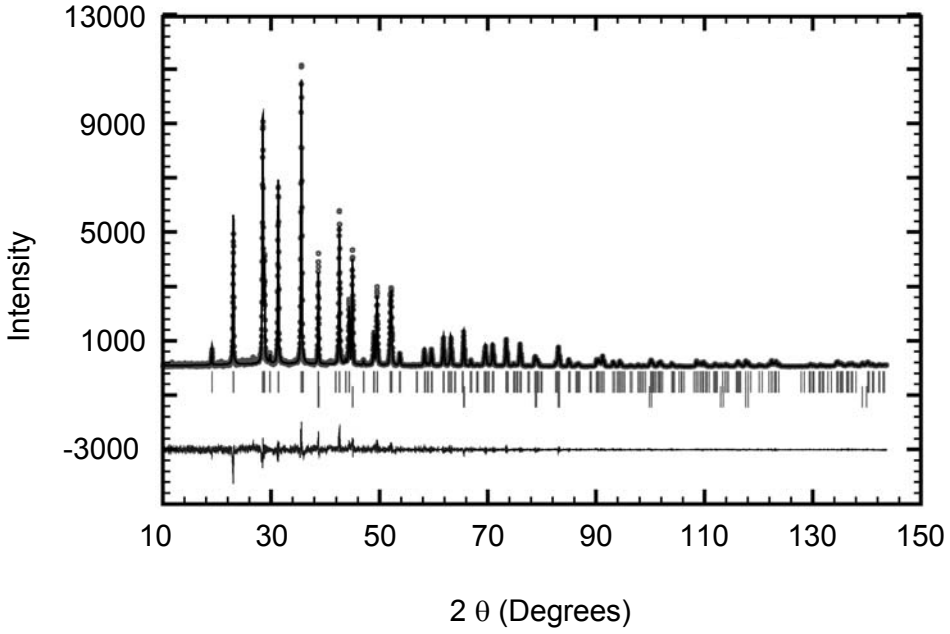

Figure 7.2. Observed (open circles) and calculated (solid line) X-ray powder diffraction pattern from refinement of BaAgSF. The bottom curve is the difference pattern on the same scale. The top vertical bars correspond to BaAgSF and the lower vertical bars correspond to LiF.

The Ag and F atoms are located on distorted tetrahedral sites with D_{2d} symmetry. The Ag, coordinated to four S atoms, has a Ag-S bond distance of 2.702(1) Å, which is similar to those observed in other systems such as LaAgOS (2.673 Å) [9] and $BaAg_2S_2$ (2.673 Å average distance) [12]. The sum of covalent radii of Ag and S is 2.48 Å [13]. The two-dimensional Ag_2S_2 tetragonal sheet structure has previously been observed in LaAgOS. These sheets are characterized by edge-sharing linkages of the distorted AgS_4 tetrahedra, which produce relatively short Ag···Ag distances. The shortest Ag···Ag distance in BaAgSF is 3.000 Å, which is longer than the 2.864-Å separation observed in LaAgOS. The longer Ag···Ag distance in BaAgSF relative to that in LaAgOS is reflected in the S-Ag-S angle involving the shared S···S edges - 112.56(1)^o for BaAgSF and 115.22(15)^o for LaAgOS. The more acute angle in BaAgSF leads to a longer Ag···Ag distance. This geometric relationship between relatively long M···M distances and acute S-M-S anles involving shared MS_4 edges is also observed in related systems such as BaCuQF (Q=S, Te) and α-$BaCu_2Q_2$ (Q=S, Te).

The absorption spectrum (Figure 7.3) of powdered BaAgSF was obtained from the diffuse reflectance spectrum by using the Kubelka-Munk method [14,15]. The absorption coefficient (α) increases slowly with decreasing wavelengths and its abrupt increase starts at about 460 nm. At wavelengths shorter than 407 nm, it is almost constant. The direct band-gap energy of 2.8 eV was extracted by extrapolating the straight-line portion of the curve of $(\alpha E)^2$ *vs.* E to the zero-absorption axis (inset in Figure 7.3). The measured band gap is smaller than those of BaCuSeF (2.9 eV) and BaCuSF (3.1 eV). The bottom of the conduction band in BaAgSF has considerable Ag 5*s* orbital character. While the Ag···Ag and Ag-S distances of BaAgSF are longer than the corresponding distances in BaCuSF, the 5*s* orbital of Ag is much more diffuse than the 4*s* orbital of Cu. As a result, a broader conduction band is expected in BaAgSF than BaCuSF, resuting in a smaller band gap for BaAgSF. If the direct gap is associated with a transition at the Γ point, the smaller gap of BaAgSF primarily derives from a lower energetic position of the Ag 5*s* orbital relative to the Cu 4*s* orbital.

The room-temperature conductivity was measured to be smaller than 10^{-6} S/cm for both of BaAgSF and $Ba_{0.9}K_{0.1}AgSF$ pellets; while it was measured as 10^{-1} S/cm for BaCuSF and 82 S/cm for $Ba_{0.9}K_{0.1}CuSF$ pellets [2]. Isostructural LaAgOS is reported to be a Ag mixed ionic conductor [16,17]. The first report of 10^{-3} S/cm room-temperature ionic conductivity by Palazzi, Carcaly, ad Flahaut in 1980 [16] was followed by the observation of $< 10^{-6}$ S/cm by another group which reported room-temperature alternating current (ac) conductivity of $< 10^{-5}$ S/cm [17].

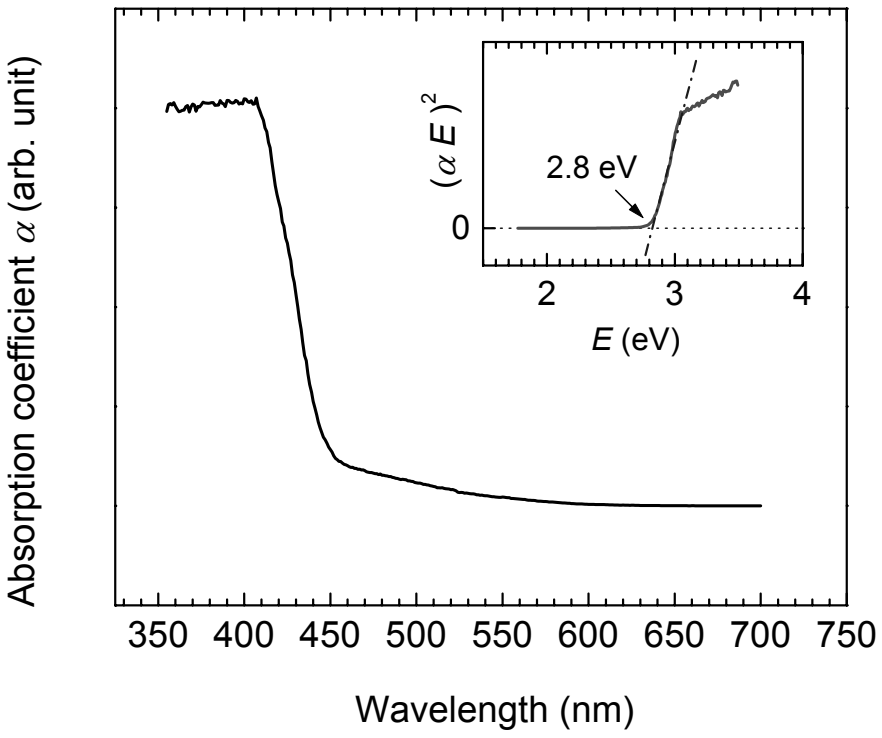

Figure 7.3. Absorption spectrum of BaAgSF at room temperature with the curve of $(\alpha E)^2$ *vs. E* (inset).

The corresponding Cu analog LaCuOS exhibits *p*-type electrical conductivity of ~10^{-2} S/cm in thin-film form [18]. Considering the structural similarity between BaAgSF and LaAgOS and the *p*-type conductivity in both BaCuSF and LaCuOS, the compound BaAgSF is expected to be an ionic conductor similar to LaAgOS. The ionic conductivity of BaAgSF as a function of temperature is being measured [19]. The small electrical conductivity of the Ag compounds, especially under *p*-type doping conditions, relative to the Cu compounds likely reflects a placement of the Ag 4*d* levels below the S 3*p* orbitals near the top of the valence band. The rich S character in the valence band leads to insulating behavior. Since considerable 5*s* character may be present in the conduction band, *n*-type behavior may be realized in the Ag compounds through suitable doping.

Attempts were made to synthesize BaAgSCl and SrAgSF by following the method described above, but reaction simply resulted in mixtures of $BaCl_2$ and unidentified phase(s) in the case of BaAgSCl, and a mixture of SrS, Ag_2S, and SrF_2 for SrAgSF. Attempts were also made to prepare the solid solution $BaCu_{1-x}Ag_xSF$ (x = 0.25, 0.5, and 0.75), but the products were found to be mixtures of BaCuSF and BaAgSF. Presumably, the significant size difference between Cu^+ (74 pm) and Ag^+ (114 pm) [20], prevents formation of the solid solution. It has been observed that Ag in BaCuSF changes the red emission of BaCuSF into a saturated green emission, even though Ag substitution in BaCuSF is not extensive [4]. The origins of the change in emission color with Ag is being investigated.

CONCLUSION

The new Ag sulfide fluoride BaAgSF was prepared by using high-temperature reaction methods, and its structure was determined via powder X-ray diffraction and Rietveld refinement method. Its band gap is estimated to be 2.8 eV from wavelength-dependent diffuse reflectance measurements, and electrical conductivity measurements have revealed insulating behavior. The derivatives BaAgSCl and SrAgSF did not form under conditions similar to those used for preparation of BaAgSF.

ACKNOWLEDGMENTS

This material is based upon work supported by the National Science Foundation under Grant No. 0245386.

REFERENCES

[1] H. Yanagi, S. Park, A. D. Draeseke, D. A. Keszler, and J. Tate, *J. Solid State Chem.*, **175**, 34 (2003).

[2] H. Yanagi, J. Tate, S. Park, C.-H. Park, D. A. Keszler, *Appl. Phys. Lett.*, **82**, 2814 (2003).

[3] C.-H. Park, D. A. Keszler, H. Yanagi, J. Tate, *Thin solid films*, 445, 288 (2003).

[4] C.-H. Park, and D. A. Keszler, *unpublished*.

[5] I. C. Madsen, R. J. Hill, *J. Appl. Crystallogr.*, **27**, 385 (1994)

[6] A. Yokochi, *unpublished*.

[7] J. Rodriguez-Carvajal, FULLPROF: A program for Rietveld Refinement and Pattern Matching Analysis, *In Abstract of the Satellite Meeting on Powder Diffraction of the XV Congress of the IUCr*, p 127, Thoulouse, France (1990).

[8] P. Stephens, *J. Appl. Crystallogr.*, **32**, 281 (1999).

[9] M. Palazzi, and S. Jaulmes, *Acta Crystallogr.*, **B37**, 1337 (1981).

[10] P.S. Berdonosov, A. M. Kusainova, L. N. Kholodkovskaya, V. A. Dolgikh, L. G. Akselrud, and B. A. Popovkin, *J. Solid State Chem.*, **118**, 74 (1995)

[11] C.-H. Park, A. Yokochi, D. A. Keszler, *unpublished*.

[12] W. Bronger, B. Lenders, J. Huster, *Z. Anorg. Allg. Chem.,* **619**, 70 (1993).

[13] D. Shriver, and P. Atkins, *Inorganic Chemistry*, 3rd ed. p.24, W. H. Freeman, New York (1999).

[14] P. Kubelka and F. Munk, *Z. Tech. Phys.* **12**, 593 (1931).

[15] P. Kubelka, *J. Opt. Soc. Am.* **38**, 448 (1948).

[16] M. Palazzi, C. Carcaly, and Flahaut, *J. Solid State Chem.*, **35**, 150 (1980).

[17] K. Ishikawa, S. Kinoshita, Y. Suzuki, S. Matsuura, T. Nakanishi, M. Aizawa, and Y Suzuki, *J. Electrochem. Soc.*, 138(4), 1166 (1991).

[18] K. Ueda, S. Inoue, S. Hirose, H. Kawazoe, and H. Hosono, *Appl. Phys. Lett.*, **77**, 2701 (2000).

[19] C.-H. Park, M. Lerner, and D. A. Keszler, *unpublished*.

[20] R. D. Shannon, *Acta Crystallogr.*, **A32**, 751 (1976).

CHAPTER 8

p-TYPE CONDUCTIVITY, GAP MODULATION, AND PHASE STABILITY OF $BaCu_2Q_2$ (Q=S,Se)

Cheol-Hee Park, Douglas A. Keszler, Robert Kykyneshi, and Janet Tate

submitted to *Journal of Solid State Chemistry*
525 B Street, Suite 1900, San Diego, CA 92101-4495

ABSTRACT

Optical and electrical properties of powder samples of $BaCu_2S_2$, $BaCu_2Se_2$, and their solid solutions were examined along with their phase stabilization. Band gaps were estimated from diffuse reflectance measurements to be 2.3 eV for the low-temperature α form of $BaCu_2S_2$ and 1.8 eV for the high-temperature β form of $BaCu_2S_2$. Sr-substitution for Ba, and Se-substitution for S stabilize the α form at high temperatures, while K- and Na-doping stabilize the β form at low temperatures. The carrier type was determined as *p*-type for all samples by Seebeck measurements. The room-temperature conductivity was measured to be 2 S/cm for α-$BaCu_2S_2$ and 20 S/cm for β-$BaCu_2S_2$ and orthorhombic $BaCu_2Se_2$. It increases with K doping, measuring as 420 S/cm for $Ba_{0.9}K_{0.1}Cu_2S_2$, and 740 S/cm for $Ba_{0.9}K_{0.1}Cu_2Se_2$. The direct band gap of the α phase can be tuned from 2.3 to 1.8 eV by the substitution of Se for S in $BaCu_2S_2$.

INTRODUCTION

The compound $BaCu_2S_2$ crystallizes in a low-temperature orthorhombic form (α) and a high-temperature tetragonal form (β). The crystal structure of the α-form is characterized by a three-dimensional linkage of CuS_4 tetrahedra that encapsulates the Ba atom in a 7-coordinate site. The CuS_4 tetrahedra are connected by sharing both vertices and edges. The β form adopts the $ThCr_2Si_2$-type structure with two-dimensional layers of edge-sharing CuS_4 tetrahedra separated by Ba sheets. The Ba atom is coordinated by eight S atoms (Figure 8.1). The α-β phase transition temperature of a single crystal of $BaCu_2S_2$ has been established to be 813 (±10) K by using high-temperature X-ray diffraction measurements [1]. Ohtani and co-workers observed the onset for the phase transition at 772 K by using DTA [2]. Substitution of Ba with smaller Sr atoms leads to stabilization of the α form up to 923 K [3]. Even with small amounts of Sr (2.5%) in $BaCu_2S_2$ significantly stabilizes the α form.

The band gap of α-$BaCu_2S_2$ was estimated to be 2.3 eV in films, which also yield a *p*-type conductivity of 17 S/cm and a Hall mobility of 3.5 cm^2/V s [4]. Relatively high Hall mobility and the band gap of 2.3 eV is desirable for polycrystalline thin-film tandem solar cell application. Polycrystalline thin-film tandem solar cells constitute a promising avenue for the realization of an economically-viable renewable energy source [5,6]. For separately connected

tandem solar cells, optimal band-gap combination for two- and three-terminal structures have been specified as 1.8/1.1 eV and 2.15/1.55/1.0 eV, respectively [7,8]. Therefore α-$BaCu_2S_2$ is highly regarded as a *p*-type window and interconnect for the high band-gap portion of the cell. Smaller band-gap *p*-type semiconductors are also desired and substitution of S with the heavier chalcogenide Se in $BaCu_2S_2$ should produce such materials. In previous work, such band-gap modulation was demonstrated in the solid-solution $BaCuS_{1-x}Se_xF$ ($0 \leq x \leq 1$) [9]. Higher *p*-type conductivity can also be achieved by doping with monovalent ions such as Na^+ or K^+, which was also demonstrated in BaCuQF (Q=S, Se) [4].

In this contribution, we describe α, β phase stabilization in $BaCu_2Q_2$ (Q=S, Se), conductivity results achieved with K doping, and band-gap modulation.

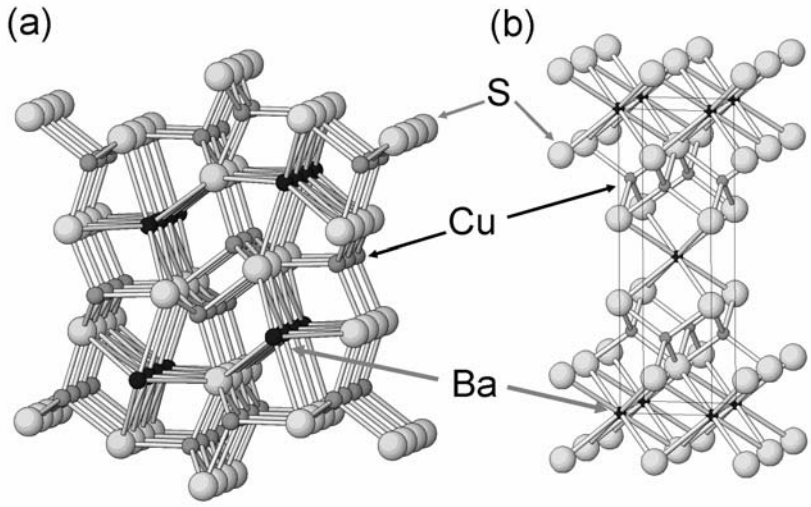

Figure 8.1. Structure of (a) α- and (b) β-$BaCu_2S_2$.

EXPERIMENTAL

Powder samples of undoped and K-doped $BaCu_2S_2$ were prepared by heating stoichiometric mixtures of $BaCO_3$ (Cerac, 99.9%), Cu_2S (Cerac, 99.5%), and K_2CO_3 (Aldrich, 99.995%) at 723 K for 1 h under a flowing stream of H_2S(g) and then cooling to room temperature under flowing Ar(g). The high-temperature phase β-$BaCu_2S_2$ was prepared by heating α-$BaCu_2S_2$ at 973 K for 5 h in an evacuated silica tube.

$BaCu_2Se_2$ powders were prepared by heating stoichiometric mixtures of BaSe (Cerac, 99.5%) and Cu_2Se (Cerac, 99.5%) in an evacuated silica tube at 823 K for 5h. For K-doped $BaCu_2Se_2$, stoichiometric mixtures of BaSe, Cu_2Se, Se (Alfa, 99.999%), and KNO_3 (Johnson-Matthey, ACS) were heated at 773 K for 1 h under a flowing stream of H_2 (5%)/N_2 (95%). The solid solution series $BaCu_2(S_{1-y}Se_y)_2$ (y = 0.25, 0.5, 0.75) was prepared by heating stoichiometric mixtures of $BaCu_2S_2$ and $BaCu_2Se_2$ in an evacuated silica tube at 923 K for 3h.

All samples were characterized by powder X-ray diffraction with Cu Kα radiation on a Siemens D-5000 powder diffractometer.

Transport properties of pellets were characterized by collinear four-probe temperature-dependent electrical conductivity and Seebeck coefficient measurements. Because of the high conductivity of the materials, metal contacts were not used. The room-temperature conductivity measurements were carried out by using the van der Pauw method. To measure transport properties of α-$BaCu_2S_2$ and $Ba_{1-x}K_xCu_2S_2$ (x = 0.05), each powder sample was pressed into a half-inch diameter pellet at 4.5 tons and annealed at 723 K for 10 h in an evacuated silica tube. After transport property measurements were made, the samples were annealed again at 923 K for 1.5 h in an evacuated silica tube. For $Ba_{1-x}K_xCu_2S_2$ (x = 0.005, 0.025, 0.075, and 0.1), each pellet was prepared at 4.5 tons and annealed at 723 K for 10 h and subsequently annealed at 923 K for 1.5 h in an evacuated silica tube. After annealing at 923 K, α-$BaCu_2S_2$ transformed into β-$BaCu_2S_2$. The

resulting pellets are orange-brown in the case of α-$BaCu_2S_2$, and dark gray-black in the cases of β-$BaCu_2S_2$, $Ba_{1-x}K_xCu_2S_2$ and $Ba_{1-x}K_xCu_2Se_2$ ($0 < x \leq 0.1$). For $Ba_{1-x}K_xCu_2Se_2$ (x = 0, 0.005, 0.025, and 0.1) each powder sample was pressed into a half-inch diameter pellet at 4.5 tons and annealed at 898 K for 1.5 h in an evacuated silica tube.

The diffuse reflectance at room temperature of powder samples were measured with $BaSO_4$ as a reference by using an Oriel 300-W Xe lamp, a Cary model-15 prism monochromator, and a Hamamatsu R636-10 photomultiplier tube, to cover the UV-visible region (360-700 nm).

RESULTS

Powder X-ray diffraction patterns of $BaCu_2S_2$ prepared at 723 K and 973 K, and $Ba_{0.995}K_{0.005}Cu_2S_2$ prepared at 723 K are depicted in Figure 8.2 along with calculated X-ray diffraction patterns of α-$BaCu_2S_2$ and β-$BaCu_2S_2$. The X-ray diffraction pattern of $BaCu_2S_2$ prepared at 723 K is composed of mainly α-$BaCu_2S_2$ and a small amount of β-$BaCu_2S_2$. The X-ray diffraction pattern of $BaCu_2S_2$ prepared at 973 K agrees well with calculated X-Ray diffraction pattern of β-$BaCu_2S_2$. Every compound of K-doped $BaCu_2S_2$ prepared at 723 K was observed

to be stabilized as β-$BaCu_2S_2$. Samples of $Ba_{1-x}K_xCu_2Se_2$ (x =0.005, 0.025, and 0.1) were observed to be isostructural to α-$BaCu_2S_2$.

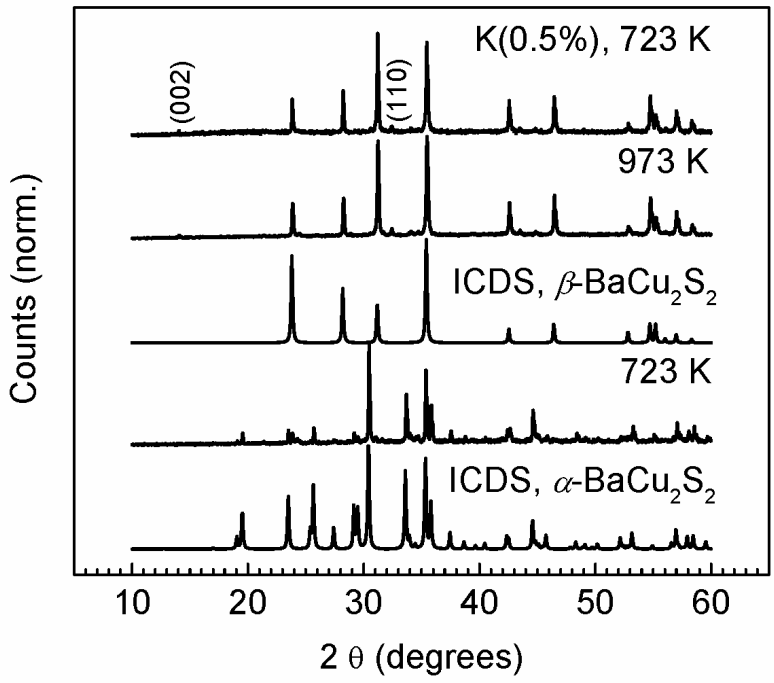

Figure 8.2. Powder X-ray diffraction patterns of $BaCu_2S_2$ prepared at 723 K and 973 K, and $Ba_{0.995}K_{0.005}Cu_2S_2$ prepared at 723 K.

X-ray diffraction patterns of $BaCu_2(S_{1-y}Se_y)_2$ (y = 0.25, 0.5, 0.75, and 1) prepared at 923 K along with α-$BaCu_2S_2$ prepared at 723 K are shown in Figure 8.3. All compounds with $0.25 \leq y \leq 1$ are isostructural to α-$BaCu_2S_2$. The sample of $BaCu_2(S_{0.975}Se_{0.025})_2$ prepared at 923 K was observed to be isostructural to β-$BaCu_2S_2$. With increasing Se concentration, diffraction lines shift to small angles as the unit-cell volume increases. The *a*-axis lattice parameter and the cell volume are plotted as a function of y for the solid-solution series $BaCu_2(S_{1-y}Se_y)_2$ ($0 \leq y \leq 1$) in Figure 8.4. The essentially linear change of the *a*-axis lattice parameter and the cell volume with y are in agreement with Vegard's law, indicating a random distribution of the S and Se atoms. The small deviation from the straight-line fit of the cell volume at y = 0 could be attributed to the lower preparation temperature (723 K) for this particular sample. The unit-cell volume of a single crystal α-$BaCu_2S_2$ is reported to be 390.1 $Å^3$ [1].

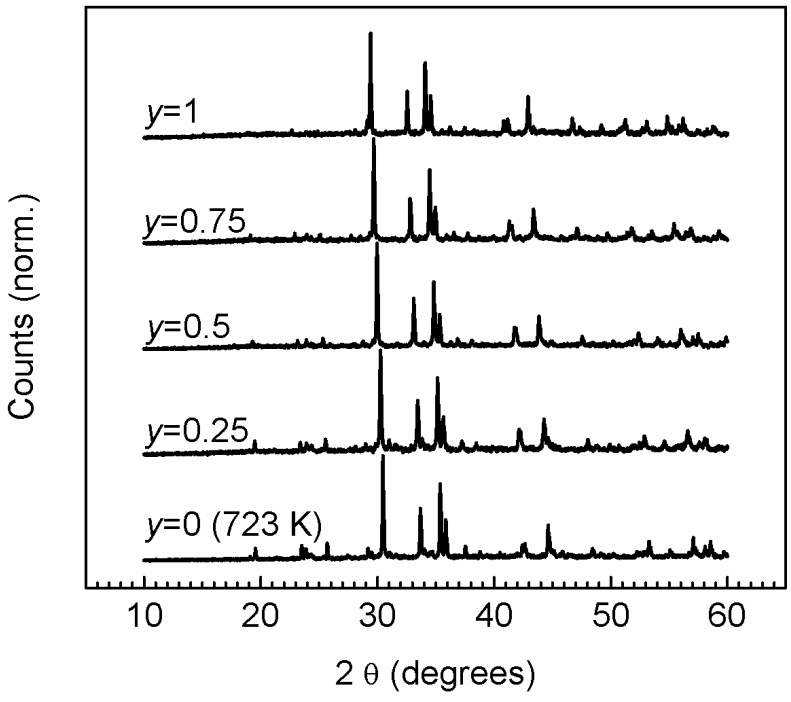

Figure 8.3. Powder X-ray diffraction patterns of $BaCu_2(S_{1-y}Se_y)_2$ (y = 0.25, 0.5, 0.75, and 1) prepared at 923 K along with α-$BaCu_2S_2$ prepared at 723 K.

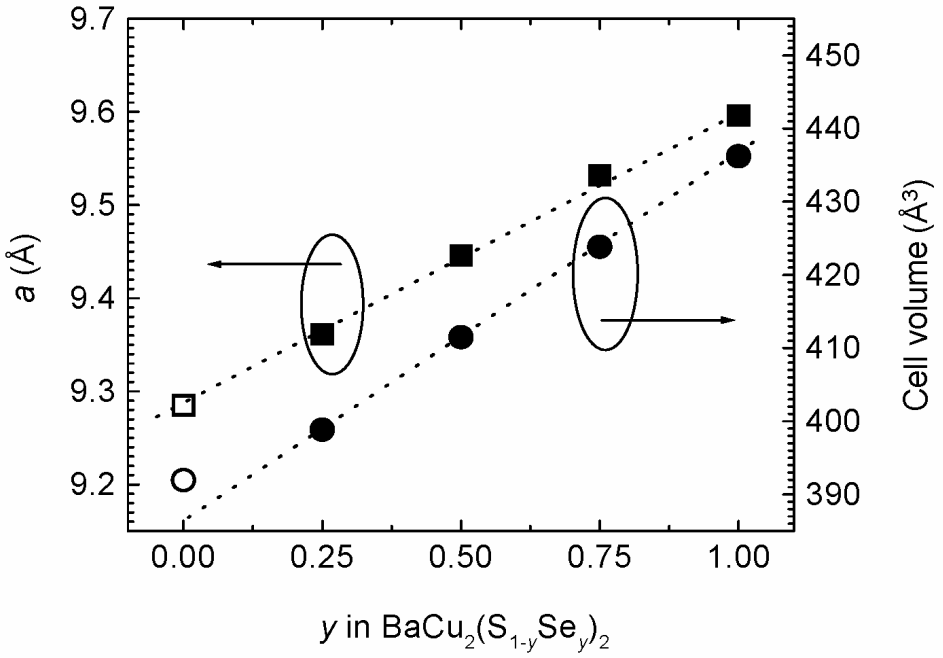

Figure 8.4. Lattice constants *a* and unit cell volumes of $BaCu_2(S_{1-y}Se_y)_2$ (y = 0.25, 0.5, 0.75, and 1) prepared at 923 K, and α-$BaCu_2S_2$ prepared at 723 K.

Transport properties

Room-temperature conductivities, Seebeck coefficients, and densities of $Ba_{1-x}K_xCu_2S_2$ (x = 0, 0.005, 0.025, 0.05, 0.075, and 0.1) pellets annealed at 923 K are summarized in Table 8.1. Seebeck measurements on all samples gave a positive sign, indicating that these materials are *p*-type conductors at all doping levels. The temperature dependence of electrical conductivity of $Ba_{1-x}K_xCu_2S_2$ (x = 0, 0.005, 0.025, 0.05, 0.075, and 0.1) pellets is illustrated in Figure 8.5. Room-temperature conductivity was measured to be 1.7 S/cm for two α-$BaCu_2S_2$ pellets annealed at 723 K with 60% theoretical density. An undoped pellet of β-$BaCu_2S_2$ has an electrical conductivity of 20 S/cm, and this conductivity increases with increasing K concentration. The room-temperature conductivity of the pellet is 420 S/cm for $Ba_{0.9}K_{0.1}Cu_2S_2$. For comparison, the room-temperature conductivity of BaCuSF was increased by over two orders of magnitude with 10 % K-doping; the room-temperature conductivity was measured as 0.88 S/cm for undoped BaCuSF and 82 S/cm for $Ba_{0.9}K_{0.1}$CuSF [4]. The temperature dependence of the electrical conductivity of $Ba_{1-x}K_xCu_2S_2$ is semiconducting for $x \leq 0.005$, and there is a crossover to degenerate semiconductor behavior for $x \geq 0.025$.

TABLE 8.1. Room temperature electrical properties (conductivity and Seebeck coefficient) and densities of $Ba_{1-x}K_xCu_2S_2$ (x = 0, 0.005, 0.025, 0.05, 0.075, and 0.1) pellets annealed at 923 K.

K (at. %)	0 (β)	0.005	0.025	0.05	0.075	0.1
σ (S/cm)	20	30	140	200	330	420
S (μV/K)	+ 226	+ 228	+ 150	+ 132	+ 112	+ 101
Density (%)	64	85	90	73	81	84

The room-temperature conductivity of $BaCu_2Se_2$ was measured to be 20 S/cm, which is similar to that of β-$BaCu_2S_2$ (Figure 8.6). With increasing K, the conductivity of $Ba_{1-x}K_xCu_2Se_2$ increases more rapidly than that of $Ba_{1-x}K_xCu_2S_2$, which could be attributed to higher covalency of the Cu-Se bonds *vs.* the Cu-S bonds. Typically, higher covalency will give broader bands and smaller effective masses, which give rise to higher carrier mobilities [10]. This is a quite substantial improvement relative to the room-temperature conductivity of 17 S/cm in undoped α-$BaCu_2S_2$ film [4], since in the potassium doped samples with x = 0.1, σ = 420 S/cm for the sulfur based compound and σ = 740 S/cm in the selenium compound.

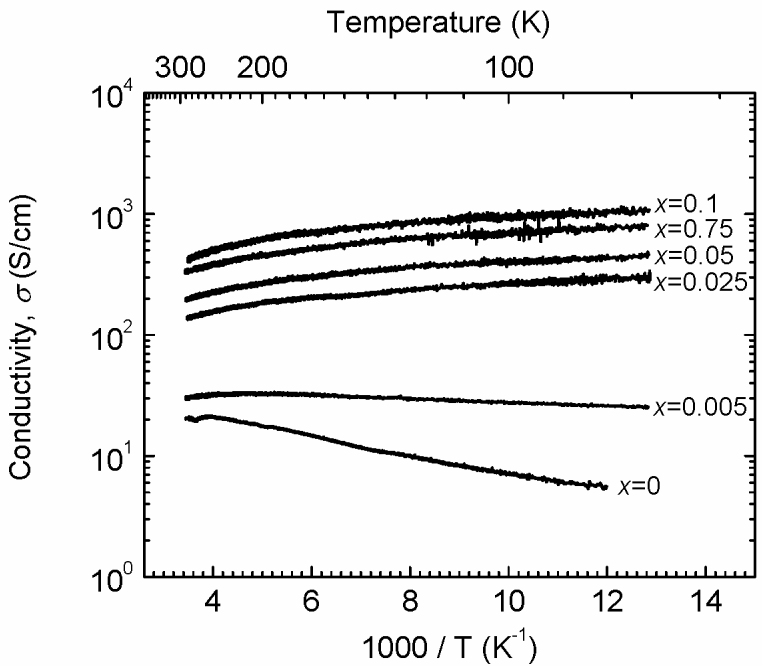

Figure 8.5. Temperature dependent conductivity measurements of $Ba_{1-x}K_xCu_2S_2$.

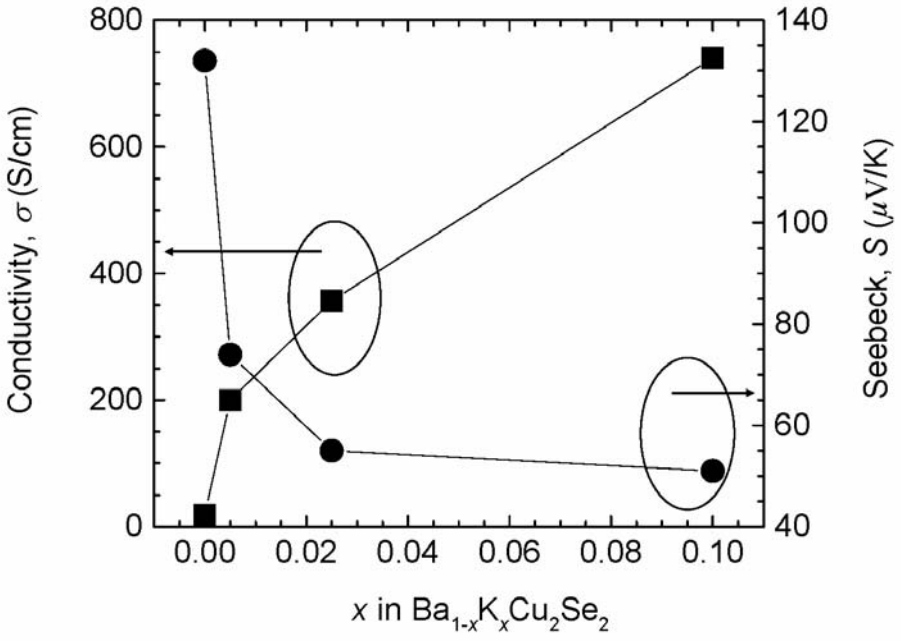

Figure 8.6. Transport properties of $Ba_{1-x}K_xCu_2Se_2$ at room temperature.

Optical Properties

Diffuse reflectance spectra for α-$BaCu_2S_2$, β-$BaCu_2S_2$, and $Ba_{0.9}K_{0.1}Cu_2S_2$ are illustrated in Figure 8.7. The diffuse reflectance spectra of β-$BaCu_2S_2$ and $Ba_{0.9}K_{0.1}Cu_2S_2$ are almost identical. The abrupt increase of the diffuse reflectance signal seen in Figure 8.7 is indicative of the onset of transmission near the energy gap. The diffuse reflectance spectra were translated into absorption spectra via the Kubelka-Munk method [11,12], and the direct band gap was extracted by extrapolating the straight-line portion of the curve of $(\alpha E)^2$ *vs.* E to the zero-absorption axis. Here α is the absorption coefficient, and E is the photon energy. The direct gap is estimated to be 2.3 eV for α-$BaCu_2S_2$, which agrees well with the reported band gap of α-$BaCu_2S_2$ film [13]. The band gap energy of β-$BaCu_2S_2$ and $Ba_{0.9}K_{0.1}Cu_2S_2$ samples were derived as 1.75-1.8 eV, which is desirable for two-terminal structure of separately connected tandem solar cells.

Plots of $(\alpha E)^2$ *vs.* E for $BaCu_2(S_{1-y}Se_y)_2$ (y = 0.25, 0.5, 0.75, and 1) prepared at 923 K and α-$BaCu_2S_2$ prepared at 723 K are shown in Figure 8.8. With increasing Se content, the absorption edge shifts to lower energy. The direct band gaps of $BaCu_2(S_{1-y}Se_y)_2$ (y = 0.25, 0.5, 0.75, and 1) prepared at 923 K and α-$BaCu_2S_2$ prepared at 723 K are depicted in Figure 8.9. The band gap can be tuned by the substitution of Se for S to 1.8 eV for $BaCu_2Se_2$. The decrease scales almost linearly with compositional change and the increase in the volume of the orthorhombic unit cell (Figure 8.10).

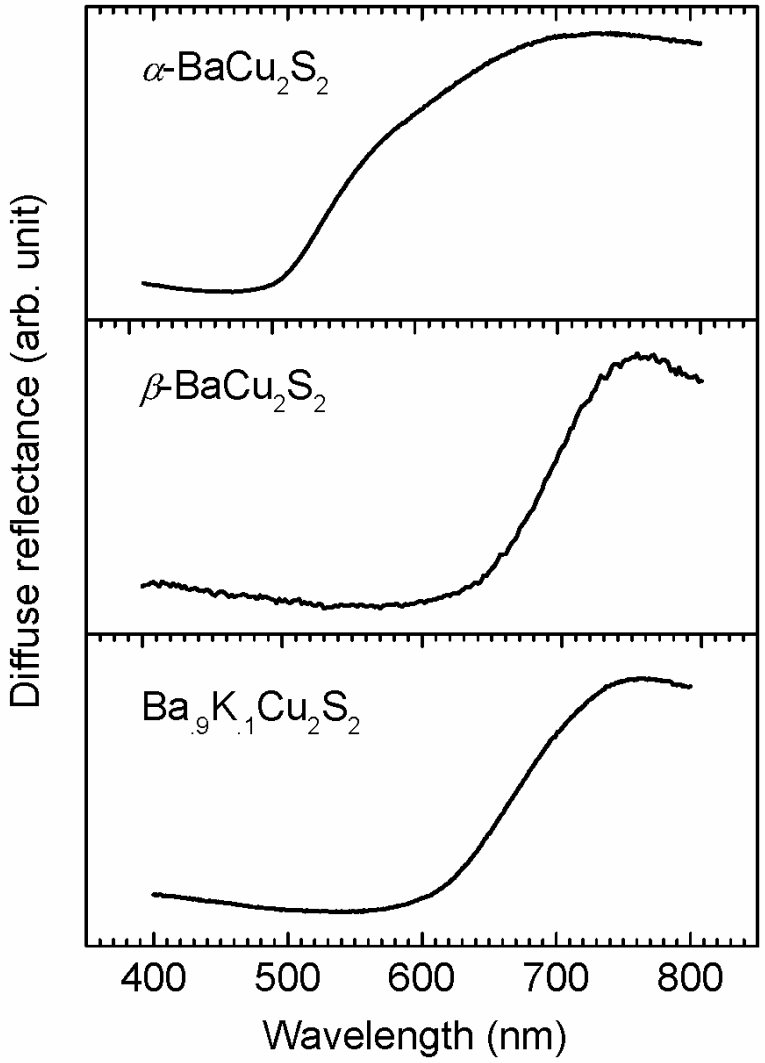

Figure 8.7. Diffuse reflectance spectra for powdered α-$BaCu_2S_2$, β-$BaCu_2S_2$, and $Ba_{0.9}K_{0.1}Cu_2S_2$.

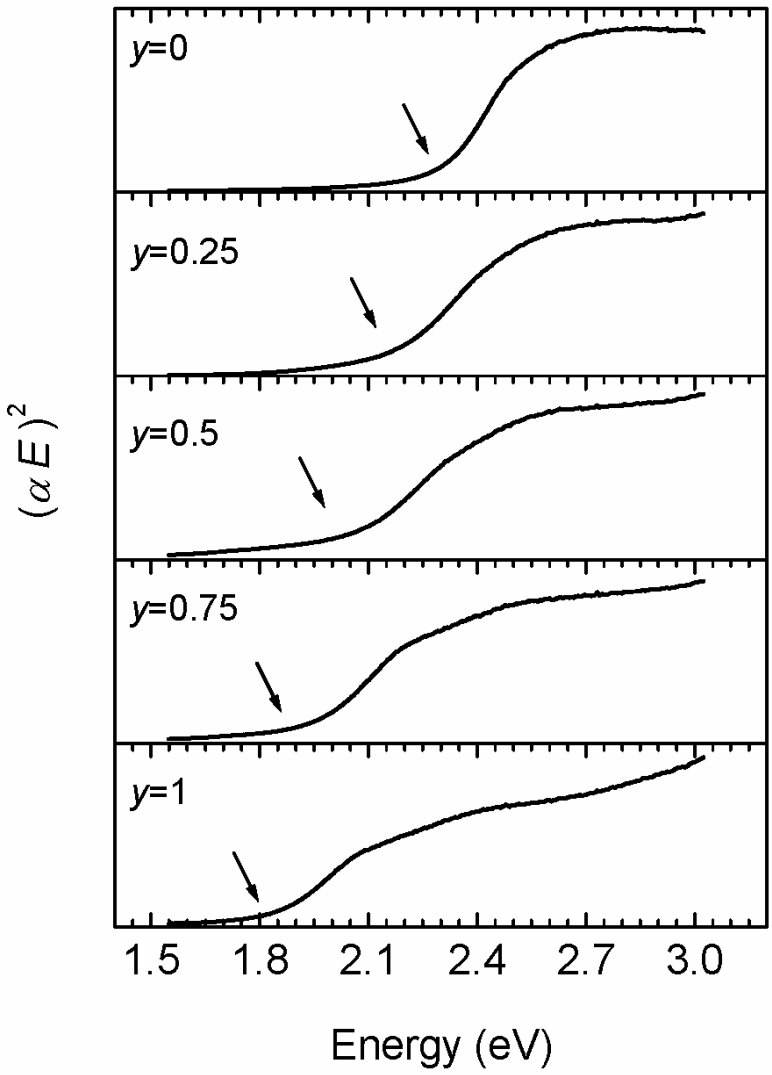

Figure 8.8. Plots of $(\alpha E)^2$ *vs. E* for $BaCu_2(S_{1-y}Se_y)_2$ (y = 0.25, 0.5, 0.75, and 1) prepared at 923 K, and α-$BaCu_2S_2$ prepared at 723 K. The arrows indicate the position of the energy gap.

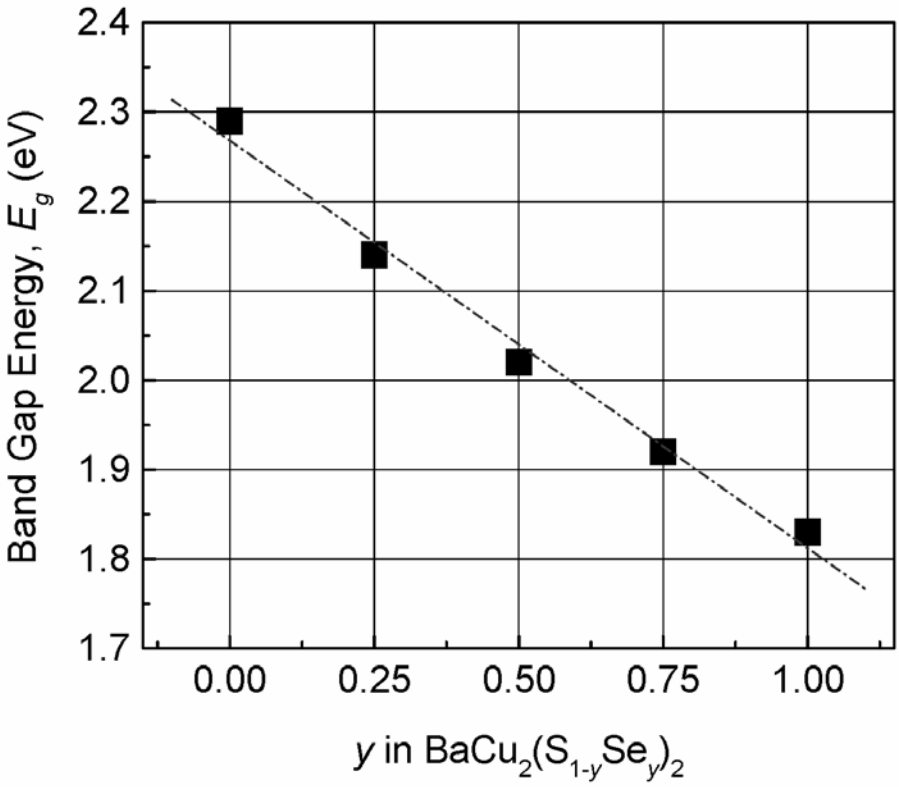

Figure 8.9. Direct band gaps of $BaCu_2(S_{1-y}Se_y)_2$ (y = 0.25, 0.5, 0.75, and 1) prepared at 923 K, and α-$BaCu_2S_2$ prepared at 723 K.

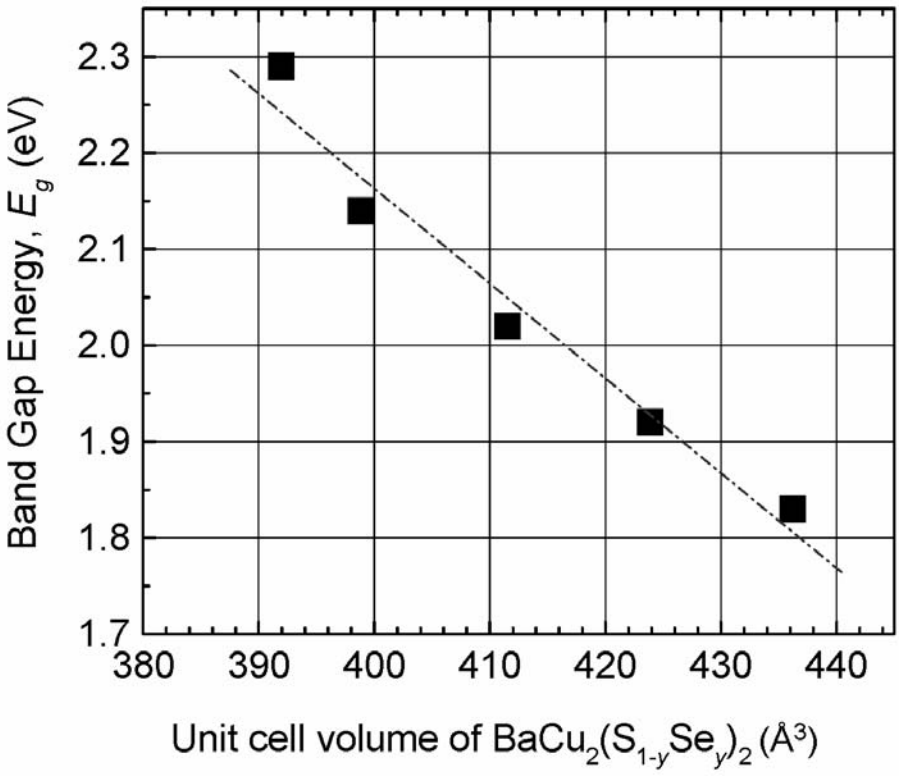

Figure 8.10. Direct band gap versus unit-cell volume in $BaCu_2(S_{1-y}Se_y)_2$.

Phase stabilization

As mentioned earlier, the α-β phase transition temperature of $BaCu_2S_2$ has been established to be approximately 813 K. The α form is readily prepared at 723 K in H_2S (g) with small amount of the high temperature β form, while the X-ray diffraction pattern of the $BaCu_2S_2$ sample prepared at 973 K in an evacuated silica tube reveals only the β form.

The stabilization of the low-temperature α form at temperatures higher than the normal transition temperature is achieved by substitution of Ba with the smaller atom Sr [3] or substitution of S with the larger atom Se. The stabilization of the α form by substitution of S with Se can be explained in view of the local structure of the Ba atom. The Ba atom is coordinated by seven and eight S atoms in the α- and β-phases, respectively. The larger Se atom limits the coordination number of the Ba atom, *i.e.*, samples of $BaCu_2(S_{1-y}Se_y)_2$ (y = 0.25, 0.5, 0.75, and 1) prepared at 923 K are stabilized in the α form.

No α-β phase transition was observed for the sample of $Ba_{0.75}Sr_{0.25}Cu_2S_2$ heated in an evacuated silica tube up to 1048 K. Substitution of the smaller Ca for Ba did not lead to stabilization of the α form, which is more likely associated with a very limited solubility of Ca in $BaCu_2S_2$.

The stabilization of the β form at low temperatures is realized by substitution of Ba with monovalent Na^+ and K^+ ions. The ionic size of K^+ (165 pm)

is larger than that of Ba^{2+} (156 pm), while Na^{+} (132 pm) is smaller than Ba^{2+} [14]. Therefore the factor to stabilize the β form is not a simple size effect. The substitution of Ba with K atom strongly stabilizes the β form; even with substitution of 0.5% leads to stabilization of the β form at all reaction temperatures. Substitution with the larger Cs atom (188 pm) for 10% of the Ba resulted only in α-phase formation. Here, it is likely that Cs substitution is quite limited.

Attempts were made to stabilize K-doped $BaCu_2S_2$ and Na-doped $BaCu_2S_2$ in the α form by substitution of Ba with Sr, and S with Se. At 873 K $Ba_{0.8}Sr_{0.15}K_{0.05}Cu_2S_2$ formed in the β form. At 798 K samples of $Ba_{0.75-x}Sr_{0.25}Na_xCu_2S_2$ ($0.01 \leq x \leq 0.05$) were stabilized in the β form, while the sample of $Ba_{0.748}Sr_{0.25}Na_{0.002}Cu_2S_2$ was a mixture of the α and β forms. At 873 K the samples of $Ba_{0.975}K_{0.025}Cu_2Se_2$ were stabilized in the α form; while samples of $Ba_{0.975}K_{0.025}Cu_2(S_{1-y}Se_y)_2$ ($0.01 \leq y \leq 0.5$) were observed to be mixtures of the α and β forms (Figure 8.11).

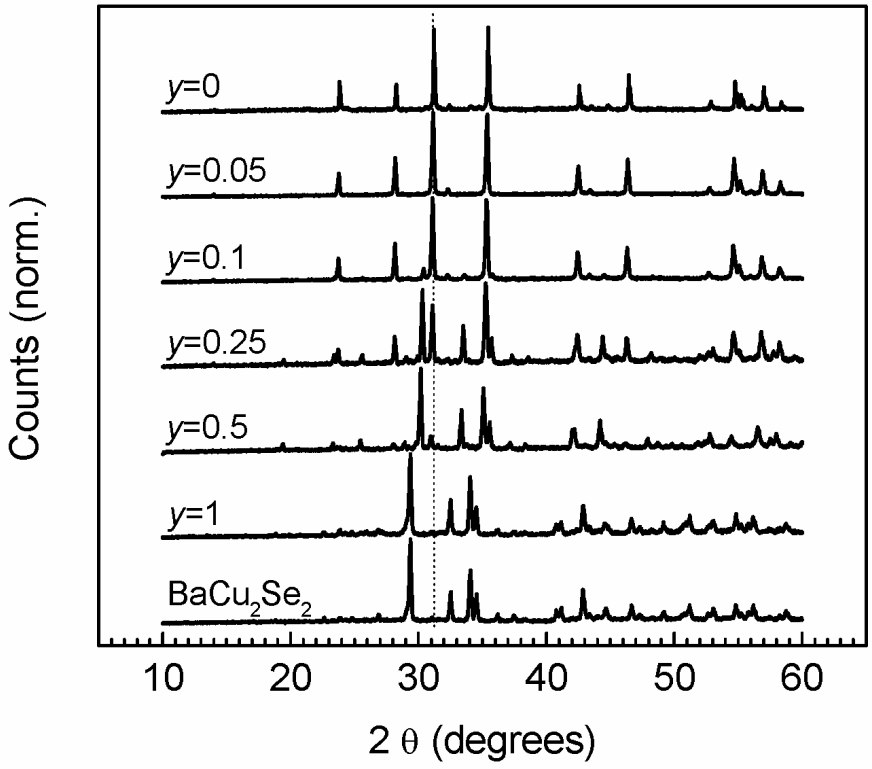

Figure 8.11. Powder X-ray diffraction patterns of the samples of $Ba_{0.975}K_{0.025}Cu_2(S_{1-y}Se_y)_2$ (y = 0, 0.05, 0.1,, 0.25, 0.5, and 1) prepared at 873 K and $BaCu_2Se_2$.

Chemical Reactivity

The stability of powder samples of α-$BaCu_2S_2$ in a concentrated NH_3(aq) solution was examined. After immersion in concentrated NH_3(aq) at room temperature for periods up to 18 h, samples did not reveal any significant change in their powder X-ray diffraction patterns (Figure 8.12). For comparison, the compound BaCuSF readily decomposes in H_2O(l), giving a black decomposition product.

At room temperature α-$BaCu_2S_2$ dissolves in concentrated HNO_3(aq), however, the deep blue color of Cu^{2+} ions is only observed after adding H_2O_2 and NH_3(aq) in turn.

In an attempt to oxidize β-$BaCu_2S_2$ into $BaCu_2O_2$, β-$BaCu_2S_2$ samples were annealed in flowing Ar(g)/H_2O(g) for 2 hours at 773-1173 K. No noticeable change, however, was observed based in the X-ray diffraction patterns. In air β-$BaCu_2S_2$ samples were annealed for 10 minutes at 573, 673, 773, 873, and 973 K, respectively. The samples annealed at or higher than 773 K were observed to decompose (Figure 8.13). The sulfide fluoride BaCuSF exhibits better stability to annealing in air; it is stable for 20 minutes at 773 K, and only limited small amount decomposition is observed after annealing for 1 h and 20 mins [9].

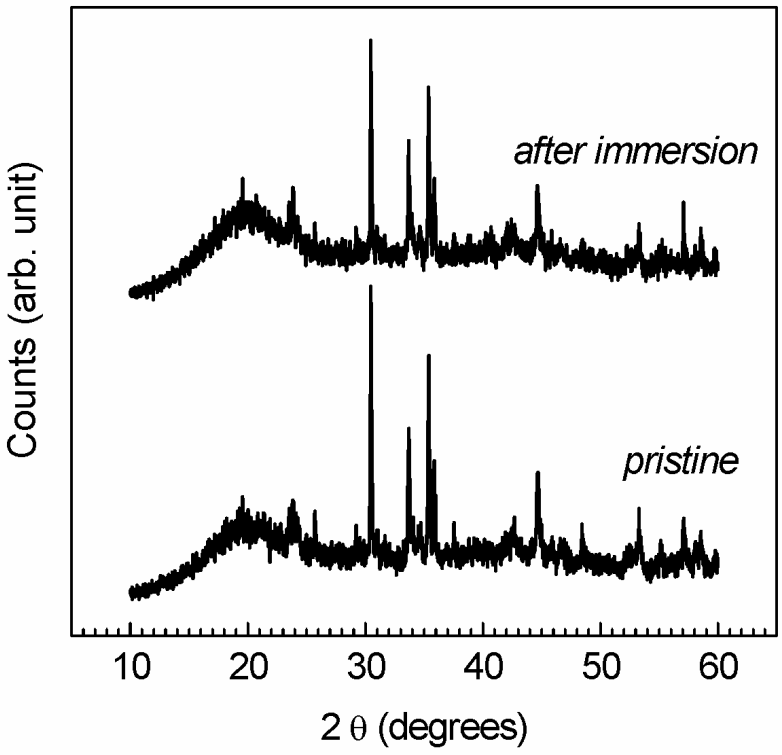

Figure 8.12. Powder X-ray diffraction patterns of α-$BaCu_2S_2$ before and after immersion in a concentrated NH_3(aq) solution for 18 h at room temperature.

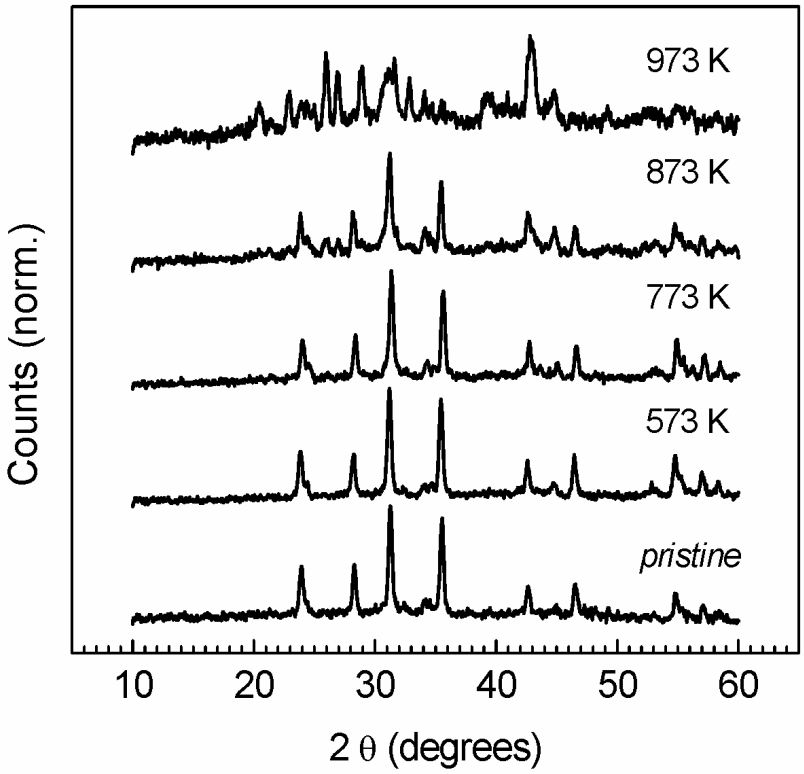

Figure 8.13. Powder X-ray diffraction patterns of β-$BaCu_2S_2$ samples annealed for 10 minutes at 573-973 K in air.

CONCLUSION

Powder samples of $BaCu_2S_2$, $BaCu_2Se_2$, and their solid solutions were prepared by high-temperature synthesis methods. Band gaps were estimated from diffuse reflectance measurements to be 2.3 eV for the low-temperature α form of $BaCu_2S_2$ and 1.8 eV for the high-temperature β form of $BaCu_2S_2$. Sr-substitution for Ba, and Se-substitution for S stabilize the α form of $BaCu_2S_2$ at high temperatures; K- and Na-doping stabilize the β form of $BaCu_2S_2$ at low temperatures. The carrier type was confirmed as *p*-type for all samples by Seebeck measurements. The room-temperature conductivity was measured to be 2 S/cm for α-$BaCu_2S_2$, and 20 S/cm for β-$BaCu_2S_2$ and $BaCu_2Se_2$. It is increased through K doping with conductivities of 420 S/cm for $Ba_{0.9}K_{0.1}Cu_2S_2$ and 740 S/cm for $Ba_{0.9}K_{0.1}Cu_2Se_2$. The direct band gap can be tuned from 2.3 to 1.8 eV by the substitution of Se for S in $BaCu_2S_2$.

ACKNOWLEDGEMENT

This material is based upon work supported by the National Science Foundation under Grant No. 0245386.

REFERENCES

[1] J. Huster, and W. Bronger, *Z. Anorg. Allg. Chem.*, **625**, 2033 (1999).

[2] T. Ohtani, H. Takeuchi, K. Koh, and T. Kaneko, *J Alloys Compd.*, **317-318**, 201 (2001).

[3] S Park, *Ph.D. Thesis*, Oregon State University (2002).

[4] H. Yanagi, J. Tate, S. Park, C.-H. Park, D. A. Keszler, *Appl. Phys. Lett.*, **82**, 2814 (2003).

[5] S. J. Fonash, *Solar Cell Device Physics*, Academic, New York (1981).

[6] A. L. Fahrebruch and R. H. Bube, *Fundamentals of Solar Cells*, Academic, New York (1983).

[7] M. D. Archer, and R. Hill, *Clean Electricity from Photovoltaic*, Imperical Collge Press, London (2001).

[8] T. J. Coutts, K. A. Emery, and J. S. Ward, *Progress in Photovotaics and Applications*, **10**, 1 (2002).

[9] C.-H. Park, D. A. Keszler, H. Yanagi, and J. Tate, *Thin Sold Films*, **445**, 288 (2003).

[10] A. Cox, *The Electronic Structure and Chemistry of Solids*, Oxford University Press, Oxford (1987).

[11] P. Kubelka and F. Munk, *Z. Tech. Phys.*, **12**, 593 (1931).

[12] P. Kubelka, *J. Opt. Soc. Am.*, **38**, 448 (1948).

[13] S. Park, D. A. Keszler, M. M. Valencia, R. L. Hoffman, J. P. Bender, and J. F. Wager, *Appl. Phys. Lett.*, **80**, 4393 (2002).

[14] R. D. Shannon, *Acta Crystallogr.*, **A32**, 751 (1976).

CHAPTER 9

STUDY ON *n*-TYPE TRANSPARENT CONDUCTING OXIDES: NEW *n*-TYPE TRANSPARENT CONDUCTORS OF W-DOPED In_2O_3 AND W-DOPED ZINC INDIUM OXIDES; TIN OXIDE AND ZINC INDIUM OXIDE TRANSPARENT THIN-FILM TRANSISTORS

Cheol-Hee Park, Douglas A. Keszler, Paul Newhouse, Robert Kykyneshi, Janet Tate, Rick E. Presley, Craig L. Munsee, David Hong, Nicci L. Dehuff, Emma S. Kettenring, Hai Q. Chiang, John F. Wager, and Randy L. Hoffman

Modified version: *Journal of Physics D: Applied Physics*
Dirac House, Temple Back, Bristol, BS1 6BE, UK
vol. **37**, 2810 (2004)

Modified version: *Journal of Applied Physics*,
Suite 1NO1, 2 Huntington Quadrangle, Melville, NY 11747-4502
in press.

ABSTRACT

Results on work related to transparent conducting oxides are summarized in this chapter. New *n*-type transparent conducting oxides of W-doped In_2O_3 and W-doped zinc indium oxides (ZIOs) films have been prepared by using pulsed laser deposition (PLD), and their optical and electrical properties have been examined. Films of $In_{2-x}W_xO_{3+\delta}$ (x = 0.025, 0.0375, 0.05, 0.0625, 0.075, 0.1, and 0.2) on silica substrates exhibit maximum mobility at x = 0.05. $In_{1.95}W_{0.05}O_{3+\delta}$ films on YSZ (yttrium stabilized zirconia) exhibit mobilities close to 120 cm^2/ V s. A conductivity of ~1100 S/cm and 90 % optical transparency has been observed in W-doped ZIO films prepared by using a $Zn_3In_{1.95}W_{0.05}O_{6+\delta}$ target. ZIO films with various compositions continue to be examined. Tin oxide transparent thin-film transistors (TTFTs) and ZIO TTFTs have been prepared and characterized. Estimation of crystallite sizes and strains of the channel layers are presented.

INTRODUCTION

Current *n*-type transparent conducting oxides such as In_2O_3:Sn (ITO), SnO_2:F, and ZnO:Al exhibit high conductivity and optical transparency; for example, ITO exhibits a conductivity of 10^4 S/cm, a mobility of ~30 cm^2/V s, and > 80% visible transparency for films having a thickness of a few hundred nm [1]. Present research on *n*-type transparent conductors focuses on new materials to replace potentially scarce indium, or to improve conductivity for specialized applications [2]. One of the approaches to identifying new *n*-type TCOs involves investigation of multicomponent oxides containing the "s-orbital" metals Zn, Cd, Ga, In, and Sn [2, 3], which has resulted in development of transparent zinc indium oxide films with high electrical conductivity [4, 5]. In attempts to develop new *n*-type transparent conductors, thin films of W-doped In_2O_3 (IWO) and W-doped zinc indium oxide (ZIWO) have been prepared by pulsed laser deposition (PLD) methods, and their transport properties have been measured.

Most transparent thin-film transistors (TTFTs) reported to date have employed polycrystalline ZnO as a channel material [6-11]. New types of TTFTs with SnO_2 or ZIO as channel layers are described here.

RESULTS

New transparent n-type conducting oxide of W-doped In_2O_3

Sintered disks for deposition of IWO films were prepared by high-temperature reaction method. Stoichiometric proportions of In_2O_3 (99.99%, Cerac) and WO_3 (99.99%, Cerac) were thoroughly mixed, and then pressed into one-inch pellets at 4.4 tons. They were ramped to 1500^{o}C at 300oC/ h and annealed for 4 h. The resulting targets were approximately 60% of theoretical density.

IWO films of thickness 400-500 nm were deposited onto GE 124 fused silica and single crystal (001) yttrium-stabilized zirconia (YSZ) substrates by PLD in oxygen ambient (1.0 x 10^{-3} Torr). A KrF excimer laser was used for the ablation of the target material. The film-deposition conditions are summarized in Table 9.1. Both the target and substrate were rotated during the deposition to enhance ablation and deposition uniformity.

Mobility values for films of $In_{2-x}W_xO_{3+\delta}$ (x = 0.025, 0.0375, 0.05, 0.0625, 0.075, 0.1, and 0.2) on silica substrates are diagrammed in Figure 9.1. The maximum mobility is observed at the composition $In_{1.95}W_{0.05}O_{3+\delta}$. Films of $In_{1.95}W_{0.05}O_{3+\delta}$ on YSZ exhibit much higher mobilities ~ 120 cm^2/ V s. Optical properties are currently being measured.

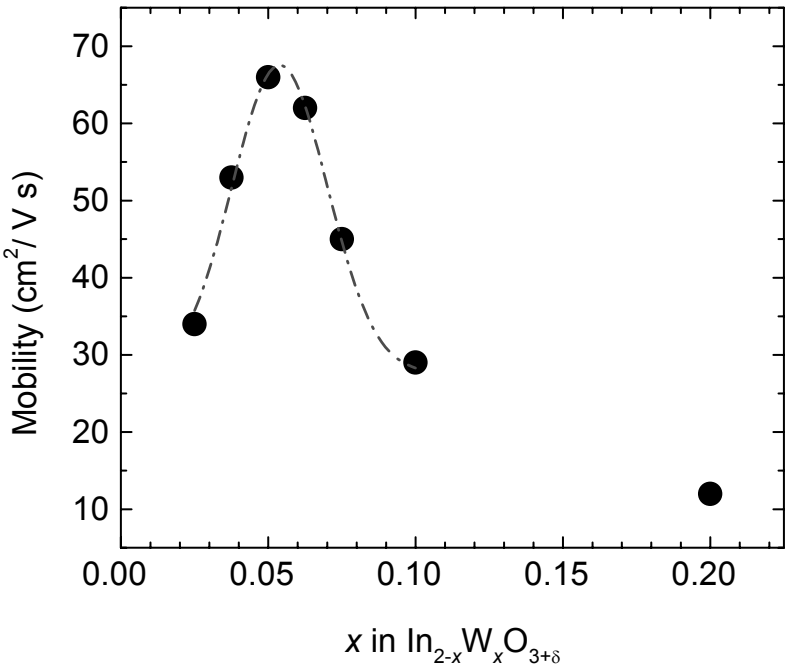

Figure 9.1. Mobilities of $In_{2-x}W_xO_{3+\delta}$ (x = 0.025, 0.0375, 0.05, 0.0625, 0.075, 0.1, and 0.2) thin films prepared by PLD. The dash-dot line represents best fit with Gaussian curve.

TABLE 9.1. Summary of IWO film preparative conditions by pulsed laser deposition.

Target	Sintered disk of $In_{2-x}W_xO_{3+\delta}$ (x = 0, 0.025, 0.0375, 0.05, 0.0625, 0.075, 0.1, and 0.2)
Laser	KrF (248 nm)
Repetition frequency (Hz)	10
Energy density (J/cm^2/pulse)	0.5
Oxygen pressure (Torr)	1.0 x 10^{-3}
Substrate	GE 124 fused silica, single crystal YSZ (001)
Substrate temperature (^{o}C)	400
Substrate-target distance (mm)	44.5

New transparent n-type conducting oxide of W-doped zinc indium oxides

Sintered disks of $Zn_3In_{1.95}W_{0.05}O_{6+\delta}$ have been used as PLD targets for deposition of ZIWO films. To fabricate the targets, stoichiometric proportions of ZnO (99.995%, Cerac), In_2O_3 (99.99%, Cerac), and WO_3 (99.99%, Cerac) were thoroughly mixed, and then pressed into one-inch pellets at 4.4 tons. They were ramped to 1500^{o}C at 200^{o}C/ h and then annealed for 3 h. The resulting targets were approximately 80% of theoretical density. Film preparation conditions are summarized in Table 9.2.

Two films have been prepared at 250 and 450^{o}C, and they exhibit similar electrical and optical properties. Conductivities of ~1100 S/cm, Hall mobilities of ~17 cm^2/V s, and carrier concentrations near 4 x 10^{20} cm^{-3} have been measured.

TABLE 9.2. Summary of W-doped zinc indium oxide films preparation condition by pulsed laser deposition.

Target	Sintered disk of $Zn_3In_{1.95}W_{0.05}O_{6+\delta}$
Laser	KrF (248 nm)
Repetition frequency (Hz)	10
Energy density (J/cm^2/pulse)	2
Oxygen pressure (Torr)	1.0 x 10^{-3}
Substrate	GE 124 fused silica
Substrate temperature (K)	250, 450
Substrate-target distance (mm)	50.8

The transmission and reflection of thin film of a ZIWO film deposited at 250^{o}C on SiO_2 substrate is depicted in Figure 9.2. Its thickness is measured as 380 nm. The effect of the interference fringes was removed by plotting $T/(1-R) \cong \exp(-\alpha d)$, where α is the absorption coefficient and d is the film thickness [12]. Overall transparency is 90% in the visible region, and the band gap is estimated to be 3.8 eV from the plot of $(\alpha E)^2$ vs. E.

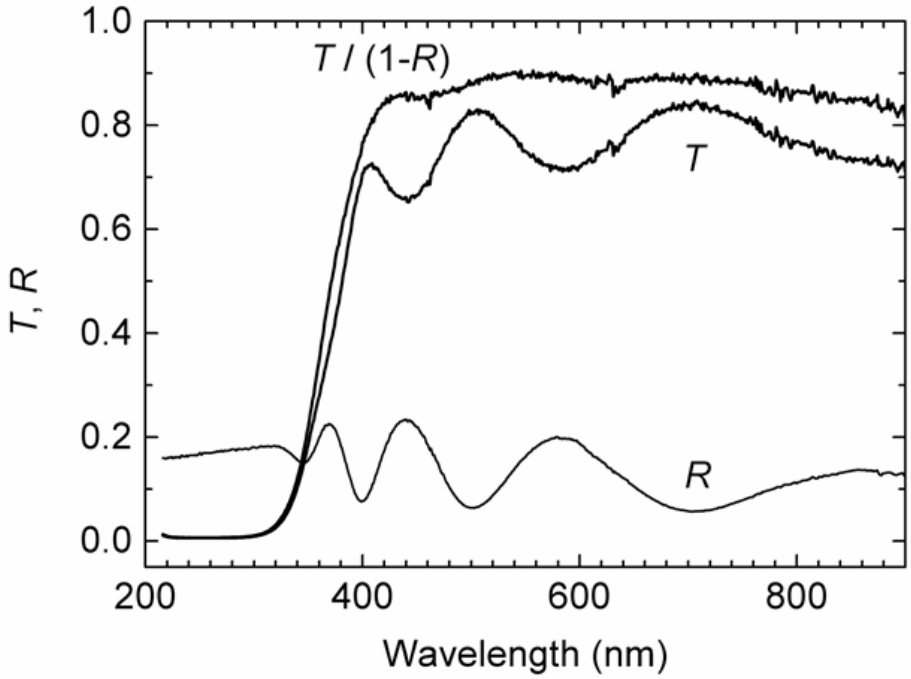

Figure 9.2. Transmittance (T) and reflectance (R) of a W-doped zinc indium oxide film deposited at 250^{o}C on SiO_2 substrate. The effect of the interference fringes was removed by plotting $T/(1-R) \cong \exp(-\alpha d)$, where α is absorption coefficient and d is the film thickness.

Tin Oxide Transparent Thin-Film Transistors

A SnO_2 transparent thin-film transistor (TTFT) has been fabricated [13]. The SO_2 channel layer was deposited by RF magnetron sputtering and then rapid thermal annealed in O_2 at 600^{o}C. The TTFT was highly transparent, and enhancement-mode behavior was achieved by employing a very thin channel layer (10-20 nm). Maximum field-effect mobilities of 0.8 cm^2/V s and 2.0 cm^2/V s were obtained for enhancement- and depletion-mode devices, respectively.

As deposited SnO_2 thin films were extremely insulating, however, they exhibit little or no gate modulation when employed as TTFT channel layers due to poor crystallinity, thus requiring a post-deposition anneal. Typically annealed SnO_2 thin films are too conductive for TTFT applications, presumably due to the tendency of SnO_2 to form oxygen vacancies. Several methods have been explored to reduce the conductivity of the SnO_2 channel layer. One approach is to evaporate SnO_2 powder in a partial pressure of microwave-activated N_2. The idea here is to incorporate nitrogen into the SnO_2 film, since nitrogen substitution onto an oxygen atomic site results if acceptor doping which would compensate oxygen vacancies or other SnO_2 donors, thereby reducing both the carrier concentration and the conductivity of the film. Although films prepared in this manner are indeed highly resistive, they unfortunately remain amorphous after heat treatment at 600^{o}C. Thus, TTFTs fabricated with such films as channel layers do not exhibit transistor action, presumably due to the very poor mobility of these amorphous films. To date, most

successful approach for minimizing the channel-layer conductivity is to increase the resistance of a relatively conductive SnO_2 channel by simply decreasing the chanel thickness (~10-20 nm).

Figure 9.3 shows X-ray diffraction patterns of two sputter-deposited SnO_2 thin films, which are heated at 600^{o}C with a furnace or rapid thermal annealing (RTA). Peak identification confirms these films to be SnO_2. Assessment of the XRD peak widths, using the Scherrer equation and a Lorentzian peak shape, yields an estimated average crystalline size of 11 nm (furnace) and 7.5 nm (RTA), whereas Williamson-Hall plots give average crystal size, strain estimates of 17.1 nm, 0.023 (furnace) and 16.5 nm, 0.036 (RTA) [14,15] Atomic force microscopy (AFM) image of the rapid thermal annealed SnO_2 film reveals averaged feature size of 18 nm.

Figure 9.4 shows the Williamson-Hall plot, $B_r \cos\theta$ *vs.* $\sin\theta$, for the SnO_2 thin film annealed in furnace. Crystallite size and strain can be obtained from the relation of the form

$$B_r \cos\theta = k \lambda / L + \eta \sin\theta$$

, where λ = wavelength of the X-ray, k = generally taken to be 0.9, L = crystallite size, and η = lattice strain. From the slope η and intercept $k \lambda / L$, crystallite size and lattice strain of the film were estimated. B_r was obtained by subtracting the full width at half maximum (FWHM) due to the instrument from the FWHM of the Gaussian peak fitting of the diffraction peak.

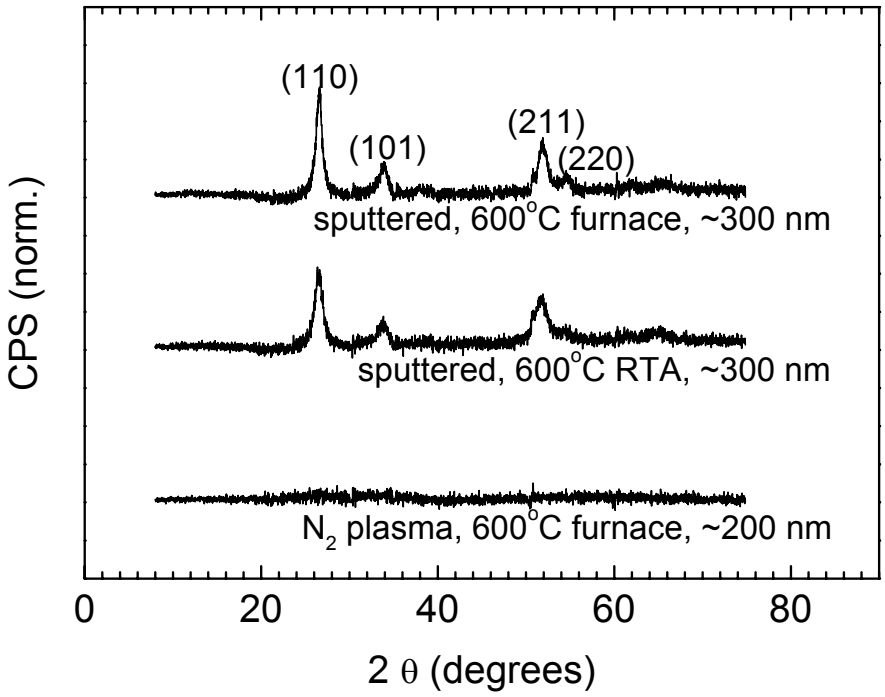

Figure 9.3. XRD patterns obtained from two sputter-deposited SnO_2 thin films which are either furnace or rapid thermal annealed at 600°C, and for a SnO_2 thin film prepared by evaporation of SnO_2 powder in a ~5 x 10^{-4} Torr pressure of icrowave-activated N_2 and subsequently furnace annealed at 600°C. The post-deposition anneal leads to increased crystallinity of the sputtered films, whereas films prepared by activated reactive evaporation in N_2 remain amorphous after annealing.

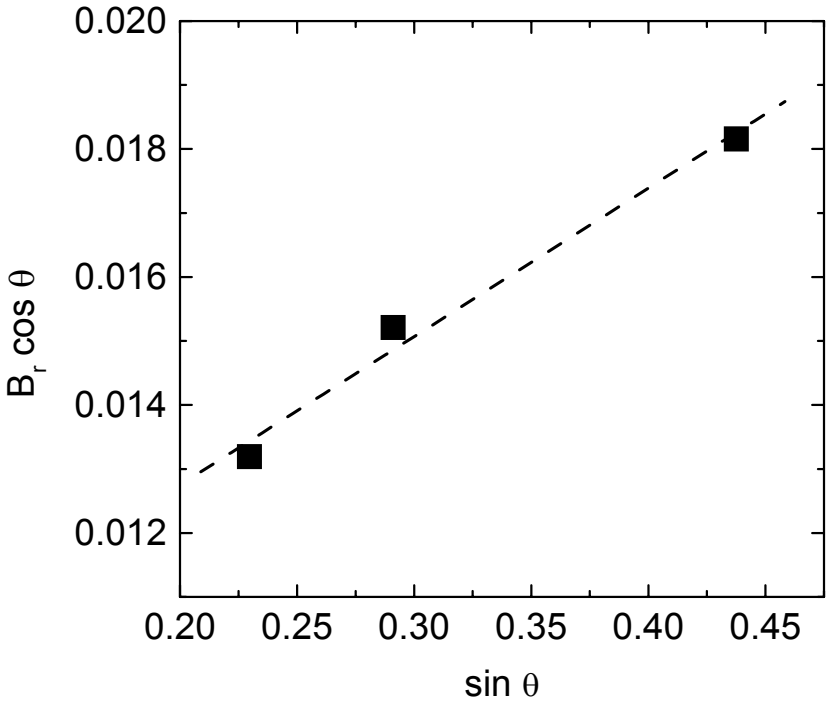

Figure 9.4. Williamson-Hall plot for the SnO_2 thin film annealed in furnace at 600^oC.

Transparent Thin-Film Transistors with Zinc Indium Oxide channel layer

A high mobility, *n*-type transparent thin-film transistor (TTFT) with a zinc indium oxide (ZIO) channel layer has been fabricated [16]. ZIO TTFTs are prepared on Nippon Electric Company glass substrates (NEG OA2) coated with a 200 nm sputtered indium tin oxide (ITO) gate electrode film and a 220 nm atomic layer deposited supperlattice of AlO_x and TiO_x (ATO) [ATO/ITO glass is supplied by Arto Pakkala, Planar systems, Inc. Espoo, Finland, arto_pakkala@planar.com.]. The ITO and ATO layers constitute the gate contact and insulator, respectively, of a bottom gate. The ZIO channel layer (typically ~85 nm) is deposited by RF sputtering, using a target purchased from Cerac, Inc. ($ZnO:In_2O_3$ molar ration is 2:1). Three different process recipes are employed for the ZIO channel layer deposition, as specified in Table 9.3. ITO (typically ~250 nm) source and drain electrodes are deposited via RF magnetron sputtering in Ar (100%). Both the ZIO channel and the ITO source and the drain electrodes are deposited with no intentional heating of the substrate. After ITO source/drain deposition, devices are furnace annealed in air at either 300 or 600^{o}C for 1 hour; alternatively, the R. T. (room temperature) devices are not subjected to a post-deposition anneal.

ZIO TTFTs are highly transparent with ~85% optical transmission in the visible portion of the electromagnetic spectrum. TTFTs annealed at 600^{o}C operate in depletion-mode with threshold voltages ~20 V to -10 V, turn-on voltages ~3 V less than the threshold voltage, peak incremental channel mobilities of ~45 to 55

$cm^2/V\ s$, and drain current on-to-off ratios of $\sim 10^6$. In contrast, ZIO TTFTs annealed at 300°C typically operate in enhancement-mode with threshold voltages of ~0 to 10 V, turn-on voltages ~1 to 2 V less than the threshold voltage, peak incremental channel mobilities of ~10 to 30 $cm^2/V\ s$, and drain current on-to-off ratios of $\sim 10^6$. R.T. ZIO TTFTs exhibit a peak incremental channel mobilities of 8 $cm^2/V\ s$ (17 $cm^2/V\ s$) and a drain current on-to-off ratios of 10^4 (3×10^3) for enhancement-mode (depletion-mode) operation.

TABLE 9.3. RF sputtering and post-deposition annealing process parameters for the three types of zinc indium oxide channel layers used in the fabrication of transparent thin-film transistors. R.T. indicates near room temperature, indicating that no intentional substrate heating or post-deposition annealing is employed.

Annealed temperature (°C)	600	300	R.T.
Ar gas flow (sccm[a])	30	45	15
O_2 gas flow (sccm[a])	3	2	5
Target-substrate distance (cm)	7.5	7.5	10
Pressure (mTorr)	5	5	1-2
Power density ($W\ cm^{-2}$)	2.5	2.5	4.9

[a] standard cubic centimeters per minute

X-ray diffraction data were obtained by using Cu Kα radiation on a Simens D5000 and a Rigaku R-Axis Rapid diffractometer equipped with a curved imaging plate. In the case of Rigaku machine, the radiation was directed through a 0.3 mm pihole collimator onto the sample at an incident angle of 10^{o} relative to the face of the substrate. Data were corrected for the scattering from the substrate. X-ray diffraction patterns of ~200-250 nm zinc indium oxide thin films deposited by RF sputtering are depicted in Figure 9.5 with post-deposition annealing temperatures. X-ray diffraction patterns are consistent with amorphous (or nanocrystalline) films for annealing at temperatures as high as 500^{o}C. In the patterns from the films produced at room temperature and annealed at 500^{o}C the broad peak near 32^{o} corresponds to scattering a dimensions representing metal-metal interatomic distances, while the peak near 58o corresponds to metal-oxygen interatomic distances. Clearly, at 600^{o}C the film has transformed into a crystalline form. There is no evidence in the pattern to indicate that separate phases of ZnO and In_2O_3 have crystallized from the amorphous precursor. The pattern has been compared with those of all known phases in the ZnO-In_2O_3 system [17-19], but no simple match to these phases can be made. This result may not be too surprising, as all of the known materials have been produced from bulk reactions at temperatures above 1000^{o}C. The crystallite size of ZIO films annealed at 500^{o}C is determined to be smaller than 5 nm on the basis of X-ray measurements and use of the Scherrer equation. For the samples annealed at 600^{o}C, X-ray measurements coupled with

atomic-force microscopy reveal that crystallite sizes are primarily distributed in the range of 25-80 nm (Figure 9.6).

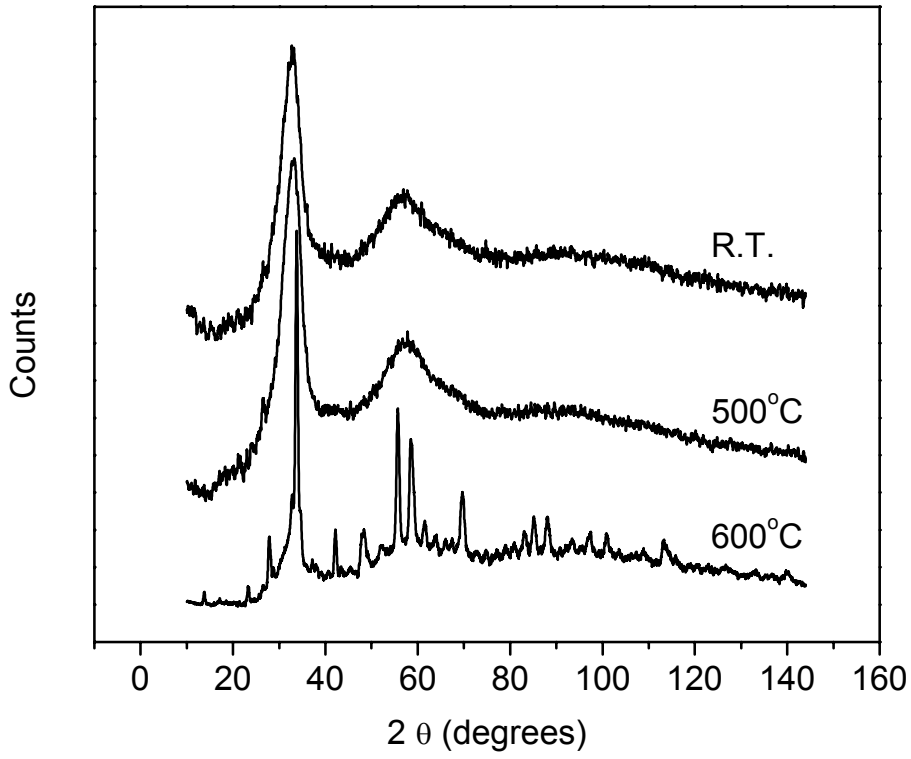

Figure 9.5. X-ray diffraction patterns obtained from ~200-250 nm zinc indium oxide thin films deposited by RF sputtering. The R.T. (room temperature) sample is not annealed, whereas the 500°C or a 600°C samples are post-deposition furnace annealed. The R.T. and 500°C samples are amorphous, while the 600°C sample has transformed into a crystalline form.

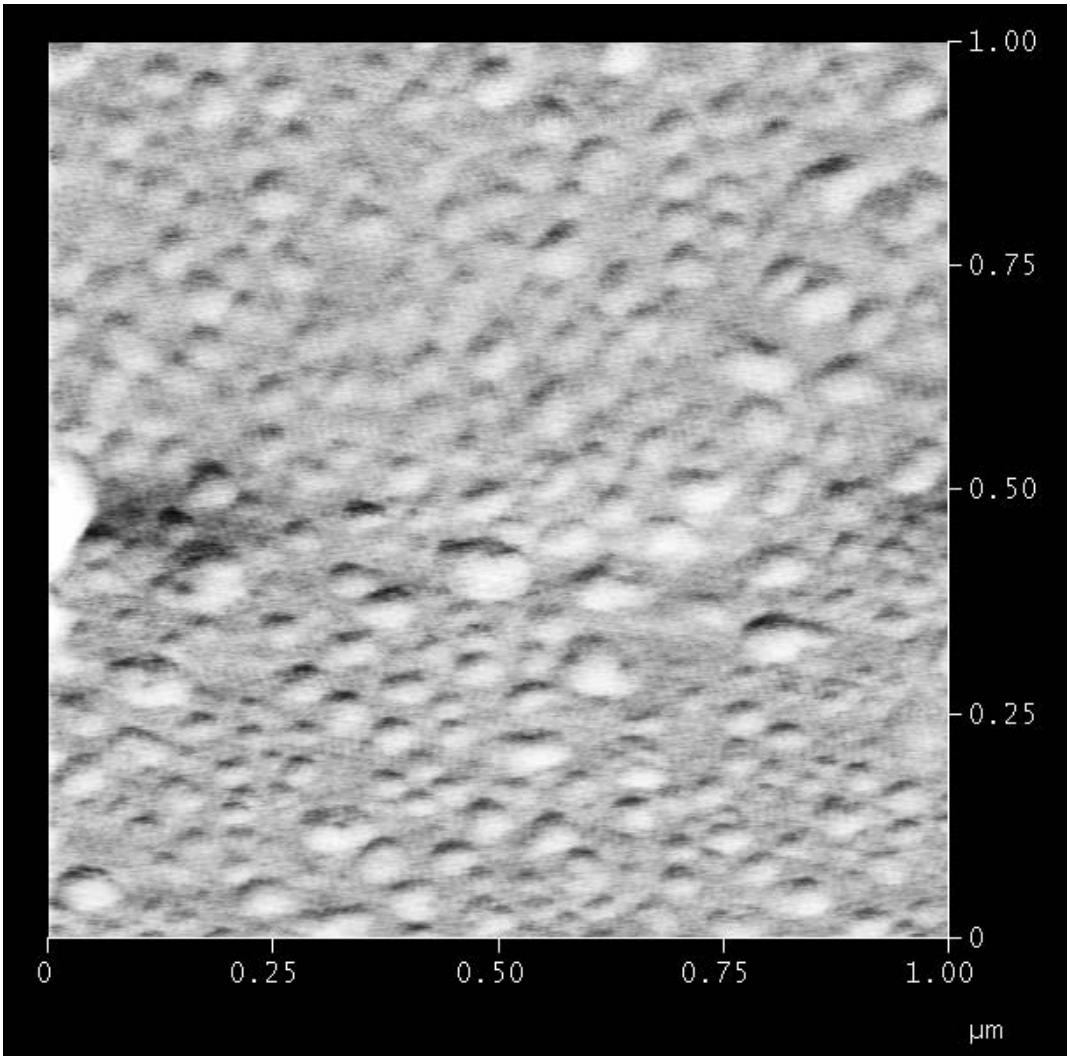

Figure 9.6. Atomic force micrograph of ZIO film annealed at 600^{o}C.

CONCLUSION

New *n*-type transparent conducting oxides of W-doped In_2O_3 and W-doped zinc indium oxide films have been prepared by using PLD; their optical and electrical properties have been examined. $In_{1.95}W_{0.05}O_{3+\delta}$ films on YSZ exhibit mobilities close to 120 cm^2/ V s. Conductivities near 1100 S/cm with 90 % optical transparency have been observed in W-doped ZIO films prepared by using PLD. High-performance tin oxide transparent thin-film transistors and ZIO TTFTs have been prepared and characterized.

ACKNOWLEDGMENTS

This material is based upon work supported by the National Science Foundation under Grant No. DMR-0071727 and by the Army Research Office under Contract No. MURI E-18-667-G3.

REFERENCES

[1] I. Hamberg, and C. G. Granqvist, *J. Appl. Phys.*, **60**, R123 (1986).

[2] T. Minami, *MRS Bull.*, **25(8)**, 38 (2000)T. Minami, *MRS Bull.*, **25(8)**, 38 (2000).

[3] A. J. Freeman, K. R. Poeppelmeier, T. O. Mason, R. P. H. Chang, and T. J. Marks, *MRS Bull.*, **25(8)**, 45 (2000).

[4] J. M. Phillips, R. J. Cava, G. A. Thomas, S. A. Carter, J. Kwo, T. Siegrist, J. J. Krajewski, J. H. Marshall, W. F. Peck, Jr., and D. H. Rapkine, *Appl. Phys. Lett.*, **67(15)**, 2246 (1995)

[5] J.-K. Lee, H.-M. Kim, S.-H. Park, J.-J. Kim, B.-R. Rhee, and S.-H. Sohn, *J. Appl. Phys.*, **92(10)**, 5761 (2002).

[6] S. Masuda, K. Kitamura, Y. Okumura, S. Miyatake, and, T. Kawai, *J. Appl. Phys.*, **93**, 1624 (2003).

[7] R. L. Hoffman, B. J. Norris, and J. F. Wager, *Appl. Phys. Lett.*, **82**, 733 (2003).

[8] P. F. Carcia, R. S. McLean, M. H. Reilly, and G. Nunes, **82**, 11117 (2003).

[9] J. F. Wager, *Science*, **300**, 1245 (2003).

[10] B. J. Norris, J. Anderson, J. F. Wager, and D. A. Keszler, *J. Phys. D*, **36**, L105 (2003).

[11] R. L. Hoffman, *J. Appl. Phys.*, **95**, 5813 (2004).

[12] Y. Hishikawa, N. Nakamura, S. Tsuda, S. Nakano, Y. Kishi, and Y. Kuwano, *Jpn. J. Appl. Phys.*, **30**, 1008 (1991).

[13] R. E. Presley, C.-L. Munsee, C.-H. Park, D. Hong, J. F. Wager, and D. A. Keszler, *J. Phys. D: Appl. Phys.*, **37**, 2810 (2004).

[14] C. Suryanarayana, and M. G. Norton, *X-Ray Diffraction A Practical Approach*, Plenum Press, New York (1998).

[15] B. D. Culliy, and S. R. Stock, *Elements of X-Ray Diffraction*, 3rd ed. (Upper Saddle River, NJ: Prentice-Hall, (2001).

[16] N. L. Dehuff, E. S. Kettenring, D. Hong, H. Q. Chiang, J. F. Wager, R. L. Hoffman, C.-H. Park, and D. A. Keszler, *J. Appl. Phys.*, in press.

[17] T. Moriga, D. D. Edwards, T. O. Mason, G. B. Palmer, K. R. Poepplemeier, J. L. Schindler, C. R. Kannewurf, and I. Nakabayashi, *J. Am. Ceram. Soc.*, **81**, 1310 (1998).

[18] M. Nakamura, N. Kimizuka, and T. Mohri, *J. Solid State Chem.*, **86**, 16 (1990).

[19] V. H. Kasper, *Z. Anorg. Allg. Chemie*, **349**, 113 (1967).

CHAPTER 10

STRONG NEAR INFRARED LUMINESCENCE IN $BaSnO_3$

Cheol-Hee Park, Douglas A. Keszler, Hiroshi Mizoguchi,
and Patrick M. Woodward

Modified version: *Journal of the American Chemical Society*
1155 Sixteenth Street, NW, Washington, DC 20036
vol. 126**(31)**, 9796 (2004)

ABSTRACT

Powdered samples of the perovskite $BaSnO_3$ exhibit strong near-infrared (NIR) luminescence at room temperature, following band-gap excitation at 380 nm (3.26 eV). The emission spectrum is characterized by a broad band centered at 905 nm (1.4 eV), tailing on the high-energy side to approximately 760 nm. The Stokes shift is 1.9 eV, and measured lifetimes in the range 7-18 ms depend on preparative conditions. These extraordinary long values indicate that the luminescence involves a defect state(s). At low temperatures, both a sharp peak and a broad band appear in the visible portion of the luminenescence spectrum at approximately 595 nm. Upon cooling, the intensity of the NIR emission decreases, while the integrated intensities of the visible emission features increase to approximately 40% of the NIR intensity at 77 K. Room-temperature photoluminescence (PL) is observed across the $Ba_{1-x}Sr_xSnO_3$ series. As the strontium content increases, the excitation maximum and band gap shift further into the UV, while the intensity of the NIR emission peak decreases and shifts further into the infrared. This combination leads to an unexpectedly large increase in the Stokes shift. The unusual NIR PL in $BaSnO_3$ may originate from recombination of a photogenerated valence band hole and an occupied donor level, probably associated with a Sn^{2+} ion situated roughly 1.4 eV above the valence-band edge.

INTRODUCTION

Main-group ions with ns^2 electronic configuration, such as Tl^+, Pb^{2+}, Sb^{3+}, Bi^{3+}, and Au^-, are well-known for their luminescent properties. As a rule, they exhibit strong absorption in the ultraviolet (UV) with emission in the UV and visible regions of the spectrum [1]. They are among the more interesting classes of luminescent ions, because both the absorption and emission are highly sensitive to changes in the crystal environment of the ns^2 ion. Considerable research has been devoted to the study of luminescence properties of such ions when doped into insulating hosts, due in part to their technological importance. Some important examples include NaI:Tl^+, which is a commercial X-ray scintillation phosphor (emission maximum ~ 415 nm); $Bi_4Ge_3O_{12}$, which is used as a scintillator in the detection of X-rays and other high-energy particles (Bi^{3+} emission maximum ~ 480 nm); and $Ca_5(PO_4)_3(Cl,F):Sb^{3+}$, Mn^{2+}, which is widely used as a fluorescent lamp phosphor (Sb^{3+} emission maximum ~ 490 nm). The electronic relaxation that leads to luminescence is usually ascribed to a transition from an ns^1np^1 excited state to an ns^2np^0 ground state [2]. The energy levels of the valence *s* and *p* orbitals of the ns^2 ion are sensitive to ligand field effects, consequently the emission wavelength is sensitive to the local coordination environment of the ns^2 ion. The Stokes shift tends to be large when the ground-state ion has an asymmetric environment, associated with the stereoactive electron lone-pair distortion commonly seen for ns^2 ions, and the excited state adopts a symmetric environment in the ns^1np^1

configuration. As an example, the Stokes shifts for Bi^{3+} emission from the regular, octahedral dopant sites in the perovskites $LaGaO_3:Bi^{3+}$ and $LaInO_3:Bi^{3+}$ are rather small (roughly 0.75 eV or 6000 cm^{-1}) [2], whereas the Stokes shift is much larger (2.38 eV or 19,000 cm^{-1}) in $LaPO_4:Bi^{3+}$, where the asymmetric Bi^{3+} environment has been confirmed by EXAFS [3]. Large Stokes shifts can also be observed when the luminescence involves relaxation from a so-called D-level excited state. The exact details of the D-level excited state are not completely understood, but it is thought to involve some degree of charge transfer from the luminescent ion to the surrounding host lattice [4].

Even though the luminescent properties of ns^2 ions have been extensively studied, luminescence in the near infrared (NIR) region has not been observed. To obtain luminescence in the NIR region, transition-metal ion centers, such as chromium, are typically required [5]. In this paper we report the observation of strong room-temperature luminescence at 905 nm in $BaSnO_3$. The luminescence does not seem to be associated with impurities and seems likely to involve Sn^{2+} ions. Previous reports regarding the luminescence of Sn^{2+} in oxide hosts show emission wavelengths falling in the 300-700 nm range [6]. Thus, the observed wavelength for luminescence in $BaSnO_3$ is considerably longer than expected. There have been some previous reports of fluorescence in $BaSnO_3$ [7]; however, it seems that the study of photoluminescence (PL) in $BaSnO_3$ has been largely overlooked because of the unexpectedly long emission wavelength. In this article

we report PL properties of $BaSnO_3$ and the $(Ba_{1-x}Sr_x)SnO_3$ ($0 \leq x \leq 1$) solid solution, and we speculate on the origin of this unusual PL.

EXPERIMENTAL

Samples for the $(Ba_{1-x}Sr_x)SnO_3$ ($0 \leq x \leq 1$) solid solution were synthesized by solid-state reaction at elevated temperature. SnO_2 (99.9%, Fisher), $BaCO_3$ (99.4%, Mallinckrodt), and $SrCO_3$ (99.9+%, Aldrich) were used as reagents. These materials were mixed with ethanol and ground in an alumina mortar and pestle. The mixture was first calcined at 1470 K for 10 h in air to decompose the carbonates. After this initial firing, the products were ground, pressed into pellets, and heated at 1720 K for 15 h in air. For some luminescence measurements, samples of $(Ba_{1-x}Sr_x)SnO_3$ were also synthesized at 1473 K in a similar manner with the reagents SnO_2 (99.9%, Cerac or 99.996%, Alfa), $BaCO_3$ (99.9%, Cerac), and $SrCO_3$ (99+%, Alfa). Hydrothermal conditions were also used for the low-temperature synthesis of $BaSnO_3$. Source materials, $BaCl_2{\cdot}2H_2O$ (Mallinckrodt) and $K_2Sn(OH)_6$ (99.9%, Aldrich), were placed with water in a Teflon lined autoclave and kept at 360 K for 1 day. Small single crystals were obtained; they were collected by filtration, washed twice with water and once with acetone, and then dried at 320 K in air. These crystals were identified as $BaSn(OH)_6$ from both powder and single-crystal X-ray diffraction (XRD) methods. These hydroxide

samples were heated in air at various temperatures for 1 h, leading to loss of water and the formation of $BaSnO_3$ powder. Powders of $BaSn(OH)_6$ were also prepared by first dissolving $BaCl_2 \cdot 2H_2O$ (High Purity Chemicals) and $SnCl_4 \cdot 5H_2O$ (98%, Alfa) in deionized water (0.6 M in each cation) and then adding to an equivalent volume of 8 M NaOH to form a precipitate. The resulting white powder was collected, rinsed several times with deionized water, and dried at 405 K for 2 h. The final product was identified as $BaSn(OH)_6$ on the basis of XRD measurements. The chemical composition of the samples was also confirmed by using energy dispersive X-ray analysis (EDX). The phase purity was confirmed, and a structure analysis was completed with laboratory X-ray powder diffraction (XRPD). A Bruker D8 diffactometer (40 kV, 50 mA) was used to collect the XRPD data. It is equipped with a Braun linear position sensitive detector and an incident beam Ge 111 monochromator for selection of Cu $K\alpha_1$ radiation. The Rietveld method [8], as implemented in the TOPAS software package [9], was used for the structural analysis of the XRPD data. UV-VIS-NIR diffuse reflectance data were collected over the spectral range 240-2600 nm by using a Perkin-Elmer Lamda 900 double-beam spectrometer with MgO as the reference material. The data were transformed into absorbance with the Kubelka-Munk function. For characterization of defect centers, electron-spin-resonance (ESR) spectra were collected at 300 K with a Bruker ESP300 X-band spectrometer. The *g* values of signals were calibrated by using the signal of DPPH ($g = 2.0036$) as an internal standard.

PL measurements were made with an Oriel 300-W Xe lamp and a Cary model-15 prism monochromator for excitation. For detection, emitted light was passed through an Oriel 22500 1/8-m monochromator and monitored with a Hamamatsu R636-10 photomulitplier tube (PMT) over the range 400 – 950 nm and a Hamamatsu R1767 PMT over the range 700 – 1200 nm. Each spectrum was corrected for the throughput and response of the system with Rhodamine B and a standardized W lamp. Variable-temperature spectra were recorded by using a Cryo Industries R102 flow cryostat equipped with a Conductus temperature controller. Lifetime data were obtained with a Q-switched, Quanta-Ray Nd:YAG laser equipped with a frequency-mixing crystal to provide excitation at 355 nm; the pulse width (FWHM) of the laser was measured as 10 ns. The sample emission signal was detected with a PMT that was connected to a 500-MHz Tektronix digital oscilloscope (Model TDS350) and interfaced to a PC for data collection. Emission lifetimes were determined from natural log plots of the decay curves.

RESULTS

X-ray powder diffraction and EDX measurements confirm that single-phase perovskite samples can be successfully prepared for the entire $(Ba_{1-x}Sr_x)SnO_3$ solid solution via conventional solid-state synthetic methods [10]. Those samples that are rich in Ba as well as the $SrSnO_3$ sample are white, while the x = 0.6 and 0.8

samples have a dull yellow color. Lattice constants obtained from Rietveld refinements are illustrated in Figure 10.1.

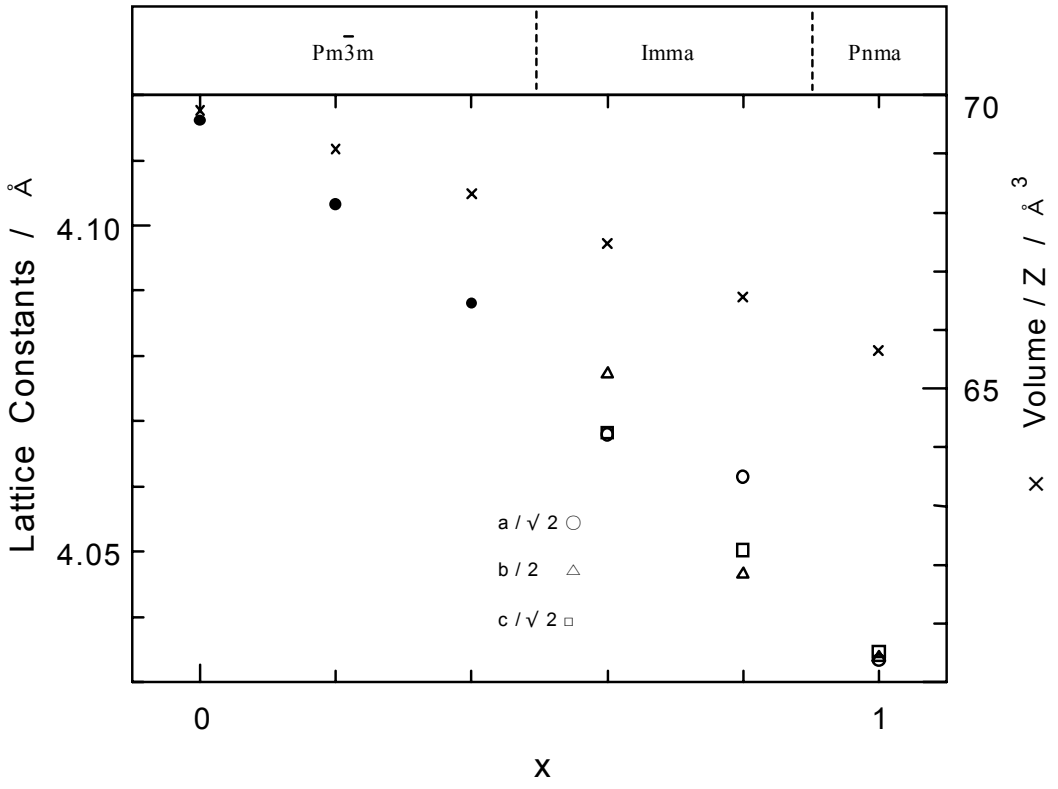

Figure 10.1. The lattice constants and cell volume per molecular unit for $(Ba_{1-x}Sr_x)SnO_3$ solid solution.

As the size of the alkaline-earth cation decreases, the space-group symmetry evolves from *Pm-3m* (x = 0, 0.2, 0.4) to *Imma* (x = 0.6) to *Pnma* (x = 0.8, 1.0). The symmetry lowering is caused by tilting of the Sn^{4+}-centered octahedra in response to the increasing mismatch in the fit of the alkaline-earth cation to the dodecahedral cavity in the corner-sharing octahedral network. This effect is very common and well understood in perovskites [11]. The optical absorbance, as measured by diffuse reflectance spectroscopy, and the optical band-gap values extracted from these spectra are shown in Figure 10.2. $BaSnO_3$ is a semiconductor with an indirect band gap [12] of 3.1 eV, whereas, $SrSnO_3$ has larger band gap of 4.1 eV. The samples with x = 0.6 or 0.8 exhibit a weak absorption around 3 eV, which gives rise to the yellowish appearance. The origin of this feature is not fully understood, although the yellowish tinge can be removed by treatment in H_2. The band gap of the solid solution changes systematically as a function of Sr^{2+} content, while the unit-cell volume approximately obeys Vegard's law. The band-gap increase can be traced to the effects of octahedral tilting. In $BaSnO_3$, the conduction-band minimum is predominantly non-bonding Sn 5s character, due to the translational symmetry restrictions of the cubic perovskite structure. Octahedral tilting lowers the symmetry to orthorhombic and distorts the linear Sn–O–Sn bonds. As the Sn–O–Sn bonds become increasingly bent the Sn 5s non-bonding character of the conduction band minimum is lost and antibonding Sn 5s-O 2p contributions become increasingly important. This pushes up the energy of the conduction band minimum, resulting in a narrowing of the conduction band and

a corresponding increase in the band gap. Details of this mechanism have been described in greater detail in a recent publication [12].

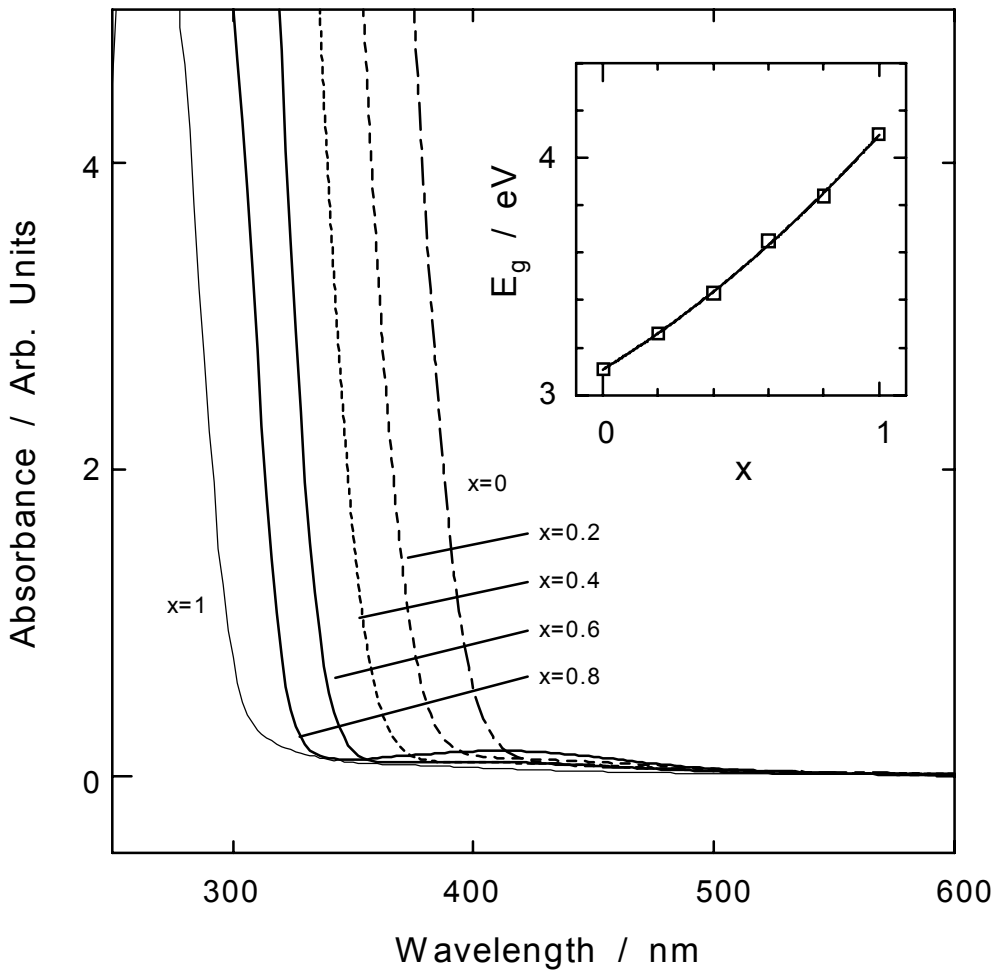

Figure 10.2. Optical absorption spectra of $(Ba_{1-x}Sr_x)SnO_3$ at 300 K. The band gap estimated is shown in the inset.

PL spectra for $(Ba_{1-x}Sr_x)SnO_3$ at 300 K are given in Figure 10.3(a). The PL is most intense in $BaSnO_3$, which exhibits a broad, strong luminescence centered at 905 nm. The emission peak tails to approximately 760 nm; no PL can be visually observed. The Stokes shift is 1.9 eV, and the lifetime ranges from 7 to 18 ms, depending on method and temperature of preparation. These extraordinarily long values suggest that the luminescence involves a defect state(s). As x increases, the central wavelength of luminescence shifts to longer wavelengths, reaching a value of 970 nm in $SrSnO_3$. It is somewhat surprising to see a red shift of the luminescence peak at the same time that the band gap is steadily increasing. Obviously this leads to a significant increase in the Stokes shift. At the same time, the luminescence intensity decreases to roughly 10% of the value seen in $BaSnO_3$; normalized excitation spectra are shown in Figure 10.3(b). The shift to higher excitation energies with increasing Sr content mirrors that of the band-gap variation shown in the inset of Figure 10.2. The correspondence between these two results implies that the initial excitation is a transition from the valence to the conduction band.

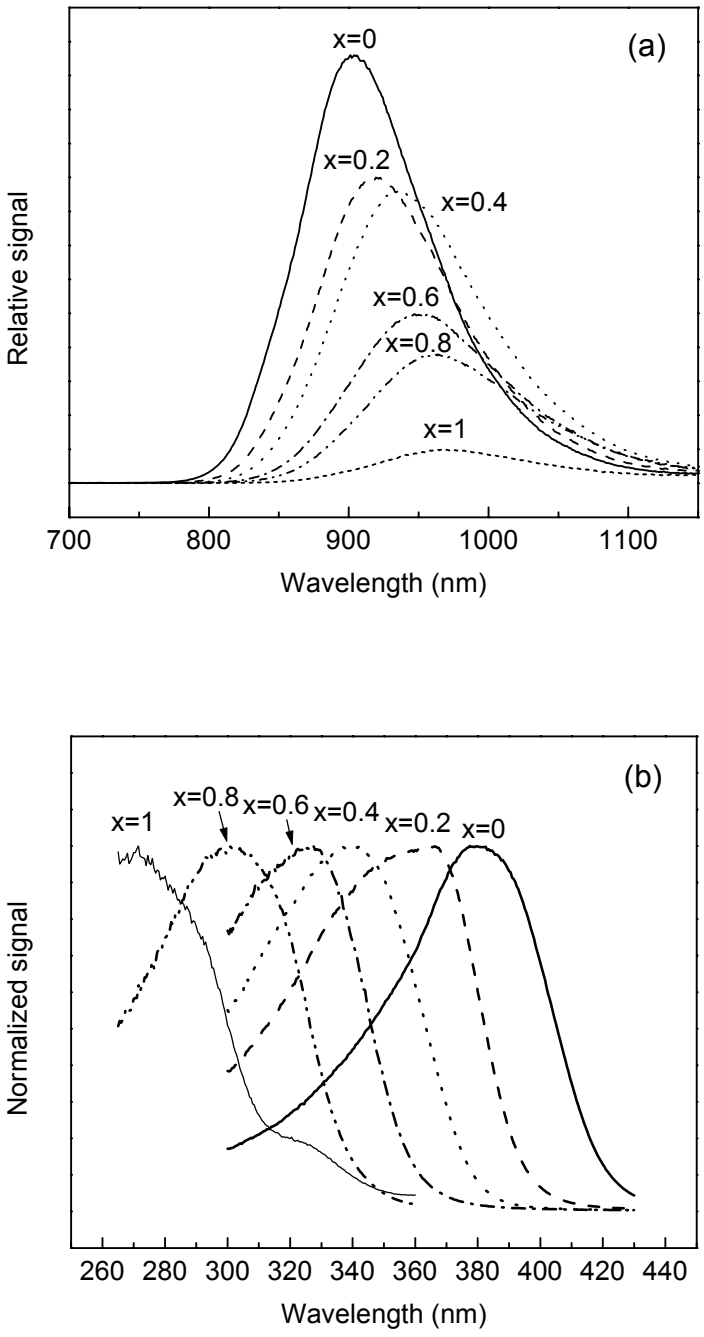

Figure 10.3. (a) Luminescence spectra and (b) excitation spectra of $(Ba_{1-x}Sr_x)SnO_3$ at 300 K.

Luminescence spectra for $BaSnO_3$ at various temperatures are provided in Figure 10.4. The intensity of the 905-nm peak decreases as the temperature decreases. Below 190 K, both sharp and broad peaks appear in the visible region near 595 nm. Unlike the NIR luminescence, the intensity of the visible PL peak increases with decreasing temperature, so that at 77 K its integrated intensity is approximately 40% of that of the NIR band. Assuming a minimal change in the optical band gap with temperature, the Stokes shift of the NIR PL peak increases by roughly 0.6 eV upon cooling from 300 to 77 K.

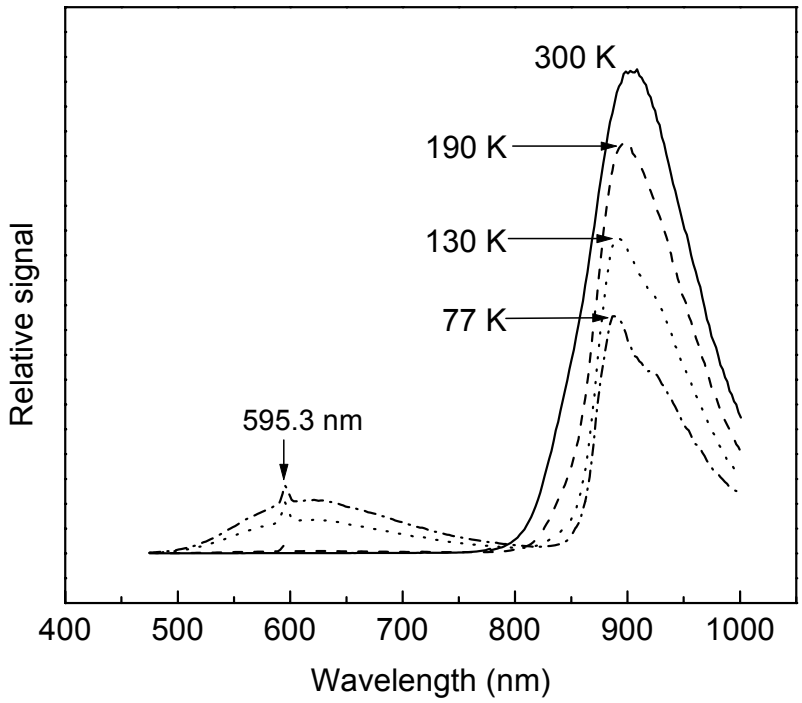

Figure 10.4. Luminescence spectra of $BaSnO_3$ made by solid state reaction measured at various temperatures.

The lattice constants of $BaSnO_3$ samples made by thermal decomposition of the hydrothermal $BaSn(OH)_6$ crystals are shown in Figure 10.5. As the annealing temperature increases, the unit-cell edge and lattice strain decrease systematically. Strain was estimated from the peak broadening seen in the XRPD patterns. Numerical estimates of the strain were obtained by fitting the peak shape with fundamental parameters [9] in the course of carrying out the Rietveld refinements. The strain and unit-cell edge attain values similar to samples made via solid-state reaction upon annealing above 1270 K. The evolution of the unit-cell edge with increasing decomposition temperature agrees with the very recent report by Buscaglia, Leoni, Viviani, *et al.* on $BaSn(OH)_6$ made by wet-chemical processing [13]. The crystallite size is not very sensitive to changes in the annealing temperature. In terms of the optical properties, we note that the hydrothermal $BaSn(OH)_6$ samples exhibit luminescence only after decomposition above 1270 K. For the directly precipitated $BaSn(OH)_6$ powders, luminescence is observed from samples decomposed at temperatures as low as 775 K. All of the samples derived from the hydroxide precursor and heated for 1 h exhibit a luminescence brightness that is approximately 25% of that of the samples prepared by solid-state methods. After annealing the $BaSnO_3$ materials derived from $BaSn(OH)_6$ for five hours at 1573 K, the luminescence brightness exceeds that observed for the solid-state preparations without any noticeable change in particles size or shape. This result indicates that the NIR luminescence in $BaSnO_3$ is a bulk rather than surface phenomenon, since its emission intensity is not a function of its particle size;

particles prepared at 1723 K by solid-state methods are larger than those prepared at 1523 K, but they exhibit similar emission intensities.

Electron spin resonance (ESR) measurements on $BaSnO_3$ powders were carried out at 300 K to probe for the formation of the luminescence center at various thermal-decomposition temperatures. Signals from Mn^{2+} or Cr^{3+} ions, which are known to be luminescent centers, were not detected. The sample made at 1720 K, however, did exhibit a very weak signal that we attribute to Mn^{4+}. The presence of manganese is thought to originate from one of the furnaces used for synthesis, judging from the fact that the sample made at 1470 K in a different furnace did not contain the same ESR signal. To investigate the possibility that manganese contamination might be linked to the photoluminescence in some way, $Ba(Sn_{1-x}Mn_x)O_3$ (x = 0.001, 0.005, and 0.01) samples were intentionally prepared. These samples did not show any NIR luminescence. A sample of $Ba(Sn_{0.99}Cr_{0.01})O_3$ was also prepared and found not to exhibit photoluminescence at room temperature. The sample annealed at 1720 K exhibited a complicated ESR spectrum. Signals were found corresponding to g values of 1.76 and 2.005. The g = 1.76 signal is ascribed to free carriers, whereas g = 2.005 is thought to correspond to a localized electron. The complicated shape of the latter signal implies that the wavefunction of the unpaired electron (at either 300 or 110 K) extends over multiple but finite number of tin sites (^{115}Sn I=1/2 (N. A.=0.35%), ^{117}Sn I=1/2 (N. A.=7.61%), ^{119}Sn I=1/2 (N. A.=8.58%)). The sample annealed at 1270 K also shows NIR-luminescence (see Figure 10.5), but it does not show the same ESR signal as seen

in the 1470 K sample. Thus, it would appear as though the ESR center may not be directly related to the luminescence center. Further study is necessary to fully understand the origins of the ESR signals.

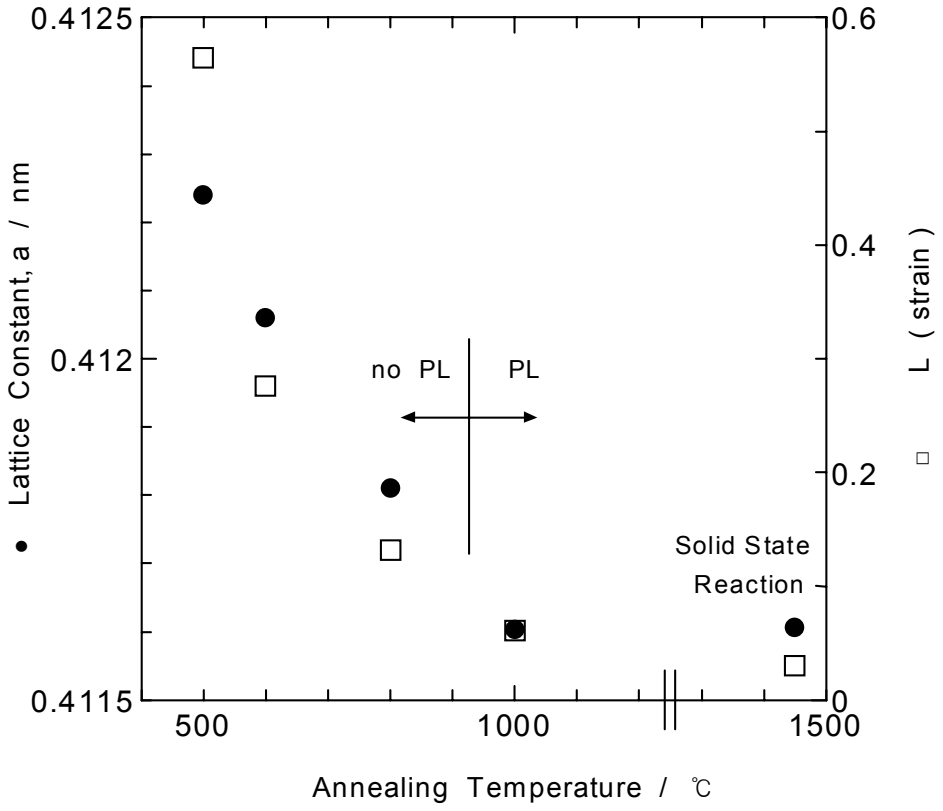

Figure 10.5. The annealing temperature dependences of lattice constant and strain for $BaSnO_3$ made by the thermal decomposition of $BaSn(OH)_6$.

DISCUSSION

Let us consider the origins of luminescence of $BaSnO_3$ and its unusually long-wavelength emission at room temperature. The fact that luminescence is only observed in samples treated at high temperature, along with the long lifetime of the excited state, suggest that strong room-temperature PL is associated with a defect in the material. Furthermore, the large Stokes shift is not consistent with self-luminescent exciton recombination, and there is no evidence to suggest that extrinsic impurities are responsible for the luminescence either. In addition to the ESR and doping studies that seem to rule out the possible role of Mn^{2+} and Cr^{3+}, we found almost identical luminescence from $BaSnO_3$ samples prepared in four different manners: (a) samples prepared at Oregon State University from 99.996% pure SnO_2, (b) samples prepared at Ohio State University from reagent grade SnO_2 and $BaSnO_3$, (c) samples prepared from high-temperature annealing of single-crystal $BaSn(OH)_6$ precursors, and (d) samples prepared from precipitated $BaSn(OH)_6$ powders. Therefore, we conclude that the unusual luminescence in the NIR region originates from an intrinsic defect center or centers in $BaSnO_3$. The most likely scenario is that high-temperature annealing creates oxygen vacancies, which are at least partially charge compensated by the creation of reduced Sn^{n+} sites ($n < 4$).

An important distinction between $BaSnO_3$ and other materials containing Sn^{2+} luminescent centers is the fact that $BaSnO_3$ is a semiconductor rather than an

insulator. Reasonably good electronic conductivity has been observed in *n*-doped $BaSn_{1-x}Sb_xO_3$ samples [14]. This fact raises the possibility that the luminescent behavior of $BaSnO_3$ is based on a mechanism different from intra-atomic excitation and recombination of an isolated ns^2 ion in an insulating host. As the value of x increases across the $(Ba_{1-x}Sr_x)SnO_3$ solid solution the changes in the band gap, as measured by diffuse reflectance methods (Figure 10.2), correspond very well to changes in the PL excitation wavelength (Figure 10.3(b)). This observation is strong evidence that the electronic excitation that ultimately leads to PL is excitation of an electron from the valence to the conduction band, particularly on the Ba-rich side of the solid solution. From this observation, it is not unreasonable to infer that the PL observed in $BaSnO_3$ may have similarities to the behavior of classic semiconductor phosphors such as $ZnS:Cu^+$ or $ZnS:Ag^+$, where the radiative transition is from the conduction band into an impurity-based acceptor level located in the band gap. Unfortunately, application of this model to the $Ba_xSr_{1-x}SnO_3$ system is not consistent with the fact that strontium substitution increases the band gap significantly, while at the same time leading to a red shift in the emission spectrum. However, a blue shift in the emission line would not necessarily be expected if the luminescence involves radiative recombination of a valence band hole and an occupied donor level located in the gap, such as Sn^{2+}. It is known that the increase in band gap for $ASnO_3$ perovskites can be traced primarily to a decrease in the width of the conduction band [12]. Therefore, in response to octahedral tilting, it is realistic to expect that the valence-band maximum will

remain largely O 2p nonbonding and at roughly the same energy level. Furthermore, the occupied 5s orbital of a Sn^{2+} ion would appear in the gap. Density functional theory calculations show that in SnO the occupied Sn 5s-5p hybrid states fall at an energy roughly ~1.0 eV above the top of the O 2p band [15], so that a Sn^{2+} 5s $\rightarrow$ VB emission at a wavelength of ~1.4 eV is of the right order of magnitude for such a radiative recombination process. The decreased PL efficiency that occurs either on doping with Sr^{2+} (figure 10.3(a)) or on lowering the temperature could originate from the reduced carrier mobility that would result from bending the Sn–O–Sn bonds in the former case and from a model based on polaronic hole transport in the latter case. Another piece of evidence consistent with this model is the observation that purposely n-doped $BaSn_{1-x}Sb_xO_3$ exhibits negligible room temperature luminescence. One questionable feature of this hypothesis is the fact that hole mobility in such oxides are normally quite small. However, the positively charged hole will be attracted to the negative site potential of a Sn^{2+} ion on a Sn^{4+} site, and it is conceivable that only holes generated within a few jumps of a Sn^{2+} center contribute to the PL. The need for a photogenerated hole to migrate to and recombine with a Sn^{2+} center is consistent with the long lifetime.

The origin of the low-temperature emission centered at 595 nm is not clear yet. One possibility is that the peak at 595 nm in BaSnO3 may originate from self-trapped exciton luminescence associated with isolated Sn^{2+} centers or those associated with isolated Sn^{2+} centers [16] or those associated with oxygen

vacancies. However, the relatively long wavelength of the visible emission casts considerable doubt on this assignment. Another possibility is that this PL is associated with conduction-band electrons trapped on oxygen vacancy sites. Measured decay curves in this emission region cannot be fit with a single exponential, but a fast component of 10 μs is observed.

CONCLUSION

In conclusion, further study is needed to conclusively determine the origin of the interesting PL in $BaSnO_3$. There can be no doubt, however, that strong room temperature near-IR luminescence occurs in this material. Photoluminescence in the near IR is a very unusual feature among oxides containing main group ions. The initial characterization points toward a model based on recombination of a photogenerated valence band hole and an occupied donor level situated roughly 1.4 eV above the valence band edge. This type of oxide semiconductor luminescence based on hole recombination is rare. It would seem to be favored in this case by the high covalency of the Sn^{4+}–O bond and the linear O–Sn–O geometry. Furthermore, it is rare to find a material that can be doped so as to become either an electrical conductor or a strongly luminescencent material. This opens the possibility that NIR electroluminescent thin-film devices based on $BaSnO_3$–

$BaSnO_{3-x}$–$BaSn_{1-x}Sb_xO_3$ heterostructures could be constructed. The lattice matching would be excellent and it is possible that efficient devices could be fabricated.

ACKNOWLEDGEMENTS

We thank Dr. C. Turro for help with the photoluminescence measurements, Dr. G. D. Renkes for help with the XRD and ESR measurements, and Dr. R. L. McCreery and A. Nowak for help with the use of a spectrophotometer at Ohio State University. We also thank D. Podkoscielny for the synthesis of two of the $BaSnO_3$ samples and Dr. J. W. Nibler for assistance with the lifetime measurements.

REFERENCES

[1] H. W. Leverenz, *An introduction to luminescence of solids*, John Wiley & Sons, New York (1950).

[2] A. M. Srivastava, *Mater. Res. Bull.*, **34**, 1391 (1999).

[3] F. B. M. Van Zon, D. C. Koningsberger, E. W. J. L. Oomen, and G. Blasse, *J. Solid State Chem.*, **71**, 396 (1987).

[4] H. F. Folkerts, F. Ghianni, and G. Blasse, *J. Phys. Chem. Solids*, **57**, 1659 (1996).

[5] For example, H. Eilers, U. Hommerich, S. M. Jacobson, W. M. Yen, K. R. Hoffmann, and W. Jia, *Phys. Rev. B*, **49**, 15505 (1994).

[6] For example, T. Miyata, T. Nakatani, T. Minami, *J. Lumin.*, **87-89**, 1183 (2000).

[7] For example, K.-Th. Wilke, *Z. Phys. Chem. (Leipzig)*, **208**, 361 (1958).

[8] R. A. Young, *The RIETVELD method*, Oxford University Press, London (1995).

[9] R. W. Cheary and A. A. Coelho, *J. Appl. Cryst.*, **25**, 109 (1992).

[10] A. J. Smith, and A. J. E. Welch, *Acta Cryst.*, **13**, 653 (1960).

[11] P. M. Woodward, *Acta Cryst. B*, **53**, 44 (1997).

[12] H. Mizoguchi, H. W. Eng, and P. M. Woodward, *Inorg. Chem.*, **43**, 1667 (2004).

[13] M. T. Buscaglia, M. Leoni, M. Viviani, V. Buscaglia, A. Martinelli, A. Testino, and P. Nanni, *J. Mater. Res.*, **18**, 560 (2003).

[14] R. J. Cava, P. Gammel, B. Batlogg, J. J. Krajewski, W. F. Peck, Jr., L. W. Rupp, Jr., R. Felder, and R. B. Dover, *Phys Rev. B*, **42**, 4815 (1990).

[15] G. W. Watson, *J. Chem. Phys.*, **114**, 758 (2001).

[16] H. Donker, W. M. A. Smit, and G. Blasse, *Phys. Stat. Sol. B*, **148**, 413 (1988).

CHAPTER 11

LUMINESCENCE OF $BaSnO_3$ FROM $BaSn(OH)_6$

Cheol-Hee Park and Douglas A. Keszler

submitted to *Materials Research Bulletin*
660 White Plains Road, Tarrytown, NY 10591-5153

ABSTRACT

Powder samples of $BaSnO_3$ were prepared by decomposing $BaSn(OH)_6$ at various temperatures between 623 K and 1723 K for 1 h and at 1573 K for periods of 20 min, 1 h, and 5 h. An increase in crystallite size was observed with increasing decomposition temperature and time. Crystallite sizes calculated from Williamson-Hall plots of X-ray data were compared with transmission-electron-microscope images. An increase in luminescence brightness of $BaSnO_3$ with increasing crystallite size was observed, which can be attributed to a decrease in the ratio of the surface area to the bulk volume and a reduction in the probability for photo generated holes to nonradiatively recombine at surface defect sites.

.

INTRODUCTION

Perovskite $BaSnO_3$ has received much attention because of its high chemical and thermal stability and attractive dielectric properties [1-5]. It is applied as a component of ceramic dielectric bodies and derivatives containing Ti, $Ba(Sn,Ti)O_3$, are used as gas, vapor, and humidity sensors. Barium stannates are also investigated for transparent conductor applications because of its large band gap (3.1 eV) and Sn^{4+} ions with $(n\text{-}1)d^{10}ns^0$ electron configuration [6]. Recently strong near-infrared (NIR) luminescence has been observed in $BaSnO_3$ under ultraviolet excitation at room temperature [7]. The emission band is centered at about 905 nm, and its lifetime varied from 7 to 18 ms, depending on preparative conditions. The luminescence is observed both in samples prepared by thermally decomposition of $BaSn(OH)_6$ and by high temperature solid-state synthesis from oxides. For the directly precipitated $BaSn(OH)_6$ powders, luminescence is observed from samples decomposed at temperatures as low as 775 K, and the brightness of this luminescence increases at higher annealing temperatures without any clear change in particle size and shape. In this contribution, we demonstrate that the emission brightness of $BaSnO_3$ is correlated to crystalline size.

EXPERIMENTAL

Samples of $BaSnO_3$ were prepared by decomposing $BaSn(OH)_6$ powders at 623, 773, 973, 1173, 1373, 1573, and 1723 K. $BaSn(OH)_6$ powders were placed in an alumina crucible, heated to the selected temperature with a ramp rate of 10 K/min, soaked for 1h; the furnace was then turned off to allow the products to cool to room temperature. Three more samples of $BaSnO_3$ were prepared by separately heating powders of $BaSn(OH)_6$ at 1573 K: one for 20 min, one for 1 h, and one for 5 h.

Powders of $BaSn(OH)_6$ were obtained by first dissolving $BaCl_2 \cdot 2H_2O$ (High Purity Chemicals) and $SnCl_4 \cdot 5H_2O$ (98%, Alfa) in de-ionized water (0.6 M in each cation) and then adding the resulting solution to an equivalent volume of 8 M NaOH solution. The products, white powders, were collected, rinsed several times with de-ionized water, dried at 405 K for 2 h, and characterized by using powder X-ray diffraction (Siemens D5000 diffractometer, Cu$K\alpha$ radiation).

The average crystalline sizes of the samples were calculated by using Williamson-Hall plots [8]. In_2O_3, annealed at 1273 K, was used to establish instrumental broadening and full width at half maximum (FWHM) of each diffraction line was calculated by using Gaussian curve fitting. For some samples Le Bail fitting [9] was also used to derive crystallite-size information. For Le Bail fitting, X-ray powder diffraction patterns of $BaSnO_3$ samples were collected over a

2θ range of 10-150^{o} at the room temperature and refined by using the Fullprof program [10].

PL measurements were made with an Oriel 300-W Xe lamp and a Cary model-15 prism monochromator for excitation. For detection, emitted light was passed through an Oriel 22500 1/8-m monochromator and monitored with a Hamamatsu R636-10 photomulitplier tube (PMT) over the range 400-950 nm and a Hamamatsu R1767 PMT over the range 700-1200 nm. Each spectrum was corrected for the throughput and response of the system with Rhodamine B and a standardized W lamp.

To compare relative brightness from different samples, an Oriel 6035 Hg lamp was used as an excitation source. Emission light was collected at the right angle to excitation, passed through a UV filter, and detected with a Hamamatsu R636-10 PMT.

Thermogravimetric analysis and differential scanning calorimetry were carried out by using Shimadzu TGA-50 and DSC-50 instruments, respectively; flowing N_2(g) was employed with heating and cooling rates of 5 K/min.

Microstructures and morphology of samples were investigated by scanning electron microscopy (SEM; AmRay 3300FE) and transmission electron microscopy (TEM; Philips CM12 STEM).

RESULTS AND DISCUSSION

As seen from the TGA curve in Figure 11.1, a mass loss of 15.0% occurs on heating $BaSn(OH)_6$ to 964 K. This loss is comparable to the 15.1% change associated with the decomposition reaction

$$BaSn(OH)_6(s) \rightarrow BaSnO_3(s) + 3H_2O(g)$$

and the loss of H_2O. At the 5 K/min heating rate most of the mass loss, 13.4%, occurs in the temperature range 473-673 K. In the DSC trace, the onset of the endothermic peak occurs at about 473 K, which also corresponds to the onset of the mass loss, agreeing with the report by Buscaglia, Leoni, Viviani, *et al.* on the dehydration of $BaSn(OH)_6$ [2].

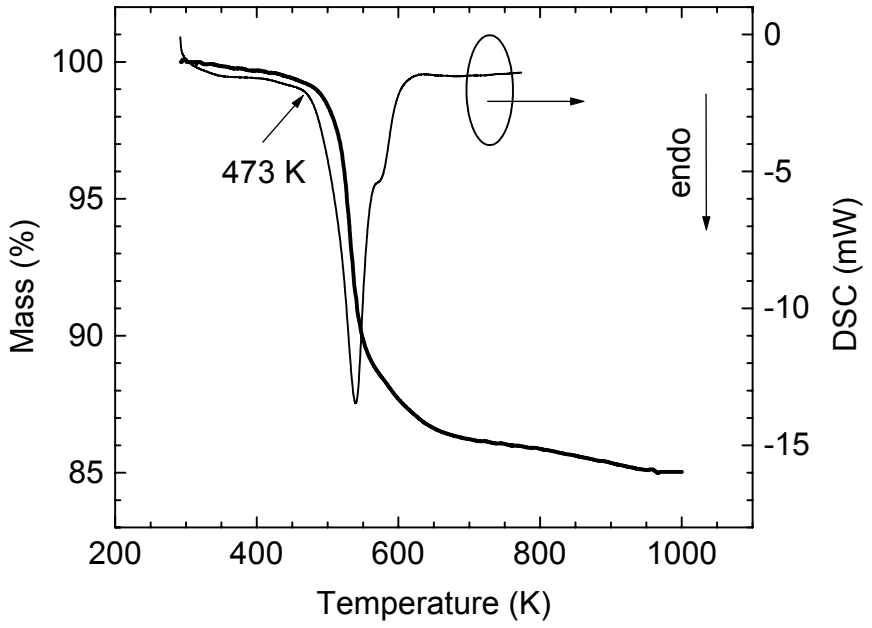

Figure 11.1. TGA (thick solid line) and DSC (thin solid line) curves for powdered $BaSn(OH)_6$ with heating rate of 5 K/min in N_2 atmosphere.

Powder X-ray diffraction patterns of $BaSn(OH)_6$ and $BaSnO_3$ samples prepared from decomposion of $BaSn(OH)_6$ at 623 and 1723 K are shown in Figure 11.2. Some diffraction lines of the pattern of $BaSn(OH)_6$ are not included in the reference pattern (JCPDS # 09-0053), but all diffraction lines of the xrd pattern are indexed to the monoclinic $BaSn(OH)_6$ cell [2]. Sharp diffraction lines for $BaSn(OH)_6$ indicate that it is well-crystallized in spite of a very short precipitation time.

Every $BaSnO_3$ sample prepared by heating $BaSn(OH)_6$ over the range 623-1723 K are identified as cubic *Pm-3m* $BaSnO_3$. Even at the temperature of 498 K where a weight loss of 1.5% is observed on the TGA curve, annealing for longer than 3 days gives mainly $BaSnO_3$ with a small amount of $BaSn(OH)_6$. No evidence of $BaCO_3$ is observed in any of the diffraction patterns.

With increasing decomposition temperature the unit-cell size of $BaSnO_3$ decreases and diffraction lines become narrower. Averaged crystallite sizes as a function of temperature from Williamson-Hall plots and Le Bail fittings are depicted in Figure 11.3. Crystallite sizes estimated from Williamson-Hall plots are larger than those from Le Bail fitting. Both methods reveal that the average crystallite size increases with increasing preparation temperature. The average crystallite sizes of $BaSnO_3$ samples prepared from $BaSn(OH)_6$ and annealed at 1573 K for 20, 60, and 300 min were also calculated by using Williamson-Hall plot, cf., inset in Figure 11.3, which clearly indicates an increase in crystallite size with increasing annealing time.

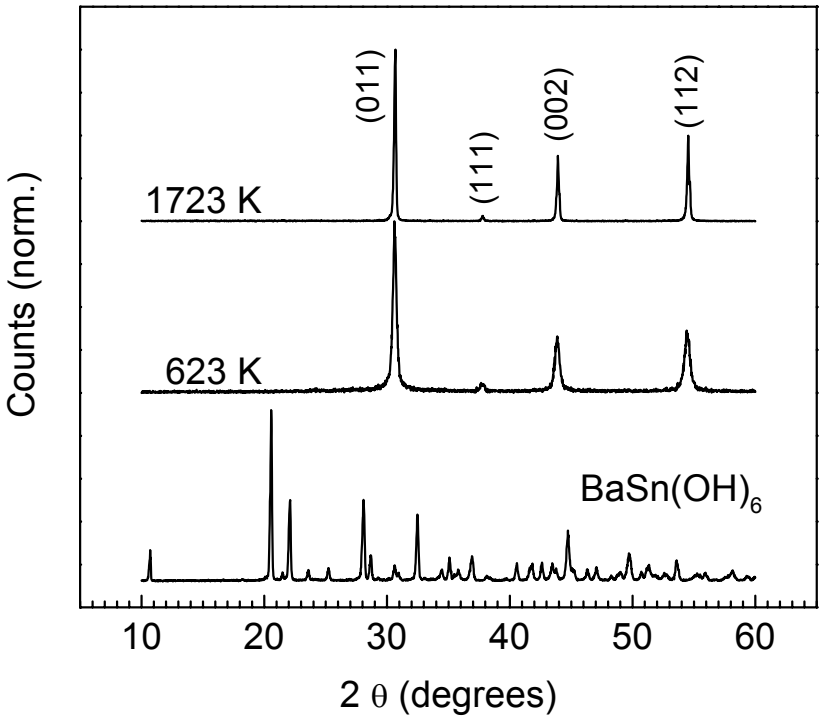

Figure 11.2. Powder X-ray diffraction patterns of powdered $BaSn(OH)_6$ and $BaSnO_3$ prepared by decomposing $BaSn(OH)_6$ at 623 K, and 1723 K for 1 h.

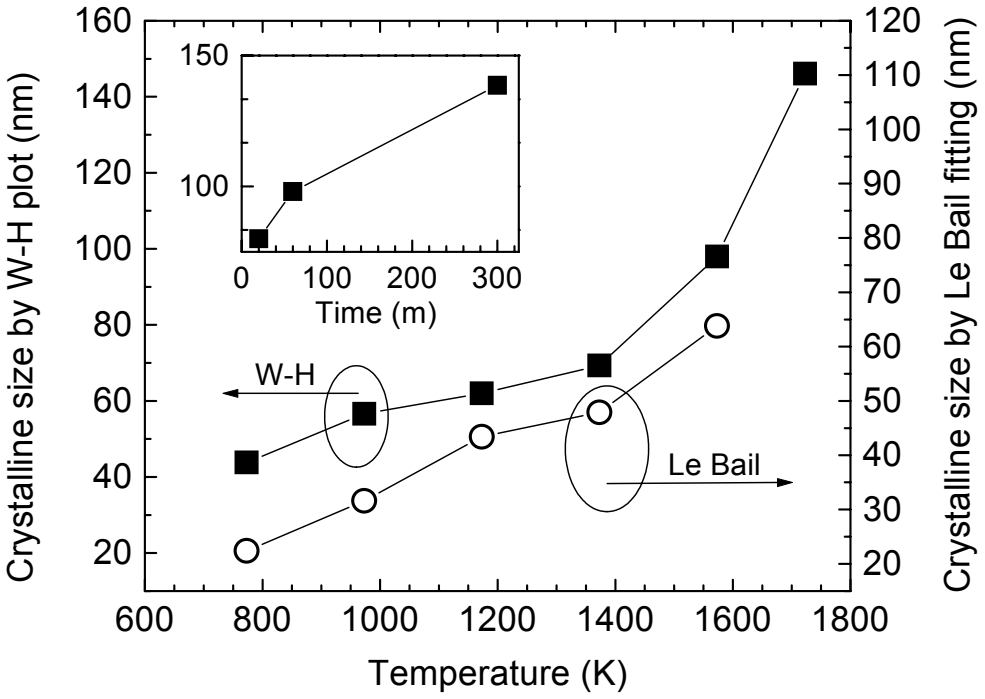

Figure 11.3. Averaged crystallite sizes of $BaSnO_3$ samples calculated from Williamson-Hall plots and Le Bail methods. (Inset) Crystallite size as a function of heating time.

Scanning electron microscope (SEM) images of as-precipitated $BaSn(OH)_6$ and $BaSnO_3$ from the hydroxide at 1573 K are shown in Figure 11.4. Particles of both $BaSn(OH)_6$ and $BaSnO_3$ have flattened needle shapes with lengths varying from 5 to 60 μm. Interestingly, the particle morphology of $BaSn(OH)_6$ is retained during decomposition. At each of the examined annealing temperatures, SEM images of $BaSnO_3$ samples do not show any noticeable change in particle morphology relative to the initial $BaSn(OH)_6$ sample.

A transmission electron microscope (TEM) image of $BaSnO_3$ prepared at 1573 K is shown in Figure 11.5. Along the edges of the acicular particles, well-developed cubes having an average size of 100 nm are observed, which agrees well with the averaged crystalline size calculated by using the Williamson-Hall plot. A TEM image of $BaSnO_3$ prepared at 1173 K reveals cubes with edge lengths in the range of 40-70 nm, while in TEM images of $BaSnO_3$ samples decomposed at 973 K or lower temperatures, cubes are not easily observed.

The relative brightness of $BaSnO_3$ samples as a function of decomposition temperatures and annealing times are shown in Figure 11.6. The brightness of $BaSnO_3$ increases with increasing decomposition temperatures and times. From the correlation between the crystallite size and the decomposition temperature and time, it is clear that the brightness of $BaSnO_3$ increases with increasing crystallite size.

The origin of the near IR luminescence of $BaSnO_3$ seems to be recombination of a photo generated valence band hole and a Sn^{2+} center [6]. With decreasing crystallite size, the ratio of the surface area to the volume of the crystal

increases, and photo generated valence holes have a higher probability to be annihilated at defect sites near the surface of the crystal before they recombine at Sn^{2+} centers.

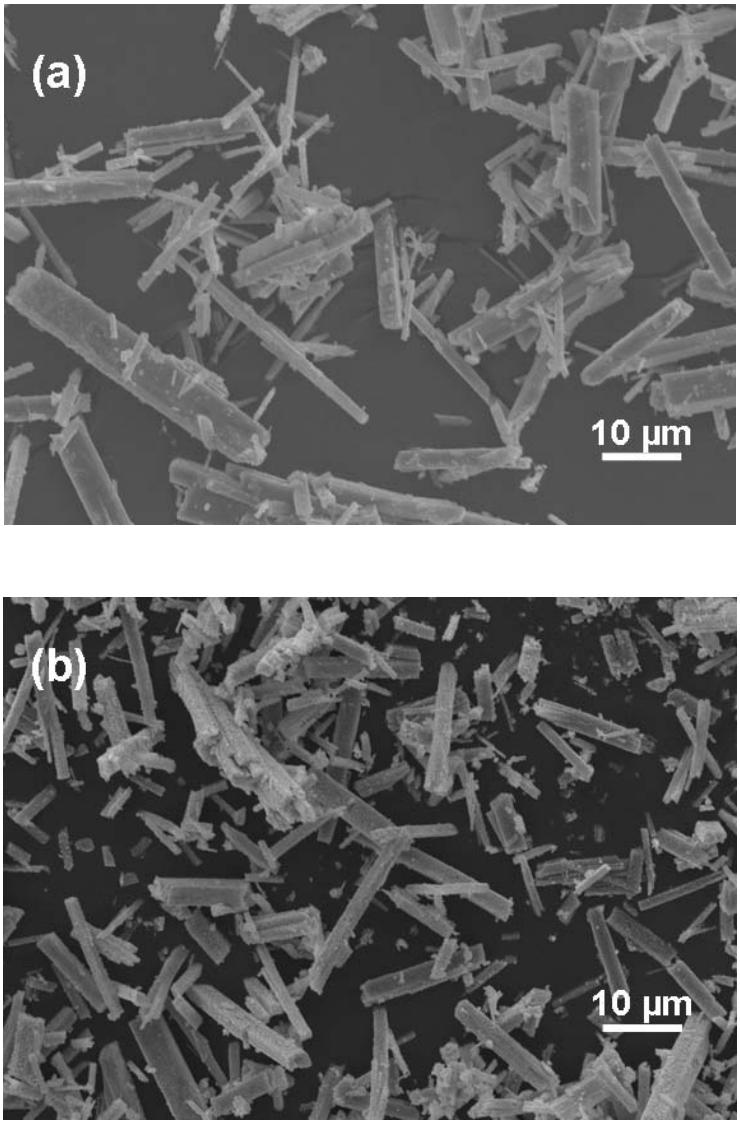

Figure 11.4. Scanning electron microscope images of (a) $BaSn(OH)_6$ and (b)$BaSnO_3$ prepared by decomposing $BaSn(OH)_6$ at 1573 K for 1 h.

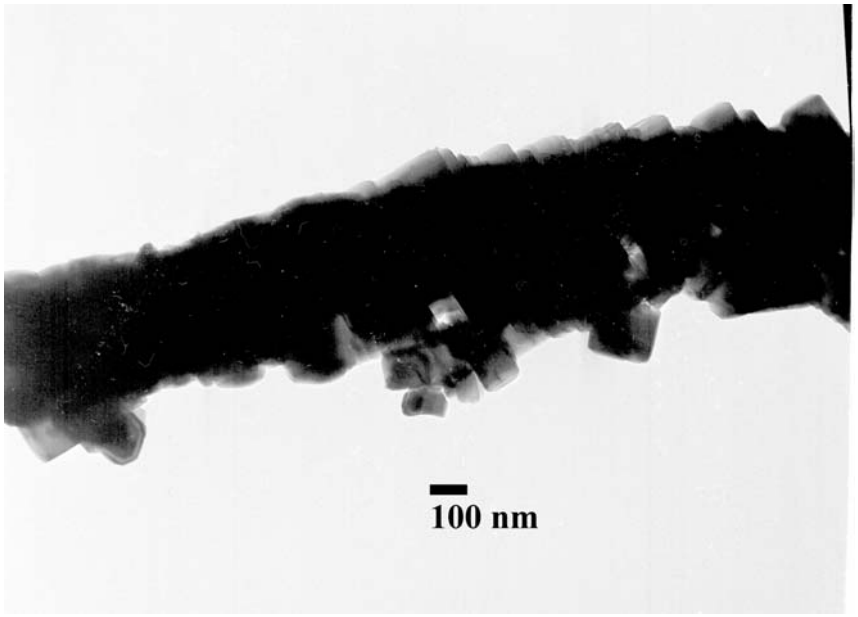

Figure 11.5. Transmission electron microscope (TEM) image of $BaSnO_3$ decomposed at 1573 K.

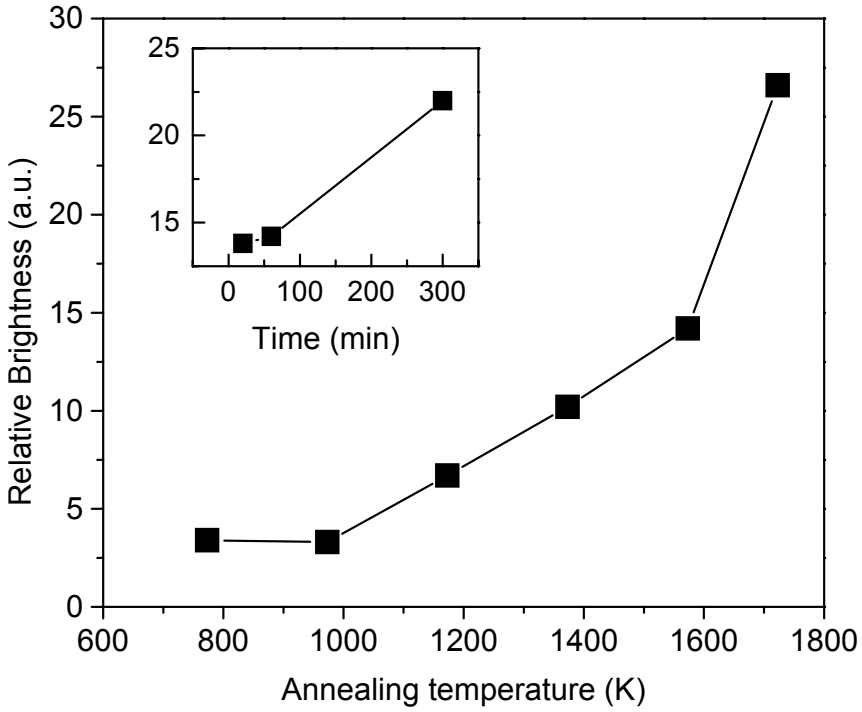

Figure 11.6. Relative luminescence brightness of $BaSnO_3$ as a function of preparative temperature. (Inset) Luminescence brightness of $BaSnO_3$ as a function of heating time.

CONCLUSION

The brightness of $BaSnO_3$ luminescence prepared by decomposing $BaSn(OH)_6$ increases with increasing temperature and annealing times. The particle morphology of $BaSn(OH)_6$ is retained during decomposition, while nano-sized cubes are directly observed on surfaces of the particles when annealed at 1173 K or higher temperature. The sizes of these nanocubes have been measured by X-ray and TEM methods, and they correlate directly to emission brightness.

ACKNOWLEDGMENTS

This work is based upon work supported by the National Science Foundation under Grant No. 0245386.

REFERENCES

[1] B. Ostrick, M. Fleischer, U. Lampe, and H. Meixner, *Sens. Actuators*, **B44**, 601 (1997).

[2] M. T. Buscaglia, M. Leoni, M. Viviani, V. Buscaglia, A. Martinelli, A. Testino, and P. Nanni, *J. Mater. Res.*, **18(3)**, 560 (2003).

[3] J. Cerda, J. Arbiol, G. Dezanneua, R. Diaz, and J. R. Morante, *Sens. Actuators*, **B84**, 21 (2002).

[4] C.P. Udawatte, and M. Yoshimura, *Mater. Lett.*, **47**, 7 (2001).

[5] T. R. N. Kutty, and R. Vivekanadan, *Mater. Res. Bull.*, **22**, 1457 (1987).

[6] H. Mizoguchi, H. W. Eng, and P. M. Woodward, *Inorg. Chem.*, **43**, 1667 (2004).

[7] H. Mizoguchi, P. M. Woodward, C.-H. Park, and D. A. Keszler, *J. Am. Chem. Soc.*, **126(31)**, 9796 (2004).

[8] B. D. Cullity and S. R. Stock, Elements of X-ray Diffraction, 3rd Edition, 2001, Prentice Hall, Upper Saddle River, NJ, USA.

[9] A. Le Bail, H. Duroy, and J. L. Fourquet, *Mater. Res. Bull.*, **23**, 447 (1988).

[10] J. Rodriguez-Carvajal, FULLPROF: A program for Rietveld Refinement and Pattern Matching Analysis, *In Abstract of the Satellite Meeting on Powder Diffraction of the XV Congress of the IUCr*, p 127, Thoulouse, France (1990).

CHAPTER 12

LUMINESCENCE OF MONOCLINIC AND TRIGONAL Eu:(La,Y)$Sc_3(BO_3)_4$

Cheol-Hee Park and Douglas A. Keszler

submitted to *Solid State Sciences*
23, rue Linois, 75724 Paris cedex 15, France

ABSTRACT

Powder samples of $La_{0.6}Y_{0.4-x}Eu_xSc_3(BO_3)_4$ ($0.05 \leq x \leq 0.4$) and $La_{1-y}Eu_ySc_3(BO_3)_4$ ($0.01 \leq y \leq 1$) were prepared, and their structures and luminescence properties were investigated. Each composition containing Y crystallizes in the trigonal huntite structure, while the compositions $La_{1-y}Eu_ySc_3(BO_3)_4$ adopt a monoclinic variant for $y \leq 0.2$ and the trigonal form for $y \geq 0.3$. Each compound exhibits saturated red emission; strong concentration quenching is observed only in the monoclinic compounds. Both the monoclinic $La_{0.9}Eu_{0.1}Sc_3(BO_3)_4$ and trigonal $La_{0.6}Y_{0.3}Eu_{0.1}Sc_3(BO_3)_4$ exhibit stronger thermal quenching than the comparable trigonal huntite $Y_{0.9}Eu_{0.1}Al_3(BO_3)_4$, and the trigonal Sc compound exhibits stronger thermal quenching than the monoclinic Sc compound.

INTRODUCTION

Crystals of $LaSc_3(BO_3)_4$, when doped with Nd^{3+} ions, are highly regarded as laser materials [1-3]. These crystals adopt structures similar to that of the trigonal mineral huntite $CaMg_3(CO_3)_4$ [4]. Undoped and lightly doped $LaSc_3(BO_3)_4$ crystallizes in a monoclinic variant of the huntite structure, while heavy doping leads to formation of the common noncentrosymmetric trigonal phase [2,5,6]. These structures are similar; in each case planar layers of BO_3 groups are connected by Sc atoms in distorted octahedral sites and lanthanide ions in distorted trigonal prismatic sites. The trigonal phase also can be stabilized by partial substitution with smaller lanthanides such as Gd [7] and Y [8]. The La sites are expected to substitutionally accommodate various lanthanides, including representative luminescent centers such as Ce, Eu, and Tb. The stoichiometric compound $CeSc_3(BO_3)_4$, for example, where all of the La in $LaSc_3(BO_3)_4$ is replaced with Ce, emits across a band range of wavelengths covering the near UV and blue regions [5]. In this contribution, we examine the luminescence properties of the monoclinic and trigonal forms of the Sc huntite materials by using composition control in $(La,Y)Sc_3(BO_3)_4$ to set the structural type and Eu^{3+} as the emitting structural probe.

Because of its fundamental and practical importance, the luminescence of the Eu^{3+} ion has been studied in numerous hosts. When it occupies a site with a center of symmetry its emission color is orange and when located in a site with a

center of symmetry, it is red [9,10]. The La dopant sites in both monoclinic and trigonal $LaSc_3(BO_3)_4$ are noncentrosymmetric, so the Eu^{3+} emission is expected and observed to be saturated red. As presented here, the structural form of the Sc huntite does have subtle effects of the concentration and thermal quenching of the Eu^{3+} emission.

EXPERIMENTAL

Powder samples of $La_{0.6}Y_{0.4-x}Eu_xSc_3(BO_3)_4$ ($0.05 \leq x \leq 0.4$) and $La_{1-y}Eu_ySc_3(BO_3)_4$ ($0.01 \leq y \leq 1$) were prepared by solid-state reaction at elevated temperature. Stoichiometric amounts of La_2O_3 (99.999%, Stanford materials), Y_2O_3 (99.999%, Stanford materials), Eu_2O_3 (99.99%, Stanford materials), Sc_2O_3 (99.95%, Stanford materials), and B_2O_3 (99.9%, Cerac) were mixed and ground with 5 wt% $LiBO_2$ (99.9%, Cerac), which serves as a flux to promote the reaction. Prior to use, La_2O_3 was heated at 1323 K for 5 h to remove carbonate and water. The mixtures were calcined at 973 K for 3 h in air followed by cooling and grinding and then heating again at 1423 K for 2 h. Some of the samples were also prepared at 1123 K with 50 wt% $LiBO_2$ as flux. The final products were washed with dilute nitric acid and de-ionized water several times followed by filtering and drying at 408 K. The products were examined by X-ray diffraction on a Siemens D5000 diffractometer by using Cu$K\alpha$ radiation.

Photoluminescence measurements were made with an Oriel 300-W Xe lamp and a Cary model-15 prism monochromator for excitation. For detection, emitted light was passed through an Oriel 22500 1/8-m monochromator and monitored with a Hamamatsu R636-10 photomultiplier tube. Each spectrum was corrected for the throughput and response of the system by using Rhodamine B and a standardized tungsten lamp. Variable-temperature spectra over the temperature range 77 – 300 K were recorded by using a Cryo Industries R102 flow cryostat equipped with a Conductus temperature controller.

RESULTS

X-ray Diffraction Analysis

Each of the Y substituted compounds $La_{0.6}Y_{0.4-x}Eu_xSc_3(BO_3)_4$ ($0.05 \leq x \leq 0.4$) was identified as a trigonal form of the huntite structure; while the samples $La_{1-y}Eu_ySc_3(BO_3)_4$ ($0.01 \leq y \leq 1$) crystallize as the monoclinic or trigonal forms and mixtures thereof, depending on the Eu concentration. We do note that the powder X-ray diffraction pattern of $La_{0.6}Y_{0.3}Eu_{0.1}Sc_3(BO_3)_4$ (Figure 12.1) reveals a small amount of an impurity calcite phase $(Y,Sc)BO_3$ [8], in addition to the trigonal phase. For the compounds with $x \geq 0.3$, this calcite phase disappears and single phase trigonal huntites are observed. The X-ray patterns of the compounds $La_{1-y}Eu_ySc_3(BO_3)_4$ ($y \leq 0.2$) can be indexed with a single phase monoclinic cell. The

compounds of $La_{1-y}Eu_ySc_3(BO_3)_4$ ($y \geq 0.3$) are observed to be single phase trigonal borates, while the pattern of $La_{0.75}Eu_{0.25}Sc_3(BO_3)_4$ reveals that it is a mixture of the monoclinic and trigonal phases.

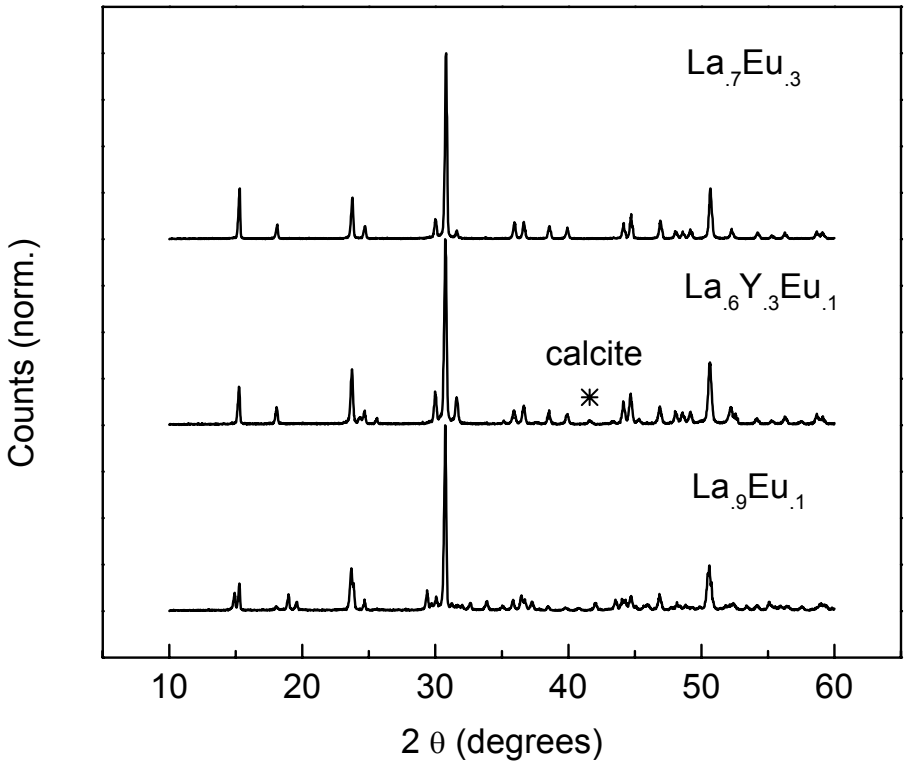

Figure 12.1. XRD patterns of $La_{0.7}Eu_{0.3}Sc_3(BO_3)_4$, $La_{0.6}Y_{0.3}Eu_{0.1}Sc_3(BO_3)_4$, and $La_{0.9}Eu_{0.1}Sc_3(BO_3)_4$.

Photoluminescence

Each of the Eu^{3+}-doped compounds exhibits under ultraviolet excitation saturated red emission with CIE chromaticity coordinates x = 0.66 and y = 0.33. The emission spectrum of $La_{0.6}Y_{0.3}Eu_{0.1}Sc_3(BO_3)_4$ under UV charge-transfer excitation is depicted in Figure12.2 (a); it is composed of emission lines mainly associated with relaxation from the $^5D_0$ level. The lack of a center of symmetry at the Eu^{3+} sites in both the monoclinic and trigonal phases leads to the strong electric-dipole transition of the $^5D_0 \rightarrow {}^7F_2$ emission at about 613.5 nm. A very weak emission line of the $^5D_1 \rightarrow {}^7F_1$ transition is also observed at around 534.3nm in both trigonal and monoclinic phases. This $^5D_1 \rightarrow {}^7F_1$ emission is seldom observed in borate compounds because of the fast nonradiative $^5D_1 \rightarrow {}^5D_0$ decay associated with high B-O vibrational frequencies [11]. The rate of this $^5D_1 \rightarrow {}^5D_0$ decay is generally quite temperature dependent, however, in $La_{0.6}Eu_{0.4}Sc_3(BO_3)_4$ the intensity ratio of the $^5D_1 \rightarrow {}^7F_1$ emission to that of the $^5D_0 \rightarrow {}^7F_2$ emission is invariant over the temperature range 77-300 K. The emissions from the $^5D_1$ level are also quenched with increasing Eu^{3+} concentrations because of the cross relaxation process $(^5D_1 \rightarrow {}^5D_0) \rightarrow ({}^7F_0 \rightarrow {}^7F_6)$; the relative emission intensities from the $^5D_1$ level are comparable to those from the $^5D_0$ level in $Y_2O_2S:Eu^{3+}$ (1% dopant level), while the emission spectrum of the $Y_2O_2S:Eu^{3+}$ (4% dopant level) does not exhibit clearly any emission from the $^5D_1$ level [12]. The intensity ratio of the $^5D_1 \rightarrow {}^7F_1$ emission

to the $^5D_0 \rightarrow {}^7F_2$ emission does not change in either the monoclinic or the trigonal phases with varying Eu^{3+} concentrations.

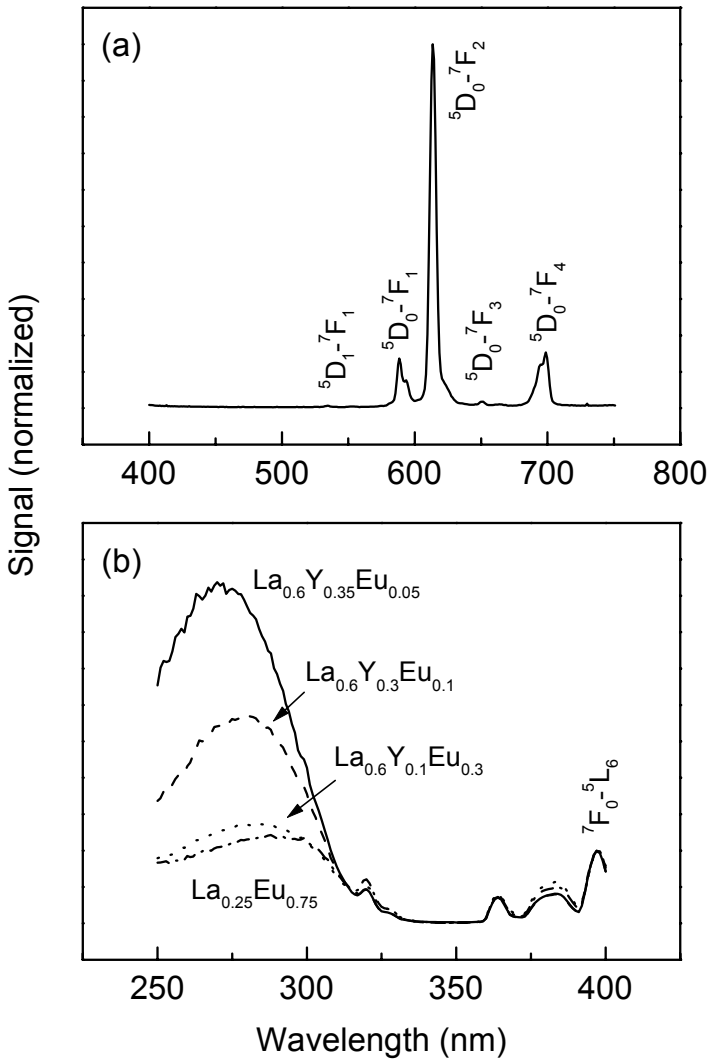

Figure 12.2. Room temperature emission spectrum of $La_{0.6}Y_{0.3}Eu_{0.1}Sc_3(BO_3)_4$ under the charge-transfer excitation (a) and excitation spectra of $La_{0.6}Y_{0.35}Eu_{0.05}Sc_3(BO_3)_4$, $La_{0.6}Y_{0.3}Eu_{0.1}Sc_3(BO_3)_4$, $La_{0.6}Y_{0.1}Eu_{0.3}Sc_3(BO_3)_4$, and $La_{0.25}Eu_{0.75}Sc_3(BO_3)_4$ monitored at 613 nm emission (b).

Excitation spectra of the trigonal borates $La_{0.6}Y_{0.35}Eu_{0.05}Sc_3(BO_3)_4$, $La_{0.6}Y_{0.3}Eu_{0.1}Sc_3(BO_3)_4$, $La_{0.6}Y_{0.1}Eu_{0.3}Sc_3(BO_3)_4$, and $La_{0.25}Eu_{0.75}Sc_3(BO_3)_4$ are shown in Figure 12.2 (b). Each excitation spectrum is composed of a broad charge transfer excitation band below 320 nm region and several f-f transition excitation peaks. The $^7F_0 \rightarrow {}^5L_6$ excitation features at 397 nm are normalized for all spectra. As the Eu^{3+} concentration decreases, excitation via the charge-transfer transition becomes more significant. This tendency is observed in the monoclinic borates too.

Excitation spectra of the monoclinic $La_{0.9}Eu_{0.1}Sc_3(BO_3)_4$ and the trigonal $La_{0.6}Y_{0.3}Eu_{0.1}Sc_3(BO_3)_4$ recorded over the range 250-390 nm at room temperature and 77K are depicted in Figure 12.3. At 77 K the charge-transfer band is located near 269 nm for monoclinic $La_{0.9}Eu_{0.1}Sc_3(BO_3)_4$ and near 272 nm for trigonal $La_{0.6}Y_{0.3}Eu_{0.1}Sc_3(BO_3)_4$. At room temperature, the charge-transfer band is observed near 272 nm for the monoclinic phase and near 280 nm for the trigonal phase. At both temperatures, the charge-transfer band of the monoclinic phase has a larger full width at half maximum (FWHM) than that of the trigonal phase. The difference in the energetic position of charge-transfer bands at 77 K and room temperature is 400 cm^{-1} for the monoclinic phase and 1100 cm^{-1} for the trigonal phase.

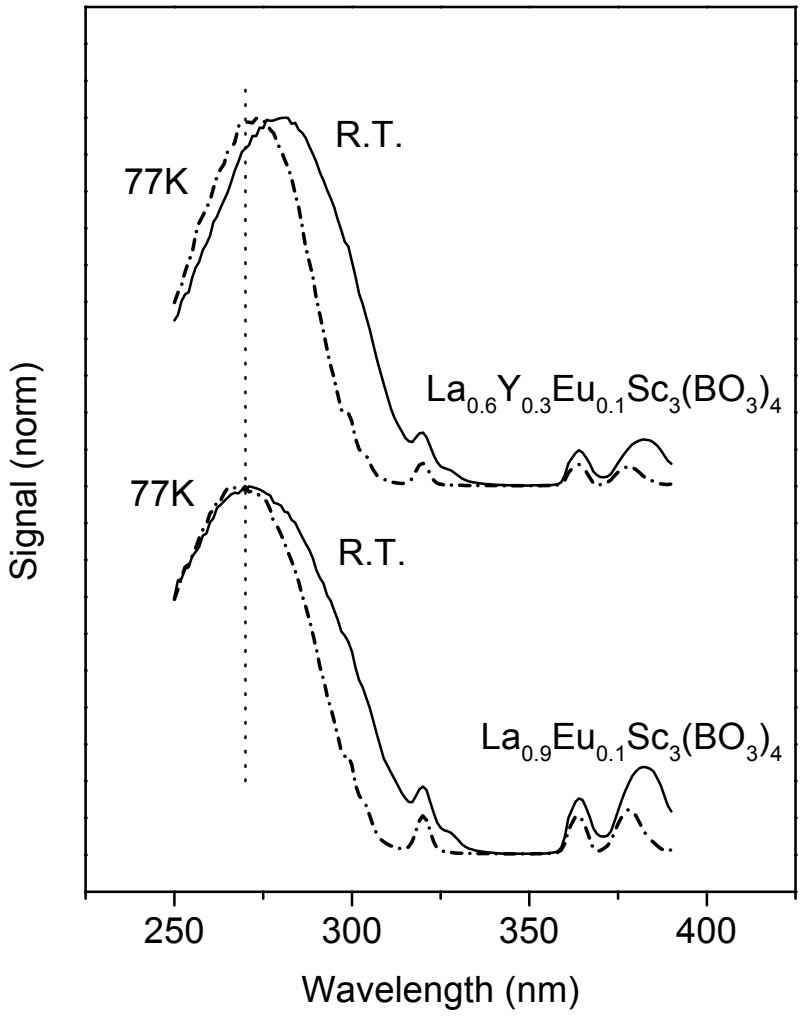

Figure 12.3. Excitation spectra of the monoclinic $La_{0.9}Eu_{0.1}Sc_3(BO_3)_4$ and the trigonal $La_{0.6}Y_{0.3}Eu_{0.1}Sc_3(BO_3)_4$ at room temperature and 77K. The $^7F_0 \rightarrow {}^5L_6$ excitation peaks at 397 nm are normalized for all spectra.

Emission brightness of the monoclinic $La_{0.9}Eu_{0.1}Sc_3(BO_3)_4$ and the trigonal $La_{0.6}Y_{0.3}Eu_{0.1}Sc_3(BO_3)_4$ was examined over the temperature range 77-300 K under charge-transfer excitation (280 nm for trigonal phase; 285 nm for monoclinic phase) and the 397 nm excitation of the $^7F_0 \rightarrow {}^5L_6$ transition (Figure 12.4). Under charge-transfer excitation, the brightness of the monoclinic $La_{0.9}Eu_{0.1}Sc_3(BO_3)_4$ at 300 K is 69% of that at 77K; the brightness of the monoclinic $La_{0.9}Eu_{0.1}Sc_3(BO_3)_4$ at 300 K is observed to be 88% of that at 77K when it is excited by the $^7F_0 \rightarrow {}^5L_6$ transition excitation. The emission of trigonal $La_{0.6}Y_{0.3}Eu_{0.1}Sc_3(BO_3)_4$ exhibits the stronger correlation to temperature. Under the charge-transfer excitation, its brightness at 300 K decreases to 51% of that at 77K; under the $^7F_0 \rightarrow {}^5L_6$ transition its brightness at 300 K decreases to 76% of that at 77K. Under charge-transfer excitation, the isomorphic huntite of $Y_{0.9}Eu_{0.1}Al_3(BO_3)_4$ exhibits constant brightness over the temperature range 77-300 K [13]. The difference seems to arise from the relatively low energy of the charge-transfer bands in monoclinic $La_{0.9}Eu_{0.1}Sc_3(BO_3)_4$ and trigonal $La_{0.6}Y_{0.3}Eu_{0.1}Sc_3(BO_3)_4$. The maximum of the charge-transfer excitation band is observed at higher energy (~256 nm) in $Y_{0.9}Eu_{0.1}Al_3(BO_3)_4$ [13,14]. This effect will be described in detail in the discussion section.

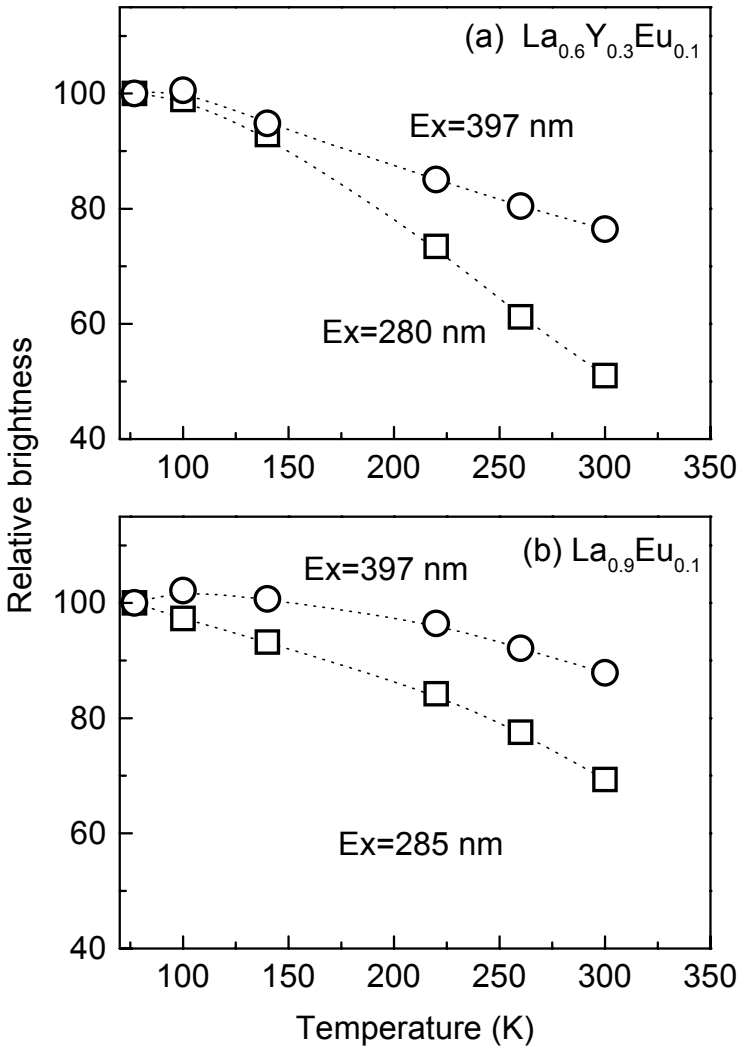

Figure 12.4. The evolution of the brightness of the monoclinic $La_{0.9}Eu_{0.1}Sc_3(BO_3)_4$ and the trigonal $La_{0.6}Y_{0.3}Eu_{0.1}Sc_3(BO_3)_4$ over the temperature range of 77-300 K under the charge transfer excitation (280 nm for trigonal phase; 285 nm for monoclinic phase) and the 397 nm excitation of the $^7F_0 \rightarrow {}^5L_6$ transition.

The relationships between Eu concentration and emission brightness for the compounds $La_{0.6}Y_{0.4-x}Eu_xSc_3(BO_3)_4$ ($0.05 \leq x \leq 0.4$) and $La_{1-y}Eu_ySc_3(BO_3)_4$ ($0.01 \leq y \leq 1$) are depicted in Figure 12.5. For the yttrium substituted compounds $La_{0.6}Y_{0.4-x}Eu_xSc_3(BO_3)_4$, concentration quenching is not observed over the whole x region. For the compounds of $La_{1-y}Eu_ySc_3(BO_3)_4$ ($0.01 \leq y \leq 1$), its brightness increases up to $y = 0.15$ and decreases at higher concentrations. Both compounds of $La_{0.6}Y_{0.4-x}Eu_xSc_3(BO_3)_4$ ($x = 0.3$) and $La_{1-y}Eu_ySc_3(BO_3)_4$ ($y \leq 0.3$) are trigonal phases and exhibit similar brightness. The compound of $La_{0.75}Eu_{0.25}Sc_3(BO_3)_4$ is a mixture of the monoclinic phase and the trigonal phase and its brightness is essentially an average of that of monoclinic $La_{0.6}Y_{0.4-x}Eu_xSc_3(BO_3)_4$ ($x = 0.2$) and trigonal $La_{0.6}Y_{0.4-x}Eu_xSc_3(BO_3)_4$ ($x = 0.3$). It is worthwhile to note that both $La_{0.6}Y_{0.4-x}Eu_xSc_3(BO_3)_4$ ($x = 0.3$) and $La_{1-y}Eu_ySc_3(BO_3)_4$ ($y \leq 0.3$) crystallize in the trigonal form, and they exhibit similar brightness under Hg-lamp excitation. The maximum excitation intensity is observed near 272 nm for monoclinic $La_{0.9}Eu_{0.1}Sc_3(BO_3)_4$ and near 280 nm for trigonal $La_{0.6}Y_{0.3}Eu_{0.1}Sc_3(BO_3)_4$. The excitation intensity at 254 nm is 78% of the maximum excitation intensity for the monoclinic phase and 53% for the trigonal phase. Therefore, under excitation at each maximum intensity wavelength the brightness of each compound is similar, even though under a Hg lamp, monoclinic $La_{0.9}Eu_{0.1}Sc_3(BO_3)_4$ exhibits emission 1.5 times as bright as trigonal $La_{0.6}Y_{0.3}Eu_{0.1}Sc_3(BO_3)_4$.

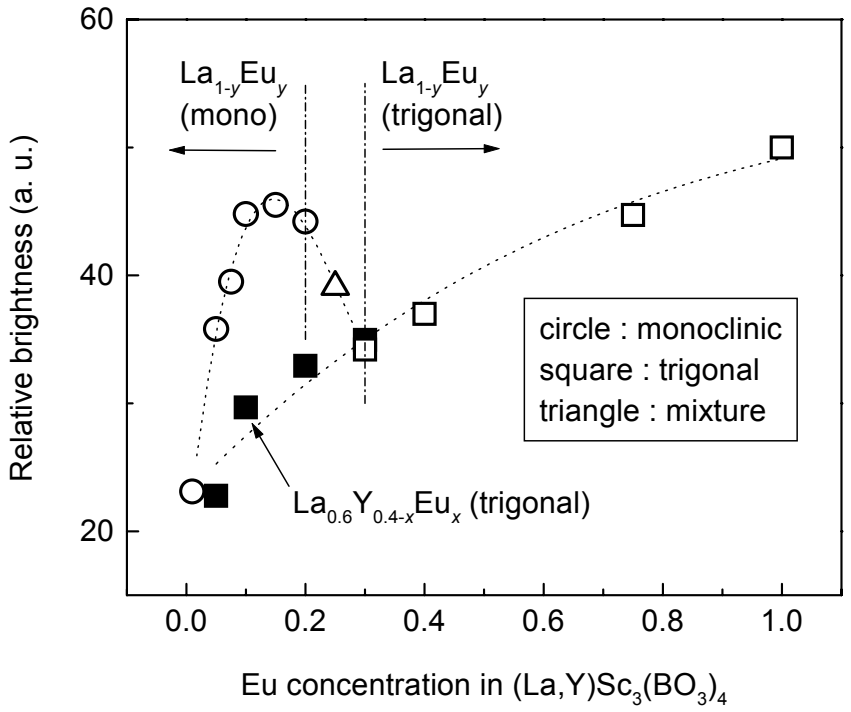

Figure 12.5. Europium concentration dependence of the brightness for the compounds of $La_{0.6}Y_{0.4-x}Eu_xSc_3(BO_3)_4$ ($0.05 \leq x \leq 0.4$) and $La_{1-y}Eu_ySc_3(BO_3)_4$ ($0.01 \leq y \leq 1$); Hg-lamp excitation.

DISCUSSION

Even though the structural difference between the monoclinic and trigonal phases of the scandium borate huntites is very small, Eu^{3+} ions in both phases show significantly different Eu-concentration dependence with respect to brightness and temperature. In addition, the brightness of $La_{0.6}Y_{0.3}Eu_{0.1}Sc_3(BO_3)_4$ under charge-transfer excitation at room temperature is approximately to 51% of that observed at

77K, while the isomorphic huntite $Y_{0.9}Eu_{0.1}Al_3(BO_3)_4$ does not exhibit thermal quenching over the temperature range 77-300 K. The thermal-quenching behavior of Eu^{3+}-doped materials can be often explained by using a configurational coordinate diagram and energetic position of the charge transfer band [10]. A schematic configurational-coordinate diagram for Eu^{3+} in $Y_{0.9}Eu_{0.1}Al_3(BO_3)_4$ and $La_{0.6}Y_{0.3}Eu_{0.1}Sc_3(BO_3)_4$ is presented in Figure 12.6. For clarity, only $^7F_0$, $^7F_6$, $^5D_0$, $^5D_2$, and charge transfer states are shown. The potential energy of the each sate is plotted as a function of the configurational coordinate *r*, *i.e.*, the distance between Eu and O. When excited by charge transfer (A→B), the system relaxes to the equilibrium state of the charge-transfer state (point C) by releasing vibrational energy to the host. At low temperatures, it mainly relaxes to ^5D_J states, return to the ^7F_J ground states through luminescence. At higher temperatures, the system may reach point D (where the curve of the ground state intersects the curve of the charge transfer state) with thermal energy and then return to point A non-radiatively.

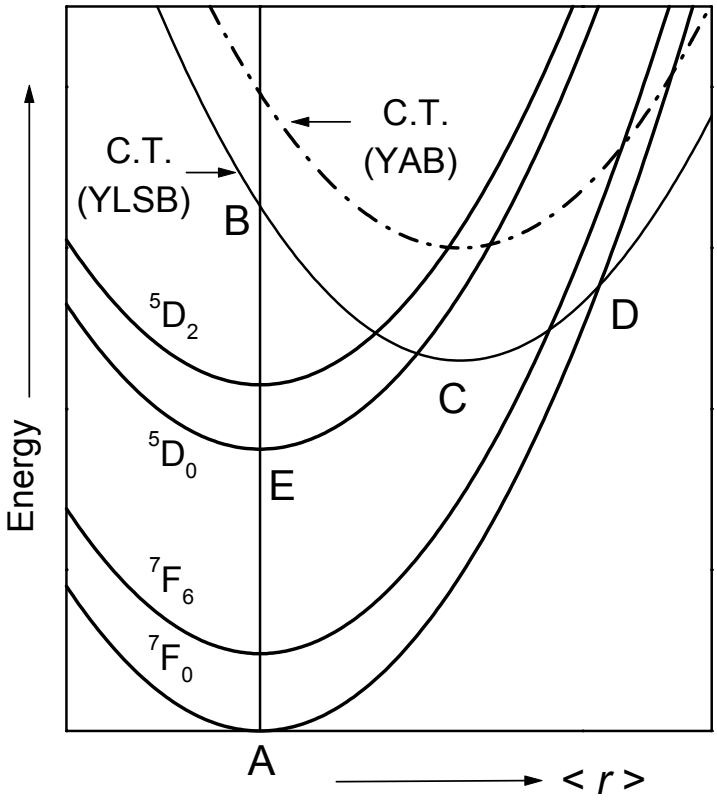

Figure 12.6. Schematic configurational coordinate diagram for Eu^{3+} ion in huntites. For simplicity only $^7F_0$, $^7F_6$, $^5D_0$, $^5D_2$, and charge transfer states are shown. C.T. (YAB) and C.T. (YLSB) represent the charge transfer states of $Y_{0.9}Eu_{0.1}Al_3(BO_3)_4$ and $La_{0.6}Y_{0.3}Eu_{0.1}Sc_3(BO_3)_4$. The difference in the energetic positions of the both states are exaggerated for clarity.

Because of the higher energetic position of the charge transfer state, the energy differences E-C and C-D of $Y_{0.9}Eu_{0.1}Al_3(BO_3)_4$ are larger than those of $La_{0.6}Y_{0.3}Eu_{0.1}Sc_3(BO_3)_4$. Therefore non-radiative processes via thermal excitations of C→D→A and E→C→D→A are less probable than in $La_{0.6}Y_{0.3}Eu_{0.1}Sc_3(BO_3)_4$ in the examined temperature region and the thermal quenching is not observed in $Y_{0.9}Eu_{0.1}Al_3(BO_3)_4$. The stronger correlation of brightness of trigonal scandium borates with temperature also can be understood in the same way.

The difference in the energetic position of charge-transfer bands at 77 K and room temperature is 400 cm^{-1} for monoclinic $La_{0.9}Eu_{0.1}Sc_3(BO_3)_4$ and 1100 cm^{-1} for $La_{0.6}Y_{0.3}Eu_{0.1}Sc_3(BO_3)_4$. The energetic position of the charge-transfer state of Eu^{3+} in the trigonal phase decreases more than in the monoclinic phase with increasing temperature, and non-radiative decay via thermal excitation will be more important in the trigonal phase than in the monoclinic phase; therefore the thermal quenching should be greater in the tetragonal phase than in the monoclinic phase. The energy of the charge-transfer band is typically affected by the crystal field, therefore it would be worthwhile to examine thermal expansion of the trigonal and monoclinic phases.

CONCLUSION

Powder samples of $La_{0.6}Y_{0.4-x}Eu_xSc_3(BO_3)_4$ ($0.05 \leq x \leq 0.4$) and $La_{1-y}Eu_ySc_3(BO_3)_4$ ($0.01 \leq y \leq 1$) were prepared and their structures and luminescence properties were investigated. All of the yttrium substituted compounds of $La_{0.6}Y_{0.4-x}Eu_xSc_3(BO_3)_4$ ($0.05 \leq x \leq 0.4$) are identified as trigonal, while the compounds of $La_{1-y}Eu_ySc_3(BO_3)_4$ have monoclinic with $y \leq 0.2$ and triclinic with $y \geq 0.3$. Every compound exhibits saturated red emission. Concentration quenching is observed only in monoclinic compounds. Both the monoclinic $La_{0.9}Eu_{0.1}Sc_3(BO_3)_4$ and trigonal $La_{0.6}Y_{0.3}Eu_{0.1}Sc_3(BO_3)_4$ exhibit lower quenching temperatures than isomorphic trigonal huntite of $Y_{0.9}Eu_{0.1}Al_3(BO_3)_4$. And the trigonal compound exhibits a stronger correlation of brightness to temperature than the monoclinic compound. A schematic configurational diagram was presented to explain the difference in thermal behavior.

ACKNOWLEDGMENTS

This material is based upon work supported by the National Science Foundation.

REFERENCES

[1] S. A. Kutovoi: S. A. Kutovoi, V. V. Laptev, and S. Yu. Matsnev, *Sov. J. Quantum Electron*, **21**, 131 (1991).

[2] J-P. Meyn :J-P. Meyn, T. Jensen, and G. Huber, *IEEE J. Quantum. Electron*, **30**, 913 (1994).

[3] D. K. Sardar, F. Castano, J. A. French, J. B. Gruber, T. A. Reynolds, T. Alekel, D. A. Keszler, and B. L. Clark, *J. Appl. Phys.*, **90**, 4997 (2001).

[4] D. L. Graf, W. F. Bradley, *Acta Crysyallogr.*, **15**, 238 (1962).

[5] G. A. Peterson, D. A. Keszler, and T. A. Reynolds, *Int. J. Inorg. Mater.*, **2**, 101 (2000).

[6] H. Sun, *PhD dissertation*, Oregon State University (1989).

[7] T. A. Reynolds, *PhD dissertation*, Oregon State University (1992).

[8] N. Ye, M. A. Hrushika, J. L. Stone-Sundberg, and D. A. Keszler, *submitted*.

[9] J. Hölsa, *Inorganica Chimica Acta*, 139, 257-259, (1987).

[10] G. Blasse, and A. Bril, *Philips Tech. Rev.*, **31**, 304 (1970).

[11] G. Blasse and B. C. Grabmaier, *Luminescent Materials*, p.75, Springer-Verlag, Berlin (1994).

[12] T. Kano, in *Phosphor Handbook*, p.190, edited by S. Shionoya, and W.M.Yen, CRC Press, Boca Raton, FL (2000).

[13] C.-H. Park, and D. A. Keszler, unpublished.

[14] Y. Hongpeng, G. Hong, X. Zeng, C.-H. Kim, C.-H. Pyun, B.-Y. Yu, and H.-S. Bae, *J. Phys. Chem. Solids*, **61**, 1985 (2000).

CHAPTER 13

LUMINESCENCE OF $LuAl_3(BO_3)_4$:Ln (Ln = Eu, Tb, and Ce) UNDER ULTRAVIOLET AND VACUUM ULTRAVIOLET EXCITATION

ABSTRACT

New materials of $LuAl_3(BO_3)_4$:Ln (Ln = Eu, Tb, and Ce) were prepared by using high-temperature methods, and their luminescence was examined under ultraviolet and vacuum ultraviolet excitation. Samples of $Lu_{1-x}Eu_xAl_3(BO_3)_4$ show maximum emission intensity at x = 0.1 under charge-transfer excitation. $Lu_{0.9}Eu_{0.1}Al_3(BO_3)_4$ exhibits saturated red emission, no thermal quenching in the temperature range 77-290 K, and a quantum efficiency similar to that of sodium salicylate for 147-nm excitation. Samples of $Lu_{1-x}Tb_xAl_3(BO_3)_4$ show maximum emission intensity at x = 0.3 under 375-nm excitation. Energy transfer from Ce^{3+} to Tb^{3+} is observed in $Lu_{0.85}Tb_{0.1}Ce_{0.05}Al_3(BO_3)_4$.

INTRODUCTION

Recently vacuum ultraviolet (VUV) phosphors have been received much interest for applications for plasma display panels (PDPs) and Hg-free lamps [1]. The most widely used red phosphor in PDPs is $(Y,Gd)BO_3:Eu^{3+}$ whose color purity is not satisfactory. Under investigation on luminescence of huntite borates in this group [2], no thermal quenching was observed in the 77–300 K range in $YAl_3(BO_3)_4:Eu^{3+}$, and its color purity satisfies the value for NTSC (National Television Standard Committee) red phosphor [3]. Several reports have been published on VUV excitation spectra of $(Y,Gd)Al_3(BO_3)_4:Ln$ (Ln = Eu, Tb) [4-6]. With smaller host-lattice ion which Eu^{3+} replaces, its quantum efficiency and quenching temperature increases. For example $Lu_{1.9}Eu_{0.1}SO_6$ gives higher quantum efficiency and higher quenching temperature than $Gd_{1.9}Eu_{0.1}SO_6$ [7]. Lu^{3+} ion (100.1 pm) is smaller than Y^{3+} ion (104 pm) and Gd^{3+} ion (107.8 pm) [8]. In this contribution, luminescence properties of $LuAl_3(BO_3)_4:Ln$ (Ln = Eu, Tb, Ce) under ultraviolet and vacuum ultraviolet excitation are described.

EXPERIMENTAL

Stoichiometric amounts of Lu_2O_3 (Stanford materials, 99.99%), Eu_2O_3 (Stanford materials, 99.99%), Tb_4O_7 (Cerac, 99.9%), CeO_2 (Cerac, 99.99%), Al_2O_3 (Cerac, 99.99%), and B_2O_3 (Cerac, 99.9%) were mixed and ground in an agate mortar and pestle with 4.8 wt% $LiBO_2$ (99.9%, Cerac), which serves as a flux to promote the reaction. The mixtures were calcined at 1423 K for 2 h in air followed by cooling and grinding and then heating again at 1423 K for 2 h.

The final products were examined by X-ray diffraction on a Siemens D5000 diffractometer by using Cu$K\alpha$ radiation.

Photoluminescence measurements were made with an Oriel 300-W Xe lamp and a Cary model-15 prism monochromator for excitation. For detection, emitted light was passed through an Oriel 22500 1/8-m monochromator and monitored with a Hamamatsu R636-10 photomultiplier tube. Each spectrum was corrected for the throughput and response of the system by using Rhodamine B and a standardized tungsten lamp. Variable-temperature spectra over the temperature range 77–300 K were recorded by using a Cryo Industries R102 flow cryostat equipped with a Conductus temperature controller.

Vacuum ultraviolet excitation spectra were obtained at the University of Georgia.

RESULTS

Samples of $Lu_{0.6}Eu_{0.4}Al_3(BO_3)_4$ were identified as single-phase trigonal huntite, while samples of $Lu_{1-x}Eu_xAl_3(BO_3)_4$ ($0 \leq x \leq 0.3$) contained $LuBO_3$ as secondary phase. Every sample of $Lu_{1-x}Tb_xAl_3(BO_3)_4$ ($0 \leq x \leq 0.4$) included a few % $LuBO_3$ as a secondary phase, cf., Figure 13.1. Solid solutions of $(Lu_{1-y}Y_y)_{0.9}Eu_{0.1}Al_3(BO_3)_4$ (y = 0.4 and 1) and $(Lu_{1-y}Y_y)_{0.85}Tb_{0.15}Al_3(BO_3)_4$ (y = 0.5 and 1) were characterized as single phase trigonal huntite (Figure 13.1). Even the existence of secondary phase of $LuBO_3$, the cell volume change of $(Lu_{1-y}Y_y)_{0.9}Eu_{0.1}Al_3(BO_3)_4$ with y is linear (Figure 13.2). The formation of secondary phase of $LuBO_3$ seems to be attributed to small size of Lu ion, for it was not observed in X-ray diffraction pattern when Lu was substituted with larger ions such as Y, and Eu, (*e.g.*, effective ionic radii for a coordination number six are 101.1 pm for Lu^{3+}, 104 pm for Y^{3+}, and 108.7 pm for Eu^{3+} [8]).

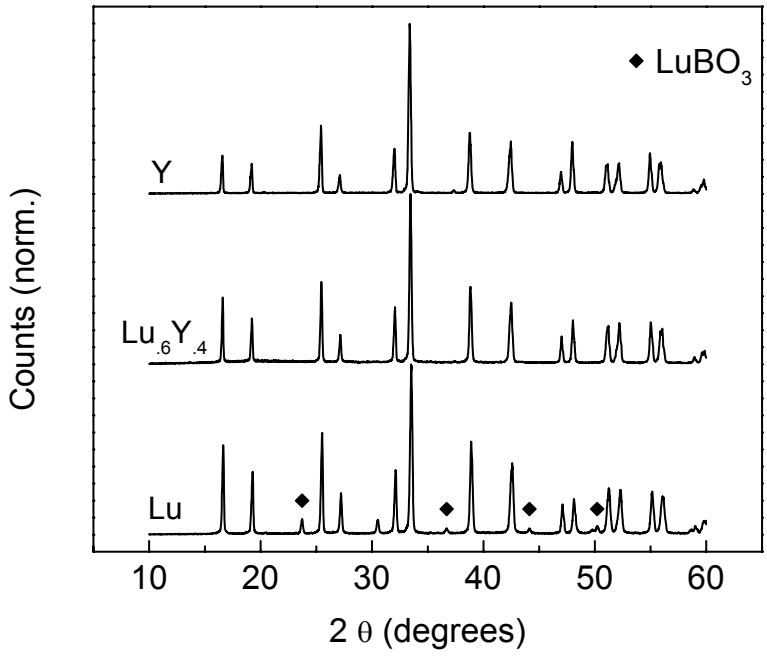

Figure 13.1. Powder X-ray diffraction patterns of solid solutions of $(Lu_{1-y}Y_y)_{0.9}Eu_{0.1}Al_3(BO_3)_4$ (y = 0, 0.4, and 1).

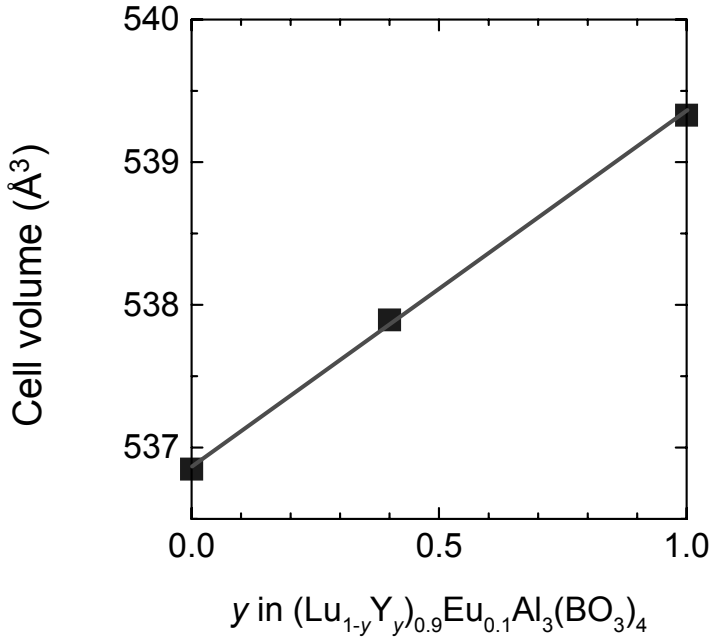

Figure 13.2. Cell volume of $(Lu_{1-y}Y_y)_{0.9}Eu_{0.1}Al_3(BO_3)_4$ (y = 0, 0.4, and 1).

Excitation and emission spectra of $Lu_{0.9}Eu_{0.1}Al_3(BO_3)_4$ and $Y_{0.9}Eu_{0.1}Al_3(BO_3)_4$ are depicted in Figure 13.3; both are almost identical to each other. Emission spectra of both compounds under the charge-transfer excitation of 270 nm reveal saturated red emission with chromaticity coordinates of (x, y) = (0.66, 0.33), which is comparable to the value of the National Television Standard Committee (NTSC) red (0.67, 0.33). Both excitation spectra, monitored at the $^5D_0 \rightarrow {}^7F_2$ emission wavelength of 616 nm, consist of broad charge-transfer bands and *f-f* transition excitation peaks. The maximum of the charge-transfer band is observed at 256 nm (39,000 cm^{-1}), which agrees with previous reports on $Y_{0.85}Eu_{0.15}Al_3(BO_3)_4$ [4].

The Eu concentration dependence of the emission brightness for the compounds of $Lu_{1-x}Eu_xAl_3(BO_3)_4$ ($0 \leq x \leq 0.4$) under the charge-transfer excitation is shown in Figure 13.4. The emission brightness increases up to $x = 0.1$ and decreases at higher concentrations. For compounds of $Gd_{1-x}Eu_xAl_3(BO_3)_4$ the critical concentration of $x = 0.1$ was observed under its charge-transfer excitation; while under *f-f* transition excitation concentration quenching was not observed [10, 11].

The temperature dependence of the brightness of $Lu_{0.9}Eu_{0.1}Al_3(BO_3)_4$ in the 77-290 K temperature range is presented in Figure 13.5. It is constant over the examined temperature region. The brightness of $Y_{0.9}Eu_{0.1}Al_3(BO_3)_4$ was also observed constant over the 77-290 K temperature region [3].

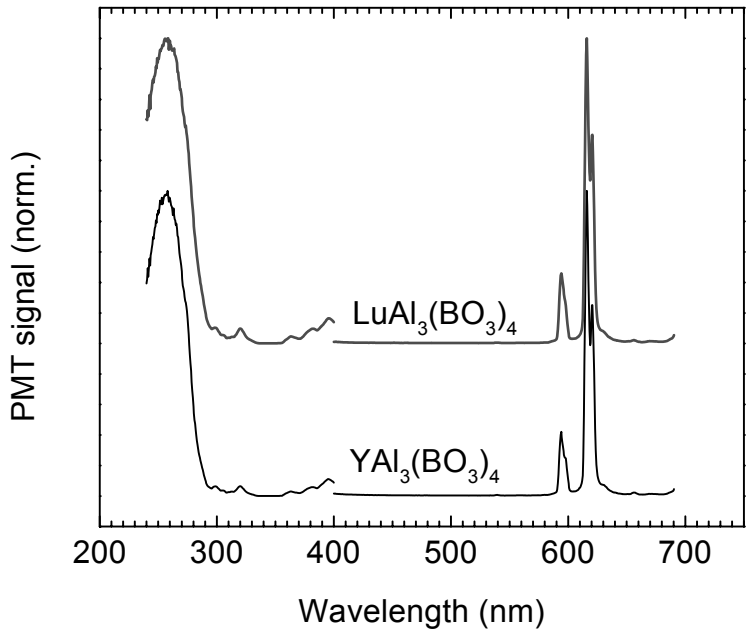

Figure 13.3. Excitation (monitored at 616 nm) and emission (under 270 nm excitation) spectra of $Lu_{0.9}Eu_{0.1}Al_3(BO_3)_4$ and $Y_{0.9}Eu_{0.1}Al_3(BO_3)_4$ at room temperature.

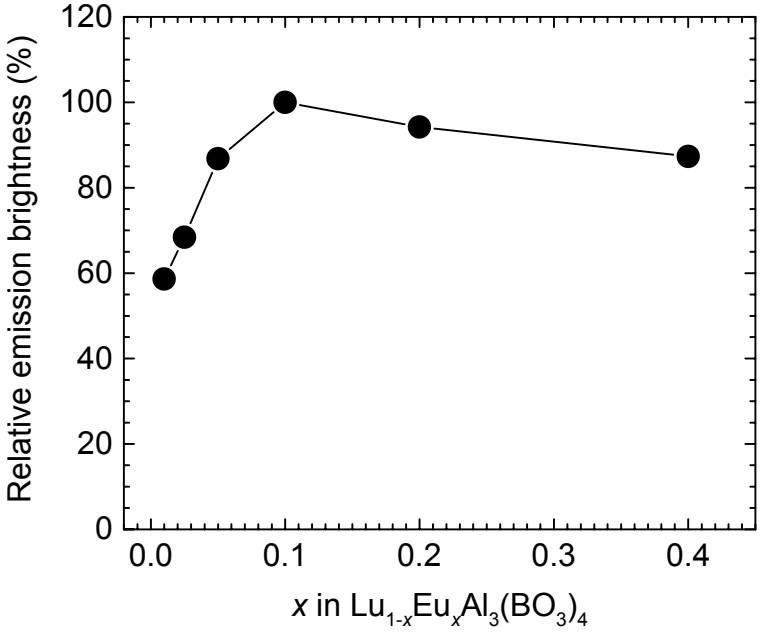

Figure 13.4. Europium concentration dependence of the brightness for the compounds of $Lu_{1-x}Eu_xAl_3(BO_3)_4$ ($0 \leq x \leq 0.4$) under the charge-transfer excitation.

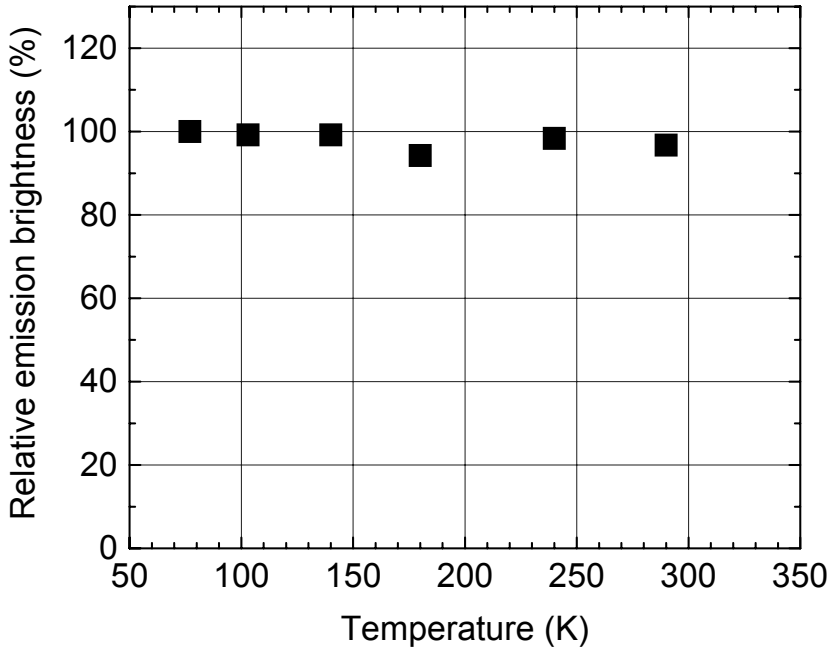

Figure 13.5. Temperature dependence of the emission brightness of the $Lu_{0.9}Eu_{0.1}Al_3(BO_3)_4$.

Vacuum ultraviolet (VUV) excitation spectra of $Lu_{0.9}Eu_{0.1}Al_3(BO_3)_4$, $Lu_{0.75}Gd_{0.15}Eu_{0.1}Al_3(BO_3)_4$, and $Lu_{0.75}Gd_{0.15}Eu_{0.1}Al_3(BO_3)_4$, along with that of $Lu_{0.9}Eu_{0.1}Al_3(BO_3)_4$ prepared without $LiBO_2$ as flux are presented in Figure 13.6. The flux improves the emission brightness of $Lu_{0.9}Eu_{0.1}Al_3(BO_3)_4$ in the 150 – 280 nm region. Co-doping with Gd^{3+} ions decreases the luminescence intensity. By using sodium salicylate as a standard, the relative quantum efficiencies in the system $(Lu_{1-y}Y_y)_{0.9}Eu_{0.1}Al_3(BO_3)_4$ (y = 0, 0.4, and 1) are estimated to be 0.70 (y = 0), 0.69 (y = 0.4), and 0.53 (y = 1) under 147-nm excitation.

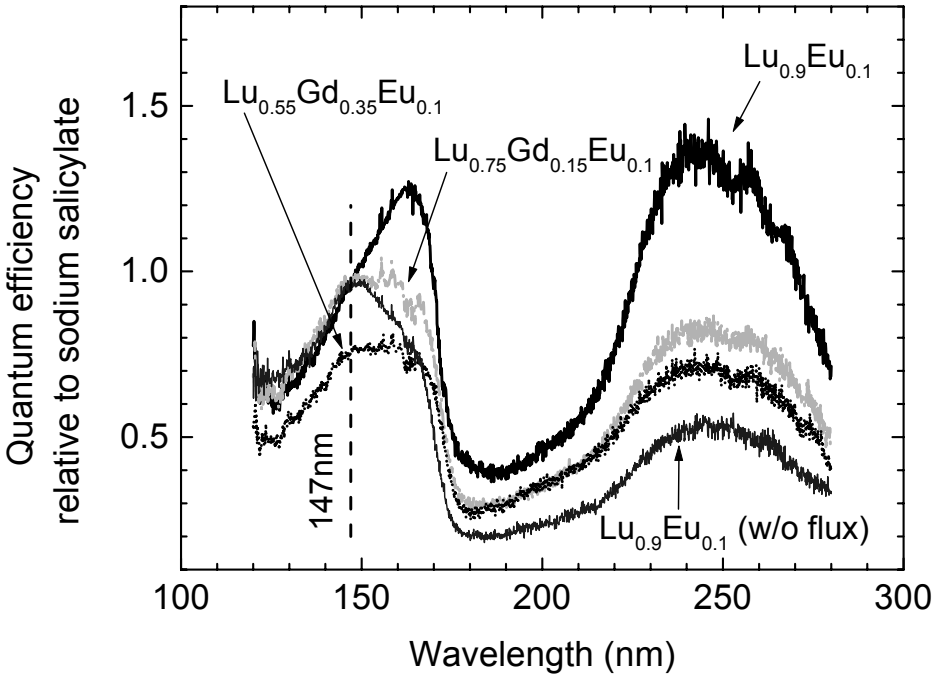

Figure 13.6. Vacuum ultraviolet (VUV) excitation spectra of $Lu_{0.9}Eu_{0.1}Al_3(BO_3)_4$, $Lu_{0.75}Gd_{0.15}Eu_{0.1}Al_3(BO_3)_4$, and $Lu_{0.75}Gd_{0.15}Eu_{0.1}Al_3(BO_3)_4$, along with that of $Lu_{0.9}Eu_{0.1}Al_3(BO_3)_4$ prepared without $LiBO_2$ as flux.

Excitation spectra of $Lu_{1-x}Tb_xAl_3(BO_3)_4$ (x = 0.05, 0.2, and 0.4) in the 250-450 nm wavelength range from monitoring the $^5D_4 \rightarrow {}^7F_5$ emission wavelength of 546 nm are depicted in Figure 13.7. They are mainly composed of transitions between the energy levels of the $4f^8$ configuration of Tb^{3+} ion. The $4f^8 \rightarrow 5f^7 5d^1$ transition of Tb^{3+} ion is not clearly observed in the 250-450 nm wavelength region. In excitation spectra of $Y_{0.85}Tb_{0.15}Al_3(BO_3)_4$ and $Gd_{.85}Tb_{0.15}Al_3(BO_3)_4$ the $4f^8 \rightarrow 5f^7 5d^1$ transition of Tb^{3+} ion was observed at around 220 nm [4].

Emission spectra of $Lu_{1-x}Tb_xAl_3(BO_3)_4$ (x = 0.05, and 0.4) under 375-nm excitation are composed of $^5D_4 \rightarrow {}^7F_J$ emission transitions (Figure 13.7). The emission of $Lu_{1-x}Tb_xAl_3(BO_3)_4$ (x = 0.05, 0.1, 0.2, 0.3, and 0.4) is centered in the green with chromaticity coordinates covering the ranges x = 0.32-0.34 and y = 0.58-0.59, which are comparable to the values x = 0.33 and y = 0.61 of commercial $YBO_3:Tb^{3+}$ [11]. The terbium concentration dependence of the brightness for the compounds of $Lu_{1-x}Tb_xAl_3(BO_3)_4$ ($0 \leq x \leq 0.4$) under 375-nm excitation is presented in Figure 13.8.

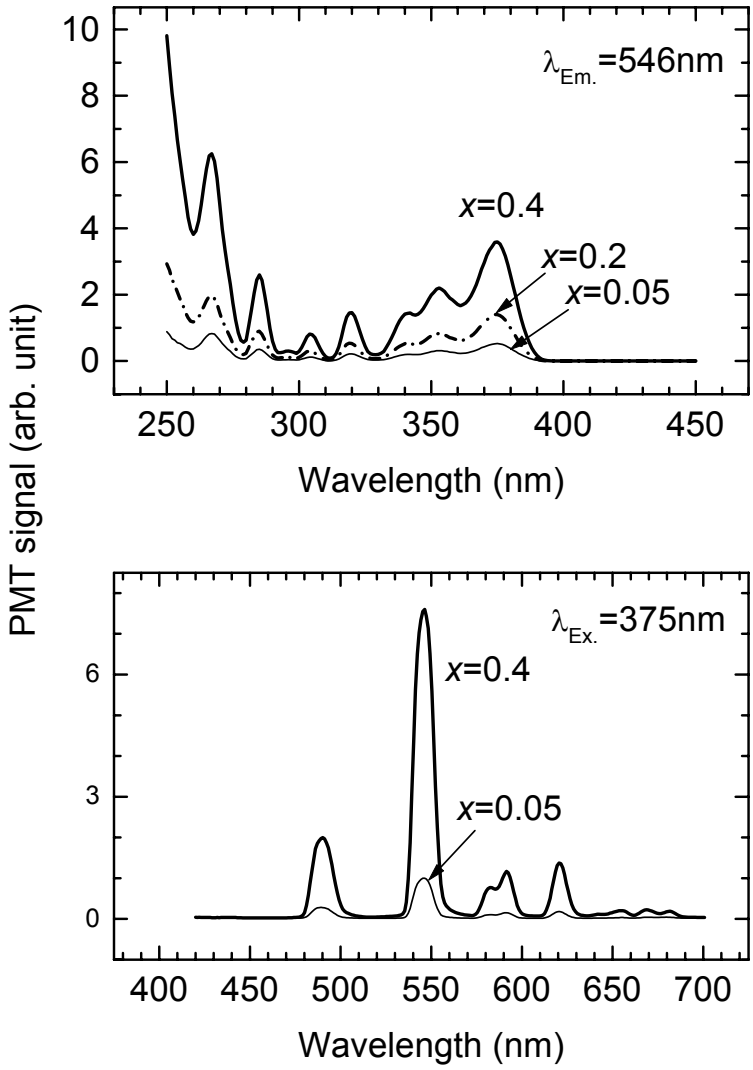

Figure 13.7. Excitation spectra of $Lu_{1-x}Tb_xAl_3(BO_3)_4$ (x = 0.05, 0.2, and 0.4) with $\lambda_{Em.}$ = 546 nm (top), and emission spectra of $Lu_{1-x}Tb_xAl_3(BO_3)_4$ (x = 0.05, and 0.4) under 375-nm excitation (bottom).

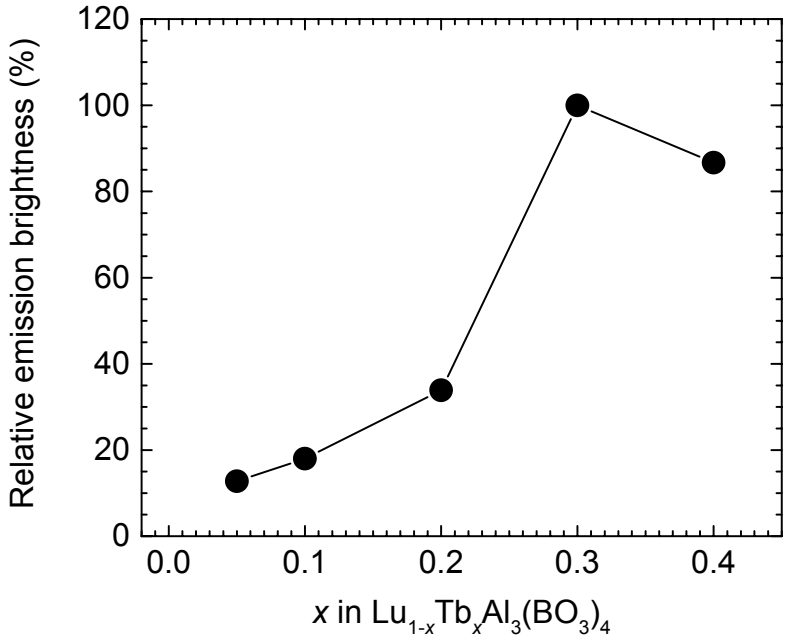

Figure 13.8. Terbium concentration dependence of the emission brightness for the compounds of $Lu_{1-x}Tb_xAl_3(BO_3)_4$ ($0 \leq x \leq 0.4$) under 375-nm excitation.

The excitation spectrum of $Lu_{0.98}Ce_{0.02}Al_3(BO_3)_4$ recorded at room temperature is composed of three bands at 31,000 cm^{-1}, 37,000 cm^{-1}, and 40,000 cm^{-1} (Figure 13.9), which correspond to the transitions from the ground state of the $4f^1$ configuration (^2F level) to three crystal –field levels (A_1 + $2E$) of the $5d^1$ configuration (^2D level) of the Ce^{3+} ion in a distorted trigonal prism (D_3 symmetry) of O^{2-} ions [12]. The excitation bands of $Lu_{0.98}Ce_{0.02}Al_3(BO_3)_4$ are almost identical to those observed in $Y_{0.99}Ce_{0.01}Al_3(BO_3)_4$ [13]. The room-temperature emission spectrum of $Lu_{0.98}Ce_{0.02}Al_3(BO_3)_4$ reveals two emission bands at 27,000 cm^{-1} and 29,000 cm^{-1}, which are assigned to transitions from the lowest crystal-field level of the $5d^1$ configuration to the two $4f^1$ state levels of $^2F_{5/2}$ and $^2F_{7/2}$. The energy difference between $^2F_{5/2}$ and $^2F_{7/2}$ levels is about 2,000 cm^{-1}. The emission spectrum of $Lu_{0.98}Ce_{0.02}Al_3(BO_3)_4$ is also very similar to the emission spectrum observed in $Y_{0.99}Ce_{0.01}Al_3(BO_3)_4$ at 300 K [14].

Excitation spectra of $Lu_{0.9}Tb_{0.1}Al_3(BO_3)_4$, $Lu_{0.95}Ce_{0.05}Al_3(BO_3)_4$, and $Lu_{0.85}Ce_{0.05}Tb_{0.1}Al_3(BO_3)_4$ along with the emission spectrum of $Lu_{0.95}Ce_{0.05}Al_3(BO_3)_4$ are summarized in Figure 13.10. Remarkable spectral overlap between the excitation spectrum of Tb^{3+} ion and the emission spectrum of Ce^{3+} ion is observed. The excitation spectrum of $Lu_{0.85}Ce_{0.05}Tb_{0.1}Al_3(BO_3)_4$ monitored at the $^5D_4 \rightarrow {}^7F_5$ emission of Tb^{3+} ion reveals mainly $4f^1 \rightarrow 5d^1$ excitation of Ce^{3+} ion, which shows clearly the energy transfer from Ce^{3+} ions to Tb^{3+} ions.

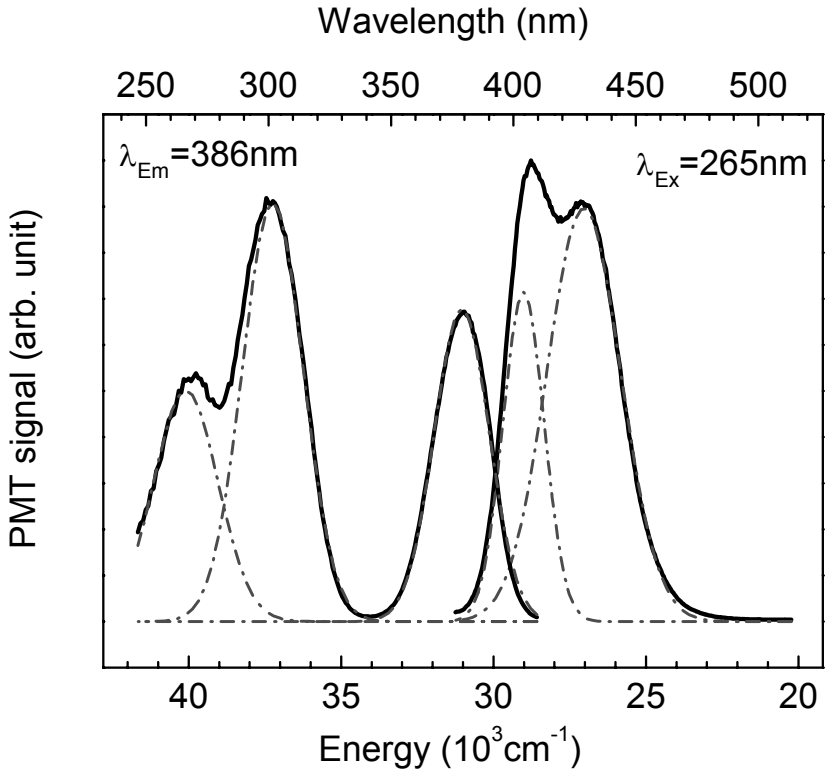

Figure 13.9. Excitation ($\lambda_{Em.}$ = 386 nm) and emission ($\lambda_{Ex.}$ = 386 nm) spectra for $Lu_{0.98}Ce_{0.02}Al_3(BO_3)_4$ at room temperature.

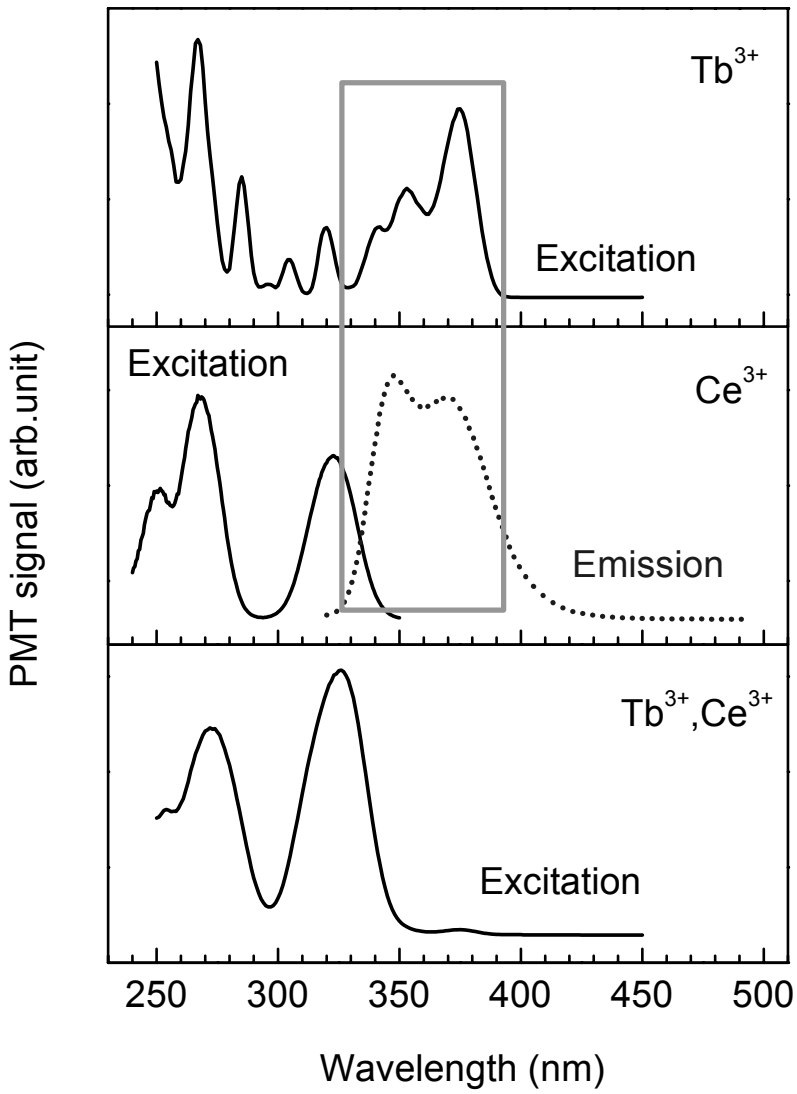

Figure 13.10. Excitation spectrum of $Lu_{0.9}Tb_{0.1}Al_3(BO_3)_4$ ($\lambda_{Em.}$ = 546 nm) (top); excitation ($\lambda_{Em.}$ = 386 nm) and emission ($\lambda_{Ex.}$ = 265 nm) spectra for $Lu_{0.95}Ce_{0.05}Al_3(BO_3)_4$ (middle); excitation spectrum ($\lambda_{Em.}$ = 546 nm) for $Lu_{0.85}Ce_{0.05}Tb_{0.1}Al_3(BO_3)_4$ (bottom).

Room temperature emission spectrum of $Lu_{0.85}Ce_{0.05}Tb_{0.1}Al_3(BO_3)_4$ under $4f^1 \rightarrow 5d^1$ excitation (265 nm) of Ce^{3+} ion is depicted in Figure 13.11. It shows emission of Tb^{3+} ion as well as emission of Ce^{3+} ion. The ratio of the integrated area of the emission band of the Tb^{3+} ion to that of the Ce^{3+} ion is 0.94. Assuming efficient energy transfer between nearest neighbors only and neglecting Ce^{3+} to Ce^{3+} transfer, the ration of the terbium to the cerium quantum output can be given as

$$q_{Tb}/q_{Ce} = [1-(1-x_{Tb})^k]/(1-x_{Tb})^k$$

, where k is the number of nearest Tb^{3+} neighbor sites to which Ce^{3+} can transfer its energy, and $(1-x_{Tb})$ represents the probability that such a site is not occupied by a Tb^{3+} ion [15, 16]. In $Lu_{0.85}Ce_{0.05}Tb_{0.1}Al_3(BO_3)_4$ the ratio is 0.89 with $k = 6$ and $x_{Tb} = 0.1$, in good agreement with the observation in the emission spectrum, supporting the negligible Ce^{3+} to Ce^{3+} energy transfer, which is observed in other systems such as $Y_{0.99-x}Ce_xTb_{0.01}Al_3(BO_3)_4$., and $La_{1-x}Ce_xP_5O_{14}$ [17]

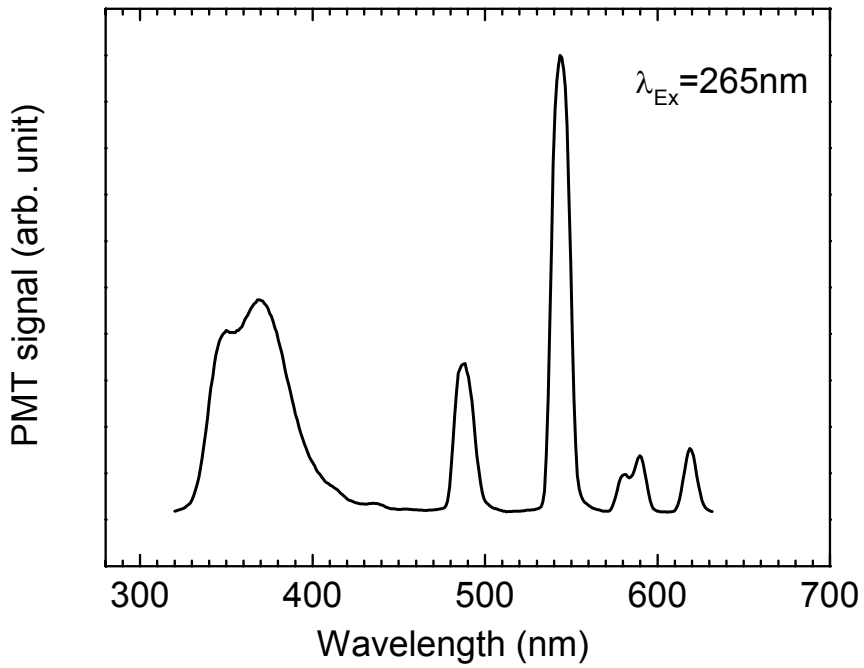

Figure 13.11. Room temperature emission spectrum of $Lu_{0.85}Ce_{0.05}Tb_{0.1}Al_3(BO_3)_4$ under $4f^1 \rightarrow 5d^1$ excitation (265 nm) of Ce^{3+} ion.

CONCLUSION

For the first time, luminescence properties of $LuAl_3(BO_3)_4$:Ln (Ln = Eu, Tb) under ultraviolet excitation were measured. Samples of $Lu_{1-x}Eu_xAl_3(BO_3)_4$ exhibit maximum emission at x = 0.1 under charge-transfer excitation. $Lu_{0.9}Eu_{0.1}Al_3(BO_3)_4$ exhibits saturated red emission, no thermal quenching in the 77-290 K temperature range, and a quantum efficiency similar to that of sodium salicylate for 147-nm excitation. Samples of $Lu_{1-x}Tb_xAl_3(BO_3)_4$ exhibit maximum emission at x = 0.3 under 375-nm excitation. Energy transfer from Ce^{3+} to Tb^{3+} has been observed in $Lu_{0.85}Tb_{0.1}Ce_{0.05}Al_3(BO_3)_4$.

ACKNOWLEDGEMENTS

We thank Yi Zhou, Dr. Weiji Jia, and Dr. Richard Meltzer at the University of Georgia for the vacuum ultraviolet excitation measurements.

REFERENCES

[1] C. R. Ronda, *J. Alloys Compd.*, **225**, 534 (1995).

[2] C.-H. Park, and D. A. Keszler, *submitted to J. Lumin.*

[3] C.-H. Park, and D. A. Keszler, *unpublished.*

[4] Y. Hongpeng, G. Hong, X. Zeng, C.-H. Kim, C.-H. Pyun, B.-Y. Yu, and H.-S. Bae, *J. Phys. Chem. Solids*, **61**, 1985 (2000).

[5] Y. Wang, K. Uheda, H. Takizawa, U. Mizumoto, and T. Endo, *J. Electrochem. Soc.*, **148(8)**, G430, (2001).

[6] K.-G. Lee, B.-Y. Yu, C.-H. Pyun, and S.-I. Moh, *Solid State Comm.*, **122**, 485 (2002).

[7] G. Blasse, and A. Bril, *Phil. Tech. Rev.*, **31**, 303 (1970).

[8] R. D. Shannon, *Acta Crystallogr.*, **A32**, 751 (1976).

[9] G. Blasse, *J. Chem. Phys.*, **46(7)**, 2583 (1967).

[10] F. Kellendonk, and G. Blasse, *J. Chem. Phys.*, **75(2)**, 561 (1981).

[11] J. Koike, T. Kojima, R. Toyonaga, A. Kagami, T. Hase, and S. Inaho, *J. Electrochem. Soc.*, **126(6)**, 1008 (1979).

[12] F. A. Cotton, *Chemical Applications of Group Theory*, 3rd ed., John Wiley & Sons, Singapore (1990).

[13] G. Blasse, and A. Bril, *J. Chem. Phys.*, **47(12)**, 5139 (1967).

[14] F. Kellendonk, T. Van den Belt, and G. Blasse, *J. Chem. Phys.*, **76(3)**, 1194 (1982).

[15] F. Kellendonk, M. A. van Os, and G. Blasse, *Chem. Phys. Lett*, **61(2)**, 239 (1979).

[16] H. S. Kiliaan, F. P. van Herwijnen, and G. Blasse, *J. Solid State Chem.*, **74**, 39 (1988).

[17] B. Blanzat, J. P. Denis, C. Pannel, and C. Barthou, *Mater. Res. Bull.*, **12**, 455 (1977).

CHAPTER 14

CRYSTAL SRUCTURES AND Eu^{2+} LUMINESCENCE OF $M_3Sc_2(BO_3)_4$ (M = Ba, Sr)

Cheol-Hee Park, Ning Ye, and Douglas A. Keszler

submitted to *Solid State Sciences*
23, rue Linois, 75724 Paris cedex 15, France

ABSTRACT

The crystal structures of the layer compounds $Ba_3Sc_2(BO_3)_4$, $BaSr_2Sc_2(BO_3)_4$, and $Sr_3Sc_2(BO_3)_4$ have been established by single-crystal X-ray diffraction. $Ba_3Sc_2(BO_3)_4$ crystallizes in space group $P\bar{3}m1$ with a = 5.295(3) Å and c = 11.068(4) Å. $BaSr_2Sc_2(BO_3)_4$ crystallizes in space group $C2/c$ with a = 9.063(4) Å, b = 5.163(4) Å, c = 21.778(4) Å and β = 90.32(3)º. $Sr_3Sc_2(BO_3)_4$ crystallizes in space group $P2_1/c$ with a = 8.977(3) Å, b = 10.371(2) Å, c = 11.509(4) Å and β = 105.00(2)º. Under Hg-lamp excitation, $Ba_{2.94}Sc_2(BO_3)_4:Eu_{0.06}^{2+}$ exhibits yellow luminescence with chromaticity coordinates x = 0.47 and y = 0.50, and $Ba_{0.94}Sr_2Sc_2(BO_3)_4:Eu_{0.06}^{2+}$ exhibits yellow-green emission with x = 0.31 and y = 0.56.

INTRODUCTION

$Ba_3La_2(BO_3)_4$ [1], $Sr_3La_2(BO_3)_4$ [2], and $Ca_3La_2(BO_3)_4$ [3] are three examples of compounds having the nominal formula $A_3M_2(BO_3)_4$. Each of these materials adopts a complex three-dimensional structure. If the La is replaced with the smaller atom Sc in $A_3La_2(BO_3)_4$, a new type of layer structure $A_3Sc_2(BO_3)_4$ may be formed. In this contribution we describe the preparation and structure of the new compounds $Ba_3Sc_2(BO_3)_4$, $BaSr_2Sc_2(BO_3)_4$, and $Sr_3Sc_2(BO_3)_4$ along with Eu^{2+} luminescence.

Substitutional alkaline-earth sites easily accommodate one of the more important activator ions of phosphors, *i.e.*, the divalent Eu ion. So, we have prepared Eu^{2+}-doped $Ba_3Sc_2(BO_3)_4$ and $BaSr_2Sc_2(BO_3)_4$ to investigate their optical properties. The luminescence of the Eu^{2+} ion in inorganic hosts is generally associated with transitions between the $^8S_{7/2}$ ($4f^7$) ground state and the crystal field components of the $4f^6 5d$ excited-state configurations, so that its emission is typically quite broad. The energetic position of the emission band is strongly dependent on the host crystal, changing from the near UV to the red. This dependence is interpreted in terms of the strength of crystal field, covalency, and the Stokes shift [4-6].

Because the emission transition ($4f^6 5d \rightarrow 4f^7$) is parity allowed, its cross section is large and its radiative lifetime is relatively short [7]. These properties present wide applications such as lamps in copying machine with

$(Sr,Mg)_2P_2O_7:Eu^{2+}$, a blue component of three-band fluorescent lamps and plasma display panels with $BaMgAl_{10}O_{17}:Eu^{2+}$, and a storage phosphor for X-ray imaging with $Ba(F,Br):Eu^{2+}$ [8].

EXPERIMENTAL

Preparation Processes

Single crystals of the title compounds were grown by the flux method, using the alkaline-earth metal meta borates as fluxes. $Ba_3Sc_2(BO_3)_4$ and $Sr_3Sc_2(BO_3)_4$ crystals were grown by using BaB_2O_4 and SrB_2O_4, respectively, with a ratio of 1:2 of $M_3Sc_2(BO_3)_4$: MB_2O_4 (M = Ba, Sr). $BaSr_2Sc_2(BO_3)_4$ was grown with BaB_2O_4 and SrB_2O_4 with a ratio of 1: 0.66: 1.33 = $BaSr_2Sc_2(BO_3)_4$: BaB_2O_4: SrB_2O_4. The initial mixtures of $BaCO_3$ (Cerac, 99.9%), $SrCO_3$ (Alfa Aesar, 99.9), Sc_2O_3 (Stanford Materials, 99.95%), and B_2O_3 (Cerac, 99.9%) in proportions corresponding to each compound were ground, placed in Pt crucibles, and heated to 1423 K until they melted homogeneously. The samples were slowly cooled (8 K/h) to 1073 K and then quenched to room temperature. Colorless, transparent crystals of $Ba_3Sc_2(BO_3)_4$, $BaSr_2Sc_2(BO_3)_4$, and $Sr_3Sc_2(BO_3)_4$ were extracted from the solidified melts for single-crystal structure determinations.

Powder samples of compositions $Ba_{3-x}Eu_xSc_2(BO_3)_4$, $Ba_{1-x}Sr_2Eu_xSc_2(BO_3)_4$, and $Sr_{3-x}Eu_xSc_2(BO_3)_4$ were prepared by heating stoichiometric oxide mixtures at 1273 K under flowing $H_2(g)(5\%)/N_2(g)(95\%)$ for 12 hours. The purities of all

samples were checked with X-ray diffraction measurements by using Cu $K\alpha$ radiation. The compounds $Ba_{3-x}Eu_xSc_2(BO_3)_4$ and $Ba_{1-x}Eu_xSr_2Sc_2(BO_3)_4$ exhibit characteristic Eu^{2+} band emission, but $Sr_{2.94}Eu_{0.06}Sc_2(BO_3)_4$ doesn't show any obvious Eu^{2+} luminescence, even when the sample is prepared under flowing H_2(g).

X-Ray and Optical Measurements

X-ray diffraction patterns of the polycrystalline products were obtained on a Siemens D5000 diffractometer by using Cu$K\alpha$ radiation. Single-crystal X-ray diffraction data were obtained at room temperature on a Rigaku AFC6R diffractometer with monochromatic Mo$K\alpha$ radiation (λ = 0.71073 Å).

Photoluminescence measurements were made with an Oriel 300-W Xe lamp and a Cary model-15 prism monochromator for excitation. For detection, emitted light was passed through an Oriel 22500 1/8-m monochromator and monitored with a Hamamatsu R636-10 photomultiplier tube. Each spectrum was corrected for the throughput and response of the system by using Rhodamine B and a standardized tungsten lamp. Variable-temperature spectra over the temperature range 77-280 K were recorded by using a Cryo Industries R102 flow cryostat equipped with a Conductus temperature controller.

Structure determinations

For each crystal, cell constants and orientation matrixes for data collection were obtained from least-squares refinements with 25 automatically centered

reflections in the range $25^{\circ} < 2\theta < 35^{\circ}$; no decay in intensity was noted during data collection. The structures were solved and then refined by using full-matrix least-squares refinement on F^2 with the program SHELXL-97 [9] as programmed in the software suite WinGX v1.64.03 [10]. Crystal data and refinement summaries are given for $Ba_3Sc_2(BO_3)_4$, $BaSr_2Sc_2(BO_3)_4$, and $Sr_3Sc_2(BO_3)_4$ in Table 14.1. Final atomic coordinates and equivalent isotropic displacement parameters are listed in Tables 14.2, 14.3, and 14.4.

TABLE 14.1. Crystal data and structure refinement for $Ba_3Sc_2(BO_3)_4$, $BaSr_2Sc_2(BO_3)_4$, and $Sr_3Sc_2(BO_3)_4$.

Formula	$Ba_3Sc_2(BO_3)_4$	$BaSr_2Sc_2(BO_3)_4$	$Sr_3Sc_2(BO_3)_4$
Formula weight (amu)	737.18	637.74	588.02
Temperature (K)	290(2)	290(2)	290(2)
Wavelength (Å)	0.71073	0.71073	0.71073
Space group	$P\bar{3}m1$	$C2/c$	$P2_1/c$
a (Å)	5.295(3)	9.063(4)	8.977(3)
b (Å)	5.295(3)	5.163(4)	10.371(2)
c (Å)	11.068(4)	21.778(4)	11.509(4)
β (°)	-	90.32(3)	105.00(2)
Volume (Å^3)	268.7(2)	1019.0(9)	1035.0(5)
Z	1	4	4
dcalc.(g/cm^3)	4.556	4.157	3.774
Absorption coefficient (mm^{-1})	12.09	15.54	16.672
F(000)	326	1160	1088
Crystal size (mm^3)	0.1×0.1×0.1	0.1×0.1×0.1	0.1×0.1×0.1
θ range for data collection (°)	1.84–30.14	1.87–30.06	2.35–30.06
Index range	$-7 \le h \le 7$, $-7 \le k \le 7$, $-15 \le l \le 15$	$0 \le h \le 12$, $-7 \le k \le 7$, $-30 \le l \le 30$	$0 \le h \le 12$, $-14 \le k \le 14$, $-16 \le l \le 15$

TABLE 14.1 (Continued)

Reflections collected	3166	3025	6262
Independent reflection	352 [R_{int} = 0.1749]	1512 [R_{int} = 0.0497]	3040 [R_{int} = 0.1394]
Reflection with $I > 2\sigma(I)$	348	1333	2057
Completeness to θ = 30.0º	99.7%	100%	100%
Absorption correction	none	none	none
Refinement method	Full-matrix least squares on F^2		
Data/restrains/parameters	352/0/28	1512/0/97	3040/0/191
Goodness-of-fit on F^2	0.917	1.11	1.042
R indices [$I>2\sigma(I)$] $R1$	0.0278	0.0458	0.0772
R indices (all data) $R1$/w$R2$	0.0280/0.0836	0.0527/0.1295	0.0962/0.2035
Largest diff. peak / hole	1.187 / -1.394 e. Å^{-3}	3.123 /-3.929 e. Å^{-3}	5.671/-3.398 e. Å^{-3}

TABLE 14.2. Atomic positions and isotropic displacement factors for $Ba_3Sc_2(BO_3)_4$.

	x	*y*	*z*	U_{eq} (Å^2) × 10^3
Ba(1)	0	0	0	18.1(3)
Ba(2)	-1/3	1/3	0.41400(4)	9.3(3)
Sc	-1/3	1/3	-0.23357(18)	9.2(4)
O(1)	-0.6968(8)	0.1516(4)	0.6370(3)	13.4(7)
O(2)	-0.4814(6)	0.0372(12)	0.1368(5)	39.3(14)
B(1)	0	0	0.3605(8)	6.3(15)
B(2)	-1/3	1/3	0.1357(10)	2.2(2)

TABLE 14.3. Atomic positions and isotropic displacement factors for $BaSr_2Sc_2(BO_3)_4$.

	x	*y*	*z*	U_{eq} (Å^2) × 10^3
Ba	½	0.04411(12)	¾	16.7(2)
Sr	0.83220(6)	0.00945(11)	0.45745(3)	9.7(2)
Sc	0.83488(13)	0.0215(2)	0.62983(6)	8.8(3)
B(1)	0.1673(8)	0.0631(15)	0.6804(3)	11.6(12)
B(2)	0.4981(8)	0.0098(13)	0.4334(3)	9.4(12)
O(1)	0.9273(5)	-0.2803(9)	0.5717(2)	13.5(8)
O(2)	0.7496(6)	-0.2221(10)	0.6944(2)	19.2(10)
O(3)	0.8449(5)	-0.4808(8)	0.4360(2)	12.1(9)
O(4)	0.5748(5)	0.2404(9)	0.4429(2)	11.5(8)
O(5)	0.5162(6)	-0.4220(13)	0.6815(3)	27.4(12)
O(6)	0.2308(7)	-0.1588(11)	0.6617(3)	25.5(12)

TABLE 14.4. Atomic positions and isotropic displacement factors for $Sr_3Sc_2(BO_3)_4$.

	x	*y*	*z*	U_{eq} (Å^2) × 10^3
Sr(1)	0.11807(8)	0.62361(7)	0.19296(6)	11.1(2)
Sr(2)	-0.34871(7)	0.85735(7)	0.17723(6)	10.6(2)
Sr(3)	-0.34520(7)	0.39242(7)	0.18465(6)	10.7(2)
Sc(1)	0.24438(15)	0.87912(13)	0.00308(11)	6.9(3)
Sc(2)	0.25445(16)	0.37102(14)	0.01725(12)	7.2(3)
O(1)	-0.1276(6)	0.7600(5)	0.0981(4)	10.9(10)
O(2)	0.1252(6)	0.4865(5)	0.3830(5)	12.2(10)
O(3)	0.1103(6)	0.3814(5)	0.1338(4)	9.5(9)
O(4)	0.1254(6)	0.7602(5)	0.3844(5)	13.9(11)
O(5)	-0.1294(6)	0.4880(5)	0.0949(5)	14.5(11)
O(6)	-0.6066(6)	1.0066(5)	0.1186(5)	13.7(11)
O(7)	0.3839(6)	0.6291(5)	0.3808(5)	14.7(11)
O(8)	0.1103(6)	0.8689(5)	0.1260(4)	9.5(9)
O(9)	0.3797(6)	0.5096(5)	0.1395(4)	11.3(10)
O(10)	-0.3924(7)	0.7397(5)	0.3660(5)	14.1(11)
O(11)	0.3694(6)	0.7386(5)	0.1231(5)	12.4(10)
O(12)	-0.4178(7)	0.6231(5)	0.0865(5)	15.9(11)
B(1)	-0.0485(9)	0.8737(7)	0.1091(8)	9.1(14)
B(2)	-0.0456(10)	0.3720(8)	0.1137(7)	8.2(14)
B(3)	0.4399(9)	0.6231(8)	0.1154(7)	7.3(13)
B(4)	-0.5374(11)	1.1239(8)	0.1231(8)	11.6(15)

TABLE 14.5. Bond lengths (Å) and angles (°) for $Ba_3Sc_2(BO_3)_4$, $BaSr_2Sc_2(BO_3)_4$ and $Sr_3Sc_2(BO_3)_4$.

$Ba_3Sc_2(BO_3)_4$	
Ba(1)-O(2) × 12	3.054(3)
Ba(2)-O(1) × 6	2.710(2)
Ba(2)-O(1) × 3	2.978(4)
Sc-O(2) × 3	2.008(5)
Sc-O(1) × 3	2.197(4)
B(1)-O(1) × 3	1.391(4)
B(2)-O(2) × 3	1.358(6)
O(1)-B(1)-O(1)	119.96(3)
O(2)-B(2)-O(2)	119.99(2)

$BaSr_2Sc_2(BO_3)_4$	
Ba-O(2) × 2	2.836(6)
Ba-O(5) × 2	2.836(6)
Ba-O(2) × 2	2.917(6)
Ba-O(5) × 2	3.138(7)
Ba-O(6) × 2	3.236(6)
Ba-O(6) × 2	3.271(6)
Sr-O(3)	2.577(5)
Sr-O(4)	2.621(5)
Sr-O(4)	2.637(5)
Sr-O(4)	2.658(5)
Sr-O(1)	2.669(5)
Sr-O(3)	2.676(5)
Sr-O(1)	2.705(5)
Sr-O(6)	2.763(6)

$Sr_3Sc_2(BO_3)_4$	
Sr(1)-O(2)	2.596(6)
Sr(1)-O(3)	2.599(5)
Sr(1)-O(4)	2.605(6)
Sr(1)-O(1)	2.610(5)
Sr(1)-O(5)	2.624(5)
Sr(1)-O(8)	2.654(5)
Sr(1)-O(7)	2.775(6)
Sr(1)-O(9)	2.836(6)
Sr(1)-O(11)	2.845(6)
Sr(2)-O(1)	2.593(6)
Sr(2)-O(10)	2.607(5)
Sr(2)-O(3)	2.639(5)
Sr(2)-O(2)	2.650(6)
Sr(2)-O(12)	2.656(6)
Sr(2)-O(9)	2.708(5)
Sr(2)-O(6)	2.721(6)
Sr(2)-O(11)	2.737(6)
Sr(2)-O(7)	2.893(6)
Sr(3)-O(5)	2.616(6)
Sr(3)-O(8)	2.622(5)
Sr(3)-O(12)	2.652(5)
Sr(3)-O(9)	2.680(6)
Sr(3)-O(4)	2.686(6)
Sr(3)-O(6)	2.690(6)
Sr(3)-O(10)	2.772(6)

TABLE 14.5 (Continued)

Sr-O(3)	2.833(5)		Sr(3)-O(11)	2.780(6)
Sc-O(5)	2.008(5)		Sr(3)-O(7)	2.832(6)
Sc-O(6)	2.025(5)		Sc(1)-O(2)	2.056(5)
Sc-O(2)	2.041(5)		Sc(1)-O(8)	2.082(5)
Sc-O(4)	2.170(5)		Sc(1)-O(4)	2.084(5)
Sc-O(3)	2.174(5)		Sc(1)-O(6)	2.094(5)
Sc-O(1)	2.178(5)		Sc(1)-O(7)	2.113(6)
B(1)-O(6)	1.347(9)		Sc(1)-O(11)	2.118(5)
B(1)-O(2)	1.370(9)		Sc(2)-O(1)	2.030(5)
B(1)-O(5)	1.372(8)		Sc(2)-O(5)	2.076(5)
B(2)-O(1)	1.369(8)		Sc(2)-O(10)	2.081(5)
B(2)-O(3)	1.390(8)		Sc(2)-O(3)	2.093(5)
B(2)-O(4)	1.394(8)		Sc(2)-O(12)	2.117(6)
			Sc(2)-O(9)	2.119(5)
O(6)-B(1)-O(2)	121.5(6)		B(1)-O(2)	1.374(9)
O(6) -B(1)-O(5)	118.8(7)		B(1)-O(1)	1.364(9)
O(2) -B(1)-O(5)	119.6(6)		B(1)-O(8)	1.390(9)
O(1) -B(2)-O(3)	121.8(6)		B(2)-O(4)	1.366(9)
O(1) -B(2)-O(4)	120.3(6)		B(2)-O(3)	1.360(9)
O(3) -B(2)-O(4)	117.5(5)		B(2)-O(5)	1.408(10)
			B(3)-O(9)	1.353(9)
Average bond lengths and angles			B(3)-O(11)	1.371(9)
$Ba_3Sc_2(BO_3)_4$			B(3)-O(12)	1.400(10)
Ba(1)-O	3.054	3.00*	B(4)-O(10)	1.378(10)
Ba(2)-O	2.800	2.85*	B(4)-O(7)	1.391(11)
Sc-O	2.103	2.13*	B(4)-O(6)	1.360(9)
B-O	1.375	1.40*		

TABLE 14.5 (Continued)

O-B-O	119.98		O(1)-B(1)-O(2)	119.0(7)
$BaSr_2Sc_2(BO_3)_4$			O(1) -B(1)-O(8)	118.3(6)
Ba-O	3.039	2.99*	O(2) -B(1)-O(8)	122.3(6)
Sr-O	2.682	2.69*	O(3) -B(2)-O(4)	125.5(7)
Sc-O	2.099	2.12*	O(3) -B(2)-O(5)	116.7(6)
B-O	1.374	1.39*	O(4) -B(2)-O(5)	117.7(7)
O-B-O	119.92		O(9) -B(3)-O(11)	122.0(7)
$Sr_3Sc_2(BO_3)_4$			O(9) -B(3)-O(12)	119.1(7)
Sr-O	2.692	2.69*	O(11)-B(3)-O(12)	118.8(7)
Sc-O	2.089	2.12*	O(6) -B(4)-O(10)	124.5(8)
B-O	1.376	1.39*	O(6) -B(4)-O(7)	118.6(7)
O -B-O	119.94		O(10)-B(4)-O(7)	116.8(7)

* Bond distances obtained from the Shannon radii [11].

RESULTS

Structure Description

Some selected bond length and bond angle values are given in Table 14.5. The values of averaged bond length and bond angle for each compound, as well as the bond distances obtained from the Shannon radii, are also given in Table 14.5. The X-ray diffraction powder patterns calculated based on these structures closely matched observed powder patterns. All three compounds crystallize in similar structures characterized by planes of aligned BO_3 triangles that are alternately interleaved by layers of Sc and alkaline-earth metal atoms (Figure 14.1).

In each structure, distorted Sc-centered octahedra share vertexes with the BO_3 groups to form the layer motif found in the mineral calcite, *cf.*, Figures 14.1 and 14.2. The structural details of these calcite-like sheets are largely determined by the amounts and disposition of the Ba and Sr atoms in the structures. As shown in Figure 14.1, the calcite layers of $Ba_3Sc_2(BO_3)_4$ pack in an ABAB. . . sequence with the crystallographically distinct atoms Ba1 and Ba2 packed in separate layers in the ratio 1:2 = Ba1:Ba2. The structure of $BaSr_2Sc_3(BO_3)_4$ mimics that of $Ba_3Sc_2(BO_3)_4$, except the calcite layers pack in an ABCABC . . . manner, and the Sr atom preferentially occupies a site that is distributed similar to that of the Ba2 atoms. In $Sr_3Sc_2(BO_3)_4$, the packing sequence returns to ABAB . . ., and the three crystallographically distinct Sr atoms are disposed in a manner similar to that of the Sr atoms in $BaSr_2Sc_3(BO_3)_4$, containing layers of parallel or nearly parallel aligned

BO_3 triangular planes linked alternately by layers of Sc and alkaline-earth metal atoms (Figure 14.1). In trigonal $Ba_3Sc_2(BO_3)_4$, layers of flat BO_3 groups extend orthogonal to the c axis. The six O atoms around the Sc atom distort slightly from an ideal octahedron.

In $Ba_3Sc_2(BO_3)_4$, Ba1 is 12-coodinated by O atoms with a unique bond length of 3.055 Å, forming a hexagonal prism with D_{3d} symmetry (Figure 14.3(a)). Ba2 is nine coordinate, sitting in a hexagonal base-trigonal base environment with C_{3v} symmetry (Figure 14.3(b)). The six O atoms lying on the hexagonal plane are bonded to the Ba2 atoms at a distance of 2.710 Å, and the three O atoms lying on the trigonal base are located at a distance of 2.978 Å. These distances are in good agreement with Ba-O distances of 2.731–2.976 Å for $Ba_2Mg(BO_3)_2$ [12] and 2.72–2.88 Å for $Ba_3Sc(BO_3)_3$ [13], all for the same type of 9-coordinate Ba atom. Each $Ba2O_9$ polyhedron is connected to three adjacent ones by sharing its three rectangular faces. The 9-vertex polyhedron also shares its trigonal base with Sc-centered octahedron, forming a relatively compact Buetschliite-like $[K_2Ca(CO_3)_2]$ [14] block compared to the Ba1 layer.

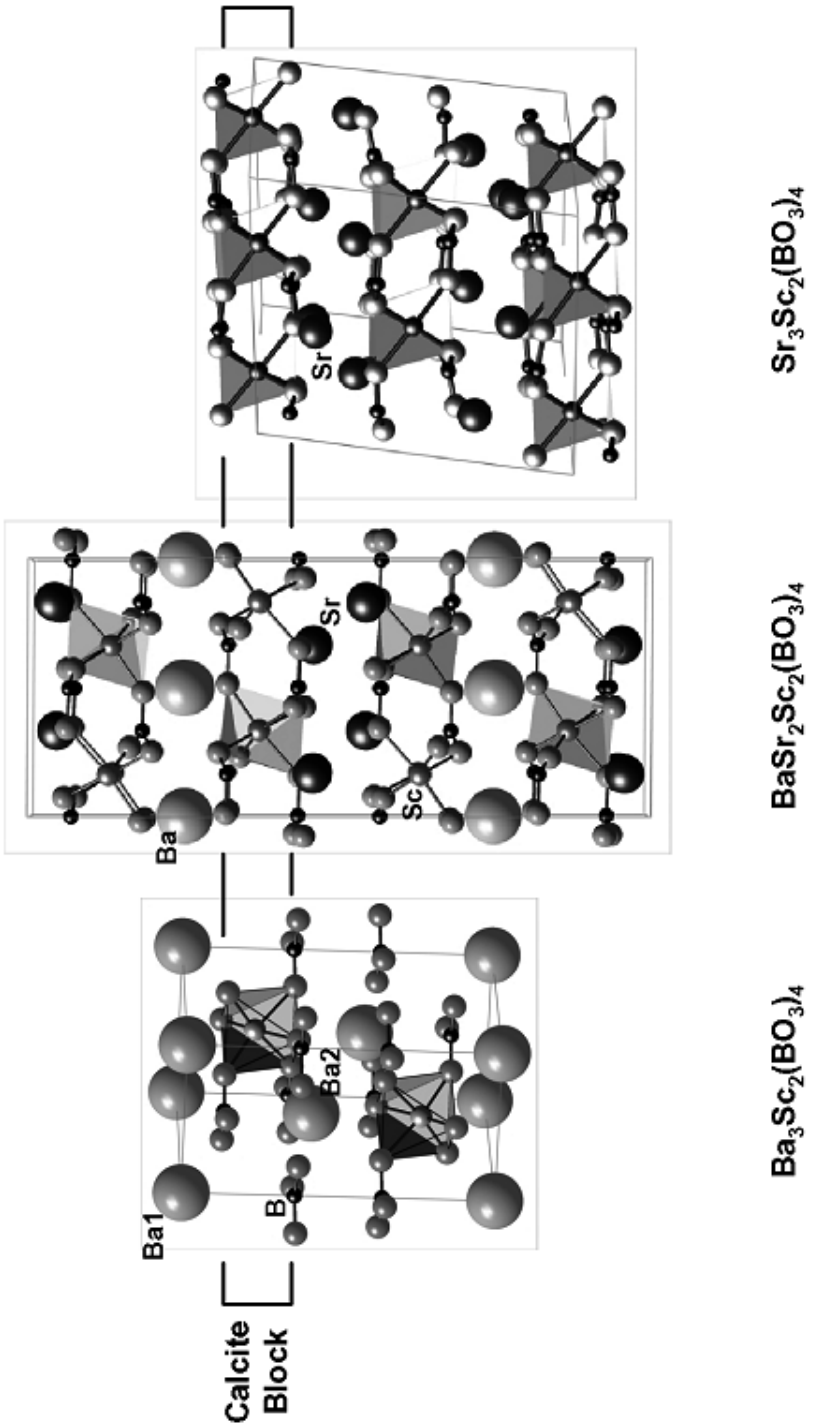

Figure 14.1. Projective view of the structures $Ba_3Sc_2(BO_3)_4$, $BaSr_2Sc_2(BO_3)_4$, and $Sr_3Sc_2(BO_3)_4$ with calcite blocks and ScO_6 octahedra.

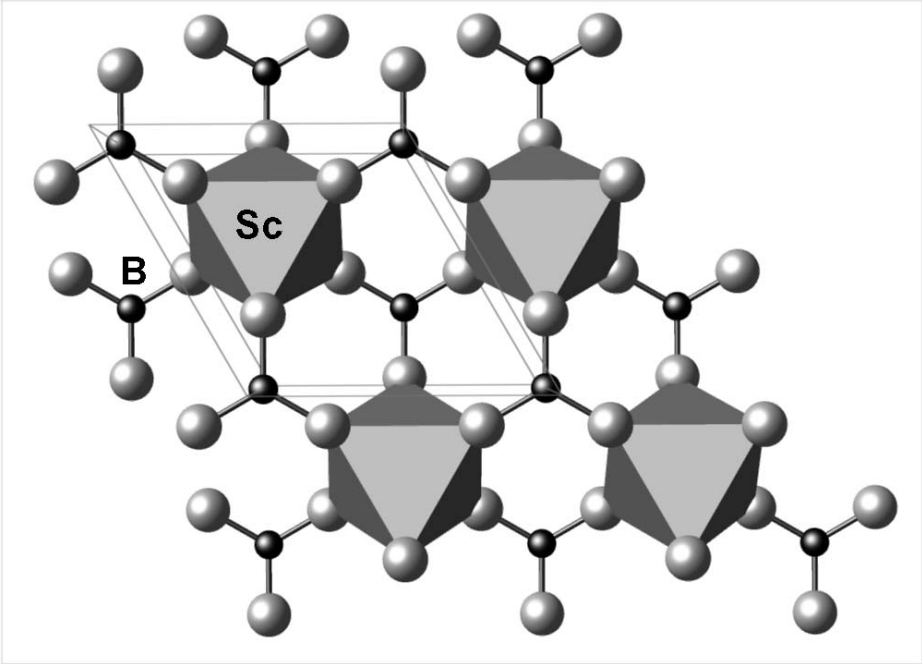

Figure 14.2. Projection of calcite block along trigonal axis with BO_3 triangular and ScO_6 octahedra.

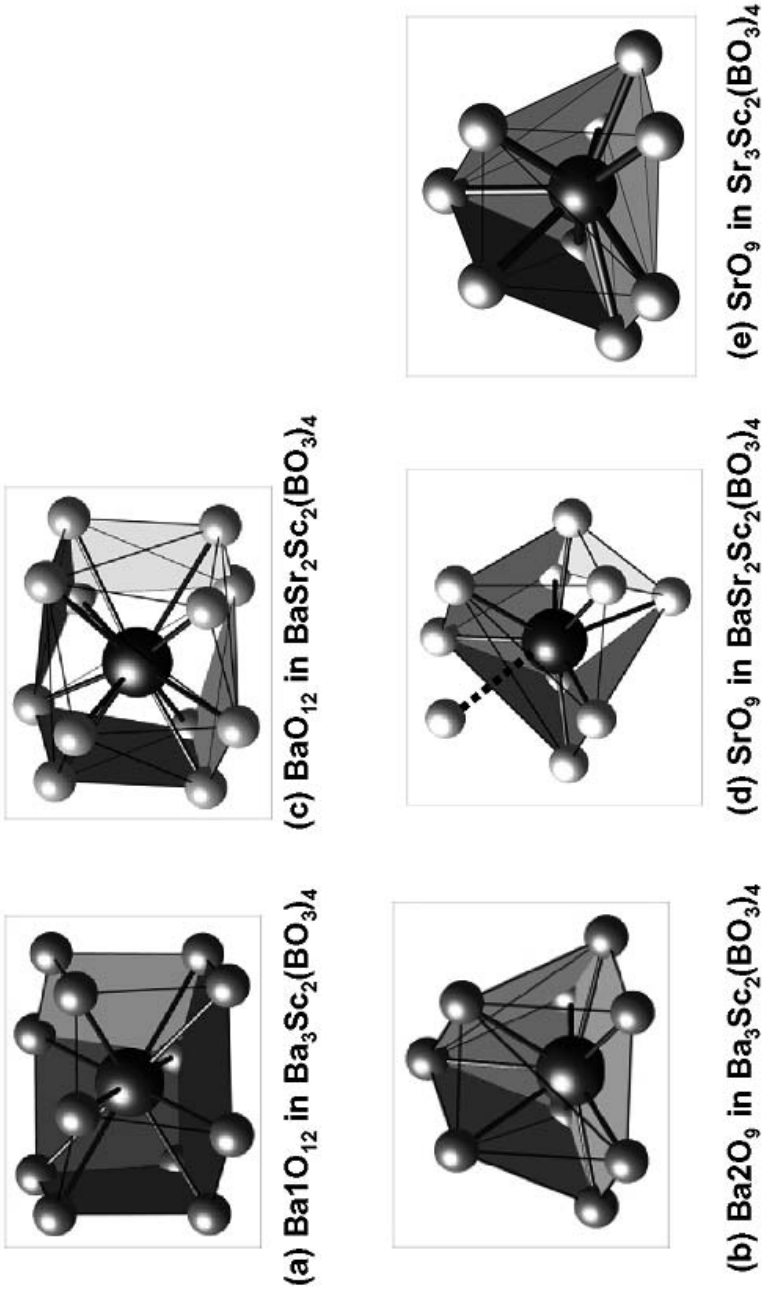

Figure 14.3. Barium and strontium oxygen environment for $Ba1O_{12}$ in (a) $Ba_3Sc_2(BO_3)_4$, (b) $Ba2O_9$ in $Ba_3Sc_2(BO_3)_4$, (c) BaO_{12} in $BaSr_2Sc_2(BO_3)_4$, (d) SrO_9 in $BaSr_2Sc_2(BO_3)_4$, and (e) SrO_9 in $Sr_3Sc_2(BO_3)_4$.

The calcite blocks in monoclinic $BaSr_2Sc_2(BO_3)_4$ remain similar to those in $Ba_3Sc_2(BO_3)_4$, except they exist in a lower symmetric manner (Figure 14.1). The BO_3 groups tilt out of the average plane and the Sc-centered octahedra are distorted. The Ba atoms are located in an environment similar to that of Ba1 in $Ba_3Sc_2(BO_3)_4$, but they are strongly distorted from an hexagonal prism (Figure 14.3(c)). The average Ba-O bond length is 3.039 Å, which is close to that of Ba1 in $Ba_3Sc_2(BO_3)_4$. The Sr atom is located in a strongly distorted environment derived from that of the Ba2 in $Ba_3Sc_2(BO_3)_4$ (Figure 14.3(d)). But the Sr atom is bound to one fewer O atoms in the trigonal base (which is shown in Figure 14.3(d) connected by a dash line), while it bonds to another O atom below the hexagonal base because of the distortion of calcite blocks lying above and below it. The average bond length of Sr-O is 2.682 Å.

In the case of $Sr_3Sc_2(BO_3)_4$, Sr atoms spread evenly between the calcite blocks (Figure 14.1). The three crystallographically distinct Sr atoms adopt a 9 coordination similar to that of Ba2 in $Ba_3Sc_2(BO_3)_4$ (Figure 14.3(e)). Each Sr-centered 9-vertex polyhedron is connected to only two adjacent ones by sharing its two rectangular faces, leaving one fourth of 9-vertex polyhedral vacancy within the Sr layer compared to the compact Buetschliite structure. The average bond length of Sr-O is 2.691 Å, which is similar to that in $BaSr_2Sc_2(BO_3)_4$.

Luminescence

Under Hg-lamp excitation, $Ba_3Sc_2(BO_3)_4$:Eu exhibits yellow luminescence with chromaticity coordinates x = 0.47 and y = 0.50, while $BaSr_2Sc_2(BO_3)_4$:Eu exhibits a yellow-green emission with x = 0.31 and y = 0.56. Excitation and emission spectra measured at room temperature for both compounds are depicted in Figure 14.4. The broad-band character of the excitation spectra obtained for emission at the peak maxima are consistent with divalent europium and the associated $4f^7(^8S_{7/2}) \rightarrow 4f^6 5d$ transitions. To determine the energetic positions of the excitation bands, each spectrum in the range 320-450 nm was fit with three Gaussian profiles (Figure 14.5). The excitation bands at the lowest energy lie at about 25100 cm^{-1} (398 nm) for $Ba_3Sc_2(BO_3)_4$ and 24700 cm^{-1} (405 nm) for $BaSr_2Sc_2(BO_3)_4$. These values agree with the previous report that excitation energies are generally lower than about 30000 cm^{-1} for Eu^{2+}-doped borates containing O atoms highly coordinated by Ba or Sr atoms [5.6]. Three Ba2 atoms are connected to O1 atoms in $Ba_3Sc_2(BO_3)_4$, and three Sr atoms are connected to O3 and O4 atoms in $BaSr_2Sc_2(BO_3)_4$.

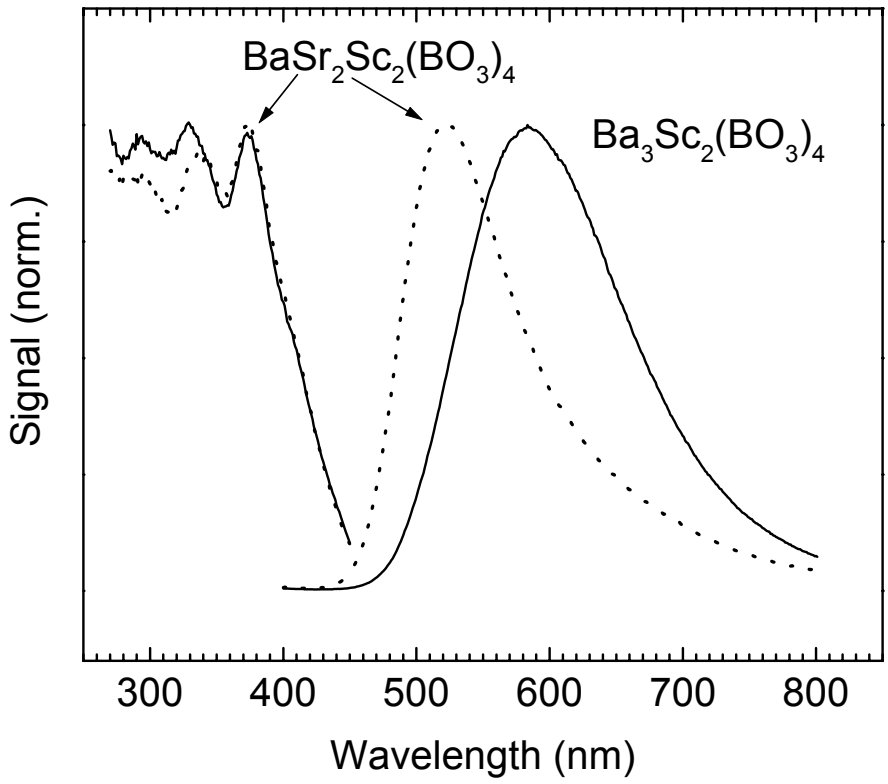

Figure 14.4. Excitation and emission spectra of $Ba_{2.94}Sc_2(BO_3)_4:Eu^{2+}_{0.06}$ (solid) and $Ba_{0.94}Sr_2Sc_2(BO_3)_4:Eu^{2+}_{0.06}$ (dotted) at room temperature.

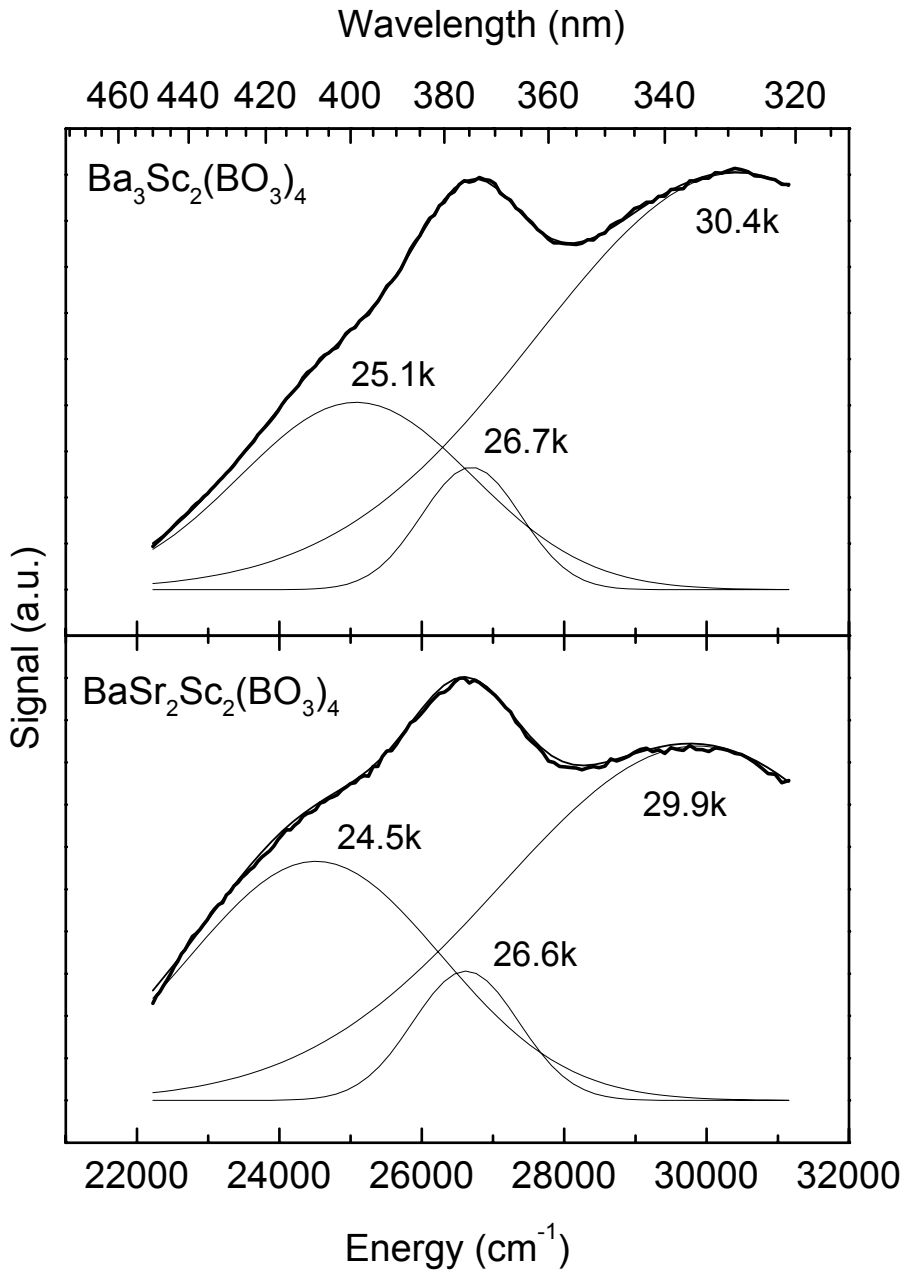

Figure 14.5. Excitation spectra of $Ba_{2.94}Sc_2(BO_3)_4:Eu^{2+}_{0.06}$ (top) and $Ba_{0.94}Sr_2Sc_2(BO_3)_4:Eu^{2+}_{0.06}$ (bottom) in the 320-450 nm regions at room temperature. Narrow lines are best-fit Gaussian profiles.

The emission spectrum for $Ba_3Sc_2(BO_3)_4$ is characterized by a broad band with a maximum at about 585 nm. It can be fit with two Gaussian profiles centered at 17500 cm^{-1} and 15900 cm^{-1}, which is likely associated with Eu^{2+} occupying two different crystallographic Ba sites. The area of the Gaussian profile at higher energy is 1.4 times as large as that at lower energy. The difference in energy between the lowest energy excitation peak and the emission maximum, the Eu^{2+} Stokes shift, is 8000 cm^{-1}. For $BaSr_2Sc_2(BO_3)_4$ the maximum of the emission band is observed at about 524 nm with the Stokes shift of 5600 cm^{-1}. The smaller Stokes shift and the position of the emission band at shorter wavelength for $BaSr_2Sc_2(BO_3)_4$ than those for $Ba_3Sc_2(BO_3)_4$ may be ascribed to the stiffness associated with shorter Sr-O bonding distance. The magnitude of the Eu^{2+} Stokes shift increases with distortions about the O-atom environment [5]. In both compounds, $Ba_3Sc_2(BO_3)_4$ and $BaSr_2Sc_2(BO_3)_4$, the amounts of distortions about O atom environments are similar. For example, both compounds contain O atoms bound by 3 Ba or Sr, 1 Sc, and 1 B atom in distorted trigonal bipyramidal geometries, and the axial Ba(Sr)-O-Ba(Sr) angles are 155^o in $Ba_3Sc_2(BO_3)_4$ and 159^o in $Ba_3Sc_2(BO_3)_4$. These angles are much more acute than the linear interaction in an ideal trigonal bipyramid.

The emission band of $BaSr_2Sc_2(BO_3)_4$ appears to be more asymmetric than that of $Ba_3Sc_2(BO_3)_4$. It can be fit with two Gaussian profiles centered at 19200 cm^{-1} and 17500 cm^{-1}, which is ascribed to Eu^{2+} ions occupying Ba site and Sr site. In general, Eu^{2+} emission in the smaller site occurs at longer wavelengths than in

larger site. However more detailed study is necessary to assign these peaks. To get site selective excitation spectra, excitation spectrum for each emission band such as at 520 nm or 660 nm was recorded, but they are too similar to each other. Long-wavelength emission at 585 nm or 524 nm agrees well with the previous report that Eu^{2+}-doped borates emitting at long wavelengths ($\lambda > 500$ nm) contain O atoms coordinated by three or more Ba or Sr atoms [6].

The Eu-concentration dependence of emission intensity for $Ba_{3-x}Sc_2(BO_3)_4:Eu^{2+}_x$ was examined under a Hg lamp in the x range between 0.01 and 0.45. With increasing europium concentration x, the emission intensity of $Ba_3Sc_2(BO_3)_4:Eu^{2+}$ increases up to $x = 0.03$ and decreases at higher concentrations (Figure 14.6). Concentration quenching is usually associated with energy transfer from one activator to another until an energy sink in the lattice is reached [15,16]. From the crystallographic data and the critical concentration of $x = 0.03$ above which concentration quenching of the luminescence occurs, the critical distance can be derived as 18 Å [15].

Variable-temperature spectra were recorded for $Ba_{2.85}Sc_2(BO_3)_4:Eu^{2+}_{0.15}$. With increasing temperature, the maximum of the emission band moves little, but its bandwidth increases. The full width at half maximum (FWHM) of the emission band at 77K is 75% of the value at room temperature. The temperature dependence of the emission intensity was obtained in the temperature range between 77 and 280 K (Figure 14.7). The emission intensity keeps decreasing with increasing temperature over the entire range, and it drops near room temperature to 66% of the

emission intensity at 77K. This temperature dependency is comparable to that for $Ba_2Mg(BO_3)_2:Eu^{2+}$ in which emission intensity begins to decrease at about 100 K and drops to 50% of its initial intensity at around 300 K [6].

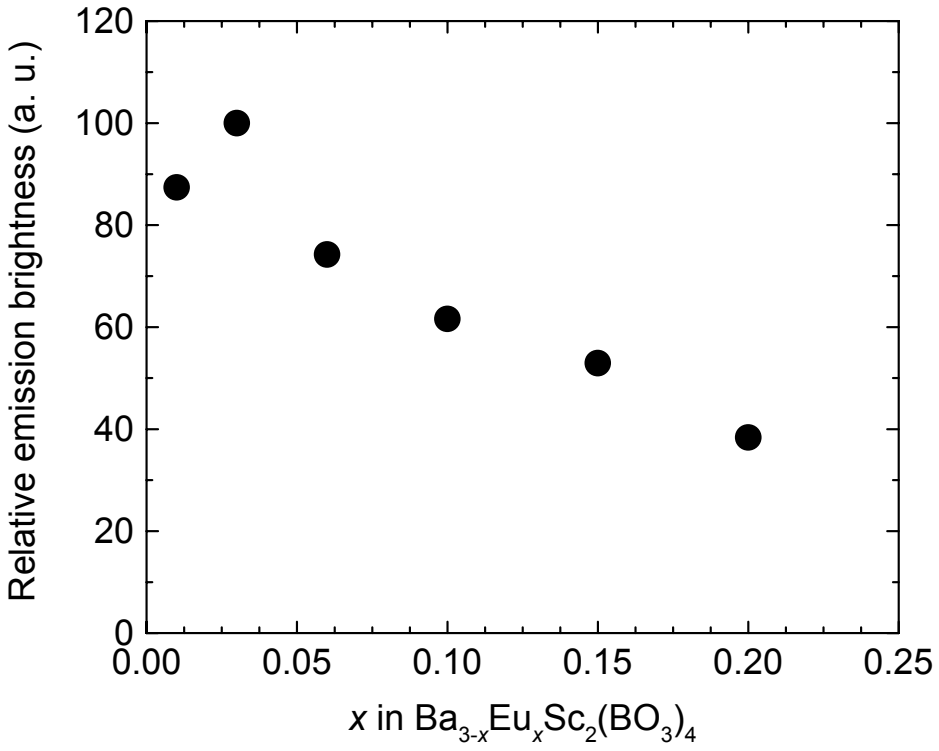

Figure 14.6. Europium-concentration dependence of emission intensity of $Ba_3Sc_2(BO_3)_4:Eu^{2+}$.

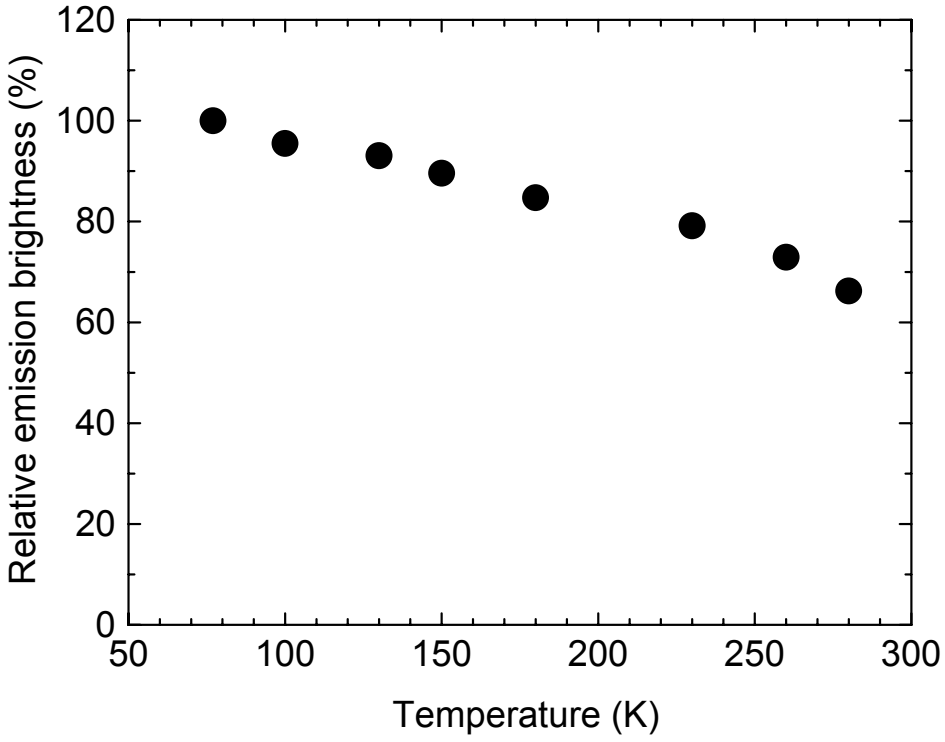

Figure 14.7. Temperature dependence of emission intensity in the temperature range of 77-280 K of $Ba_{2.85}Sc_2(BO_3)_4:Eu^{2+}_{0.15}$.

CONCLUSION

The series of layer compounds $M_3Sc_2(BO_3)_4$ (M = Ba, Sr) was identified, and single-crystal structure determinations were completed. Under Hg-lamp excitation $Ba_{2.94}Sc_2(BO_3)_4:Eu^{2+}_{0.06}$ exhibits yellow luminescence with chromaticity coordinates of x = 0.47 and y = 0.50, and $Ba_{0.94}Sr_2Sc_2(BO_3)_4:Eu^{2+}_{0.06}$ exhibits a yellow-green emission with x = 0.31 and y = 0.56. The excitation band at the lowest energy is observed around 25100 cm^{-1} (398 nm) for $Ba_3Sc_2(BO_3)_4$ and 24700 cm^{-1} (405 nm) for $BaSr_2Sc_2(BO_3)_4$. The maximum of the emission band is observed around 585 nm with the Stokes shift of 8000 cm^{-1} for $Ba_{2.94}Sc_2(BO_3)_4:Eu^{2+}_{0.06}$ and at about 524 nm with the Stokes shift of 5600 cm^{-1} for $Ba_{0.94}Sr_2Sc_2(BO_3)_4:Eu^{2+}_{0.06}$ at room temperature. The critical concentration (x) of $Ba_{3-x}Sc_2(BO_3)_4:Eu^{2+}_x$ is approximately $x = 0.03$, which gives the critical distance of 18 Å. At 280 K the emission intensity of $Ba_{2.94}Sc_2(BO_3)_4:Eu^{2+}_{0.06}$ is observed to be 66% of the value at 77K.

ACKNOWLEDGMENT

This work was supported by the National Science Foundation.

REFERENCES

[1] T. N. Hamaganova, V. K. Trunov, B. F. Dzhurinskii, and V. A. Efremov, *Kristallografiya*, **35**, 856 (1990).

[2] G. K. Abdullaev, K. S. Mamedov, and S. T. Amirov, *Kristallografiya*, **18**, 1075 (1973).

[3] Z. Pei, Q. Su, Y. Chui, and J. Zhang, *Mater. Res. Bull*., **26**(10), 1059 (1991).

[4] G. Blasse and B. C. Grabmaier, *Luminescent Materials*, Springer-Verlag, Berlin (1994).

[5] A. Diaz, and D. A. Keszler, *Mater. Res. Bull.*, **31**, 147 (1996).

[6] A. Diaz, and D. A. Keszler, *Chem. Mater.*, **9**, 2071 (1997).

[7] A. Meijerink, and G. Blasse, *J. Lumin.*, **47**, 1 (1990).

[8] T. Kano, in *Phosphor Handbook*, p.192, edited by S. Shionoya, and W.M.Yen, CRC Press, Boca Raton, FL (2000).

[9] G. M. Sheldrick, SHELXS-97 – A program for automatic solution of crystal structure refinement, 1997, Release 97-2.

[10] L. J. Farrugia, *J. Appl. Crystallogr.*, **32**, 837 (1999).

[11] R. D. Shannon, *Acta Crystallogr. Sect*. *A* **32**, 751 (1976)

[12] A. Akella, and D. A. Keszler, *Mater. Res. Bull*., **30**(1), 105 (1995).

[13] J. R. Cox, D. A. Keszler, and J. Huang, *Chem. Mater*., **6**(11), 2008 (1994).

[14] A. Pabst, *American Mineralogist*. **59**, 353 (1974).

[15] G. Blasse, *Philips Res. Rep.*, **24**, 131 (1969).

[16] D. L. Dexter, and J. H. Schulman, *J. Chem. Phys.*, **22**, 1063 (1954).

CHAPTER 15

LUMINESCENCE OF Lu_2O_2S:Ln (Ln = Eu, Tb)

ABSTRACT

The synthesis and luminescent properties of Lu_2O_2S:Ln (Ln = Eu, Tb) under ultraviolet radiation and X-ray excitation are presented. Samples were prepared by heating mixtures of lanthanide oxides, Na_2CO_3, and elemental sulfur at 950^oC in air. Emission colors were found to change with activator concentration; at the composition $(Lu_{1.7}Eu_{0.3})O_2S$ saturated NTSC red emission was observed. The activator concentrations of $(Lu_{2-x}Ln_x)O_2S$ giving the maximum emission brightness under a Hg lamp were determined to be $x = 0.01$ (Ln = Eu) and $x = 0.2$ (Ln = Tb). Under X-ray excitation $(Lu_{2-x}Eu_x)O_2S$ exhibits the highest emission brightness with $x = 0.01$; while $(Lu_{2-x}Tb_x)O_2S$ has maximum emission brightness in the range $0.05 \leq x \leq 0.1$. Under similar preparative conditions, phosphors of Lu_2O_2S:Ln exhibit higher emission intensity than the corresponding Gd derivative $(Gd_{1.8}Tb_{0.2})O_2S$, which might derive form the larger particle sizes of the Lu phosphors.

INTRODUCTION

X-rays do not efficiently expose photographic film, so X-ray phosphors have been developed and used over the past several decades as an indirect means to provide an improved detection method for X-rays [1]. X-ray phosphors are materials that absorb X-rays and convert the absorbed energy efficiently into luminescence that can be readily detected by photographic film or typical photomultiplier tubes (PMTs). Their required properties are known as follows: high X-ray absorption and high density; high conversion efficiency for X-ray to light conversion; an emission spectrum that covers film sensitivity; stability; and acceptable cost [2]. $Gd_2O_2S:Tb^{3+}$ is one of the more widely used commercial X-ray phosphors as an intensifying screen. It was primarily developed during efforts to identify new color TV and lamp phosphors, and its potential as an X-ray phosphor was first described by Tecotzky [3]. It has a high density, 7.34 g/cm^3, and it exhibits high X-ray absorption and a significant quantum yield (18%) for X-ray to visible light conversion [1].

The linear X-ray absorption coefficient, μ, increases with increasing density and atomic number approximately according to the relation

$$\mu = k \lambda^3 Z^3 \rho,$$

where k = a constant, λ = X-ray wavelength, Z = atomic number of absorber, and ρ = density [4] Therefore, X-ray absorption should be more efficient in a material with higher density. The density of Lu_2O_2S containing the heaviest lanthanide is

calculated as 8.91 g/cm^3 from its cell parameters [5]. Therefore, it seems to be important to investigate Lu_2O_2S as an X-ray phosphor. Among known X-ray phosphors, Eu and Tb are two of the more important emission centers. Europium-activated phosphors such as $(Y,Gd)_2O_3$:Eu are used as X-ray phosphors for computed tomography medical imaging [6], and Gd_2O_2S:Tb is used in CCD-based detectors [7].

In this contribution the synthesis and photoluminescence properties of Lu_2O_2S:Ln (Ln = Eu, Tb) are presented.

EXPERIMENTAL

The starting materials for phosphor synthesis were Lu_2O_3 (Stanford materials, 99.99%), Eu_2O_3 (Stanford materials, 99.99%), Tb_4O_7 (Cerac, 99.9%), Na_2CO_3 (Aldrich, A.C.S.), and S (Mallinckrodt, U.S.P.). Intimate mixtures of Ln_2O_3 (Lu_2O_3 + Eu_2O_3 or Tb_4O_7) + Na_2CO_3 + 8 S were placed in covered alumina crucibles, heated in air at 950°C for 20 min, and then quenched to room temperature. After cooling, products were ground in an agate mortar with 4 parts of S to 1 part of product, followed by heating again at 950°C for 20 min. Products were twice washed with de-ionized water to remove Na_2SO_4 and NaS_x, filtered, rinsed with absolute ethanol, and dried on the lab bench. To compare relative brightness under X-ray excitation, $(Gd_{1.8}Tb_{0.2})O_2S$ was prepared by heating an intimate mixture of 0.9 Gd_2O_3 (Stanford materials, 99.99%) + 0.05 Tb_4O_7 + 0.5 Na_2CO_3 + 4 S in a covered alumina crucible at 950°C for 20 min followed by washing with de-ionized water. The final products were identified by using powder X-ray diffraction (Siemens D5000, Cu$K\alpha$).

Photoluminescence measurements were made with an Oriel 300-W Xe lamp and a Cary model-15 prism monochromator for excitation. For detection, emitted light was passed through an Oriel 22500 1/8-m monochromator and monitored with a Hamamatsu R636-10 photomulitplier tube (PMT) over the range 400-750 nm. Each spectrum was corrected for the throughput and response of the system with Rhodamine B and a standardized W lamp. To compare emission brightness under

UV excitation, an Oriel 6035 Hg lamp was used as an excitation source. Emission light was collected at the right angle to excitation, passed through a UV filter, and detected with a Hamamatsu R636-10 photomulitplier tube.

Relative emission brightness under X-ray excitation was measured by using a Rigaku ultraX-18 rotating anode generator equipped with a Cu target operating at 50 kV and 270 mA. X-rays were directed onto the phosphor powders with an incident angle of 45^{o} through the collimation system of a Rigaku R-Axis Rapid diffractometer, and luminescence was collected by using a liquid light guide and a Hamamatsu R636-10 photomulitplier tube at room temperature. In this setup a $BaSO_4$ film gives a null signal on the PMT.

Microstructures and morphologies of samples were investigated by scanning electron microscopy with an AmRay 3300FE instrument.

RESULTS AND DISCUSSION

The powder X-ray diffraction pattern (Figure 15.1) of $(Lu_{1.8}Tb_{0.2})O_2S$ reveals the presence of a small amount of residual Lu_2O_3 in addition to the product phase [5]. In an attempt to eliminate this Lu_2O_3, one sample of $(Lu_{1.95}Tb_{0.05})O_2S$ was heated five times with additional S, but a decrease in the amount of Lu_2O_3 with additional heating was not observed in the X-ray diffraction pattern. After the first heating, a considerable amount of Lu_2O_3 was observed in the X-ray diffraction pattern. After the second heating, the quantity was reduced, but ensuing heatings had no additional effect. In the case of La_2O_2S and Gd_2O_2S, single phases can be readily prepared by single heating with less Na_2CO_3 and S [8]. The difficulty in obtaining a single phase of Lu_2O_2S compared to La_2O_2S and Gd_2O_2S seems to arise from the smaller size of the Lu atom in comparison to those of the La and Gd atoms (for example, effective ionic radii for 8 coordination are 111.7 pm for Lu^{3+}, 119.3 pm for Gd^{3+}, and 130 pm for La^{3+} [9]; the coordination number of La site in La_2O_2S is 7 [10]). Because of its higher charge-to-size ratio, Lu^{3+} has a higher chemical hardness and a stronger preference for oxide relative to sulfide in comparison with Gd^{3+} and La^{3+} [11].

As seen from the scanning electron microscope image (Figure 15.2) particles of the Lu_2O_2S phosphor crystallize as polyhedra with sizes in the range 0.5-2 μm. For practical applications, an average particle size of 5-10 μm is desirable, because smaller particles lose their emission intensity from internal

scattering and larger particles cause difficulty in making smooth thin screens [2]. The particle size of Lu_2O_2S is observed to increase with repeating heatings and increased heating times, and larger amounts of Na_2CO_3. Under the same preparative conditions, the average particle size of $(Gd_{1.8}Tb_{0.2})O_2S$ is smaller than that of the Lu_2O_2S phosphors; particles of $(Gd_{1.8}Tb_{0.2})O_2S$ are distributed in the range 0.2-1 μm.

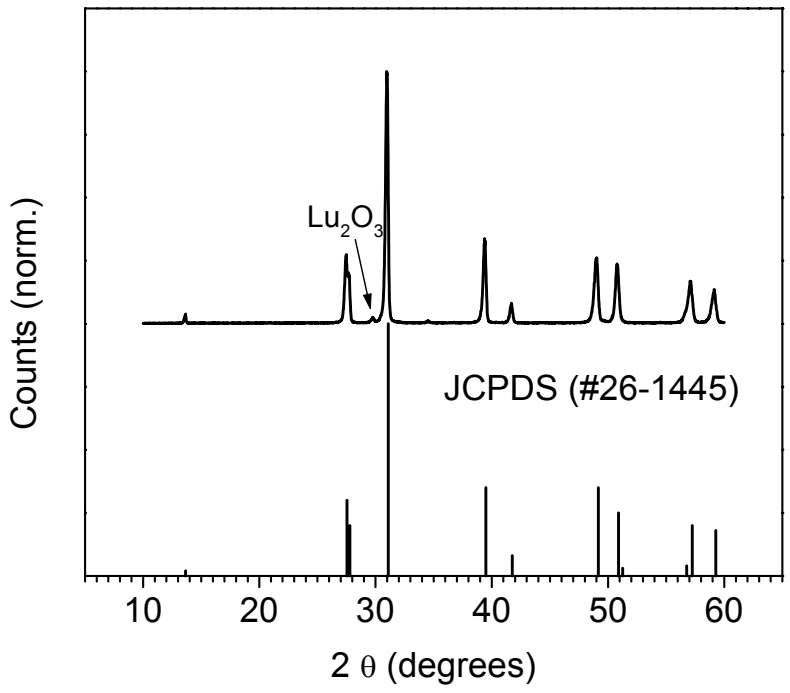

Figure 15.1. Powder X-ray diffraction pattern of $(Lu_{1.8}Tb_{0.2})O_2S$ and JCPDS pattern (#26-1445).

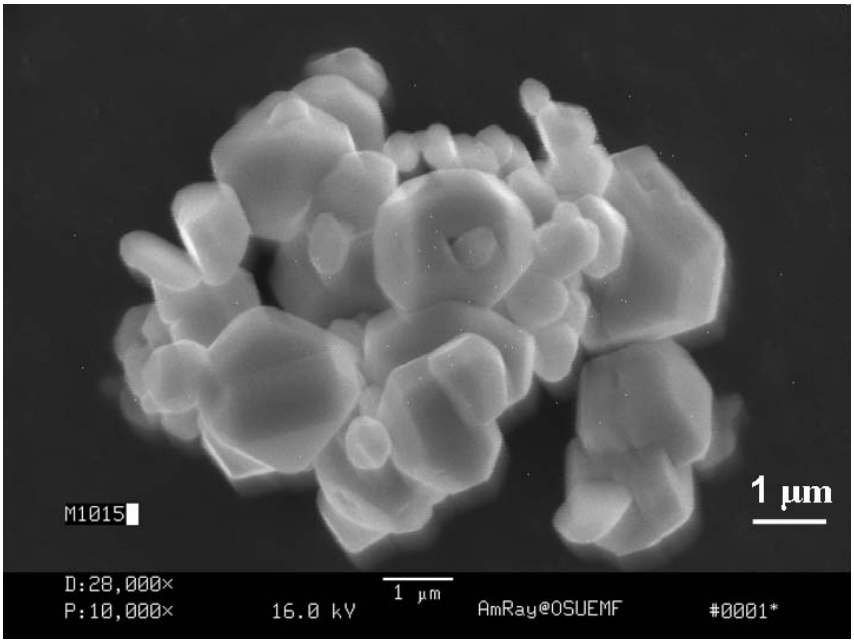

Figure 15.2. Scanning electron microscopy image of $(Lu_{1.98}Eu_{0.02})O_2S$.

Excitation spectra of $(Lu_{2-x}Eu_x)O_2S$ (x = 0.04, 0.3) monitored at the $^5D_0 \rightarrow {}^7F_2$ emission wavelength of 625.5 nm are depicted in Figure 15.3. Both excitation spectra consist of broad charge-transfer bands and *f-f* excitation peaks. Charge-transfer bands of both compounds are observed to be centered near 330 nm, which agrees with observations in $Ln_2O_2S:Eu^{3+}$ (Ln = La, Gd, Y) by Reddy et al. [12]. Both bands are located at lower energy than in oxide hosts because of the lower electronegativity of S relative to O [13]. With increasing activator concentration, the charge-transfer band becomes broader, consistent with the expected increase in inhomogeneous broadening at high dopant concentrations.

Emission spectra of $(Lu_{2-x}Eu_x)O_2S$ (x = 0.04, 0.3) excited through the charge-transfer transition are given in Figure 15.4. The emission spectrum of $(Lu_{2-x}Eu_x)O_2S$ (x = 0.04) reveals emission lines from $^5D_2$, $^5D_1$, and $^5D_0$ levels; while the spectrum of $(Lu_{2-x}Eu_x)O_2S$ (x = 0.3) is mainly composed of emissions from $^5D_0$ level. The quenching of emission from the higher levels with increasing Eu concentration arises from the cross-relaxation process $(^5D_1 \rightarrow {}^5D_0) \rightarrow ({}^7F_0 \rightarrow {}^7F_6)$ [14]. A similar phenomenon is observed in $(Y_{2-x}Eu_x)O_2S$ phosphors [15]. The quenching of the emission from the higher levels also affects emission color; chromaticity coordinates of $(Lu_{2-x}Eu_x)O_2S$ ($0.04 \leq x \leq 0.3$) are summarized on the chromaticity diagram (Figure 15.5). The sample $(Lu_{2-x}Eu_x)O_2S$ (x = 0.3) exhibits chromaticity coordinates x = 0.67 and y = 0.33, which corresponds to the National Television Standard Committee (NTSC) red.

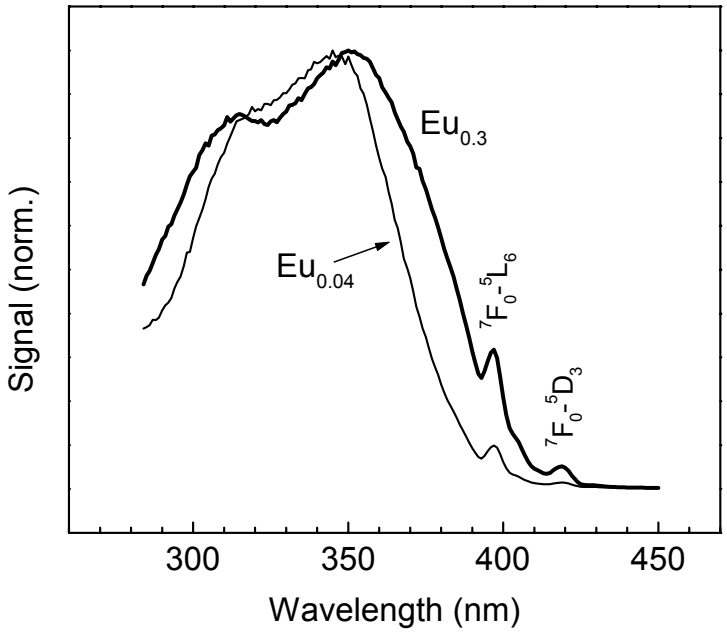

Figure 15.3. Excitation spectra of $(Lu_{2-x}Eu_x)O_2S$ (x = 0.04, 0.3) monitored at the $^5D_0 \rightarrow {}^7F_2$ emission wavelength of 625.5 nm at room temperature.

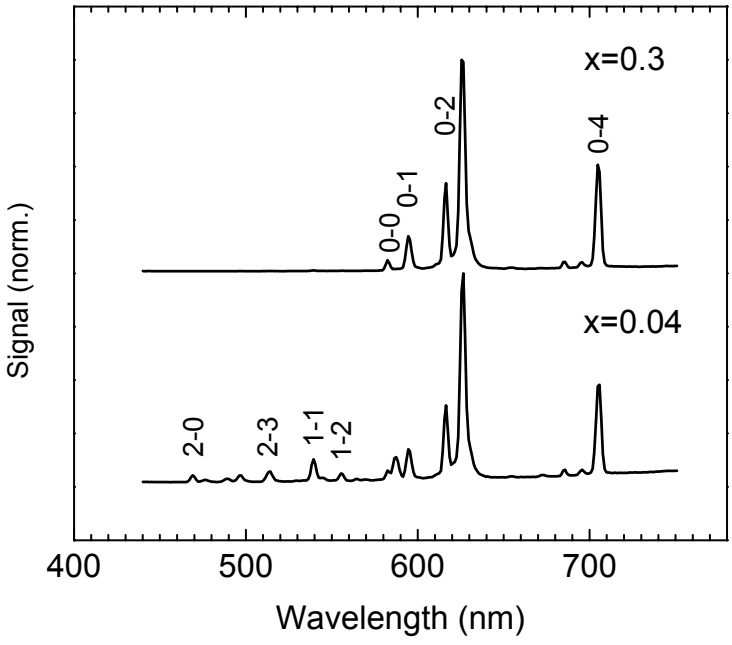

Figure 15.4. Emission spectra of $(Lu_{2-x}Eu_x)O_2S$ (x = 0.04, 0.3) excited by the charge-transfer transition at room temperature.

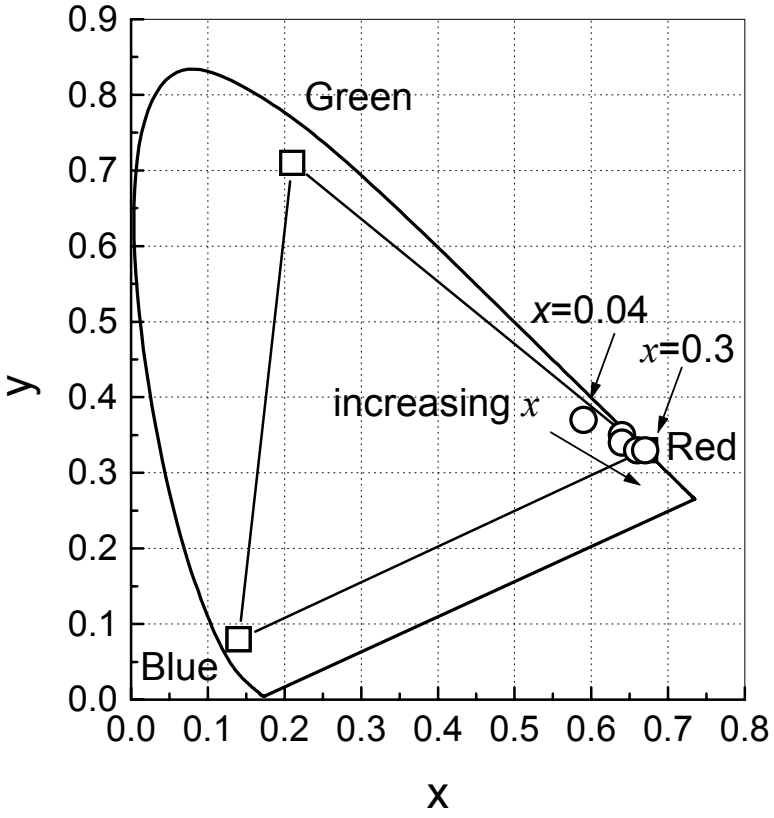

Figure 15.5. Chromaticity coordinates of $(Lu_{2-x}Eu_x)O_2S$ (x = 0.04, 0.1, 0.15, 0.2, and 0.3) excited by charge-transfer transition at room temperature. Squares represent NTSC red, green, and blue.

Excitation spectra of $(Lu_{2-x}Tb_x)O_2S$ (x = 0.02, 0.2) monitored at the $^5D_4 \rightarrow {}^7F_5$ emission wavelength of 543 nm are depicted in Figure 15.6 along with that of $(Gd_{1.8}Tb_{0.2})O_2S$. The broad excitation bands correspond to $4f^8 \rightarrow 5f^7 5d^1$ transition of Tb^{3+} ion. The excitation intensities of *f-f* transitions in the wavelength region of 330-400 nm are very weak compared with that of the parity-allowed $4f^8 \rightarrow 5f^7 5d^1$ transition. As expected, an increase in the excitation bandwidth of the $4f^8 \rightarrow 5f^7 5d^1$ transition at higher Tb^{3+} concentration is observed.

Emission spectra of $(Lu_{2-x}Tb_x)O_2S$: (x = 0.02, 0.2) under the excitation of the $4f^8 \rightarrow 5f^7 5d^1$ transition (285 nm) are composed of $^5D_J \rightarrow {}^7F_J$ emission transitions (Figure 15.7). The emission spectrum of $(Lu_{2-x}Tb_x)O_2S$ (x = 0.02) exhibits transitions from $^5D_3$, and $^5D_4$ levels, while the emission spectrum of $(Lu_{2-x}Tb_x)O_2S$ (x = 0.3) exhibits mainly transitions from the $^5D_4$ level. This phenomenon is also related to the cross-relaxation process $(^5D_3 \rightarrow {}^5D_4) \rightarrow (^7F_6 \rightarrow {}^7F_0)$ [14]. The change in chromaticity coordinates of $(Lu_{2-x}Tb_x)O_2S$ with Tb concentration is depicted in Figure 15.8.

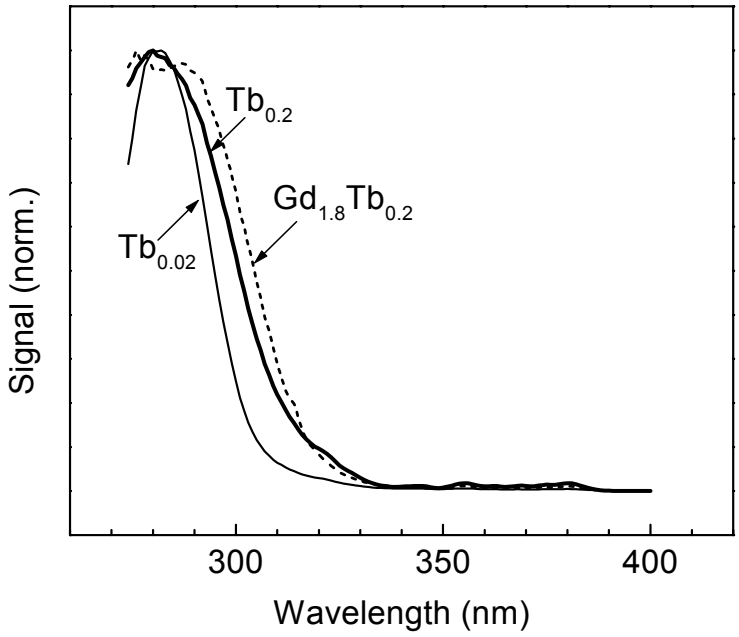

Figure 15.6. Excitation spectra of $(Lu_{2-x}Tb_x)O_2S$ (x = 0.02, 0.2) monitored at the $^5D_4 \rightarrow {}^7F_5$ emission wavelength of 543 nm at room temperature.

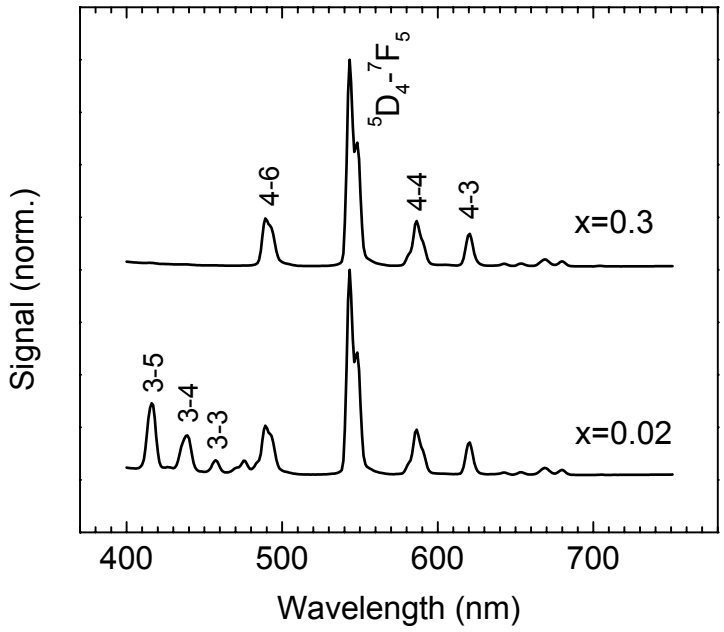

Figure 15.7. Emission spectra of $(Lu_{2-x}Tb_x)O_2S$ (x = 0.02, 0.2) under the excitation of the $4f^8 \rightarrow 5f^{\,7}5d^{\,1}$ transition of 285 nm at room temperature.

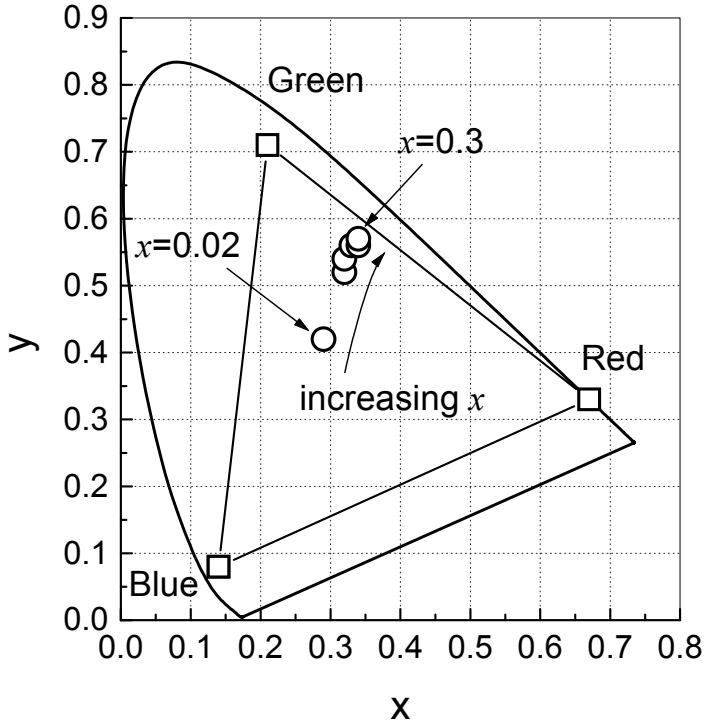

Figure 15.8. Chromaticity coordinates of $(Lu_{2-x}Tb_x)O_2S$ (x = 0.02, 0.05, 0.1, 0.15, 0.2, and 0.3) with excitation of the $4f^8 \rightarrow 5f^7 5d^1$ transition at 285 nm.

Emission brightness as a function of Eu concentration for $(Lu_{2-x}Eu_x)O_2S$ ($0.003 \leq x \leq 0.3$) with Hg-lamp excitation is presented in Figure 15.9. The maximum brightness is observed at $x = 0.01$, which is comparable to the optimum activator concentration of $x = 0.01$ for emission from $^5D_2$ and $^5D_1$ levels under the charge-transfer excitation in $(Y_{2-x}Eu_x)O_2S$ [16]. For transitions from the $^5D_0$ level under the charge-transfer excitation, the optimum Eu concentration was observed to be $x = 0.06$ in $(Y_{2-x}Eu_x)O_2S$. Under the host excitation of 254 nm, the optimum Eu concentration is reported to be $x = 0.003$ for emissions from $^5D_2$ and $^5D_1$ levels, and $x = 0.04$ for emissions from the $^5D_0$ level.

The relative emission intensity of $(Lu_{2-x}Eu_x)O_2S$ ($0.003 \leq x \leq 0.3$) under X-ray excitation is shown in Figure 15.10. The concentration dependence of the brightness under X-ray excitation is very similar to that under a Hg lamp with an optimum Eu concentration of $x = 0.01$. The emission intensity of $(Lu_{2-x}Eu_x)O_2S$ ($x = 0.01$) under X-ray excitation is 150 % of that of $(Gd_{1.8}Eu_{0.2})O_2S$: prepared under the same conditions.

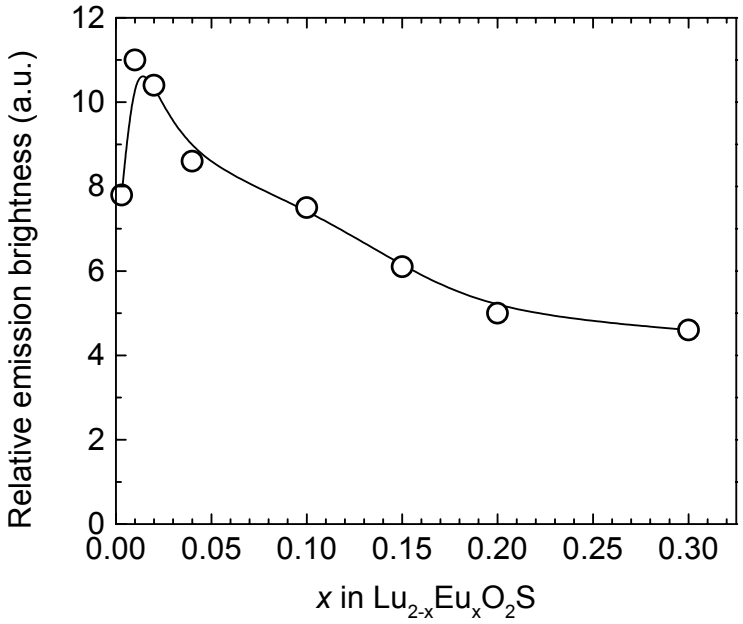

Figure 15.9. Relative emission brightness of $(Lu_{2-x}Eu_x)O_2S$ ($0.003 \leq x \leq 0.3$) with Hg-lamp excitation.

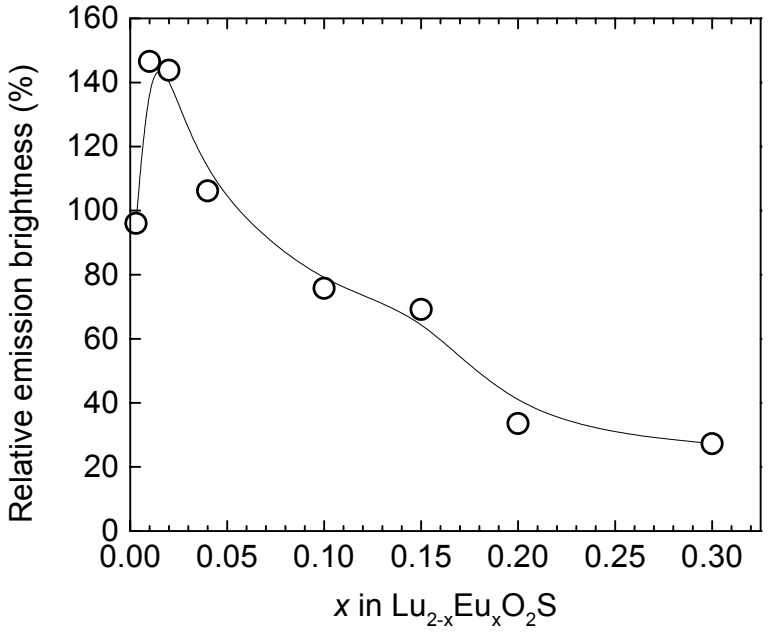

Figure 15.10. Relative emission brightness of $(Lu_{2-x}Eu_x)O_2S$ ($0.003 \leq x \leq 0.3$) to that of $(Gd_{1.8}Tb_{0.2})O_2S$ under X-ray excitation.

Relative emission brightness of $(Lu_{2-x}Tb_x)O_2S$ ($0.05 \leq x \leq 0.3$) under a Hg lamp is shown in Figure 15.11. The optimum Tb concentration is $x = 0.20$, which is pretty high concentration compared to $(Y_{2-x}Tb_x)O_2S$ phosphors. The optimum Tb concentration for emission from $^5D_4$ and $^5D_1$ levels is reported as $x = 0.05$ under the host excitation of 254 nm, and $x = 0.08$ under the $4f^8 \rightarrow 5f^7 5d^1$ transition excitation of 290 nm in $(Y_{2-x}Tb_x)O_2S$ [16].

Figure 15.12 presents relative emission brightness of $(Lu_{2-x}Tb_x)O_2S$ ($0.05 \leq x \leq 0.3$) to that of $(Gd_{1.8}Tb_{0.2})O_2S$ under X-ray excitation. The concentration dependence of the brightness under X-ray excitation is much different from that under a Hg lamp. Relative emission brightness of $(Lu_{2-x}Tb_x)O_2S$ increases with decreasing Tb concentration down to $x = 0.10$ and exhibits similar emission intensity down to $x = 0.05$. The emission bightness of $(Lu_{2-x}Tb_x)O_2S$ ($x = 0.05$) under X-ray excitation is 310 % of that of $(Gd_{1.8}Tb_{0.2})O_2S$ prepared in this study. $(Lu_{2-x}Tb_x)O_2S$ ($x = 0.20$) with the same Tb concentration as $(Gd_{1.8}Tb_{0.2})O_2S$ exhibits 200 % of the emission intensity of $(Gd_{1.8}Tb_{0.2})O_2S$.

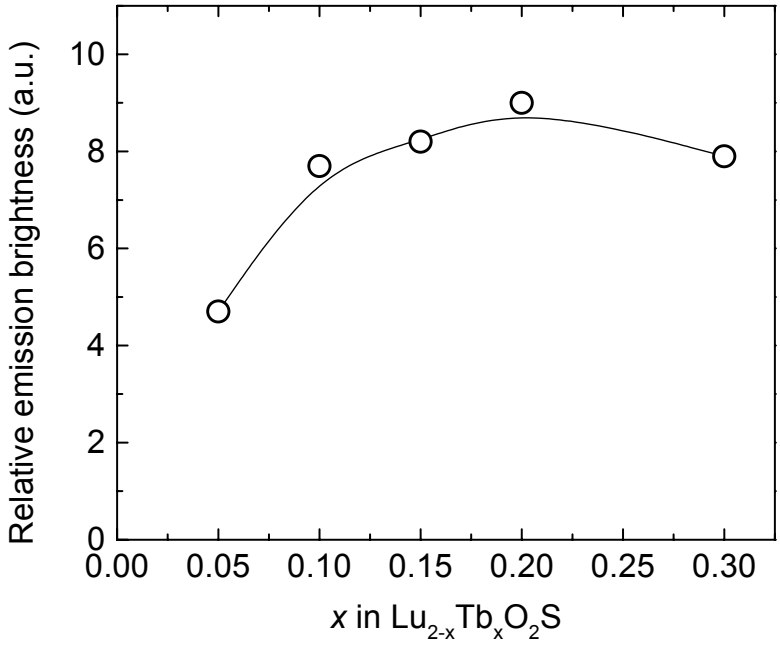

Figure 15.11. Relative emission brightness of $(Lu_{2-x}Tb_x)O_2S$ ($0.05 \leq x \leq 0.3$) under Hg-lamp excitation.

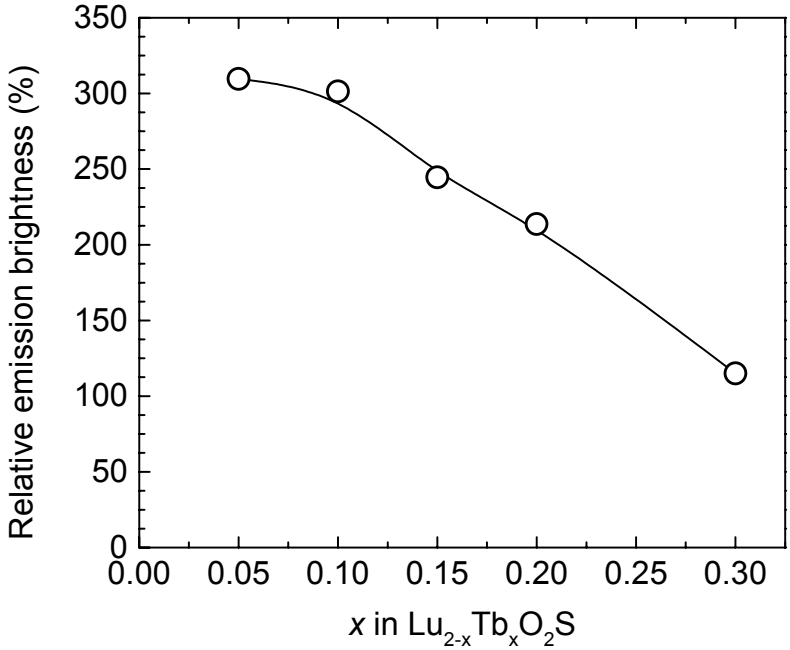

Figure 15.12. Relative emission brightness of $(Lu_{2-x}Tb_x)O_2S$ ($0.05 \leq x \leq 0.3$) to that of $(Gd_{1.8}Tb_{0.2})O_2S$ under X-ray excitation.

CONCLUSION

Phosphors of Lu_2O_2S:Ln (Ln = Eu, Tb) were prepared and their luminescent properties were investigated along with emission intensity under X-ray excitation. Lu_2O_2S:Eu phosphors exhibit charge-transfer excitation near 330 nm, and the composition $(Lu_{1.7}Eu_{0.3})O_2S$ exhibits NTSC red emission. Activator concentrations, $(Lu_{2-x}Ln_x)O_2S$, for maximum emission brightness under Hg-lamp excitation were measured as $x = 0.01$ (Ln = Eu) and $x = 0.2$ (Ln = Tb). Under X-ray excitation $(Lu_{2-x}Eu_x)O_2S$ reveals the highest emission brightness with $x = 0.01$, while $(Lu_{2-x}Tb_x)O_2S$ exhibits maximum emission brightness in the range $0.05 \leq x \leq 0.1$. When prepared under similar conditions, phosphors of Lu_2O_2S:Ln (Ln = Eu, Tb) exhibit higher emission under X-ray excitation intensity than $(Gd_{1.8}Tb_{0.2})O_2S$.

REFERENCES

[1] L. H. Brixner, *Mat. Chem. Phys.*, **16**, 253 (1987).

[2] G. Blasse and B. C. Grabmaier, *Luminescent Materials*, chapter 8, Springer-Verlag, Berlin (1994).

[3] M. Tekotzky, Electrochem. Soc. Meeting, Boston, May (1968).

[4] B. D. Cullity and S. R. Stock, Elements of X-ray Diffraction, 3rd Edition, Prentice Hall, Upper Saddle River, NJ (2001).

[5] JCPDS #26-1445.

[6] S. J. Duclos, C. D. Greskovich, R. J. Lyons, J. S. Vartuli, D. M. Hoffman, R. J. Riedner, and M. J. Lynch, *Nucl. Instr. and Meth.*, **A 505**, 68 (2003).

[7] A. Koch, and C, Riekel, *Rev. Sci. Instrum.*, **67(5)**, 1737 (1996).

[8] C-H. Park, and D. A. Keszler, *unpublished.*

[9] R. D. Shannon, *Acta Crystallogr.*, **A32**, 751 (1976).

[10] Zachariasen, W. H., *Acta Cryst.*, **2**, 60 (1949).

[11] D. Shriver, and P. Atkins, *Inorganic Chemistry*, 3rd Edition, p.168, W. H. Freeman and Company, New York (1999).

[12] K. R. Reddy, K. Annapurna, and S. Buddhudu, *Mater. Res. Bull.*, **31(11)**, 1355 (1996).

[13] G. Blasse and B. C. Grabmaier, *Luminescent Materials*, p.17, Springer-Verlag, Berlin (1994).

[14] G. Blasse and B. C. Grabmaier, *Luminescent Materials*, p.100, Springer-Verlag, Berlin (1994).

[15] T. Kano, in *Phosphor Handbook*, p.190, edited by S. Shionoya and W.M.Yen, CRC Press, Boca Raton, FL (2000).

[16] L. Ozawa, H. Forest, P. M. Jaffe, and G. Ban, *J. Electrochem. Soc.*, **118(3)**, 482 (1971).

CHAPTER 16

CONCLUSIONS AND FUTURE WORK

New chalcogenide fluoride *p*-type transparent semiconductors of MCuQF (M=Ba, Sr; Q=S, Se, and Te) were prepared by high-temperature reaction methods and their structures, optical and electrical properties were examined. Considering the ease in achieving band-gap modulation, the relatively low processing temperatures, the high *p*-type conductivity, and light emission, the materials MCuQF certainly represent a rich family for continued studies and exploitation. BaCuSF films were prepared by thermal evaporation and pulsed laser deposition methods, and their optical and electrical properties were measured. Continued work on thin-films of MCuQF is planned.

The new Ag compound BaAgSF was synthesized and characterized. Phase stabilization and the optical and electrical properties of *p*-type conductors of $BaCu_2S_2$ and $BaCu_2Se_2$ were examined.

New *n*-type transparent conducting films of W-doped In_2O_3 and W-doped zinc indium oxide were prepared and their optical and electrical properties were examined. Transparent thin-film transistors (TTFTs) containing SnO_2 or zinc indium oxide as channel materials were also demonstrated.

Strong near-infrared (NIR) luminescence of $BaSnO_3$ was observed and characterized, and the relationship between crystallite size and luminescence brightness was established.

New luminescent materials of monoclinic and trigonal $(La,Y)Sc_3(BO_3)_4:Eu^{3+}$ were prepared, and their structures and luminescence properties were examined. New potential vacuum ultraviolet phosphors $LuAl_3(BO_3)_4$:Ln (Ln = Eu, Tb, and Ce) were prepared and characterized. New –ray phosphor Lu_2O_2S:Ln (Ln = Eu, Tb) were prepared and their luminescent properties were examined under X-ray excitation.

The new layered borates $Ba_3Sc_2(BO_3)_4$, $BaSr_2Sc_2(BO_3)_4$, and $Sr_3Sc_2(BO_3)_4$ were structurally characterized by single crystal X-ray diffraction, and Eu^{2+} luminescence following relatively low-energy excitation was discovered.

BIBLIOGRAPHY

G. K. Abdullaev, K. S. Mamedov, and S. T. Amirov, *Kristallografiya*, **18**, 1075 (1973).

A. Akella, and D. A. Keszler, *Mater. Res. Bull*., **30**(1), 105 (1995).

M. D. Archer, and R. Hill, *Clean Electricity from Photovoltaic*, Imperial College Press, London (2001).

K. Badeker, *Ann. Phys.*, **22**, 749 (1907).

J. Bass, "Themoelectricity" in *Solid-State Physics Source Book*, S. P. Parker, Ed.; McGRAW-HILL, New York (1988).

B. Blanzat, J. P. Denis, C. Pannel, and C. Barthou, *Mater. Res. Bull.*, **12**, 455 (1977).

G. Blasse, *J. Chem. Phys.*, **46(7)**, 2583 (1967).

G. Blasse, *Philips Res. Rep.*, **24**, 131 (1969).

G. Blasse, and A. Bril, *J. Chem. Phys.*, **47(12)**, 5139 (1967).

G. Blasse, and A. Bril, *Philips Tech. Rev.*, **31**, 304 (1970).

G. Blasse, and B. C. Grabmaier, *Luminescent Materials*, Springer-Verlag, Berlin (1994).

P.S. Berdonosov, A. M. Kusainova, L. N. Kholodkovskaya, V. A. Dolgikh, L. G. Akselrud, and B. A. Popovkin, *J. Solid State Chem.*, **118**, 74 (1995).

W. Borchert, *Z. Kristallogr.*, **107**, 357 (1956).

T. C. Bourland, R. G. Carter, and A. Yokochi, *Org. Biomol. Chem.*, **2**, 1315 (2004).

L. H. Brixner, *Mat. Chem. Phys.*, **16**, 253 (1987).

W. Bronger, B. Lenders, J. Huster, *Z. Anorg. Allg. Chem.,* **619**, 70 (1993).

M. T. Buscaglia, M. Leoni, M. Viviani, V. Buscaglia, A. Martinelli, A. Testino, and P. Nanni, *J. Mater. Res.*, **18**, 560 (2003).

P. F. Carcia, R. S. McLean, M. H. Reilly, and G. Nunes, **82**, 11117 (2003).

R. J. Cava, P. Gammel, B. Batlogg, J. J. Krajewski, W. F. Peck, Jr., L. W. Rupp, Jr., R. Felder, and R. B. Dover, *Phys Rev. B*, **42**, 4815 (1990).

R. W. Cheary and A. A. Coelho, *J. Appl. Cryst.*, **25**, 109 (1992).

J. Cerda, J. Arbiol, G. Dezanneua, R. Diaz, and J. R. Morante, *Sens. Actuators*, B 84, 21 (2002).

F. A. Cotton, *Chemical Applications of Group Theory*, 3rd ed., John Wiley & Sons, Singapore (1990).

T. J. Coutts, K. A. Emery, and J. S. Ward, *Progress in Photovotaics and Applications*, **10**, 1 (2002).

P. A. Cox, *The Electronic Structure and Chemistry of Solids*, Oxford University Press, Oxford (1987).

J. R. Cox, D. A. Keszler, and J. Huang, *Chem. Mater.*, **6**(11), 2008 (1994).

B. D. Culliy, and S. R. Stock, *Elements of X-Ray Diffraction*, 3rd ed., Prentice-Hall, Upper Saddle River, NJ (2001).

D. L. Dexter, and J. H. Schulman, *J. Chem. Phys.*, **22**, 1063 (1954).

A. Diaz, and D. A. Keszler, *Mater. Res. Bull.*, **31**, 147 (1996).

A. Diaz, and D. A. Keszler, *Chem. Mater.*, **9**, 2071 (1997).

H. Donker, W. M. A. Smit, and G. Blasse, *Phys. Stat. Sol. B*, **148**, 413 (1988).

N. Duan, A. W. Sleight, M. K. Jayaraj, and J. Tate, *Appl. Phys. Lett.*, **77(9)**, 1325 (2000).

S. J. Duclos, C. D. Greskovich, R. J. Lyons, J. S. Vartuli, D. M. Hoffman, R. J. Riedner, and M. J. Lynch, *Nucl. Instr. and Meth.*, **A 505**, 68 (2003).

H. Eilers, U. Hommerich, S. M. Jacobson, W. M. Yen, K. R. Hoffmann, and W. Jia, *Phys. Rev. B*, **49**, 15505 (1994).

A. L. Fahrebruch and R. H. Bube, *Fundamentals of Solar Cells*, Academic, New York (1983).

L. J. Farrugia, *J. Appl. Crystallogr.*, **32**, 837 (1999).

H. F. Folkerts, F. Ghianni, and G. Blasse, *J. Phys. Chem. Solids*, **57**, 1659 (1996).

S. J. Fonash, *Solar Cell Device Physics*, Academic, New York (1981).

E. R. Franke, and H. Schaefer, *Z. Naturforsch.* **27B**, 1308 (1972).

A. J. Freeman, K. R. Poeppelmeier, T. O. Mason, R. P. H. Chang, and T. J. Marks, *Mater. Res. Soc. Bull.*, **25(8)**, 45 (2000).

D. S. Ginley, and C. Bright, *Mater. Res. Soc. Bull.*, **25(8)**, 15 (2000).

S. M. Girvin, "Hall Effect" in *Solid-State Physics Source Book*, S. P. Parker, Ed.; McGRAW-HILL, New York (1988).

H. Gong, Y. Wang, and Y. Luo, *Appl. Phys. Lett.*, **76(26)**, 3959 (2000).

R. G. Gordon, *Mater. Res. Soc. Bull.*, **25(8)**, 28 (2000).

D. L. Graf, W. F. Bradley, *Acta Crysyallogr.*, **15**, 238 (1962).

O. J. Guentert, and A. Faessler, *Z. Kristallogr.*, **107**, 357 (1956).

H. Hahn, G. Frank, W. Klingler, A. D. Meyer, and G. Stoerger, *Z. Anorg. Allg. Chem.*, **271**, 153 (1953).

H. Hahn, and V. de Lorent, *Z. Anorg. Allg. Chem.*, **290**, 68 (1957).

T. N. Hamaganova, V. K. Trunov, B. F. Dzhurinskii, and V. A. Efremov, *Kristallografiya*, **35**, 856 (1990).

I. Hamberg, and C. G. Granqvist, *J. Appl. Phys.*, **60**, R123 (1986).

H. Hiramatsu, M. Orita, M. Hirano, K. Ueda, and H. Hosono, *J. Appl. Phys.*, **91**, 9177 (2002).

H. Hiramatsu, K. Ueda, H. Ohta, M. Hirano, T. Kamiya, and H. Hosono, *Appl. Phys. Lett.*, **82(7)**, 1048 (2003).

Y. Hishikawa, N. Nakamura, S. Tsuda, S. Nakano, Y. Kishi, and Y. Kuwano, *Jpn. J. Appl. Phys.*, **30**, 1008 (1991).

R. Hoffmann, *Solids and Surfaces: A chemist's view of Bonding in Extended Structures*, VCH Publishers, New York (1988).

R. L. Hoffman, *J. Appl. Phys.*, **95**, 5813 (2004).

R. L. Hoffman, B. J. Norris, and J. F. Wager, *Appl. Phys. Lett.*, **82**, 733 (2003).

J. Hölsa, *Inorg. Chim. Acta*, 139, 257 (1987).

Y. Hongpeng, G. Hong, X. Zeng, C.-H. Kim, C.-H. Pyun, B.-Y. Yu, and H.-S. Bae, *J. Phys. Chem. Solids*, **61**, 1985 (2000).

H. Hosono, H. Ohta, K. Hayashi, M. Orita, and M. Hirano, *J. Cryst. Growth*, **237-239**, 496 (2002), and references therein.

H. Hosono, M. Yasukawa, and H. Kawazoe, *J. Non-Cryst. Solids*, **203**, 334 (1996).

J. E. Huheey, *Inorganic Chemistry: Principles of Structure and Reactivity*, 3rd ed., Harper & Row, New York (1983).

J. Huster, and W. Bronger, *Z. Anorg. Allg. Chem.*, **625**, 2033 (1999).

S. Inoue, K. Ueda, and H. Hosono, *Phys. Rev. B*, **64**, 245211 (2001).

K. Ishikawa, S. Kinoshita, Y. Suzuki, S. Matsuura, T. Nakanishi, M. Aizawa, and Y Suzuki, *J. Electrochem. Soc.*, **138(4)**, 1166 (1991).

A. Janosi, *Acta Crystallogr.*, **17(3)**, 311 (1964).

M. K. Jayaraj, A. D. Draeseke, J. Tate, and A. W. Sleight, *Thin Soild Films*, **397(1,2)**, 244 (2001).

M. Jinno, H. Kurokawa, and M. Aono, *Jpn. J. Appl. Phys.*, **38**, 4608 (1999).

M. Julien-Pouzol, S. Jaulmes, A. Mazurier, and M. Guittard, *Acta Crystallogr.*, B**37**, 1901 (1981).

T. Jűstel, and H. Nikol, *Adv. Mater.*, **12(7)**, 527 (2000).

V. H. Kasper, *Z. Anorg. Allg. Chemie*, **349**, 113 (1967).

H. Kawazoe, N. Ueda, H. Un'no, H. Hsono, and H. Tanoue, *J. Appl. Phys.*,**76**, 7935 (1994).

H. Kawazoe, M. Yasukawa, H. Hyodo, M. Kurita, H. Yanagi, and H. Hosono, *Nature*, **389**, 939 (1997).

F. Kellendonk, and G. Blasse, *J. Chem. Phys.*, **75(2)**, 561 (1981).

F. Kellendonk, T. Van den Belt, and G. Blasse, *J. Chem. Phys.*, **76(3)**, 1194 (1982).

F. Kellendonk, M. A. van Os, and G. Blasse, *Chem. Phys. Lett*, **61(2)**, 239 (1979).

H. S. Kiliaan, F. P. van Herwijnen, and G. Blasse, *J. Solid State Chem.*, 74, 39 (1988).

C. Kittel, *Introduction to Solid State Physics*, 7th ed., John Wiley & Sons, New York (1996).

W. Klee, and H. Schaefer, *Z. Anorg. Allg. Chem.*, **479**, 125 (1981).

A. Koch, and C, Riekel, *Rev. Sci. Instrum.*, **67(5)**, 1737 (1996).

N. Kodama, K. Tanaka, T. Utsunomiya, Y. Hoshino, F. Maruma, N. Ishizawa, and M. Kato, *Solid State Ionics*, **14**, 17 (1984).

J. Koike, T. Kojima, R. Toyonaga, A. Kagami, T. Hase, and S. Inaho, *J. Electrochem. Soc.*, **126(6)**, 1008 (1979).

P. Kubelka, *J. Opt. Soc. Am.*, **38**, 448 (1948).

P. Kubelka and F. Munk, *Z. Tech. Phys.*, **12**, 593 (1931).

A. Kudo, H. Yanagi, H. Hosono, H. Kawazoe, *Appl. Phys. Lett.*, **73(2)**, 220 (1998).

S. A. Kutovoi: S. A. Kutovoi, V. V. Laptev, and S. Yu. Matsnev, *Sov. J. Quantum Electron*, **21**, 131 (1991).

T. R. N. Kutty, and R. Vivekanadan, *Mater. Res. Bull.*, **22**, 1457 (1987).

R. Kykyneshi, *MS thesis*, Oregon State University (2004).

R. Kykyneshi, B. C. Nielsen, J. Tate, J. Li, A. W. Sleight, *J. Appl. Phys.*, **96(11)**, 6188 (2004).

J. R. Lakowicz, *Principles of Fluorescence Spectroscopy*, Plenum Press, New York (1983).

J.-K. Lee, H.-M. Kim, S.-H. Park, J.-J. Kim, B.-R. Rhee, and S.-H. Sohn, *J. Appl. Phys.*, **92(10)**, 5761 (2002).

K.-G. Lee, B.-Y. Yu, C.-H. Pyun, and S.-I. Moh, *Solid State Comm.*, **122**, 485 (2002).

H. W. Leverenz, *An introduction to luminescence of solids*, John Wiley & Sons, New York (1950).

B. G. Lewis, and D. C. Paine, *Mater. Res. Soc. Bull.*, **25(8)**, 22 (2000).

C. K. Lowe-Ma, T. A. Vanderah, *J. Solid State Chem.*, **117(2)**, 363 (1995).

O. Madelung, and M. Schulz (Eds.), *Landolt-Bornstein: Numerical Data and Functional Relationships in Science and Technology: Group III*, vol. 22a, Springer-Verlag, Berlin (1987).

I. C. Madsen, and R. J. Hill, *J. Appl. Crystallogr.*, **27**, 385 (1994).

S. Masuda, K. Kitamura, Y. Okumura, S. Miyatake, and, T. Kawai, *J. Appl. Phys.*, **93**, 1624 (2003).

A. Meijerink, and G. Blasse, *J. Lumin.*, **47**, 1 (1990).

J-P. Meyn :J-P. Meyn, T. Jensen, and G. Huber, *IEEE J. Quantum. Electron*, **30**, 913 (1994).

T. Minami, *Mater. Res. Soc. Bull.*, **25(8)**, 38 (2000).

T. Miyata, T. Nakatani, T. Minami, *J. Lumin.*, **87-89**, 1183 (2000).

H. Mizoguchi, N. S. P. Bhuvanesh, P. M. Woodward, *Chem. Commun.*, 1084 (2003).

H. Mizoguchi, H. W. Eng, and P. M. Woodward, *Inorg. Chem.***, 43**, 1667 (2004).

H. Mizoguchi, P. M. Woodward, C.-H. Park, and D. A. Keszler, *J. Am. Chem. Soc.*, **126(31)**, 9796 (2004).

T. Moriga, D. D. Edwards, T. O. Mason, G. B. Palmer, K. R. Poepplemeier, J. L. Schindler, C. R. Kannewurf, and I. Nakabayashi, *J. Am. Ceram. Soc.*, **81**, 1310 (1998).

R. Nagarajan, A. D. Draeseke, A. W. Sleight, and J. Tate, *J. Appl. Phys.*, **89(12)**, 8022 (2001).

M. Nakamura, N. Kimizuka, and T. Mohri, *J. Solid State Chem.*, **86**, 16 (1990).

X. Nie, S.-H. Wei, S. B. Zhang, *Phys. Rev. Lett.*, **88**, 066405 (2002).

B. J. Norris, J. Anderson, J. F. Wager, and D. A. Keszler, *J. Phys. D: Appl. Phys.*, **36**, L105 (2003).

H. Ohta, and H. Hosono, *Materials Today*, **7(6)**, 42 (2004).

H. Ohta, K. Nomura, M. Orita, M. Hirano, K. Ueda, T. Suzuki, Y. Ikuhara, and H. Hosono, *Adv. Funct. Mater.*, **13**, 139-144 (2003).

H. Ohta, M. Orita, M. Hirano, I. Yagi, K. Ueda, and, H. Hosono, *J. Appl. Phys.*, **91(5)**, 3074 (2002).

T. Ohtani, H. Takeuchi, K. Koh, and T. Kaneko, *J Alloys Compd.*, **317-318**, 201 (2001).

B. Ostrick, M. Fleischer, U. Lampe, and H. Meixner, *Sens. Actuators*, **B44**, 601 (1997).

L. Ozawa, H. Forest, P. M. Jaffe, and G. Ban, *J. Electrochem. Soc.*, **118(3)**, 482 (1971).

A. Pabst, *American Mineralogist*., **59**, 353 (1974).

M. Palazzi, *Acad. Sci., Paris, C. R.*, **292**, 789 (1981).

M. Palazzi, C. Carcaly, and . Flahaut, *J. Solid State Chem.*, **35**, 150 (1980).

M. Palazzi, and S. Jaulmes, *Acta Crystallogr.*, **B37**, 1337 (1981).

C.-H. Park, D. A. Keszler, H. Yanagi, J. Tate, *Thin solid films*, 445, 288 (2003).

S Park, *Ph.D. Thesis*, Oregon State University (2002).

S. Park, D. A. Keszler, M. M. Valencia, R. L. Hoffman, J. P. Bender, and J. F. Wager, *Appl. Phys. Lett.*, **80**, 4393 (2002).

Z. Pei, Q. Su, Y. Chui, and J. Zhang, *Mater. Res. Bull*., **26**(10), 1059 (1991).

G. A. Peterson, D. A. Keszler, and T. A. Reynolds, *Int. J. Inorg. Mater.*, **2**, 101 (2000).

J. M. Phillips, R. J. Cava, G. A. Thomas, S. A. Carter, J. Kwo, T. Siegrist, J. J. Krajewski, J. H. Marshall, W. F. Peck, Jr., and D. H. Rapkine, *Appl. Phys. Lett.*, **67(15)**, 2246 (1995)

R. E. Presley, C.-L. Munsee, C.-H. Park, D. Hong, J. F. Wager, and D. A. Keszler, *J. Phys. D: Appl. Phys.*, **37**, 2810 (2004).

K. R. Reddy, K. Annapurna, and S. Buddhudu, *Mater. Res. Bull.*, **31(11)**, 1355 (1996).

T. A. Reynolds, *PhD dissertation*, Oregon State University (1992).

J. Rodriguez-Carvajal, FULLPROF: A program for Rietveld Refinement and Pattern Matching Analysis, *In Abstract of the Satellite Meeting on Powder Diffraction of the XV Congress of the IUCr*, p 127, Thoulouse, France (1990).

C. R. Ronda, *J. Alloys Compd.*, **225**, 534 (1995).

R.C.Ropp, *Luminescence and the Solid State*, Elsevier Science, Amsterdam (1991).

D. K. Sardar, F. Castano, J. A. French, J. B. Gruber, T. A. Reynolds, T. Alekel, D. A. Keszler, and B. L. Clark, *J. Appl. Phys.*, **90**, 4997 (2001).

M. Sauvage, *Acta Crystallogr.*, **B30**, 2786 (1974).

G. Savelsberg, and H. Schaefer, *Z. Naturforsch.* 33**B**, 370 (1978).

E. F. Schubert, *Light-Emitting Diodes*, Cambridge University Press, Cambridge (2003).

R. D. Shannon, *Acta Crystallogr.*, **A32**, 751 (1976).

G. M. Sheldrick, SHELXS-97 – A program for automatic solution of crystal structure refinement, 1997, Release 97-2.

T. Shiga, L. C. Pitchford, J.-P. Boeuf, and S. Mikoshiba, *J. Phys. D: Appl. Phys.*, **36**, 512 (2003).

S. Shionoya, and W. M. Yen (Eds.), *Phosphor Handbook*, CRC Press, Boca Raton, FL (2000).

D. Shriver, and P. Atkins, *Inorganic Chemistry*, 3rd ed., W. H. Freeman and Company, New York (1999).

A. J. Smith, and A. J. E. Welch, *Acta Cryst.*, **13**, 653 (1960).

A. M. Srivastava, *Mater. Res. Bull.*, **34**, 1391 (1999).

P. Stephens, *J. Appl. Crystallogr.*, **32**, 281 (1999).

H. Sun, *PhD dissertation*, Oregon State University (1989).

C. Suryanarayana, and M. G. Norton, *X-Ray Diffraction A Practical Approach*, Plenum Press, New York (1998).

A. P. Sutton, *Electronic Structure of Materials*, Oxford University Press, Oxford (1996).

J. Tate, M. K. Jayaraj, A. D. Draeseke, T. Ulbrich, A. W. Sleight, K. A. Vanaja, R. Nagarayan, J. F. Wager, and R. L. Hoffman, *Thin Soild Films*, **411(1)**, 119 (2002).

Chr. L. Teske, . *Anorg. Allg. Chem.,* **419**, 67 (1976).

G. Thomas, *Nature*, **389**, 907 (1997).

C.P. Udawatte, M. Yoshimura, *Mater. Lett.*, **47**, 7 (2001).

K. Ueda, T. Hase, H. Yanagi, H. Kawazoe, H. Hosono, H. Ohta, M. Orita, and M. Hirano, *J. Appl. Phys.*, **89**, 1790 (2001).

K. Ueda, and H. Hosono, *J. Appl. Phys.*, **91(7)**, 4768 (2002).

K. Ueda, S. Inoue, S. Hirose, H. Kawazoe, and H. Hosono, *Appl. Phys. Lett.*, **77(17)**, 2701 (2000).

K. Ueda, S. Inoue, H. Hosono, N. Sarukura, and M. Hiranu, *Appl. Phys. Lett.*, **78(16)**, 2333 (2001).

F. B. M. Van Zon, D. C. Koningsberger, E. W. J. L. Oomen, and G. Blasse, *J. Solid State Chem.*, **71**, 396 (1987).

J. F. Wager, *Science*, **300**, 1245 (2003).

Y. C. Wang, and F. J. DiSalvo, *J. Solid State Chem.*, **156**, 44 (2001).

Y. Wang, K. Uheda, H. Takizawa, U. Mizumoto, and T. Endo, *J. Electrochem. Soc.*, **148(8)**, G430, (2001).

G. W. Watson, *J. Chem. Phys.*, **114**, 758 (2001).

A. R. West, *Solid State Chemistry and its Applications*, John Wiley & Sons, Singapore, (1989).

K.-Th. Wilke, *Z. Phys. Chem. (Leipzig)*, **208**, 361 (1958).

P. M. Woodward, *Acta Crystallogr.*, **B53**, 44 (1997).

H. Yanagi, T. Hase, S. Ibuki, K. Ueda, and H. Hosono, *Appl. Phys. Lett.*, **78(11)**, 1583 (2001).

H. Yanagi, S.-I. Inoue, K. Ueda, H. Kawazoe, H. Hosono, and N. Hamada, *J. Appl. Phys.*, **88(7)**, 4159 (2000).

H. Yanagi, H. Kawazoe, A. Kudo, M. Yasukawa, and H. Hosono, *J. Electroceram.*, **4(2/3)**, 407 (2000).

H. Yanagi, S. Park, A. D. Draeseke, D. A. Keszler, and J. Tate, *J. Solid State Chem.*, **175**, 34 (2003).

H. Yanagi, J. Tate, S. Park, C.-H. Park, D. A. Keszler, *Appl. Phys. Lett.*, **82**, 2814 (2003).

R. A. Young, *The RIETVELD method*, Oxford University Press, London (1995).

W. H. Zachariasen, *Acta Crystallogr.*, 2, 60 (1949).

W. J. Zhu, Y. Z. Huang, F. Wu, C. Dong, H. Chen, and Z. X. Zhao, *Mater. Res. Bull.*, **29(5)**, 505 (1994).

APPENDICES

APPENDIX A: BaCuSF films by pulsed laser deposition

BaCuSF films were prepared by using pulsed laser depositon. Amorphous BaCuSF films were annealed by using a variant of the reactive solid phase epitaxy (R-SPE) at 650^{o}C for 15h or in flowing H_2S(g) at 350-400^{o}C for 2h. Films annealed by using R-SPE exhibit red luminescence, and they are insulating with high transmittance (85% transmittance at 550 nm) (Figures A-1 and A-2). Annealing in flowing H_2S(g) at 350^{o}C produces highly conducting (σ = 710 S/cm, μ = 0.9 cm^2/V s) films with 50% transmittance at 550 nm; while films annealed in flowing H_2S(g) at 400^{o}C are highly transparent (85% transmittance at 550 nm), insulating ($\sigma \sim 8.5 \times 10^{-3}$ S/cm), and exhibit no luminescence. The highest conductivity and mobility (σ = 1400 S/cm, μ = 4 cm^2/V s) have been observed in 2% K-doped BaCuSF films annealed in flowing H_2S(g) at 350^{o}C, which exhibit 60% transmittance at 550 nm (Figure A-3).

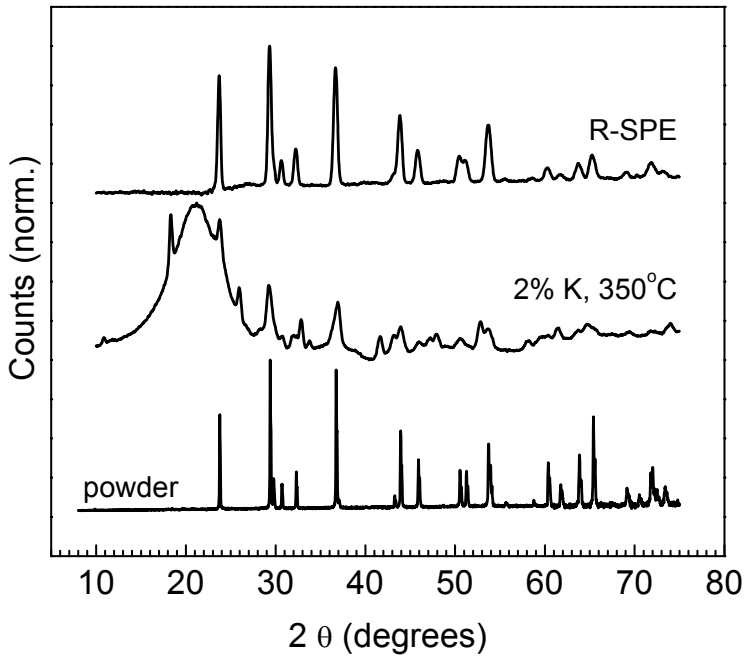

Figure A-1. XRD patterns of BaCuSF powder sample, BaCuSF film annealed by R-SPE, and BaCuSF:K (2%) film annealed in flowing H_2S(g). .

Table A-1. Summary of amorphous BaCuSF film preparation by pulsed laser deposition.

Target	Sintered disks of BaCuSF, $Ba_{0.975}K_{0.025}CuSF$, and $Ba_{0.9}K_{0.1}CuSF$
Laser	KrF (248 nm)
Repetition frequency (Hz)	10
Energy density (J/cm^2/pulse)	2
Pressure (Torr)	4×10^{-9}
Substrate	GE 124 fused silica
Substrate temperature	Room temperature
Substrate-target distance (mm)	50.8

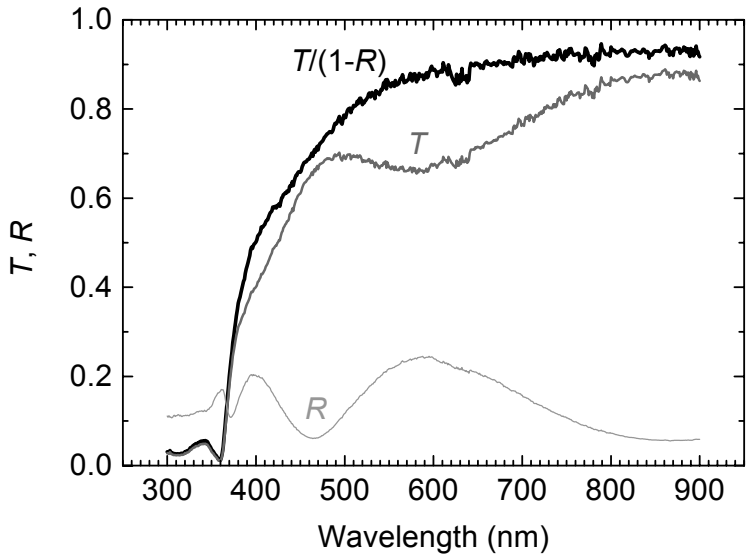

Figure A-2. Transmittance (T) and reflectance (R) of BaCuSF film annealed by R-SPE. The substrate is SiO2. The effect of the interference fringes was removed by plotting $T/(1-R) \cong \exp(-\alpha d)$, where α is the absorption coefficient and d is the film thickness.

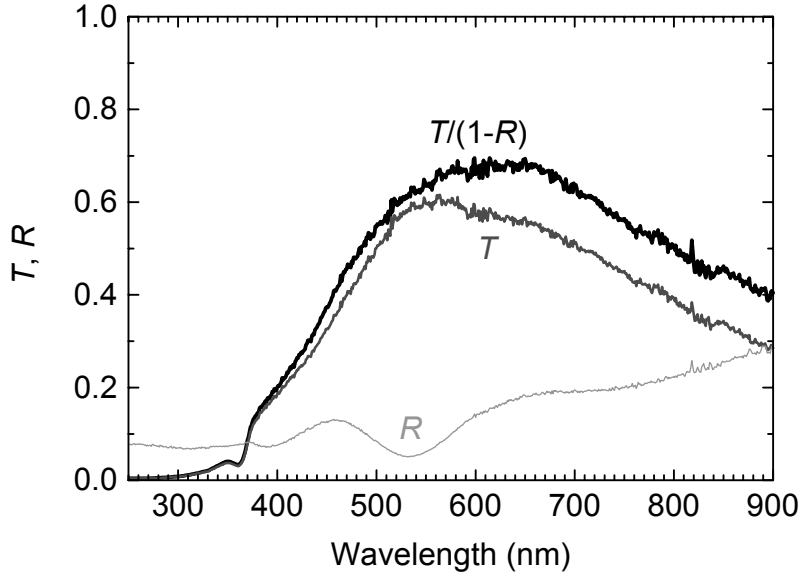

Figure A-3. Transmittance (T) and reflectance (R) of BaCuSF film annealed in flowing H_2S(g) at 350^{o}C.

APPENDIX B. CURRICULUM VITA

EDUCATION

Ph.D., Inorganic Chemistry, Oregon State University, Corvallis, OR (2005)

M.S., Inorganic Chemistry, Seoul National University, Seoul, Korea (1994)

B.S., Chemistry, Seoul National University, Seoul, Korea (1992)

EXPERIENCE

Graduate Research Assistant, Oregon State University, Corvallis, OR
[Description: p-type Transparent Semiconductor Research / Development for Polycrystalline Thin-Film Solar Cells /] (2001-2005)

Research Scientist, Korea Institute of Science and Technology, Seoul, Korea
[Description: Development of Luminescent Materials] (1994-2001)

Graduate Teaching Assistant, Seoul National University, Seoul, Korea (1992-1994)

FELLOWSHIP

Shoemaker Award for outstanding senior graduate student (2004)

Benedict Award for outstanding second-year graduate student (2003)

Ingram Award for outstanding first-year graduate student (2002)

PUBLICATIONS

27. **C.-H. Park**, D. A. Keszler, A. Yokochi, R. Kykyneshi, and J. Tate, "Structre, *p*-type Conductivity in wide-band-gap SrCuSF, and Gap Modulation in $SrCu[Q_{1-y}Q'_y]F$ (Q, Q' = S, Se, Te)", *in preparation.*

26. **C.-H. Park**, and D. A. Keszler, "Luminescence of $BaSnO_3$ prepared via $BaSn(OH)_6$", *submitted to Mater. Res. Bull.*

25. **C.-H. Park**, D. A. Keszler, R. Kykyneshi, and J. Tate, "*p*-type Conductivity, Gap Modulation, and Phase Stabilization in $BaCu_2Q_2$ (Q=S, Se)", *in preparation.*

24. **C.-H. Park**, D. A. Keszler, A. Yokochi, R. Kykyneshi, and J. Tate, "Structre, *p*-type Conductivity in wide-band-gap SrCuSF, and Gap Modulation in $SrCu[Q_{1-y}Q'_y]F$ (Q, Q' = S, Se, Te)", *in preparation.*

23. **C.-H. Park**, D. A. Keszler, and A. Yokochi, "Structure and Physical Properties of BaAgSF", *in preparation.*

22. **C.-H. Park**, D. A. Keszler, and A. Yokochi, "Crystal Structures of Single Crystal BaCuSF and BaCuQF (Q=S, Se)", *in preparation.*

21. N. L. Dehuff, E. S. Kettenring, D. Hong, H. Q. Chiang, J. F. Wager, R. L. Hoffman, **C.-H. Park**, and D. A. Keszler, "Transparent Thin-Film Transistors with Zinc Indium Oxide Channel Layer", *J. Appl. Phys.*, *in print*.

20. **C.-H. Park**, D. A. Keszler, A. Yokochi, R. Kykyneshi, and J. Tate, "Optical and Electrical Properties of BaCuTeF", *submitted to J. Solid State Chem.*

19. **C.-H. Park**, and D. A. Keszler, "Luminescence Properties of Eu^{3+}-doped Monoclinic and Trigonal $(La,Y)Sc_3(BO_3)_4$", *submitted to Solid State Sciences*

18. N. Ye, **C.-H. Park**, and D. A. Keszler, "Crystal Structures of $M_3Sc_2(BO_3)_4$ (M = Ba, Sr) and Eu^{2+} Luminescence", *in preparation*

17. R. E. Presley, C. L. Munsee, **C.-H. Park**, J. F. Wager, and D. A. Keszler, "Tin Oxide Transparent Thin-Film Transistors", *J. Phys. D: Appl. Phys.*, **37**, 2810-2813 (2004).

16. H. Mizoguchi, P. M. Woodward, **C.-H. Park**, and D. A. Keszler, "Strong Near Infrared Luminescence in $BaSnO_3$", *J. Am. Chem. Soc.*, **126(31)**, 9796-9800 (2004).

15. **C.-H. Park**, D. A. Keszler, H. Yanagi, J. Tate, "Gap modulation in $MCu[Q_{1-x}Q'_x]F$ (M=Ba, Sr; Q, Q'=S, Se, Te) and related materials" *Thin Solid Films*, **445**, 288 (2003)

14. H. Yanagi, J. Tate, S. Park, **C.-H. Park**, D. A. Keszler, "p-type conductivity in wide bandgap BaCuQF (Q=S, Se)" *Appl. Phys. Lett.*, **82(17)**, 2814 (2003)

13. X. Wu, H. You, H. Cui, X. Zeng, G. Hong, C.-H. Kim, C.-H. Pyun, B.-Y. Yu, **C.-H. Park**, "Vacuum ultraviolet optical properties of $(La,Gd)PO_4:RE^{3+}$ (RE=Eu, Tb)", *Mat. Res. Bull.*, **37**(9), 1531 (2002)

12. H. You, X. Wu, X. Zeng, G. Hong, C.-H. Kim, C.-H. Pyun, and **C.-H. Park**, "Infrared spectra and VUV excitation properties of BaLnB9O16RE (Ln=La, Gd; RE=Eu, Tb)", *Materials Science and Engineering B*, **86**, 11-14 (2001)

11. C.-H. Pyun, **C.-H. Park**, S.-J. Park, B.-Y. Yu, H.-S. Bae, and C.-H. Kim, "Luminescence of $SrY_2O_4:Eu^{3+}$", *J. Rare Earth*, **18(3)**, 14-17 (2000)

10. C.-H. Choi, **C.-H. Park**, C.-H. Pyun, C.-H. Kim and H.-K. Chae, "Sol-Gel Approach to Eu^{3+} Doped Yttrium-Rich Borate Phosphors", *J. Rare Earth*, **18(3)**, 18-23 (2000)

9. G. Song, H. You, G. Hong, S. Gan, C.-H. Kim, C.-H. Pyun, B.-Y. Yu, H-S. Bae, I.-E. Kwon and **C.-H. Park**, "VUV Spectra of $Y_{1.95-x}Gd_xSiO_5:Eu_{0.05}$", *Chinese J. Lumin.*, **21(2),** 145-149 (2000)

8. C.-H. Kim, I.-E. Kwon, **C.-H. Park**, Y.-J. Hwang, H.-S. Bae, B.-Y. Yu, C.-H. Pyun, G.-Y. Hong, "Phosphors for plasma display panels", *J. Alloys Comp.*, **311**, 33 (2000)

7. **C.-H. Park**, C.-H. Kim, C.-H. Pyun, J.-H. Choy, "Luminescence of Sr_2CeO_4", *J. Luminescence*, **87-89**, 1062 (2000)

6. **C.-H. Park**, S.-J. Park, B.-Y. Yu, H.-S. Bae, C.-H. Kim, C.-H. Pyun, G.-Y. Hong, "VUV excitation of $Y_3Al_5O_{12}$:Tb phosphor prepared by a sol-gel process", *J. Mat. Sci. Lett.*, **19**(4), 335 (2000)

5. H. You, G. Hong, X. Zeng, C.-H. Kim, C.-H. Pyun, B.-Y. Yu, H.-S. Bae, **C.-H. Park** and I.-E. Kwon, "Study on vacuum-UV luminescent properties of $YAl_3B_4O_{12}$:RE (RE=Eu, Tb)", *J. Chinese Rare Earth Soc.*, **17**, 656-658 (1999)

4. G.-Y. Hong, X. Zeng, H. You, C.-H. Kim, C.-H. Pyun, **C.-H. Park**, B.-Y. Yu, H.-S. Bae and I.-E. Kwon, "Influence of flux on the structure and luminescence of the phosphor $BaAl_{12}O_{19}$:Mn", *Chinese J. Lumin.*, **20(4)**, 311-315 (1999)

3. S.-J. Park, **C.-H. Park**, B.-Y. Yu, H.-S. Bae, C.-H. Kim, C.-H. Pyun, "Structure and Luminescence of SrY_2O_4:Eu", *J. Electrochem. Soc.*, **146**(10) 3903 (1999).

2. O.-S. Jung, S.-H. Park, **C.-H. Park**, and C.-G. Park, "Zigzag double-strands consisting of coordination-gallery, $Ag_3(NO_3)_3(Py_2S)_2 \cdot 2H_2O$", *Chemistry Letters*, **9**, 923-924 (1999)

1. J. C. Park, S. G. Kang, D. H. Kim, **C.-H. Park**, G. Demazeau, and J. H. Choy, "Variation of high T_c superconducting property of $La_2Li_xCu_{1-x}O_{4+\delta}$ upon

electrochemically induced structural and magnetic transformations", Proc. 5th ICMAS, 115-120 (1993)

CONFERENCES

25. D. A. Keszler, **C.-H. Park**, "New Solid State Borates", The 227th ACS National Meeting, Mar. 28-Apr 1, 2004, Anaheim, CA

24. **C.-H. Park**, Y.-I. Kim, S.-J. Park, B.-Y. Yu, H.-S. Bae, C.-H. Pyun, C.-H. Kim and J.-H. Choy, "Localization of Eu^{3+} in SrY_2O_4:Eu with the $^5D_0$-$^7F_0$ transition", The 198th Meeting of the Electrochemical Society, Oct. 22-27, 2000, Phoenix, USA

23. **C.-H. Park**, B.-Y. Yu, H.-S. Bae, I.-E. Kwon, C.-H. Pyun, C.-H. Kim and J.-H. Choy, "Two Eu sites in Sr_2CeO_4:Eu", The 84th Chemical Society Meeting (2000)

22. **C.-H. Park**, B.-Y. Yu, I.-E. Kwon, H.-S. Bae, Y.-J. Hwang, C.-H. Kim and C.-H. Pyun, "Controllable Color of Eu^{2+} in $(Ba_{1-\alpha}Sr_\alpha)_2SiO_4$", The 5th International Conference on the Science and Technology of Display Phosphors, Nov. 8-10, 1999, San Diego, California

21. H.-R. Kim, **C.-H. Park**, C.-H. Pyun, C.-H. Kim, and H.-K.Chae, "Preparation and Characterization of Zinc Silicate Phosphor by Sol-Gel Process", The 84th Chemical Society Meeting (1999)

20. **C.-H. Park**, C.-H. Kim, C.-H. Pyun, and J.-H. Choy, "Luminescence Properties of Sr_2CeO_4", ICL'99 (International conference on Luminescence and Optical Spectroscopy of Condensed Matter), August 23-27, 1999, OSAKA, Japan

19. **C.-H. Park**, S.-J. Park, B.-Y. Yu, H.-S. Bae, Y.-J. Hwang, I.-E. Kwon, C.-H. Kim, and C.-H. Pyun, "Luminescence Properties of SrY_2O_4:Eu", ICL'99 (International conference on Luminescence and Optical Spectroscopy of Condensed Matter), August 23-27, 1999, OSAKA, Japan

18. H.-R. Kim, H.-K.Chae, **C.-H. Park**, C.-H. Pyun, and C.-H. Kim, "Evolution of Sr_2CeO_4 Phosphor from the Molecular Precursors, The 3rd Korea-China Joint Workshop on Advanced Materials, August 23-27, 1999, Cheju, Korea

17. B.-Y. Yu, H.-S. Bae, **C.-H. Park**, I.-E. Kwon, C.-H. Pyun, and C.-H. Kim, "PDP Phosphors & VUV Spectrophotometry", The 3rd Korea-China Joint Workshop on Advanced Materials, August 23-27, 1999, Cheju, Korea

16. X.-Q. Zeng, G.-Y. Hong, I.-E. Kwon, B.-Y. Yu, H.-S. Bae, **C.-H. Park**, C.-H. Pyun, and C.-H. Kim, "VUV and UV Excitation Spectra of Some Eu^{3+} Doped Phosphors", The 3rd Korea-China Joint Workshop on Advanced Materials, August 23-27, 1999, Cheju, Korea

15. C.-H. Kim, I.-E. Kwon, **C.-H. Park**, Y.-J. Hwang, H.-S. Bae, B.-Y. Yu, C.-H. Pyun, G.-Y. Hong, "Phosphors for plasma display panels", IUMRS-ICAM'99, June 13-18, 1999, Beijing, China

14. I.-E. Kwon, B.-Y. Yu, H.-S. Bae, **C.-H. Park**, T.-W. Kwon, Y.-J. Hwang, C.-H. Kim and C.-H. Pyun, "VUV excitation of borate phosphors", The 83th Korean Chemical Society Meeting (1999)

13. Y.-J. Hwang, B.-Y. Yu, H.-S. Bae, **C.-H. Park**, T.-W. Kwon, I.-E. Kwon, C.-H. Kim and C.-H. Pyun, "Preparation of Silicate phosphors doped with Tb^{3+}", The 83th Korean Chemical Society Meeting (1999)

12. **C.-H. Park**, B.-Y. Yu, H.-S. Bae, T.-W. Kwon, Y.-J. Hwang, I.-E. Kwon, C.-H. Kim and C.-H. Pyun, "Controllable Color of Eu^{2+} in $(Ba_{1-\alpha}Sr_{\alpha})_2SiO_4$", The 83th Korean Chemical Society Meeting (1999)

11.**C.-H. Park**, C.-H. Kim, C.-H. Pyun, and J.-H. Choy, "Luminescence Properties of Sr_2CeO_4", The 83th Korean Chemical Society Meeting (1999)

10. H.-R. Kim, C.-H. Choi, **C.-H. Park**, C.-H. Pyun, C.-H. Kim, H.-S. Youn, and H.-K.Chae, "Evolution of Sr_2CeO_4 phosphor from $Sr_2Ce_2O_2(OiPr)_8$", The 83th Chemical Society Meeting (1999)

9. **C.-H. Park**, B.-Y. Yu, H.-S. Bae, S.-J. Park, T.-W. Kwon, I.-E. Kwon, C.-H. Kim, and C.-H. Pyun, G.-Y. Hong, "Synthesis of $Y_3Al_5O_{12}$:Tb Phosphor by Sol-Gel Method", The 82th Chemical Society Meeting (1998)

8. **C.-H. Park**, B.-Y. Yu, H.-S. Bae, S.-J. Park, T.-W. Kwon, I.-E. Kwon, C.-H. Kim, and C.-H. Pyun, G.-Y. Hong, "Effects of Aluminum Fluoride on Formation of $BaMgAl_{10}O_{17}$:Eu", The 82th Chemical Society Meeting (1998)

7. I.-E. Kwon, B.-Y. Yu, H.-S. Bae, **C.-H. Park**, S.-J. Park, T.-W. Kwon, C.-H. Kim, C.-H. Pyun, and G.-Y. Hong, "Synthesis and Properties of YBO_3:Tb,Gd Phosphor", The 82th Chemical Society Meeting (1998)

6. **C.-H. Park**, S.-J. Park, B.-Y. Yu, H.-S. Bae, I.-E. Kwon, C.-H. Kim, C.-H. Pyun, and G.-Y. Hong, "Synthesis of $Y_3Al_5O_{12}$:Tb Phosphor by Sol-Gel Method", The

18th IDRC (International Display Research Conference & Exhibition), Sep. 28-Oct. 1, 1998, Seoul, Korea

5. **C.-H. Park**, B.-Y. Yu, H.-S. Bae, S.-J. Park, I.-E. Kwon, C.-H. Kim, and C.-H. Pyun, G.-Y. Hong, "Effects of Aluminum Fluoride on Formation of $BaMgAl_{10}O_{17}$:Eu", The 18th IDRC (International Display Research Conference & Exhibition), Sep. 28-Oct. 1, 1998, Seoul, Korea

4. **C.-H. Park**, B-Y. You, H.-S, Bae, S.-J. Park, T.-W. Kwon, C.-H. Kim, and C.-H. Pyun, "Luminescence of the Pr^{3+} ion in $ATiO_3$ (A=Ca, Sr, Ba)", The 80th Korean Chemical Society Meeting (1997)

3. C.-H. Kim, H. Choi, **C.-H. Park**, B-Y. You, H.-S, Bae, C.-I. Jeon, and C.-H. Pyun, "Luminescence of $Ca_{1-x}La_xS$:Eu", The 79th Korean Chemical Society Meeting (1997)

2. **C.-H. Park**, C.-I. Jeon, B-Y. You, H. Choi, H.-S, Bae, C.-H. Kim, and C.-H. Pyun, "Crystal Structure of $Ca_{1-x}Sr_xTiO_3$", The 79th Korean Chemical Society Meeting (1997)

1. J. C. Park, S. G. Kang, D. H. Kim, **C. H. Park**, G. Demazeau, and J. H. Choy, "Variation of high Tc superconducting property of $La_2Li_xCu_{1-x}O_{4+}$ upon electrochemically induced structural and magnetic transformations", The 5th International Conference ICMAS-93 (1993)